

**Molecular Responses of *Arabidopsis thaliana* to
Environmental Metal Stressors: Root Cadmium Exposure
and Metallic Ultra-Fine Particles from Traffic**

DISSERTATION

zur Erlangung eines akademischen Grades eines

Doktors der Naturwissenschaften (Dr. rer. nat.)

in der Graduiertenschule für Mathematik und Naturwissenschaften

(BayNAT)

der Universität Bayreuth

vorgelegt von

Ludwig Richtmann

aus Neustadt a. d. Waldnaab

Bayreuth, 2025

Die vorliegende Arbeit wurde in der Zeit vom Mai 2020 bis November 2025 in Bayreuth am Lehrstuhl für Pflanzenphysiologie unter Betreuung von Herrn Professor Dr. Stephan Clemens angefertigt.

Vollständiger Abdruck der von der Bayreuther Graduiertenschule für Mathematik und Naturwissenschaften (BayNAT) der Universität Bayreuth genehmigten Dissertation zur Erlangung des akademischen Grades eines Doktors der Naturwissenschaften (Dr. rer. nat).

Form der Dissertation: Monographie

Dissertation eingereicht am: 04.07.2025

Zulassung durch das Leitungsgremium: 15.07.2025

Wissenschaftliches Kolloquium: 30.10.2025

Amtierender Direktor: Prof. Dr. Jürgen Senker

Prüfungsausschuss:

Prof. Dr. Stephan Clemens (Gutachter)

Prof. Dr. Angelika Mustroph (Gutachterin)

Prof. Dr. Klaus Ersfeld (Vorsitz)

Prof. Dr. Claus-D. Kuhn

Teile der Arbeit sind bereits in folgenden Publikationen erschienen:

Richtmann, L.; Prochetto, S.; Thiébaut, N.; Sarthou, M. C. M.; Boutet, S.; Hanikenne, M.; Clemens, S.; Verbruggen, N. Arabidopsis Thaliana Root Responses to Cd Exposure: Insights into Root Tip-Specific Changes and the Role of HY5 in Limiting Cd Accumulation and Promoting Tolerance. *Plant J.* **2025**, 122 (6), e70298. <https://doi.org/10.1111/tpj.70298>.

Diese Publikation ist in der vorliegenden Arbeit mit Literaturstelle 179 zitiert.

Richtmann, L.; Opel, T.; Maier, M.; Langhof, N.; Clemens, S. Establishment of a System to Analyze Effects of Airborne Ultra-Fine Particulate Matter from Brake Wear on Plants under Realistic Exposure Conditions. *J. Hazard. Mater.* **2024**, 469, 134084. <https://doi.org/10.1016/j.jhazmat.2024.134084>.

Diese Publikation ist in der vorliegenden Arbeit mit Literaturstelle 169 zitiert.

Thiébaut, N.; Sarthou, M.; Richtmann, L.; Pergament Persson, D.; Ranjan, A.; Schloesser, M.; Boutet, S.; Rezende, L.; Clemens, S.; Verbruggen, N.; Hanikenne, M. Specific Redox and Iron Homeostasis Responses in the Root Tip of Arabidopsis upon Zinc Excess. *New Phytol.* **2025**, 246 (4), 1796–1815. <https://doi.org/10.1111/nph.70105>.

Diese Publikation ist in der vorliegenden Arbeit mit Literaturstelle 180 zitiert

Table of contents

1	Abstract	1
2	Zusammenfassung	2
3	List of abbreviations	4
4	Introduction	6
4.1	Humans shape the environment: The Anthropocene.....	6
4.2	The dual nature of metals: Essential but toxic in excess.....	6
4.2.1	Macro- and microelements in plant physiology	6
4.2.2	Metal toxicity and oxidative stress	7
4.2.3	Toxicity from metal-ligand interactions	8
4.3	Metal uptake through the root system	9
4.3.1	Root-mediated metal uptake: Transport mechanisms and bioavailability	9
4.3.2	The dilemma of iron – ubiquitous yet scarce	10
4.3.3	Low specificity Fe uptake promotes the entry of Cd	12
4.3.4	Cd sources and its toxicity for humans	13
4.3.5	Cd toxicity in plants	14
4.3.6	The modulation of root system architecture by edaphic conditions.....	15
4.4	The role of particulate matter (PM) in metal exposure	16
4.4.1	PM as a vector for the introduction of novel substances.....	16
4.4.2	The consequences of air pollution for human health and the environment.....	17
4.4.3	Ultra-fine particles: A toxicological perspective	18
4.4.4	Air quality regulations and the challenge of monitoring UFP	19
4.4.5	Foliar absorption of particulate matter: A pathway for metal exposure	20
4.5	Aim of this thesis.....	21
4.5.1	The effects of Cd on the root with a special focus on the root tip.....	21
4.5.2	The effects of metallic UFP on <i>A. thaliana</i>	22
5	Material and methods	23
5.1	The effects of Cd on the root of <i>A. thaliana</i> with a special focus on the root tip	23
5.1.1	Plant material and growth conditions.....	23
5.1.2	Extraction of genomic DNA.....	24
5.1.3	Polymerase chain reaction and agarose gel-electrophoresis	24
5.1.4	Root growth assays.....	25
5.1.5	ICP-MS.....	25
5.1.6	Metabolomic analysis	26

5.1.7	RNA sequencing.....	26
5.1.8	Comparison with scRNA-Seq data	27
5.1.9	Analysis of HY5 target genes.....	27
5.1.10	ICP-OES.....	27
5.1.11	HPLC.....	28
5.2	The effects of metallic UFP on <i>A. thaliana</i>	28
5.2.1	Plant material and growth conditions.....	28
5.2.2	UFP generation and exposure.....	28
5.2.3	Measurement of aerial UFP concentration with ELPI+	29
5.2.4	Measurement of particles collected with ELPI+ using spICP-MS	29
5.2.5	X-Ray fluorescence measurement of brake pads	29
5.2.6	Outdoor exposure of <i>A. thaliana</i>	30
5.2.7	Particle extraction from plant material.....	30
5.2.8	spICP-MS	30
5.2.9	RNA-Sequencing	31
5.2.10	Scanning electron microscopy.....	31
6	Results	32
6.1	The effects of Cd on the root of <i>A. thaliana</i> with a special focus on the root tip	32
6.1.1	The impact of Cd on primary root elongation.....	32
6.1.2	Analysis of elemental profiles under Cd exposure.....	32
6.1.3	The impact of Cd on metabolite contents.....	34
6.1.4	The impact of Cd on the root transcriptome	37
6.1.5	The response of root tips to Cd	41
6.1.6	<i>hy5</i> mutants display increased sensitivity to Cd.....	46
6.1.7	HY5 loss-of-function leads to increased Cd accumulation.....	48
6.1.8	Comparison of gene expression and elemental contents in RR and RT.....	52
6.1.9	Comparison of Zn- and Cd excess on gene regulation in RT and RR.....	55
6.2	The effects of metallic UFP on <i>A. thaliana</i>	56
6.2.1	Development and characterization of controlled exposure experiments.....	56
6.2.2	Controlled exposure and UFP deposition on leaf surfaces.....	57
6.2.3	RNA sequencing of <i>A. thaliana</i> exposed to UFP from brake abrasion	59
6.2.4	Evaluation of aerial UFP concentration and leaf deposition in the field.....	62
7	Discussion	65
7.1	The effects of Cd on the root of <i>A. thaliana</i> with a special focus on the root tip	65

7.1.1	Differences in elemental contents between RT and RR	65
7.1.2	The effect of Cd on the root metabolome.....	66
7.1.3	The effect of Cd on the root transcriptome	67
7.1.4	The specific impact of Cd on gene expression in root tips	69
7.1.5	HY5 affects Cd tolerance and accumulation.....	72
7.2	The effects of metallic UFP <i>A. thaliana</i>	75
7.2.1	Development of controlled exposure experiments.....	75
7.2.2	RNA sequencing of <i>A. thaliana</i> exposed to UFP from brake abrasion	76
7.2.3	Comparison of field exposure with controlled dynamometer exposure	77
8	Supplementary information.....	79
9	References	103
10	Acknowledgements	128
11	Eidesstaatliche Versicherungen und Erklärungen	129

1 Abstract

The development of human civilization has profoundly changed the environment, including the alteration of metal concentrations. The accumulation of cadmium (Cd) in soils is caused by agricultural practices or industrial activities and represents a threat to human health via the uptake into edible parts of crops. Beyond its implications for human health, Cd exposure strongly inhibits plant growth, including the root system, even though the precise mechanisms underlying this inhibition remain incompletely understood. Therefore, the first section of this thesis analyses the specific impact of Cd stress on *Arabidopsis thaliana* root tips (RT), where the root apical meristem (RAM) and elongation zone (EZ) facilitate growth. Using a multi-omics approach, including the analysis of metal contents with ICP-MS, untargeted metabolomics and RNA sequencing, the molecular mechanisms governing root growth inhibition by Cd were analysed by separating Cd-treated roots into RT and the remaining root (RR). This revealed strong differences in Cd accumulation between the two root sections and highlighted responses related to iron (Fe) and sulfur (S) homeostasis as well as secondary metabolism. The transcriptomic analysis furthermore suggested a role of the photomorphogenetic transcription factor HY5 in the response to Cd stress in RT. Further characterization of *hy5* mutants confirmed the functional involvement of HY5 and revealed a role in limiting Cd accumulation.

Metals are furthermore released into the environment by particulate matter (PM) emissions resulting from industry or vehicular transport. Especially ultra-fine particles (UFP) have been recognized as particularly harmful for humans and ecosystems. Even though brake wear represents an important source for metallic UFP emissions, its effects on organisms, including plants, have rarely been studied in a realistic, airborne exposure setting. Therefore, the second part of this thesis describes the establishment of a system to study the effects of aerial brake dust particles on plants by integrating an exposure chamber into the exhaust system of a brake dynamometer. The exposure conditions, including UFP deposition on leaves, were thoroughly characterized using state-of-the-art analytical methods, such as electrical low-pressure impactor (ELPI+) and single particle ICP-MS (spICP-MS). As a proof of concept and to gain first insights into the physiological processes triggered by metallic UFP exposure, transcriptomic data with *A. thaliana* were generated, which showed perturbations in the regulation of genes related to Fe and copper (Cu) homeostasis as well as herbivory defense and specialized metabolism. A comparison with different outdoor exposure sites indicated that UFP-deposition in controlled exposures were within the same order of magnitude compared to a traffic-heavy location.

2 Zusammenfassung

Die Entwicklung der menschlichen Zivilisation hat die Umwelt tiefgreifend verändert, unter anderem durch die Veränderung von Metallkonzentrationen. Die Anreicherung von Cadmium (Cd) in Böden wird durch landwirtschaftliche oder industrielle Aktivitäten verursacht und stellt durch die Aufnahme in essbare Teile von Pflanzen eine Gefahr für die menschliche Gesundheit dar. Darüber hinaus inhibiert Cd-Exposition das Pflanzenwachstum, einschließlich des Wurzelsystems. Mit dem Ziel, die molekularen Mechanismen dieser Inhibition besser zu verstehen, analysiert der erste Abschnitt dieser Arbeit die spezifischen Auswirkungen von Cd-Stress auf die Wurzelspitzen (RT) von *Arabidopsis thaliana*, wo das Wurzelapikalmeristem (RAM) und die Elongationszone (EZ) das Wachstum fördern. Mithilfe eines Multi-Omics-Ansatzes, einschließlich der Analyse von Metallkonzentrationen mittels ICP-MS, Non-Targeted Metabolomics und RNA-Sequenzierung, wurden die molekularen Mechanismen der Wurzelwachstumshemmung durch Cd analysiert, indem RT und die verbleibende Wurzel (RR) getrennt betrachtet wurden. Diese Analysen zeigten unter anderem starke Unterschiede in der Cd-Akkumulation beider Wurzelabschnitte und hoben die Bedeutung von Antworten im Bereich der Eisen (Fe)- und Schwefel (S)-Homöostase sowie des Sekundärmetabolismus hervor. Die Transkriptomanalyse deutete zudem auf eine Rolle des photomorphogenetischen Transkriptionsfaktors HY5 bei der Reaktion auf Cd-Stress in RT hin. Die weitere Charakterisierung von *hy5*-Mutanten bestätigte die funktionelle Beteiligung von HY5 und zeigte eine Rolle bei der Limitierung der Cd-Akkumulation.

Darüber hinaus gelangen Metalle durch Feinstaubemissionen aus der Industrie und dem Verkehr in die Umwelt. Insbesondere ultrafeine Partikel (UFP) gelten als besonders schädlich für Mensch und Ökosysteme. Obwohl Bremsenabrieb eine wichtige Quelle für metallische UFP-Emissionen darstellt, wurden seine Auswirkungen auf Organismen, einschließlich Pflanzen bisher selten in einer realistischen Expositionsumgebung untersucht. Daher beschreibt der zweite Teil dieser Arbeit die Etablierung eines Systems zur Untersuchung der Auswirkungen von luftgetragenen Bremsstaubpartikeln auf Pflanzen durch die Integration einer Expositionskammer in das Absaugsystem eines Bremsenprüfstandes. Die Expositionsbedingungen wurden mithilfe verschiedener Analysemethoden, einschließlich eines elektrischen Niederdruckimpaktors (ELPI+) und single-particle-ICP-MS (spICP-MS) gründlich charakterisiert. Als Proof-of-Concept und um erste Einblicke in physiologische Antworten zu bekommen, wurde eine Transkriptomanalyse mit *Arabidopsis thaliana* nach der Exposition durchgeführt. Dies zeigte Veränderungen in der Regulationen von Genen, die mit

der Fe- und Kupferhomöostase (Cu) sowie dem spezialisierten Metabolismus zusammenhängen. Ein Vergleich mit verschiedenen Freiland-Expositionsstandorten ergab, dass die UFP-Ablagerungen bei kontrollierten Expositionen in einer vergleichbaren Größenordnung lagen wie an einem Standort mit hohem Verkehrsaufkommen.

3 List of abbreviations

CB	Carbon black
CCRG	Cell cycle regulatory gene
DAF	Differentially abundant feature
DEA	Differential expression analysis
DEG	Differentially expressed gene
DEP	Diesel exhaust particles
DW	Dry weight
DZ	Differentiation zone
EDX	Energy dispersive X-ray spectroscopy
EFSA	European Food Safety Agency
ELIP	EARLY LIGHT INDUCIBLE PROTEIN
ELPI	Electrical low-pressure impactor
FER	FERRITIN
GSH	Glutathione
HMA	HEAVY METAL P-TYPE ATPase
HPLC	High-performance liquid chromatography
HY5	ELONGATED HYPOCOTYL 5
ICP	Inductively coupled plasma
IMA	IRONMAN
IPCC	Intergovernmental Panel on Climate Change
IRT1	IRON REGULATED TRANSPORTER 1
LC	Liquid chromatography
LC-MS	Liquid chromatography–mass spectrometry
NRAMP	NATURAL RESISTANCE-ASSOCIATED MACROPHAGE PROTEIN
OES	Optical emission spectrometry
PAH	Polycyclic aromatic hydrocarbons
padj	Adjusted p-value
PC	Phytochelatin

PCS	PHYTOCHELATIN SYNTHASE
PLA	Polylactic acid
PM	Particulate matter
PNC	Particle number concentration
PYE	POPEYE
RAM	Root apical meristem
RCS	Root covered system
ROS	Reactive oxygen species
RR	Remaining root
RSA	Root system architecture
RT	Root tip
SEM	Scanning electron microscopy
spICP-MS	Single particle ICP-MS
TF	Transcription factor
UFP	Ultra-fine particle
VTL	VACUOLAR IRON TRANSPORTER-LIKE
ZIP	ZRT- / IRT-RELATED PROTEIN

4 Introduction

4.1 Humans shape the environment: The Anthropocene

Changing environments direct the course for the adaptation of species during the process of evolution. Fluctuations in biotic and abiotic selection pressures create new surroundings, where individuals with advantageous traits are favoured, while others are gradually outcompeted ¹. Since the origin of life, ~3.8-4 billion years ago, dynamic selective pressures have driven the rise and fall of species and the environment was modulated by natural forces ²⁻⁵. With the origins of the genus *Homo* dating back approximately 2.4-1.4 million years, the history of humans covers only a fraction of this timescale ⁶. Yet from the mastery of fire and large-scale megafauna hunting over the Neolithic and Industrial Revolutions, human influence on the environment has continuously expanded ⁷⁻⁹. Modern societies have become a dominant force in reshaping the planet, to an extent that some refer to the current geochronological era as the ‘Anthropocene’, as opposed to the ‘Holocene’ ¹⁰.

As global temperatures rise at an unprecedented rate, the anthropogenic surge in greenhouse gases and widespread deforestation are among the most recognized drivers of anthropogenic environmental transformation ¹¹. But the disruption of biogeochemical flows, freshwater change, loss of genetic and functional biosphere integrities, ocean acidification, ozone depletion, land system change, atmospheric aerosol loading and the introduction of novel entities form additional pillars of Earth’s transition into the Anthropocene ^{12,13}. Among these, the introduction of novel entities into ecosystem surroundings stands out as a key factor, as it is considered to occur at a magnitude that significantly threatens the resilience of Earth as a whole and therefore its hospitability for civilization. Human activities have continuously generated and dispersed previously non-existent substances into the environment, including microplastic and organic pollutants ¹⁴. Another form of novel entity introduction arises from changes in the concentration of naturally occurring elements, such as (heavy-) metals or metalloids. Agricultural activities, mining, industrial and vehicular emissions are tied to the mobilization of elements like Cadmium (Cd), Lead (Pb) and Mercury (Hg) far beyond their natural geochemical baselines ¹⁵.

4.2 The dual nature of metals: Essential but toxic in excess

4.2.1 Macro- and microelements in plant physiology

Plants represent only a fraction of the species that are affected by the anthropogenic introduction of novel entities into ecosystems, but due to their immobile lifestyle, they are inevitably exposed

to them. Through contamination of fertilizers with trace metals, fertilization represents a pathway of novel entity introduction, and its necessity results from the dependence of plant development on the availability of various essential elements. Based on the quantity required, these elements are broadly categorized as macronutrients (nitrogen (N), potassium (K), phosphorous (P), sulfur (S), calcium (Ca) and magnesium (Mg)) or micronutrients (iron (Fe), manganese (Mn), boron (B), zinc (Zn), copper (Cu), molybdenum (Mo), nickel (Ni) and chlorine (Cl))¹⁶.

Many of these elements are metals and they serve a variety of functions in plants. K for example is imperative for the regulation of gas exchange and water transpiration through the control of stomatal aperture¹⁷. As a secondary messenger, cytosolic Ca-signalling is crucial for mediating responses to diverse environmental stimuli and regulating growth, development and stress adaptation¹⁸. Zn acts as a cofactor for many enzymes and transcription factors, estimations even suggest that up to 10 % of all eukaryotic proteins contain Zn atoms¹⁹. With a tetra-manganese cluster residing in the active site of photosystem II, Mn is indispensable for the water oxidation reaction and the initiation of the photosynthetic electron transfer chain²⁰. Fe-containing proteins such as ferredoxin and cytochromes and Cu within plastocyanin and cytochrome-C-oxidase are central to electron transport in photosynthesis and respiration and therefore fundamental participants in energy metabolism^{21–24}.

Even though many metals are essential, their beneficial roles are restricted to specific concentration ranges. Outside of these, either deficiency or excess can impair plant development, with the latter leading to toxicity. This contrasts with non-essential metals such as Cd, Pb, thallium (Tl) and Hg, which serve no biological functions²⁵.

4.2.2 Metal toxicity and oxidative stress

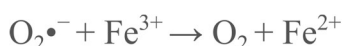
Similar to other abiotic and biotic plant stressors, metal toxicity results in a disturbed homeostasis of reactive oxygen species (ROS). ROS are natural byproducts of cellular processes like photosynthesis and respiration and they also serve important functions as signalling molecules²⁶. However, metal toxicity leads to excessive ROS production which has far reaching effects like the destruction of macromolecules, DNA damage, lipid peroxidation or the deterioration of membrane potential and ion leakage^{27–30}.

Possible mechanisms for metal induced oxidative stress are interferences with electron transfer reactions or ROS detoxifying enzymes³¹. Moreover, metals like Fe or Cu can exist in different oxidation states in cellular environments and their interaction with existing ROS may result in highly toxic hydroxyl radicals ($\bullet\text{OH}$). Hydroxyl radicals are considered the most reactive ROS

molecule, capable of damaging virtually any other molecule in its proximity and they have an estimated lifespan of 10^{-9} seconds³². For example in the Fenton reaction, Fe^{2+} (or Cu^+ in a Fenton-type reaction³³) reacts with H_2O_2 , resulting in the formation of $\bullet\text{OH}$ ²⁷:



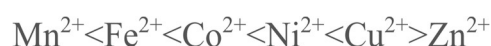
Moreover, in the two-step Haber-Weiss reaction, the formation of $\bullet\text{OH}$ from H_2O_2 and superoxide radicals ($\text{O}_2^{\bullet-}$) can be catalysed by Fe^{3+} as well as Cu^{2+} ^{34,35}:



Another mechanism of metal-induced oxidative stress, whose relevance remains debated, is their interaction with free thiols and the cellular glutathione (GSH) pool^{36,37}. This interaction stems from the importance of GSH in the intracellular binding and distribution of Cd, Cu and Fe and a role in binding Zn^{27,38}. Moreover, a variety of metals (As, Cd, Zn, Cu, Hg and Pb) induce the synthesis of phytochelatins (PCs), which are metal-binding, cysteine-rich polypeptides that play a key role in metal detoxification³⁹⁻⁴¹. PCs depend on the GSH pool because they are formed by oligomerization of GSH and show the structure of $(\gamma\text{-GluCys})_n\text{-Gly}$, where $n = 2-11$ ⁴². However, the cytosolic concentration of GSH is at all times likely to be far higher than those of metal stressors (cytosolic levels of 3-4 mM^{43,44}). Therefore, it is rather implausible that GSH depletion by metals contributes significantly to metal-induced oxidative stress³⁴.

4.2.3 Toxicity from metal-ligand interactions

In part, metals are essential for biological functions because they interact with ligands in macromolecules, for example as cofactors in enzymes. Yet in a state of disrupted metal homeostasis, this property emerges as a source of toxicity. The thermodynamic stability of metal-ligand interactions is determined by various chemical factors and consequently some interactions are more stable than others. For the first-row transition metals, a general hierarchy of increasing stability for complexes of divalent metal ions with any kind of ligand is given by the Irving Williams series^{19,34,45}:



Consequently, under equimolar concentrations, metals ranking high in the Irving Williams series would consistently displace others from complexed positions within enzymes or other macromolecules. Using the example of Cu, which would always form the most stable

complexes, the implication of the Irving Williams order is clearly reflected in the low cellular concentrations of its free ion, that are located in the attomolar range ^{34,46}. High concentrations of free Cu^{2+} would inevitably lead to the mis-metallation of metalloproteins and compromise their function. Even during the synthesis of Cu-metalloproteins, free Cu^{2+} ions must be bound by metallochaperones and securely directed towards their designated destination ^{46,47}. In addition to the thermodynamic dominance of Cu^{2+} highlighted in the Irving-Williams series, the toxicity of monovalent Cu^+ by the displacement of Fe from Fe-S clusters in dehydratases such as isopropylmalate isomerase was demonstrated ⁴⁸. With its high ranking in the Irving-Williams series, a rationale similar to Cu^{2+} applies to free cytosolic Zn. Although the total content of Zn in cells is estimated to be between 100-500 μM , the concentration of free Zn is kept very low, around 50-500 pM ^{19,49}. When the correct metal is displaced from its intended site, this can result in the loss of enzymatic functions necessary for DNA repair, energy metabolism or the antioxidative system and impair the stability of structural cellular components like the cell wall ⁵⁰⁻⁵⁴.

4.3 Metal uptake through the root system

4.3.1 Root-mediated metal uptake: Transport mechanisms and bioavailability

Metals enter plants primarily through root-mediated uptake, a process that requires membrane-embedded transporter proteins to facilitate the translocation of metals or metal-ligand complexes from the rhizosphere into epidermal root cells and subsequently to other plant organs and organelles. These transporters are very diverse, and hitherto, members of several families such as the ZRT/IRT-related proteins (ZIPs), the natural resistance-associated macrophage proteins (NRAMPs), the ATP-binding cassette (ABC) transporters or the heavy metal P-type ATPases (HMAs) have been characterized ⁵⁵.

In natural environments, the root system of most plants is entirely embedded in the soil where it faces metals that occur in various chemical forms, influencing their mobility and bioavailability. They can be dissolved in the soil solution as free ions or soluble metal complexes, adsorbed onto inorganic soil constituents at ion exchange sites, associated with organic matter, bound to oxides, hydroxides and carbonates or incorporated into silicate minerals ^{56,57}. Several variables such as for instance pH, moisture content or temperature influence the occurrence of these different forms ⁵⁷. Yet, some metal ions are generally more available for plants than others. For instance, Cd^{2+} and Zn^{2+} are present largely in exchangeable bioavailable forms, whereas Pb^{2+} is rather immobile and appears mostly in the form of insoluble precipitates ^{56,58}.

4.3.2 The dilemma of iron – ubiquitous yet scarce

Due to its indispensability for life and its entwinement with Earth's geochemical history, Fe serves as an interesting illustration for the dilemma of widespread presence coupled with low bioavailability. It takes the fourth place in the list of the most abundant elements in the Earth's crust and exists mostly in the form of ferrous Fe^{2+} or ferric Fe^{3+} oxidation states⁵⁹. The latter is favoured under neutral to alkaline, aerobic conditions and forms insoluble oxides and hydroxides that are largely unavailable to plants^{60–62}. By contrast, acidic or anaerobic environments increase the proportion of soluble Fe^{2+} which can be taken up by plants more easily⁶³. Consequently, the Great Oxidation Event, resulting from the emergence of oxygenic photosynthesis ~ 2.4 billion years ago, shifted the balance more towards oxidized Fe^{3+} and promoted a sharp decline in bioavailable Fe^{2+} ⁵.

The current perception focusses on two major strategies that terrestrial plants utilize to cope with Fe limitation. Strategy I, which is used by all non-graminaceous plants, including *Arabidopsis thaliana*, relies on the acidification of the rhizosphere by proton pumps such as AHA2, which facilitates the solubilization of Fe^{3+} and enables its reduction by NADPH dependent ferric reduction oxidases such as FRO2. The reduced Fe^{2+} can then be taken up by membrane transporters such as IRT1^{64,65}. Additionally, non-grass species secrete phenylpropanoid metabolites, such as coumarins, to assist in Fe reduction and uptake. Recent studies also point towards a role in the formation of Fe-coumarin complexes that may be taken up into roots by an hitherto unknown transporter^{66,67} (Figure 1). This challenges the sharp differentiation of strategy I from strategy II, which is utilized by graminaceous species such as *Zea mays* or *Oryza sativa*. In strategy II, the solubilization of Fe^{3+} is facilitated by high-affinity iron chelating compounds, called phytosiderophores. Known members of this family are structurally based on the mugineic acid and avenic acid and are released by the efflux transporter TOM1⁶⁸. Fe^{3+} -phytosiderophore complexes are then taken up by YELLOW STRIPE1 and YELLOW-STRIFE-like transporters^{65,69}.

Because of its essential role in many physiological processes on one side, and its potential to drive ROS accumulation to toxic levels on the other side, plants rely on a complex regulatory network to maintain optimal cellular Fe levels. Under conditions of Fe deficiency, *A. thaliana* increases the transcription of genes involved in Fe mobilization and uptake such as *FRO2*, *IRT1* and *AHA2*. The activation of these genes is facilitated by the formation of heterodimeric complexes between the subgroup IIIa bHLH TF FIT and the group Ib bHLH TFs (e.g. bHLH38, bHLH39, bHLH100 and bHLH101)^{70,71}. Transcriptional upregulation of these genes requires

the transcription factor UPSTREAM OF IRT1 (URI), which accumulates in its phosphorylated state upon Fe deficiency. URI forms heterodimeric complexes with the subgroup IVc bHLH TFs (bHLH34, bHLH104, bHLH115 and bHLH105/ILR3) that directly bind to the promoters of group Ib bHLHs ^{71,72}.

To avoid toxicity, excessive Fe accumulation is prevented by the activity of negative regulators of Fe uptake genes. One of them is BRUTUS (BTS), which together with BTS-LIKE1 and BTS-LIKE2 inhibits the group IVc bHLHs via degradation by its E3 ligase activity ^{73–75}. Because it contains three hemerythrin domains, it can associate with Fe and the stability of BTS itself is directly related to intracellular Fe levels ⁷⁶. Intuitively, the fact that BTS, as a negative regulator of Fe uptake, is stabilized by Fe deficiency appears paradoxical. However, the precise titration of its activity is facilitated by the inhibitory effect that the IMA (IRONMAN) peptides exert on BTS mediated IVc bHLH degradation ⁷⁷. Interestingly, reciprocal grafting experiments with IMA1 overexpression lines and WT plants suggest, that IMAs are shoot-to-root mobile peptides with the ability to induce an Fe deficiency response in roots ⁷⁸. Another negative regulator of Fe homeostasis related genes is POPEYE (PYE), which was shown to directly bind to the promoters of Ib bHLHs and repress their transcription ⁷³. Additionally, PYE exerts a negative regulation on Fe storage and transport genes. It was shown to interact with the subgroup IVc bHLH TF ILR3, which leads to the transcriptional downregulation of *NICOTIANAMINE SYNTHASE4 (NAS4)*, *FERRITINs* and *VACUOLAR IRON TRANSPORTER-LIKE2 (VTL2)* ^{79,80} (Figure 1).

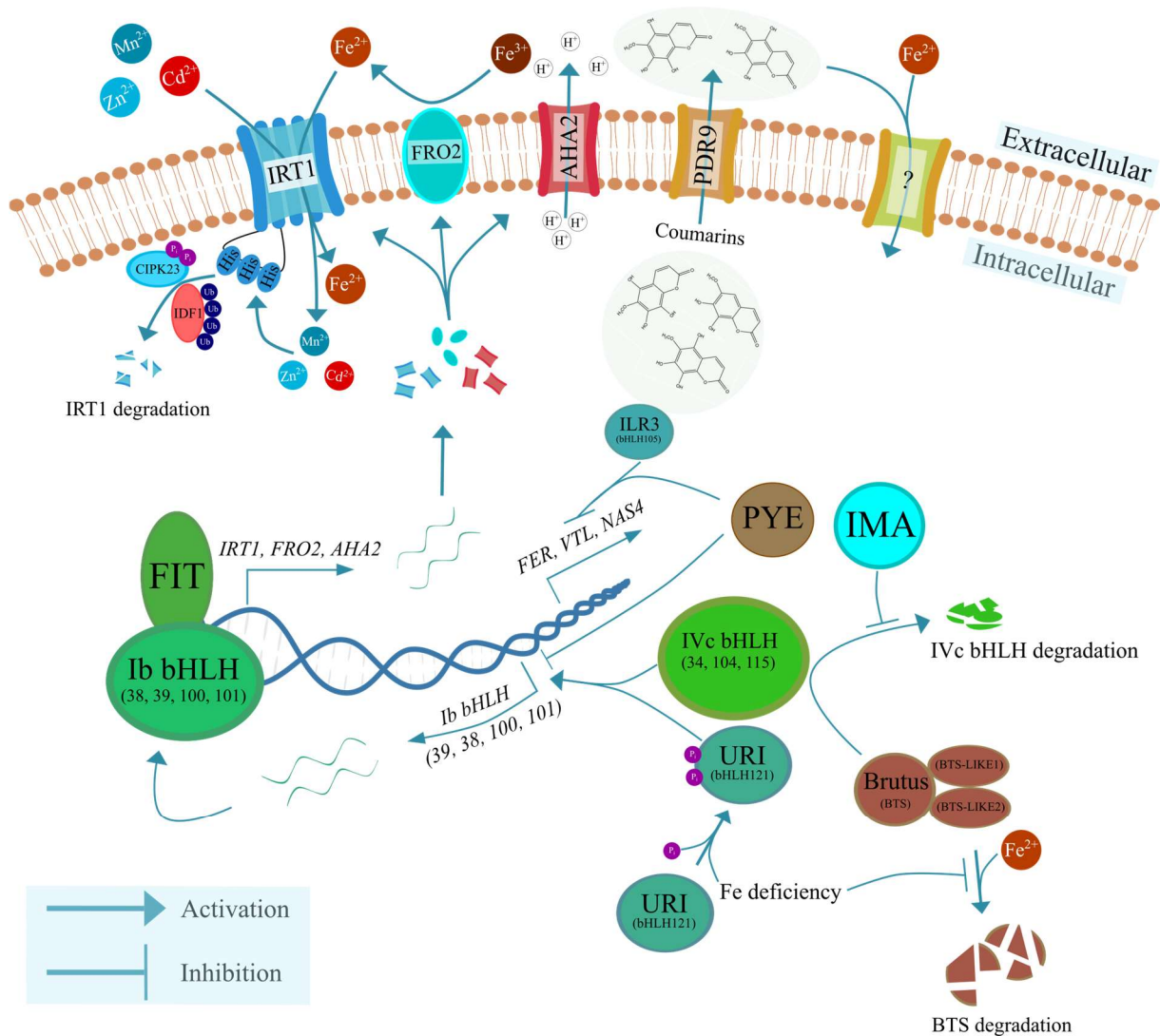


Figure 1: Schematic illustration depicting the regulation of Fe homeostasis in *A. thaliana*.

4.3.3 Low specificity Fe uptake promotes the entry of Cd

These descriptions do not capture the entire complexity of the Fe homeostasis network, but they illustrate the rigidity needed to promote sufficient supply with an essential metal while simultaneously preventing its toxicity by restricting maximum cellular concentrations. But yet another risk for toxicity arises from the broad substrate range of metal ion uptake transporters, which in the case of IRT1 also includes Mn²⁺, Zn²⁺, Co²⁺ and Cd²⁺ ^{81,82}. In fact, IRT1 is perceived as the most important uptake transporter for Cd²⁺, which is substantiated by studies with *irt1* knockout lines and heterologous expression of *AtIRT1* in yeast ^{81,83,84}.

An interesting property of IRT1 is its ability to recognize non-Fe metal ions by their binding to a histidine rich stretch within the cytoplasmic domain. This leads to its phosphorylation and the recruitment of the E3 ligase IDF1, which results in the degradation of IRT1 (Figure 1). IRT1

merges the properties of a transporter and a receptor, therefore it is referred to as a “transceptor” that optimizes Fe uptake while preventing excessive uptake of non-Fe substrates^{85,86}. There are additional transporters that facilitate the entry of Cd into plants. For instance, in the hypertolerant species *Arabidopsis halleri*, another ZIP family transporter, AhZIP6, was shown to be involved in Cd uptake⁸⁷. In *Arabidopsis thaliana*, one study also showed a contribution to Cd acquisition by the nitrate transporter NRT2.1⁸⁸. In rice, the Mn transporter OsNRAMP5, was shown to be a major entry route for Cd into the roots⁸⁹.

4.3.4 Cd sources and its toxicity for humans

Cd is a non-essential metal for virtually all living organisms and is recognized as one of the most important environmental metallic pollutants because it has such a high potential to cause toxic effects⁹⁰. It is ubiquitously present in soils with concentrations usually reaching from 0.01 to 1 mg/kg and a global mean of 0.36 mg/kg⁹¹. There are natural sources for Cd in soils, such as the weathering of high-Cd rocks like phosphorites, which gradually releases the metal into the soil solution and into weak associations with mineral and organic matter surfaces¹⁵. Moreover, human activities such as mining, smelting, application of livestock manure, sewage treatment or waste incineration are tied to the release of Cd into the environment¹⁵. Agricultural practices, in particular the application of P fertilizers, are a major contributor to Cd input in soils, as they often contain traces of Cd^{92,93}. Human activities can lead to localized soil contamination, resulting in strongly elevated Cd levels. A notable example is the endemic outbreak of Itai-itai disease in Japan, which was traced to Cd release from a Pb-Zn mining plant into the Jinzu River. The use of Cd-contaminated river water for irrigating rice paddies led to grain Cd accumulation and human exposure, causing severe osteomalacia and osteoporosis alongside with renal dysfunction^{92,94}.

Cd accumulation in crops and its entry into the human food chain is considered a major threat to human health, since the consumption of contaminated food accounts for a share of 90% of Cd exposure in the general, non-smoking population and most Cd in the human diet stems from agricultural products^{15,92,95}. This is particularly concerning in the background of the biological half-life of Cd in the human body, ranging from 16-30 years⁹⁶, which results in the fact, that even the exposure to low levels over a long period can result in serious adverse health effects.

With the existence of sufficient evidence for carcinogenicity in humans, Cd is classified as a group 1 carcinogenic substance by the International Association for Research on Cancer (IARC)⁹⁷. Kidneys are a primary site for Cd accumulation in the human body, which is why renal diseases are a common outcome. Cd deposition in the proximal tubule is associated with

adverse effects on epithelial cells and polyuria and proteinuria ⁹⁸. Additionally, Cd exposure is associated with various types of cancers, including those affecting kidneys, prostate, breast and the endometrium ⁹⁹. Additionally, pathological outcomes of Cd exposure include effects in the skeletal system such as osteoporosis or osteomalacia, the reproductive system, the respiratory system and the cardiovascular system ⁹⁶. To reduce the likelihood of long-term adverse health effects, the European Food Safety Agency (EFSA) has imposed the limit for dietary Cd intake at 2.5 µg/kg body weight per week ¹⁰⁰. Zhao et al. 2023 provide an estimation of dietary Cd intake levels in the general population of several countries and conclude that in many cases, the EFSA limit is exceeded, especially in countries like Bangladesh or Japan ¹⁰¹.

4.3.5 Cd toxicity in plants

Similarly, Cd is a non-essential element for plants, inducing general growth inhibition and chlorosis. This is a result of toxicity mechanisms like oxidative stress, lipid peroxidation, DNA damage, enzymatic inhibition and diminished photosynthetic activity ^{25,102}. Mitigating Cd toxicity depends on the presence of effective detoxification mechanisms, which is exemplified by the extreme Cd hypersensitivity of *cad1-3*. The *PCS1* (*PHYTOCHELATIN SYNTHASE1*) allele of this mutant significantly impairs its ability to produce PCs, which in concert with vacuolar sequestration of PC-Cd²⁺ complexes is essential for Cd detoxification ^{25,103}.

Another important aspect of Cd toxicity is its interference with mineral uptake. Due to shared uptake mechanisms, Cd affects Fe homeostasis resulting in a reduction of Fe contents in plant tissues ¹⁰⁴. One common finding across many transcriptomic studies is the induction of Fe-deficiency signalling as a result of Cd exposure ^{105–107}. Apart from Fe, Cd interferes with the homeostasis of other essential elements, as it has been shown to affect N, P, K, Cu, Zn, Ca, Mg, Mn and Mo contents ¹⁰⁸.

In the plant kingdom, there is also considerable variation towards the extent to which growth on Cd contaminated soil can be tolerated. Several species such as *Arabidopsis halleri*, *Noccaea caerulescens*, *Thlaspi praecox* and *Sedum alfredii* display hypertolerance and may grow and thrive on Cd contaminated soils. With the ability to store large amounts of Cd in shoots, some of these plants can even be described as Cd hyperaccumulators (importantly, the phenomenon of hyperaccumulation is not found in all natural accessions of these species) ¹⁰⁹. Outside the plant kingdom, the marine diatom *Thalassiosira weissflogii* represents an exception to the general absence of Cd in cellular processes, because it displays a carbonic anhydrase in which Zn²⁺ ions can be replaced by Cd²⁺ as a cofactor under Zn-deficient conditions ¹¹⁰.

4.3.6 The modulation of root system architecture by edaphic conditions

The root system forms the primary interface between plants and the soil and its morphology governs anchorage as well as water and nutrient uptake. It consists of a primary root and multiple lateral roots, with root hairs further increasing overall surface area. Root system architecture (RSA) conceptually describes the organisation of these components and is continuously modulated in response to environmental conditions ^{111,112}. This is exemplified by the drastic morphological alterations observed in *A. thaliana* seedlings grown under phosphate-deficient conditions, where primary root growth is inhibited, while lateral roots and root hairs exhibit stronger elongation ¹¹³.

Likewise, the exposure of plants to toxic metal ions like Cd^{2+} also induces major changes to RSA such as an inhibition of lateral root development and increasing root hair density ^{102,114–117}. These changes occur along with a general reduction in primary root growth, which is driven by cell proliferation in the root apical meristem (RAM) and cellular elongation in the elongation zone (EZ). Within the stem cell niche above the quiescent center, cells divide asymmetrically and generate transit-amplifying cells that continue to divide until they reach the EZ. At this point, cell division comes to an end and structural changes in the cell wall enable longitudinal expansion and the gradual formation of specialized root cells begins, while the cells reach the differentiation zone (DZ), which is characterized by the presence of root hairs ^{118,119}. To ensure continuous, indeterminate root growth, there must be a tight balance between the rate of cell division in the RAM and the onset of cellular differentiation starting from the EZ. This equilibrium, which is known as meristem maintenance, is orchestrated by intricate signalling networks involving hormonal gradients. A high auxin concentration in the RAM is essential to facilitate cell division, whereas cytokinin promotes differentiation and displays high concentrations in the EZ and DZ ¹¹⁸. In parallel, meristem maintenance is influenced by the distribution of ROS, because the rates of differentiation and proliferation depend on a gradient between H_2O_2 and O_2^- ¹²⁰ (Figure 2). This balance was demonstrated to be regulated by the photomorphogenetic TF ELONGATED HYPOCOTYL5 (HY5), which represses meristematic H_2O_2 accumulation by controlling the expression of peroxidase genes ¹²¹.

Previous studies have demonstrated that root growth inhibition upon Cd exposure is the result of premature differentiation in the RAM along with a reduction in meristem size. These morphological changes were observed together with increased cytokinin concentrations and decreased auxin concentrations in the RAM ^{122,123}. Additionally, Cd affects nutrient homeostasis

and cell cycle regulation in the RAM, although the specific impact on underlying signalling pathways remains elusive^{124,125}.

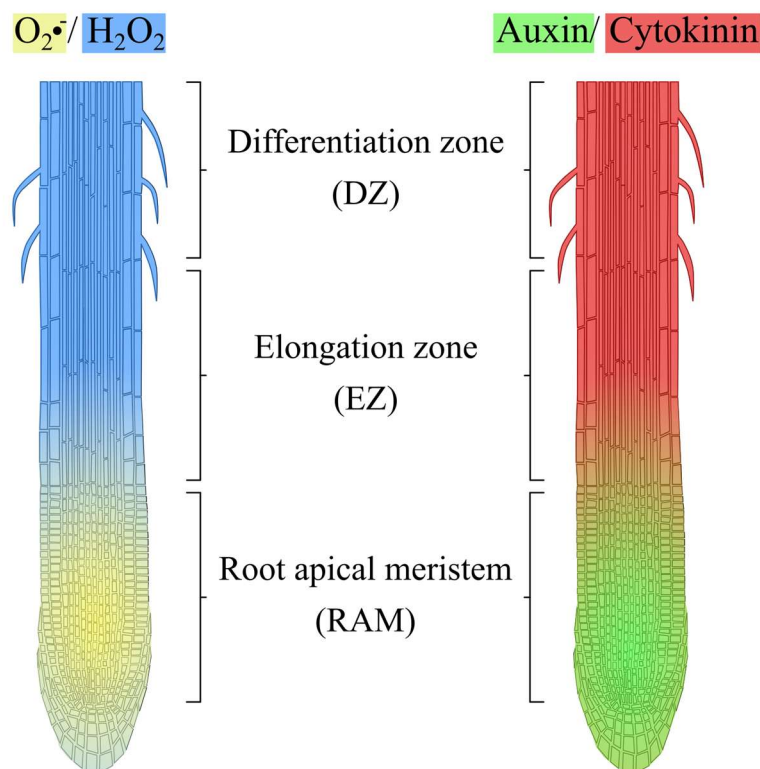


Figure 2: Hormonal and ROS gradients controlling cell division and elongation/ differentiation in the root apex. Color gradients represent concentrations of O_2^- (yellow) and H_2O_2 (blue) on the left side and auxin (green) and cytokinin (red) on the right side in a simplified manner.

4.4 The role of particulate matter (PM) in metal exposure

4.4.1 PM as a vector for the introduction of novel substances

With a shift from manual labour to large-scale mechanized production, the Industrial Revolution was a turning point in human history. A cornerstone of this transformation was the dramatically increasing reliance on combustible resources, which went hand in hand with fundamental alterations in atmospheric composition. The current atmospheric CO_2 levels are unprecedented during the past 420 000 years and clearly result from a sharp increase starting approximately 250 years ago^{126,127}. Because every combusive process is inevitably tied to the generation of particles, we are currently facing an environment with an extent of ambient PM pollution that has never existed before¹²⁸. Anthropogenic PM sources are the dominant drivers of this pollution and include power plants, industrial facilities, residential heating, agriculture and transportation. Only a fraction of atmospheric PM loading occurs naturally by the

resuspension of mineral dust, sea spray, volcanic activity, wildfires or biogenic emissions such as pollen or secondary organic aerosols ^{129,130}.

As introduced further above (4.1), the introduction of novel entities into the environment is considered a critical challenge for ecological balance on a global scale ¹⁴. In this regard, the anthropogenic release of PM represents yet another mode of novel substance introduction into natural environments. Polycyclic aromatic hydrocarbons (PAH), for example, are organic pollutants and as byproducts of fuel combustion in vehicular traffic, they are adsorbed onto diesel exhaust particles (DEP) ^{131,132}. Another example is the addition of tetra-alkyl-Pb compounds to gasoline as a measure to reduce engine knocking in the early 20th century. This resulted in widespread environmental Pb contamination from vehicular emissions until the prohibition of leaded gasoline ^{133–136}. Nonetheless, metallic particles continue to be emitted by humans in metallurgical industries, through waste incineration or power plants and in vehicular traffic by tire and brake abrasion ^{137–139}.

4.4.2 The consequences of air pollution for human health and the environment

Air pollution is nowadays recognized as one of the leading concerns for human health, with some studies estimating, that on a global level, it accounts for more premature deaths than obesity and alcohol consumption combined ¹⁴⁰. The consequences of PM for human health are exceptionally drastic at the hotspots of civilization. For example, in the metropolitan area of the Indian capital New Delhi, with a population of more than 30 million people, life expectancy is estimated to be reduced by six years due to PM exposure ¹⁴¹.

The specification of concrete outcomes for human health has to be introduced by first emphasizing the far-reaching impact of PM on various parts of the body (reviewed in ¹⁴²). As the primary contact interface for inhaled particles, the respiratory tract is an evident target, where PM exposure is linked to acute and chronic conditions such as laryngitis, bronchitis, chronic obstructive pulmonary disease (COPD) and lung cancer ^{143,144}. PM exposure also has effects on the central nervous system, which is reflected in epidemiological studies that report a connection to impaired cognitive performance in children ¹⁴⁵. A large-scale Canadian study with 4.4 million individuals even suggested, that living distance from high-traffic roadways was correlated with the incidence of dementia in a dose-dependent way ¹⁴⁶.

In addition to representing a major concern for human health, air pollution with PM also has consequences for the environment. This involves effects on the formation of clouds, the intensity of monsoon rainfalls and glacial melting ¹². Moreover, the Intergovernmental Panel on Climate Change (IPCC) thematized particulate pollutants and their implications for climate

change. Some air pollutants, including carbon black (CB), organic aerosols, sulphate or nitrate particles are considered short lived climate forcers and they can have both warming and cooling effects on the climate as direct drivers of radiative forcing. Nitrate or sulphate particles change the global energy balance by scattering sunlight back to space and producing net surface cooling. By contrast, dark particles such as CB increase the temperature of the ambient atmosphere by absorbing incoming light ^{147,148}.

4.4.3 Ultra-fine particles: A toxicological perspective

On the basis of aerodynamic particle diameter, PM is categorized into PM₁₀ (“coarse PM”, $\varnothing < 10 \mu\text{m}$), PM_{2.5} (“coarse PM”, $\varnothing < 2.5 \mu\text{m}$) and PM_{0.1} (“ultra-fine PM”, $\varnothing < 100 \text{ nm}$) ¹⁴⁹. Especially ultra-fine particles (UFP) have recently attracted growing attention due to toxicological studies that raise concerns about their detrimental effects on health compared to larger particles ^{150–154}. Interpreting toxicological studies on UFP requires recognition of the explicit challenges in establishing realistic exposure conditions, their evaluation and their representation of real-life scenarios. Extrapolating results is for example complicated by the artificially high concentrations used in controlled laboratory experiments. Furthermore, particle assessments at a given temporal or spatial distance from the emission source are also obscured by the physiochemical properties of UFP, as they for example form larger agglomerates based on electrostatic- or van der Waals forces ^{149,155}. It has been emphasized, that the lack of standardized UFP generation and delivery leads to inconsistencies in toxicological studies ¹⁵⁶.

Bearing this in mind, the explicit toxic potential of UFP was demonstrated for example by Ferin et al. ¹⁵⁷, who showed that exposure to ultra-fine TiO₂ particles led to a more pronounced inflammatory response in rat lungs compared to an exposure to the same mass concentration of fine TiO₂ particles. This is remarkable, because TiO₂ particles were regarded non-toxic and had often been used as a control in studies on particle toxicology. Similarly, CB particles with an average diameter of 14 nm caused a 2-3 times higher inflammatory response than CB with a diameter of 260 nm ¹⁵⁸.

In part, these findings may be attributable to the superior access into “target” sites that UFP have over larger particles. Research in animal models has demonstrated the direct translocation of inhaled metallic UFP via the olfactory nerve to the brain, where they trigger inflammatory stress responses ¹⁵⁹. Moreover, the entry of UFP into the brain through the lungs and the circulatory system by crossing the blood-brain barrier has been shown ¹⁶⁰.

Apart from this, the reasons for the high toxicity also lie within the physiochemical properties of UFP, most importantly their high surface-area-to-mass ratio. This can be illustrated with a hypothetical thought experiment, where one perfectly spherical particle with a diameter of 10 μm and a given mass could be divided into 64 equal particles with a diameter of 2.5 μm . These, in turn, could be further divided into 1 000 000 particles with a diameter of 0.1 μm . While the coarse particle exhibits a total surface area of 314 μm^2 , the combined surface area of the ultra-fine particles is 100 times as high (Figure 3) ¹⁶¹.

This high ratio of surface-area to mass renders UFP more capable to adsorb hazardous compounds compared to larger particles. For instance, DEP consist of a carbon core and adsorbed transition metals as well as PAHs. PAHs may lead to genotoxicity over the formation of DNA adducts and transition metals can induce ROS, which are also linked to DNA damage ¹³¹. On the other hand, particles inherently possess reactive surfaces in the absence of adsorbed materials when they are composed of reactive materials. This is, for example, the case for brake-wear particles, which in part consist of metallic components (including redox-active metals such as Cu and Fe) and often fall into the ultra-fine size fraction ^{139,162}.


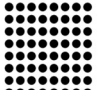
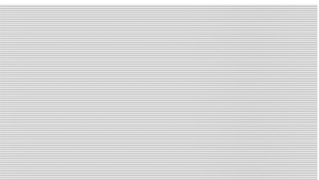
	Coarse particle	Fine particles	Ultra-fine particles
			
Diameter [μm]	10	2.5	0.1
Particle number	1	64	1 000 000
Surface area per particle [μm^2]	314.16	19.63	0.0314
Total surface area per mass [μm^2]	314.16	1256.32	31400

Figure 3: Surface area of particles with different diameters. The scheme is based on calculations that assume perfectly spherical particles and was modified from ¹⁶¹.

4.4.4 Air quality regulations and the challenge of monitoring UFP

The recognition of negative health-related effects due to PM has driven the establishment of air quality directives with PM concentration thresholds, with the intention to reduce human exposure and mitigate health-related risks. In the European Union (EU), the history of these directives reflects the increasing recognition of toxicological studies emphasizing the harmful effects associated with finer particles. While Directive 1999/30/EC mandated a limit value for

PM₁₀, it only established monitoring requirements for PM_{2.5}, without the definition of a limit value ¹⁶³. It was not until Directive 2008/50/EC that a PM_{2.5} limit was introduced, setting an annual concentration threshold of no more than 25 µg/m³ to be met by 2015 and a threshold of 20 µg/m³ by 2020 ¹⁶⁴. In the Directive 2024/2881, the European Parliament and the Council adopted another drastic reduction of the annual PM_{2.5} threshold value to 10 µg/m³ by the year 2030 ¹⁶⁵. By contrast, the WHO already set its annual air quality guideline (AQG) for PM_{2.5} at 10 µg/m³ in 2005 and further tightened it to 5 µg/m³ in 2021 ¹⁶⁶. Despite an increase in public awareness and all these regulatory efforts, actual compliance with air quality standards proves difficult. According to the 2022 status report of the WHO ambient air quality database, most settlements around the globe exceed the 2021 AQG. For instance, in Europe, only 13 % of all recorded settlements exhibit annual PM_{2.5} values below the AQG, while settlements in Africa and South-East Asia display even lower compliance rates ¹⁶⁷.

While regulatory efforts have progressively tightened limits for PM_{2.5} and PM₁₀, PM_{0.1} has mostly remained outside the scope of environmental policy frameworks. The most notable recognitions so far came with the WHO 2021 Air Quality Guidelines and the EU-Directive 2024/2881, which recommended the integration of UFP measurements into the existing air quality monitoring stations ^{165,168}. Nevertheless, concrete regulations for PM_{0.1} do not exist, which is also attributable to a lack of appropriately standardized measurement protocols. To an extent, their establishment is complicated by the uneven distribution of UFP in the environment, which appear in high concentrations near emission sources and rapidly decline in number as the distance to the source increases ¹⁵². But most importantly, due to their low mass, UFP contribute only very little to the total mass of ambient particles. Established air-quality monitoring strategies, such as those for PM_{2.5}, rely to a large extent on the determination of mass concentrations by gravimetric analysis and therefore risk an underestimation of the actual quantity of UFP in a given sample ^{169,170}. The reliable surveillance of PM_{0.1} requires methods that enable the determination of particle number concentrations (PNC), such as condensation particle counters (CPC), fast mobility particle sizers (FMPS) or electrical low-pressure impactors (ELPI) ¹⁷¹.

4.4.5 Foliar absorption of particulate matter: A pathway for metal exposure

The interaction of plants with PM is linked to air quality, as strong associations between foliage and particles have been reported many times (reviewed in ¹⁷²). A notable example is provided by a Chinese study, that evaluated the ability of urban vegetation in Guangzhou to retain atmospheric particles. A total above-ground biomass of 5.2*10⁵ t with a leaf area of 459 km²

was estimated to capture approximately 8000 t of airborne particles per year^{172,173}. As a result of this interaction, targeted greening strategies have the potential to enhance air quality in urban areas, including the mitigation of human UFP exposure^{174,175}.

As described further above, PM emissions act as a vector for metal introduction into the environment, and thereby they represent an exposure route for plants towards these elements. In this context, UFP represent a particularly important category of particles, as it has been shown that they can enter plant leaves directly via the stomata, which are pores on leaf surfaces responsible for gas exchange^{176,177}. Alternatively, deposited particles can gradually degrade and release metals that are subsequently absorbed through the cuticle and transported within the plant^{172,178}. Yet, how plants physiologically respond to foliar uptake of metals through airborne PM represents a largely unexplored topic, which is also attributable to a lack of appropriate exposure systems.

4.5 Aim of this thesis

In this thesis, the impact of metallic stress on the model species *Arabidopsis thaliana* by two different exposure routes was thematized: (i) metal (i.e. Cd) uptake by the root system and (ii) foliar metal exposure through airborne UFP from brake wear. While the first topic is a detailed analysis of the effects of Cd on growth regulating tissues in the root apex, the latter focusses on the establishment of a novel system to study the effects of metallic UFP on plants and a first exploration of physiological effects.

4.5.1 The effects of Cd on the root with a special focus on the root tip

The effects of Cd on the root of *A. thaliana* have been extensively studied, with some investigations focussing on the growth-promoting tissues in the root tip^{122–125}. This section of the thesis expands on previous research through a comprehensive analysis of the molecular networks governing growth and nutrient homeostasis in the root apex. To this purpose, the roots of *A. thaliana* seedlings were exposed to Cd and separated into the root tip (RT) and the remaining root (RR) for a multidirectional omics approach, involving the analysis of (i) metal homeostasis with ICP-MS (ii) the metabolomic landscape with LC-MS and (iii) gene expression with RNA-sequencing. The results of this section were published in the journal “The Plant Journal” in June 2025 with the title “*Arabidopsis thaliana* root responses to Cd exposure: insights into root-tip specific changes and the role of HY5 in limiting Cd accumulation and promoting tolerance”¹⁷⁹. The study was conducted in parallel with an assessment of the effects that Zn excess exerted on the root of *A. thaliana*¹⁸⁰.

4.5.2 The effects of metallic UFP on *A. thaliana*

Unlike root-mediated metal uptake, foliar exposure of plants to metals through airborne PM has hardly been investigated and represents a frontier in environmental science. One source of metallic PM is brake wear, which causes emissions that often lie in the especially harmful ultra-fine size fractions. The effects of brake wear particles on plants have previously been analysed by applying them to soil, which does not represent realistic, airborne exposure conditions and most likely neglects the toxicological properties of UFP^{181,182}. Therefore, this section focusses on the establishment of a novel system for the controlled exposure of *A. thaliana* to airborne metallic UFP from brake abrasion. Using advanced analytical methods such as ELPI+ and single-particle ICP-MS (spICP-MS), the exposure conditions were thoroughly characterized with regards to emission characteristics and particle deposition on plant leaves. As a proof of concept and to get insights into physiological responses, RNA-sequencing with plants exposed to UFP was performed. Furthermore, a quantification of UFP after outdoor exposure of *A. thaliana* at locations with varying traffic degree was done to contextualize the experimental results with real-world UFP deposition. The results of this section were published in the “Journal of Hazardous Materials” under the title “Establishment of a system to study the effects of ultra-fine particulate matter from brake wear on plants under realistic exposure conditions” in May 2024¹⁶⁹.

5 Material and methods

5.1 The effects of Cd on the root of *A. thaliana* with a special focus on the root tip

5.1.1 Plant material and growth conditions

Seedlings were grown vertically on agar plates with Hoagland medium consisting of 1.5 mM Ca(NO₃)₂, 0.28 mM KH₂PO₄, 0.75 mM MgSO₄, 1.25 mM KNO₃, 0.5 µM CuSO₄, 1µM ZnSO₄, 5 µM MnSO₄, 25 µM H₃BO₃, 0.1 µM Na₂MoO₄, 50 µM KCl, 10 µM Fe-HBED, 0.5 g/l MES, 1 % sucrose (w/v) and 0.8 % agar (M-type, Sigma). Prior to autoclaving, the pH of the medium was adjusted to 5.7 with KOH. All plants were grown under long day conditions (16 h light (100 PAR), 8 h darkness, 21 °C). Prior to growth, seeds were stratified (4 °C, 2 days, darkness).

For growth assays in a root covered system (RCS), self-made polylactic acid (PLA) inlays for petri dishes were used in combination with aluminium foil to cover the roots (Figure 36). For growth in darkness, petri dishes were wrapped entirely in aluminium foil.

The lines used were Col-0 (= wild-type), *hy5_1* (SALK_0966551C), *hy5_215*¹⁸³, *myb12-1-f*¹⁸⁴, *elip1/2* (GABI DUPLO 1202/1a1.16.1, NASC ID N2103098), *hrg1* (GK578C04), *hrg2* (GK_772A03), *cyp82c4* (SALK_001585), *xth26* (SALK_042683C), *xth20* (SALK066689C). All lines were assessed for homozygous presence of the mutant allele by either sequencing or PCR based inspection of the T-DNA insertion using the following primers.

Table 1: Primers used for the genotyping of mutant lines (Sequences are given in 5'→3' orientation).

Primer	Sequence
LBa1	TGGTTCACGTAGTGGGCCATCG
CYP82C4-Fw	AAAAGCTCCTGCACCAAGTGG
CYP82C4-Rev	TATGACCCAAGTGCGTCTCTC
Elip1-Fw	GATCACCCGTCCTATAAATACATACG
Elip1-Rev	CACACAGTAGGCCTAACACAG
Elip2-Fw	GAAGAGATAATCCTACAGTTACACC
Elip2-Rev	CTATGCGTTACATAATCATTCTCCA
HRG1-Fw	TTTCTCCATTTTCGTTACGCAC
HRG1-Rev	CGTCGGAATATTCTTTTGCAG
HRG2-Fw	TTAGCGAAGCCATAGCTTGAG
HRG2-Rev	ATTTCTTGGTGGACAAGCATG

HY5-LP	ATTCCTTCCCAAATGTCTCG
HY5-RP	ATGCGAGTGAATGACCATTTC
myb12ex3Seq-Fw	TGGTCACTAATCGCGGGTCAT
myb12ex3Seq-Rev	TACCAGGGAGAACAGACAACG
XTH12-Fw	ATGTCGATGATGGAACCTCCAC
XTH12-Rev	ACATCCACGAGTTGCTATTTCG
XTH20-Fw	ATACCTGTGGCGTTGATGAAG
XTH20-Rev	AGGCTCTATGCTAGCCTTTGG
XTH26-Fw	AACGAATTTACAGTCCGTCCC
XTH26-Rev	AATGCTCATCAAACCTTGTGCC

5.1.2 Extraction of genomic DNA

Approximately 100 mg of leaf material from adult plants was ground in liquid nitrogen and thoroughly mixed with extraction buffer (500 μ l, 200 mM Tris/HCl (pH 7.5), 250 mM NaCl, 25 mM EDTA, 0.5 % (v/v) SDS) and centrifuged (5 min, 12 000 g). 300 μ l of the supernatant was transferred into a new reaction tube, mixed with 300 μ l isopropanol and centrifuged (5 min, 12 000 g). The supernatant was discarded and the pellet was washed with EtOH (70 %, 1 ml). After centrifugation (5 min, 12 000 g), the supernatant was discarded and the pellet was air-dried for 20 minutes. The pellet was dissolved in milliQ H₂O by heating (20 μ l, 50 °C, 5 min). The solution was centrifuged again (1 min, 12 000 g). The supernatant was transferred into a new reaction tube and stored at 4 °C for further use.

5.1.3 Polymerase chain reaction and agarose gel-electrophoresis

PCR was done by creating a master mix with the desired primers following the scheme depicted in Table 2. The 10 x Taq buffer consisted of 100 mM Tris/HCl (pH 9), 500 mM KCl, 15 mM MgCl₂, 1 % Triton X-100.

Table 2: Composition of a PCR reaction.

Reagent	Volume for 1 reaction
Taq buffer (10 x)	2.5 μ l
dNTP mix (200 mM)	2.5 μ l
Primer forward (20 μ M)	2.5 μ l
Primer reverse (20 μ M)	2.5 μ l
Taq polymerase	1 μ l

milliQ H ₂ O	13 µl
Template	1 µl

PCR reactions were done in a SensoQuest Labcycler using the following program. The annealing temperature and the extension time were set individually for each pair of primers.

Table 3: Temperature programm of a PCR. $T_{\text{Annealing}}$ is the annealing temperature, $t_{\text{Extension}}$ is the time set for the polymerase reaction to occur.

Cycles	Time	Temperature
1	2:00 min	96°C
10	0:30 min	96°C
	1:30 min	$T_{\text{Annealing}}$
	$t_{\text{Extension}}$	72°C
30	0:30 min	96°C
	0:30 min	$T_{\text{Annealing}}$
	$t_{\text{Extension}}$	72°C
1	5:00 min	72°C

Following the PCR, the reactions were mixed with loading buffer (30 % glycerol, 0.25 % bromophenol blue, 0.25 % xylencyanole) and loaded on agarose gels with ethidium bromide (1 % agarose in TAE buffer consisting of 40 mM Tris/HCl (pH 8), 40 mM acetic acid, 1 mM EDTA). Electrophoresis was done at 100 V for 30 min in chambers filled with TAE buffer.

5.1.4 Root growth assays

All growth assays were performed on petri dishes as described above. Seedlings were transferred to new plates after 7 days and grown for 7 additional days. Only the additional growth after the transfer was quantified. An exception to this is the data regarding primary and lateral root growth (Figure 22). In this case, the total root growth, including growth before the transfer was quantified.

5.1.5 ICP-MS

For ICP-MS seeds were surface sterilized with ethanol (70 %, 3 min) and bleach (2 %, 2 min), washed 3 times with sterile H₂O and suspended in sterile agar (0.1 %). The seeds were then sown on pre-cut nylon meshes on the agar plates. After 7 days of growth, the meshes were transferred to either control or cadmium (25 µM) plates. 24 h and 48 h after the transfer, RT samples were collected by cutting the roots 2-3 mm from the apex. The remaining roots

represented the RR samples. The samples were then washed twice in desorption solution (5 mM CaCl_2 , 1 mM MES, pH 5.7, 10 min, 4 °C) and twice in distilled water (5 min, 4 °C). The material was then dried, weighed and transferred to polytetrafluoroethylene (PTFE) tubes for digestion in a high-performance microwave reactor (Ultraclave 4, MLS) using nitric acid (0.5 ml, 67-69 %). For elemental analysis (Sector Field High Resolution (HR)-ICP-MS, Element 2, Thermo Fisher Scientific), a 6-point external calibration curve was created from a commercial multielement standard (Bernd Kraft). Rhodium (Rh) and germanium (Ge) were infused online as internal standards. Extraction and measurement of the samples was conducted at the department of Molecular Plant Nutrition at the Leibniz Institute of Plant Genetics and Crop Plant Research (IPK) in Gatersleben, Germany.

5.1.6 Metabolomic analysis

For the analysis of metabolites, seedlings were grown and treated with Cd as described above (5.1.5). 48 h after the onset of Cd treatment, RT samples were taken by cutting the roots 2-3 mm from the apex, RR samples were collected by cutting equally sized pieces from the mid length of the primary root. Extraction and LC-MS/MS analysis was done as described ¹⁸⁵. Metabolite data were first normalized to estimated biomass of each sample (i.e. the amount of collected root pieces). Extraction, measurement and data preprocessing were conducted by Stéphanie Boutet (INRAE – Centre de Versailles-Grignon, Institut Jean-Pierre Bourgin).

For further statistical analysis of differentially abundant features (DAF), the data were normalized to the total metabolite count of each sample. A linear model was then fitted to the log₂ transformed data with limma using empirical Bayes moderation of the linear model fits ¹⁸⁶. Features were considered significantly differential abundant when $\log_2\text{FoldChange} > 1$ or $\log_2\text{FoldChange} < -1$ and $p_{\text{adj}} \leq 0.05$.

5.1.7 RNA sequencing

For RNA sequencing, seedling growth, Cd treatment and sample collection was done as above (5.1.5). Directly after cutting the roots, the samples were frozen in liquid nitrogen. Isolation of total RNA and DNase I-treatment was done with a Maxwell 16 (Promega) and the Maxwell RSC Plant RNA kit. An Agilent 2100 Bioanalyzer Expert with the Agilent Nano 6000 kit was used for the determination of RNA quality and concentration. 1 µg of RNA was used as to perform library preparation with a TruSeq Stranded mRNA sample preparation kit. The QIAxcel screening kit was used to assess library quality. Libraries were quantified, diluted and pooled using the KAPA SYBR fast universal qPCR kit and an Applied Biosystems 7900HT

Real-Time PCR system. A NovaSeq6000 was used with standard workflow to perform sequencing of 2x150 bp paired-end reads. Library preparation and RNA-Sequencing was performed at the GIGA Genomics platform (ULiège, Liège, Belgium). FastQC and Trimmomatic were used for data quality assessment and trimming. Together with the TAIR10 genome assembly and the Araport11 annotation, HISAT2 was used for mapping of the reads and counting was done with htseq-count. Differentially expressed genes (DEG) were identified with DESeq2 (\log_2 fold change > 1 or \log_2 fold change < -1 and $p_{\text{adj}} \leq 0.05$)¹⁸⁷. The PANTHER website (pantherdb.org) was used to perform GO overrepresentation analysis.

5.1.8 Comparison with scRNA-Seq data

To integrate information on cell-type-specific expression of genes, a published scRNA-Seq atlas from root tips was used¹⁸⁸. Specifically, for each cluster of genes specific to a particular cell type, the number of significant Cd-DEG for a given timepoint (24 h/ 48 h) and root section (RR/ RT) was identified and divided by the number of total genes in that cluster. This resulted in the proportion of differentially expressed genes for each cluster. To increase the number of DEG, DEA was done with \log_2 fold change > 0.58 or \log_2 fold change < -0.58 and $p_{\text{adj}} \leq 0.05$).

5.1.9 Analysis of HY5 target genes

To assess the regulation of HY5 target genes, the mean fold change of 297 high-confidence target genes from Burko et al.¹⁸⁹ was calculated for a given timepoint (24 h/ 48 h) and root section (RR/ RT). This was done by inferring fold changes for the target genes without a threshold during DEA (DESeq2 with \log_2 FoldChange $>/< 0$ and $p_{\text{adj}} \leq 0.05$).

To assess the significance of the collective regulation of HY5 targets, null distributions were generated. To this end, calculated for a given timepoint (24 h/ 48 h) and root section (RR/ RT), 10 000 lists of 297 randomly chosen AGI codes were generated (DESeq2 with \log_2 fold change $>/< 0$ and $p_{\text{adj}} \leq 0.05$), and the mean fold change of each list was calculated. Statistical significance was then calculated as follows:

$$p = \frac{\text{Number of null means } \geq F \text{ (297 HY5 target genes)}}{\text{Total number of null samples}}$$

5.1.10 ICP-OES

For ICP-OES, seeds were surface sterilized for 45 min using chlorine gas. Seedlings were then grown and transferred as described (5.1.1, 5.1.5). Samples of roots and shoots were collected 72 h after the transfer. The samples were desorbed with Milli-Q H₂O (4 °C, 10 min), washed with 20 mM CaCl₂ twice (4 °C, 10 min, pH 5.7) and H₂O (4 °C, 10 min). After drying for at

least 72 h at 50°C, samples were weighed into PTFE tubes and microwave-digested at 80°C for 10 min and 180°C for 15 min (2:1 (HNO₃ (65 %):H₂O₂ (30 %)) START 1500, MLS). An iCAP 6500 series ICP-OES (Thermo Fisher Scientific) was used to measure element concentrations after calibrating the device with a 4-point calibration curve determined with a commercial multielement standard (Thermo Fisher Scientific).

5.1.11 HPLC

For the analysis of PCs and GSH with HPLC, seedlings were grown on nylon meshes for 9 days before the transfer to control or cadmium (25 µM) plates. Samples of roots and shoots were collected 72 h after the transfer. The extraction of thiols was done by adding extraction buffer (0.1 % (v/v) trifluoroacetic acid, 6.3 mM diethylene triamine pentaacetic acid (DTPA), 40 µM N-acetylcysteine as internal standard) at three times the volume of the sample's weight. Labelling was done with 50 mM monobromobimane (30 min, 45°C) using a master mix (200 mM EPPS, 6.3 mM DTPA (pH 8.2) and 20 µM tris-(2-carboxyethyl)-phosphine dissolved in 200 mM EPPS (pH 8.2). 1 M methanesulfonic acid was added to stop the labelling reaction. Measurement of PCs and GSH was done as described in ¹⁹⁰.

5.2 The effects of metallic UFP on *A. thaliana*

5.2.1 Plant material and growth conditions

A. thaliana (Col-0) was grown for 4-5 weeks in short day conditions (8 h light (100 PAR)/ 16 h darkness, 25 °C) on standard potting soil using 5 cm x 5 cm x 5.5 cm pots.

5.2.2 UFP generation and exposure

Generation of UFP and plant exposure were done using a self-built dynamometer brake test stand consisting of an electric motor (45 kW), a 800 kg fly wheel, a pneumatically actuated calliper and a flange with adapters for different discs (Figure 39). Grey cast iron (GJL-150) brake discs with an outer diameter of 450 mm and a thickness of 356 mm together with LowMet brake pads supplied by TMD Friction GmbH with a size of 30 mm x 30 mm x 10 mm were used.

Three different use-cases (i.e. a city braking maneuver with $v_{\text{start}} = 5 \text{ m}\cdot\text{s}^{-1}$; $E_{\text{brake}} \approx 0.04 \text{ MJ}$), a cross-country road braking maneuver ($v_{\text{start}} = 10 \text{ m}\cdot\text{s}^{-1}$; $E_{\text{brake}} \approx 0.15 \text{ MJ}$) and a highway braking maneuver ($v_{\text{start}} = 20 \text{ m}\cdot\text{s}^{-1}$; $E_{\text{brake}} \approx 0.59 \text{ MJ}$) were analysed with respect to their emission behaviour by determining the wear coefficient k after 20 brakings and braking pressures of 2 and 3 MPa.

To conduct controlled exposure experiments, an exposition chamber including a custom-made specimen mount was integrated into the exhaust system of the dynamometer rig. To ensure better dispersion of particles in the chamber and reduce mechanical stress from the suction unit, two windshields at the entrance and the exit of the chamber were integrated. The control group was placed next to the exposure chamber. The background exposure group was placed inside the chamber, with only the exhaust system activated. The treatment group was placed inside the chamber and subjected to 45 full-stop highway brakings. To prevent excessive heat (i.e. more than 30 °C) in the chamber, the wear of 45 brakings to the treatment group was delivered in an alternating nesting with the background exposure group. All work on the brake test bench was carried out by Thorsten Opel (Department of Ceramic Materials Engineering, University of Bayreuth).

5.2.3 Measurement of aerial UFP concentration with ELPI+

An electrical low-pressure impactor (ELPI+, Dekati Ltd.) consisting of 15 impactor stages was used to separate particles from 6 nm to 10 000 nm. The device was operated according to the manufacturer's instructions with a flow rate of 10 l*min⁻¹. Particles were captured on polycarbonate foils (\varnothing = 25mm, Whatman Nucleopore, GE Healthcare). To prevent particle bouncing, DS-515 collection substrate spray (Dekati Ltd.) was applied. Moisture content was eliminated by using ELPI+ in combination with the DD 603 dryer (Dekati Ltd.). ELPI+ measurements and data processing were done by Marina Maier (Bavarian State Office for Environment, Augsburg).

5.2.4 Measurement of particles collected with ELPI+ using spICP-MS

To recover sampled particles from polycarbonate foils, they were transferred into 15 ml of micelle-forming tenside solution (0.25 % Triton-X-114, VWE International). The foils were shaken (3 min) and treated in an ultrasonic bath (10 s). spICP-MS measurement was done as described below (5.2.8). The measurement method was previously validated with monodisperse gold nanoparticles (NIST RM 8013, 60 nm, $1.5 \cdot 10^7$ particles/foil), resulting in a recovery rate of 85-87 %. Validation and execution of the method was done by Marina Maier (Bavarian State Office for Environment, Augsburg).

5.2.5 X-Ray fluorescence measurement of brake pads

The elemental composition of ground LowMet brake pads (5.2.2) was analysed by Marina Maier (Bavarian State Office for Environment, Augsburg) with the spectrometer SPETRO XEPOS (SPECTRO Analytical Instruments, Germany).

5.2.6 Outdoor exposure of *A. thaliana*

From 19.09.2022 to 04.10.2022, rosette-stage plants (see 5.2.1) were placed on ground level at a rural location (Coordinates: 47.96875, 11.22017), a suburban location (Coordinates: 48.32601, 10.90305) and an inner-city location (Coordinates: 48.37027, 10.89628). Plants were inspected regularly and watered if necessary.

5.2.7 Particle extraction from plant material

Plants were grown as described in 5.2.1 and exposed to metallic UFP as described in 5.2.2. A modification of the methanol-based extraction described in ¹⁹¹ was used to extract UFP from leaves of *A. thaliana*. Frozen leaf material was weighed into 50 ml tubes (Greiner) with 20 ml of 10 mM 3-(cyclohexylamino)-2-hydroxypropane-1-sulfonic acid (CAPSO, pH 9 with KOH) and homogenized with a Witeg HG-15A homogenizer. Samples were probe sonicated (3 min, 10 s intervals) with a Bandelin Sonopuls HD 200. Three aliquots of each sample were extracted by transferring 500 µl to a new 15 ml tube (Greiner) and adding 3.75 ml of 50 % aqueous methanol. The resulting sample was placed on an orbital shaker (150 rpm, 1 h) and 1.25 ml of 1 % Tween 80 was added. The ultrasonication step was then repeated. The samples were filtered (1 µm pore size) and diluted 10-fold with milli-Q H₂O. sp-ICP-MS was done as described below (5.2.8).

The efficiency of the extraction procedure was assessed by adding commercially available Cu-nanoparticles. Different volumes of dispersions made from commercially available Cu nanoparticles (Copper Nanopowder APS 25 nm / 99.5% SSA 30-50 m²/g – spherical, CAS no. 7440-50-8, 100 mg·l⁻¹, 10 mg·l⁻¹, 1 mg·l⁻¹, 0.1 mg·l⁻¹, dispersed in 1 % Tween 80) were added to a defined amount of leaf material with extraction buffer. The extracts were prepared and used for spICP-MS as described below (5.2.8).

5.2.8 spICP-MS

Particles were measured using a 8900 triple-quadrupole ICP-MS (Agilent) with an acquisition time of 60-300s and a dwell time of 100 µs. The transport efficiency was determined with gold nanoparticles (NIST RM 8013, 60 nm, $2.9 \cdot 10^{13} \pm 3$ % particles·l⁻¹, Gaithersburg, MD, USA). A multielement standard solution (Merck) was used to calibrate signal sensitivity. Ultra-fine Pb particles were determined additionally using cloud point extraction ¹⁹². spICP-MS provides comprehensive information about the number of particles for each element in a sample, however it cannot determine the composition of individual particles ^{193,194}. For this reason, the measured signals are referred to as ultra-fine particle constituents (UFPC).

MassHunter Version 4.6 was used for data acquisition of the metallic particles. SpICP-MS measurements and data preprocessing were done by Marina Maier (Bavarian State Office for Environment, Augsburg). PCA of the data was done using the R packages “FactoMineR” and “factoextra”. An integer of 1 was added to all data before \log_2 -transformation for PCA.

5.2.9 RNA-Sequencing

Plants were grown as described in 5.2.1 and exposed to metallic UFP as described in 5.2.2. 24 h after the exposure, plant rosettes were flash frozen in liquid nitrogen. Every sample consisted of the rosettes from 6 individual plants. Extraction of RNA was done by adding TRIsure (Bioline) to frozen, ground plant material (1 ml TRIsure, ~ 200 mg material) and vortexing (1 min). The samples were incubated (room temperature, 5 min) and vortexed again (1 min). This was followed by the addition of chloroform (200 μ l), shaking (20 sec) and incubation (room temperature, 5 min). The samples were then centrifuged (12 000g, 10 min, 4°C), the aqueous supernatant was transferred into a new reaction tube, mixed with isopropanol (500 μ l), incubated (room temperature, 10 min) and centrifuged (12 000g, 10 min, 4°C). The supernatant was discarded and the pellet washed with EtOH (70 %, 1 ml). The samples were then centrifuged (12 000 g, 5 min, 4°C) and the supernatant was discarded. The pellets were air dried (room temperature, 20 min) and solubilized in milliQ H₂O (20 μ l, 5 min, 50°C). After this, one more centrifugation step was done (room temperature, 1 min, maximum g) and the supernatant representing the finished sample was transferred into a new reaction tube. In order to improve sample purity, the RNA samples were purified using an RNeasy Mini 250 kit (Qiagen) according to the manufacturers recommendations. Preparation of libraries, sequencing and data processing were done as described in ¹⁹⁰. For further data analysis, including differential expression analysis, PCA and extraction of normalized counts, DESeq2 was used (\log_2 fold change > 1 or \log_2 fold change < -1 and $p_{\text{adj}} \leq 0.05$) ¹⁸⁷. The PANTHER website (pantherdb.org) was used to perform GO overrepresentation analysis.

5.2.10 Scanning electron microscopy

For assessment of particles on plant material with scanning electron microscopy, leaves were vacuum freeze-dried for 4 h directly after the exposure. Samples were coated with a 2 nm Pt-layer in a Leica EM ACE600 sputter-device. Microscopy was done with a JSM-IT-500 (JEOL).

6 Results

6.1 The effects of Cd on the root of *A. thaliana* with a special focus on the root tip

In this section, Cd was applied to *A. thaliana* seedlings in the form of CdCl₂, which dissociates in the aqueous, agar-based setup (see Methods 5.1.1). The designation “Cd” is used throughout the results and discussion sections to refer specifically to the divalent cation Cd²⁺.

6.1.1 The impact of Cd on primary root elongation

The effect of Cd on primary root growth was evaluated by germinating *A. thaliana* seedlings for 7 d on control plates and then transferring them to uncontaminated plates (Control) or 25 µM Cd (Cadmium) plates.

Quantification of root elongation 7 d after the onset of Cd exposure showed that a concentration of 25 µM Cd resulted in a reduction of primary root growth by 50 % compared to the control (Figure 4, A). The treatment resulted in a rapid reduction of root growth, as already after 24 h, root growth was significantly lower compared to the control (Figure 4, A).

To investigate the relationship between root growth inhibition and cellular division in the RAM on one side and cellular elongation in the EZ on the other side, these zones were measured following Cd exposure. RAM length was unaffected after 24 h and significantly smaller in the Cd conditions after 48 h. The size of the EZ was found to be lower in Cd exposed seedlings compared to control seedlings at both timepoints. These results imply an earlier impairment of the EZ compared to the RAM (Figure 33).

Because the experimental setup led to a significant reduction of root growth after 24 h and 48 h and growth was inhibited by 50 % after one week, all further analyses were conducted after these timepoints.

6.1.2 Analysis of elemental profiles under Cd exposure

With the aim to quantify Cd accumulation and investigate its impact on metal homeostasis in RT and RR, an ICP-MS analysis was performed. This revealed a striking difference in the degree of Cd accumulation between the two sections. At both timepoints, Cd contents in RT were noticeably lower than in RR. In both RR and RT, an increase of Cd contents from 24 h to 48 h by ~100% was observed (Figure 4, B).

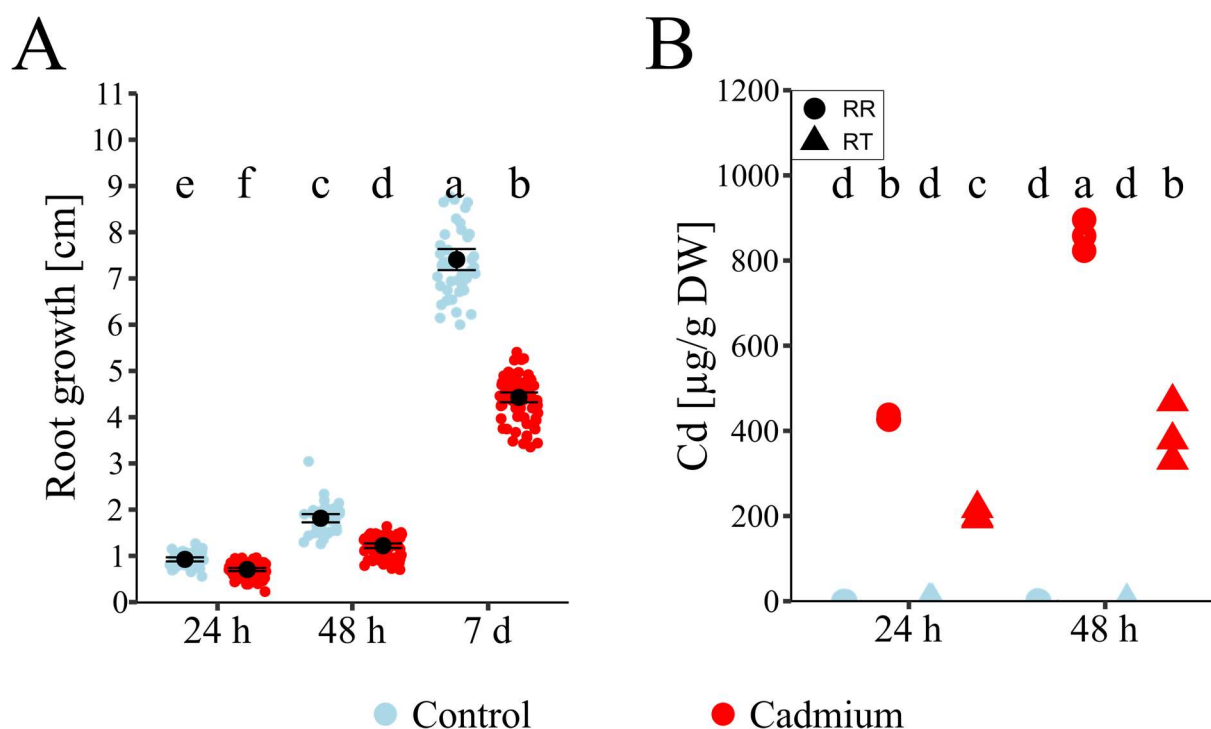


Figure 4: Growth inhibition by Cd and Cd accumulation in RR and RT. A: Effects of 25 μ M Cd on primary root growth. Seven-day old seedlings were transferred to control or cadmium plates and the growth progression after the transfer was recorded. Displayed are single values and mean values \pm standard deviation. Letters indicate statistical groups (ANOVA and Tukey HSD, ≤ 0.05 , $n = 46-76$, data from three independent replicates). B: Cd contents in RT and RR upon exposure to 25 μ M Cd. Seven-day old seedlings were transferred to control or cadmium plates and collected for ICP-MS after 24 h or 48 h. Letters indicate statistical groups (ANOVA and Tukey HSD, ≤ 0.05 , $n = 3$, data from three independent biological replicates). ICP-MS measurements were conducted at the Leibniz Institute of Plant Genetics and Crop Plant Research (IPK) in Gatersleben, Germany.

Apart from this, a significant reduction of P contents in RT under Cd exposure was found after 24 h. This was transient, as P contents in RT after 48 h were comparable in the control and Cd samples. Cu contents were also decreased after 24 h in RT. Except for RT at 48 h, Zn concentrations in all Cd treated groups were lower than in the controls. Significant reductions in Mn contents were observed in both RR and RT after both timepoints, except for 24 h RR. Fe concentrations were associated with high variance and no significant differences between the samples were detected (Figure 5). However, Fe contents of entire Col-0 roots were found to be reduced following Cd exposure in the context of the mutant analysis described further below (Figure 20).

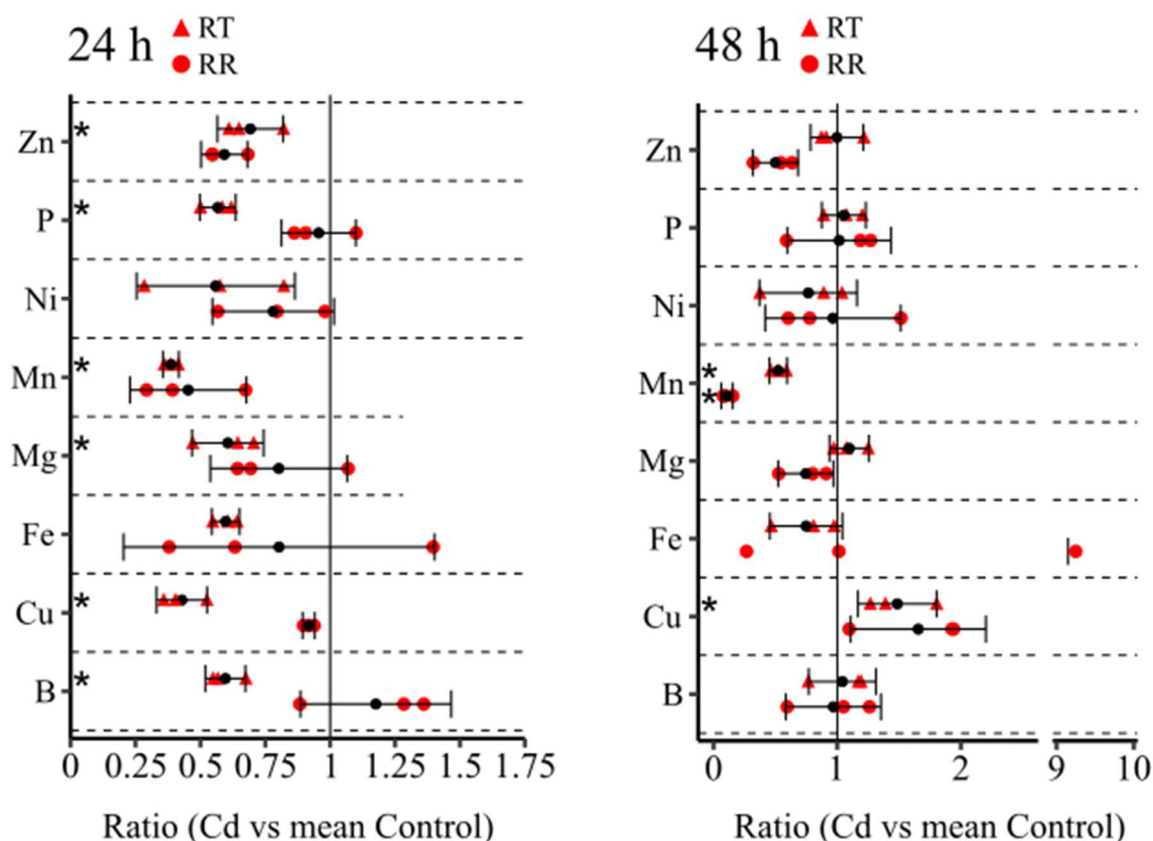


Figure 5: Elemental contents of RT and RR under Cd exposure. Ratios were calculated by dividing the elemental contents ($\mu\text{g}\cdot\text{g}^{-1}$ DW) by the mean of the respective control. Displayed are single ratio values (red), mean ratio values (black) and standard deviation. Asterisks indicate statistically significant differences (Mann-Whitney U-test, $p \leq 0.05$). Data are from three independent replicates). ICP-MS measurements were conducted at the Leibniz Institute of Plant Genetics and Crop Plant Research (IPK) in Gatersleben, Germany.

6.1.3 The impact of Cd on metabolite contents

To explore the impact of Cd on the metabolomic landscape in the two root sections, untargeted metabolite analysis with LC-MS was done 48 h after Cd exposure. In total, 2961 features were detected and 169 of them were annotated with putative metabolites.

For an estimation of total metabolite content and principal component analysis (PCA), feature signals were normalized to estimated sample biomass, i.e. the amount of collected root pieces (5.1.6). In total, 3052 features were detected, and RR displayed higher feature contents overall (Figure 6, A). PCA highlighted the root part and not the treatment with Cd as the main driver for variance in the dataset, as PC1 separates the RT and RR samples and accounts for 69.7 % of variance. By contrast PC2 separates the Cd and control groups and accounts for only 14.9 % of the variance observed. RR samples were separated by greater distance along PC2 than RT samples, indicating a larger impact of the treatment on RR (Figure 6, B).

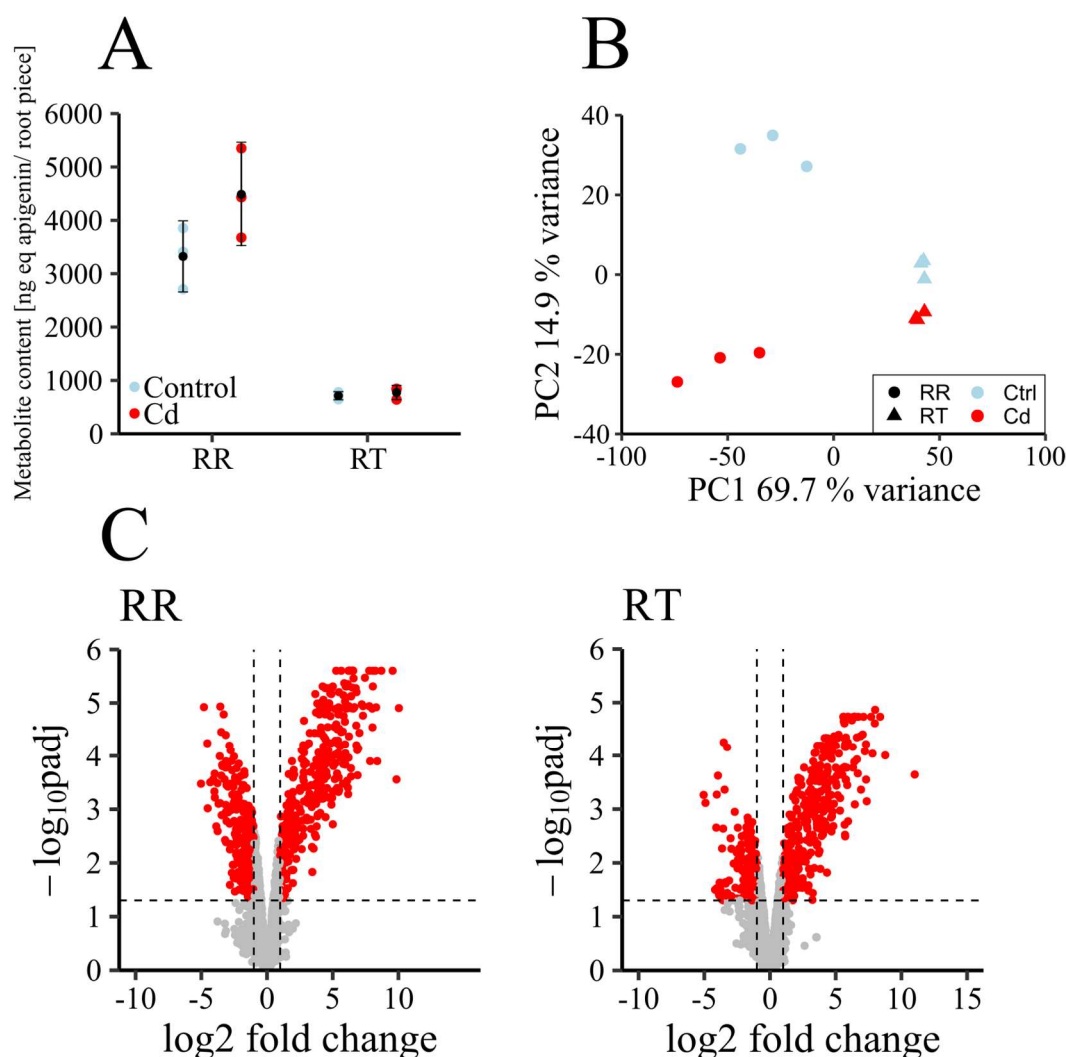


Figure 6: Metabolomic analysis of *A. thaliana* RT and RR following exposure to 25 μ M Cd for 48 h. A: Content of all detected features of RR and RT. Data are given as relative quantification in ng equivalent to the internal standard apigenin. Displayed are mean \pm standard deviation. B: Principal component analysis (PCA) showing the similarities of the different samples along the first two principal components. The percentage of variance explained by each principal component is indicated. C: Volcano plots showing the amount of significant differentially abundant features (DAF), for which $p_{adj} < 0.05$ and \log_2 fold change is greater than 1 or smaller than -1. Extraction, measurement and data preprocessing were conducted by Stéphanie Boutet.

To perform statistical analysis for differentially abundant features (DAF), metabolite contents in each sample were normalized to the total count of metabolites in the sample. Separate linear models for RR and RT were fitted for differential metabolite analysis¹⁸⁶. In RR, 369 DAF were more abundant after treatment with Cd and 362 features were less abundant (Figure 6, C). In RT, 317 DAF were more abundant and 175 DAF were less abundant (Figure 6, C).

In both RR and RT, features annotated as phytochelatins were characterized by higher abundance following Cd treatment. PC contents were elevated to the same extent in both root parts ($\emptyset \log_2$ fold change_{RT} = 5.2, SD_{RT} = 1.9, ($\emptyset \log_2$ fold change_{RR} = 5.7, SD_{RT} = 1.9). In RT,

also two features referring to metabolites of the flavonoid and lipid families were present with higher abundance upon Cd exposure, respectively. By contrast, three flavonoid related features were significantly less abundant in RR after Cd treatment. Glucosinolate derived features were found to be both more and less abundant in RR and RT (Figure 7).

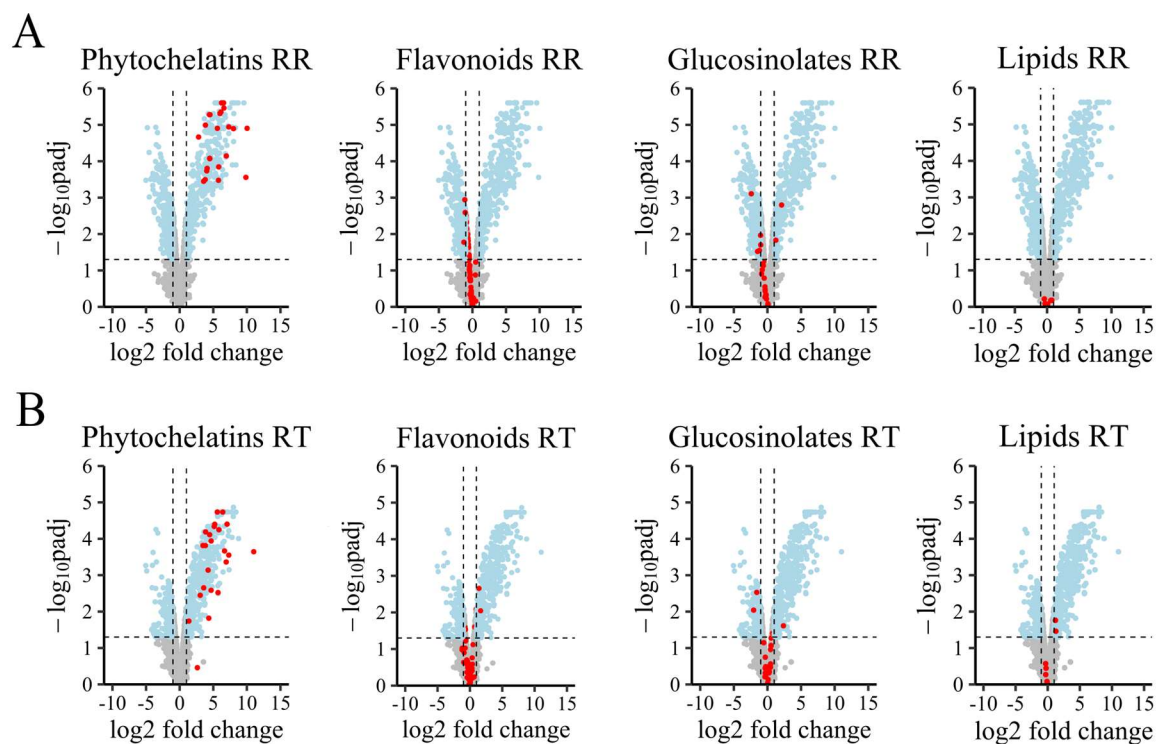


Figure 7: Metabolic changes of substance classes in RR (A) and RT (B) shown with volcano plots. Features belonging to the respective substance class are labelled red. Horizontal and vertical dashed lines indicate the cutoff values for significance ($\text{padj} \leq 0.05$; \log_2 fold change greater than 1 or smaller than -1).

Moreover, sideretin, a secondary metabolite belonging to the family of coumarins was measured with lower concentration in Cd compared to control conditions in RR (Figure 8).

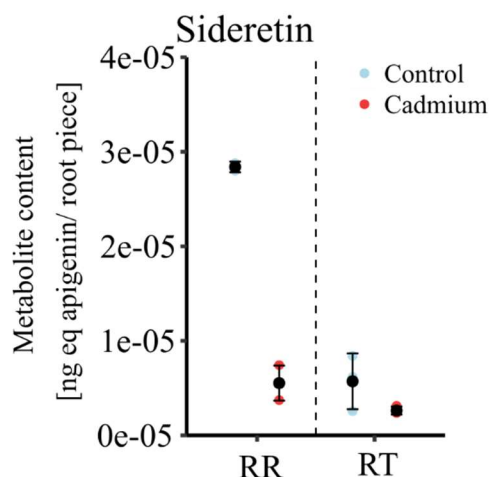


Figure 8. Abundance of sideretin in RR and RT in control conditions and after 48 h of Cd exposure. Data are given as relative quantification in ng equivalent to the internal standard apigenin per root piece.

6.1.4 The impact of Cd on the root transcriptome

To further analyse the effects of Cd exposure in the two root sections of *A. thaliana*, RNA sequencing was performed after 24 and 48 h of Cd exposure. PCA was done to investigate the influence of the growth condition, the harvesting timepoint and the root section on global gene expression. This showed, that PC1 which separated the two root parts explained for 96 % of the variance observed in the dataset. By contrast, PC2, which only explained 2 % of the variance, separated the Control from the Cd transcriptomes. Cd had a lower impact on RT, since the RT samples are in closer proximity along PC2 than the RR samples. Compared to this, the harvesting timepoint had only very little impact on gene expression. Taken together, these results clearly demonstrate that the main driver for variance in the transcriptomes is the root part and not the treatment (Figure 9, A). A more detailed analysis of the differences between RT and RR is provided in 6.1.8.

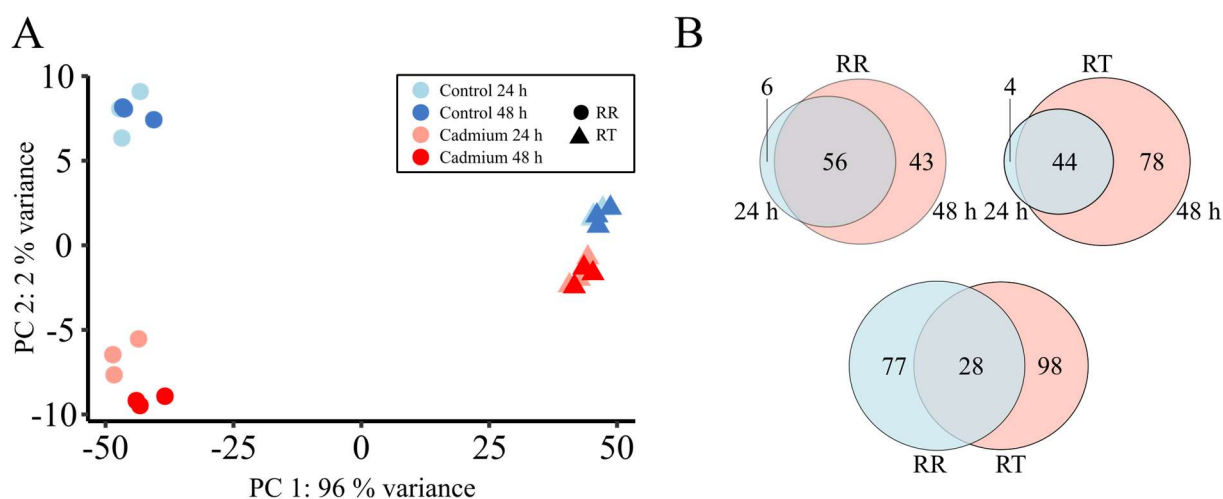


Figure 9: RNA-Sequencing of *A. thaliana* root tip (RT) & rest of root (RR) after Cd-exposure. A: Distribution of control & Cd samples in RT & RR according to the first two principal components. The percentage of variance for each component is shown. B: Top: Number of differentially expressed genes in RR/ RT after 24/48h of Cd-exposure with overlap between the timepoints. Bottom: Number of DEG in RR and RT and the overlap. Up- & downregulated genes are shown together. Differential expression was determined with DESeq2 ($\text{padj} \leq 0.05$; \log_2 fold change greater than 1 or smaller than -1, data from three independent experiments).

Differential expression analysis (DEA) yielded a total of 105 differentially expressed genes (DEG) in RR and 126 DEG in RT. In RR, most DEG of the 24 h timepoint were differentially expressed also after 48 h, i.e. only 6 DEG were exclusive to 24 h and 56 DEG are shared between the timepoints. The same trend was observed in RT, where only 4 genes were specific to the 24 h timepoint and 44 genes are shared between 24 h and 48 h. In RR after 48 h, 43 genes were differentially expressed, and RT after 48 h had 78 DEG. When comparing all up- and downregulated DEG from RT with RR at both timepoints, 77 are specific to RR, 98 specific to RT and 28 DEG are shared (Figure 9, B).

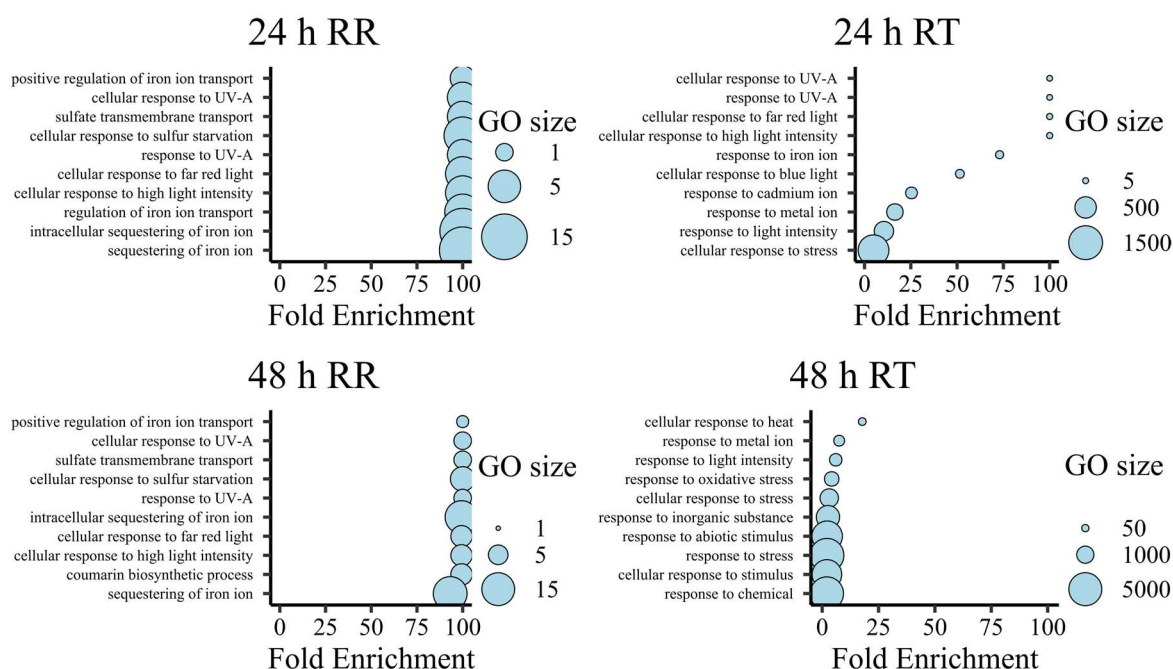


Figure 10: "Biological process" GO overrepresentation analysis with DEG in RR (top) & RT (bottom). Up- & downregulated genes from the respective timepoints were pooled. Analysis was done with Panther (see Methods, 5.1.7).

To get insights into the functional categories of the Cd-DEG, GO overrepresentation analysis was done. The analysis of the response of RR to Cd showed a significant enrichment of processes associated with Fe homeostasis and S assimilation (Figure 10, left panels). For example the genes *RESPONSE TO LOW SULFUR 1, 2, and 3* as well as *SULPHATE TRANSPORTER 1;1* showed significant expression changes in RR (Table 5, Table 6).

Changes in the expression of Fe-homeostasis genes occurred in both upward and downward directions. For instance, Cd treatment led to higher transcript abundance of *BASIC HELIX-LOOP-HELIX 38, 39, and 100*, *FEP 1 and 2*, *FERRIC REDUCTION OXIDASE 3* and a decreased expression of *VACUOLAR IRON TRANSPORTER-LIKE 1, 2, and 5* and *FERRITIN 1 and 4*. *S8H* and *CYP82C4*, which are involved in the biosynthesis of catechol type-coumarins, were also downregulated (Figure 11, Table 6). In agreement with this, the metabolite quantification described in 6.1.3 showed a decrease of sideretin contents in RR after Cd treatment (Figure 8). Furthermore, many Fe-related DEG were characterized by lower expression in RT compared to RR.

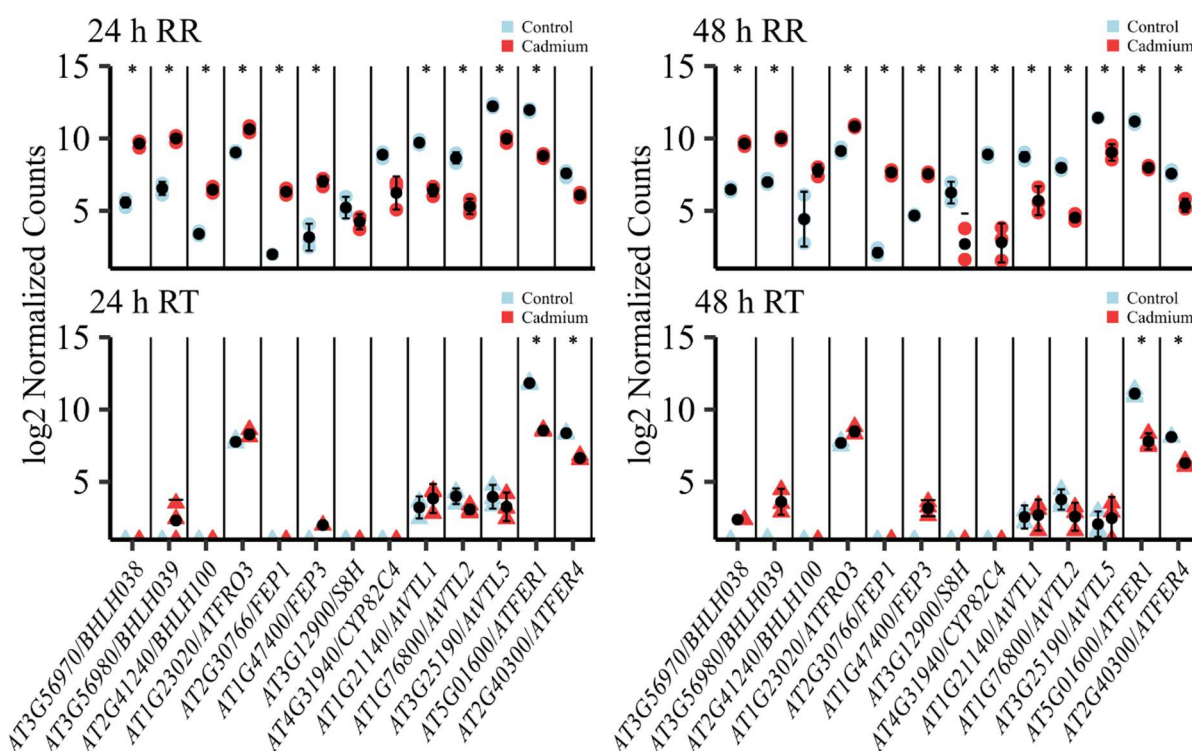


Figure 11: Expression of Fe-homeostasis related genes in RR and RT after 24h. Displayed are single values (red/blue), mean ratio values (black) and the standard deviation of log2 normalized counts for each gene. Asterisks indicate statistical significance. Differential expression was determined with DESeq2 (padj ≤ 0.05; log2 fold change greater than 1 or smaller than -1, data from three independent experiments).

In RT, the functional categories of DEGs seemed to encompass broader biological functions, with GO terms showing lower fold enrichment compared to RR. Identified GO terms were related, for example, to Cd and metal ions or stress response in general. GO terms associated with light intensity/ irradiation or UV light were found to be overrepresented in both root parts. They included genes like *EARLY LIGHT INDUCIBLE (ELIP)* and *ELIP2* (Table 7, Table 8).

To analyse whether growth reduction of the root was accompanied by an alternative regulation of the cell cycle, the response of cell cycle regulatory genes (CCRG) was investigated. Even though a growth reduction at the timepoints for which the RNA-seq samples were taken was clearly demonstrated (Figure 4), no differential expression of CCRG was found. Not a single gene from a set of cell-cycle related genes from Vandepoele *et al*¹⁹⁵ was significantly deregulated after Cd exposure in RT at both timepoints (Figure 12).

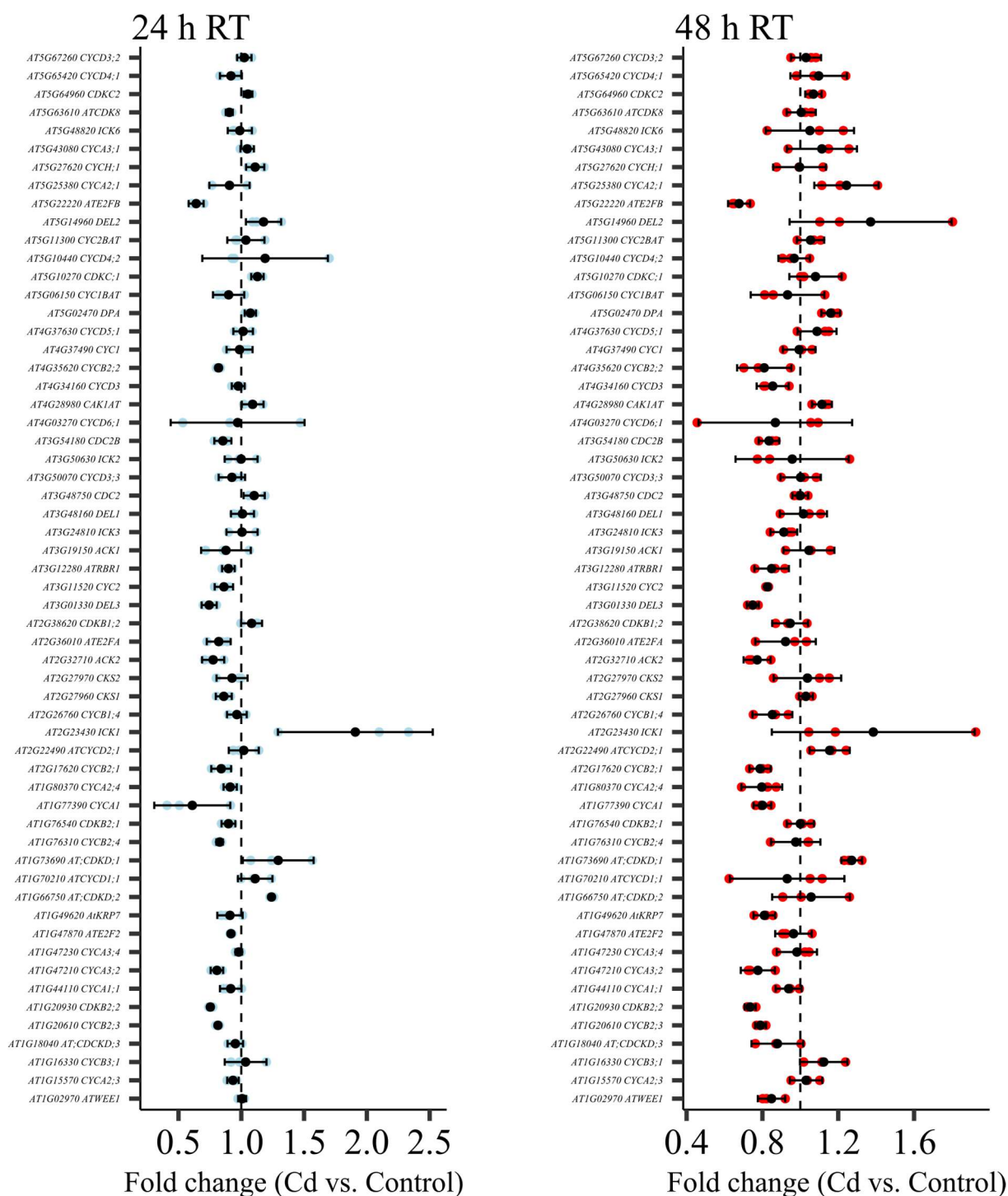


Figure 12: The regulation of cell cycle related genes in RT following Cd exposure. Values were calculated by dividing the normalized counts for every gene in the Cd exposed sample by the mean of the control sample. Displayed are single ratio values (red/blue), mean ratio values (black) and the standard deviation. Differential expression was determined with DESeq2 ($\text{padj} \leq 0.05$; \log_2 fold change greater than 1 or smaller than -1, data from three independent experiments).

6.1.5 The response of root tips to Cd

In order to obtain a better understanding of the tissue and cell-type specific response to Cd, the data were mapped to a published scRNA-seq atlas of RT, which provides clusters of genes that are expressed predominantly in specific cell types of the root tip¹⁸⁸. Specifically, each cluster

of the atlas was assessed for the share of genes found to be differentially expressed upon Cd treatment after each of the timepoints in both RR and RT (see Methods, 5.1.8). Generally, this showed that the greatest extent of differential expression occurred in clusters with genes specific to mature cell types and a higher degree of differential expression occurred along with treatment duration (Figure 13). For example, the highest proportion of DEG was found when comparing DEG after 48 h Cd exposure from RT to clusters with genes specific to “Mature Cortex”, “Mature Trichoblast” and “Mature Atrichoblast” (Figure 13, top). Also, stronger overlap between nearly all gene clusters representing mature and elongating cells with the DEG from RT was observed when compared to RR (Figure 13, Top & middle).

In addition to this, Cd-DEG that mapped to meristematic cell clusters were mined for functions related to the regulation of the cell cycle, which resulted in the identification of *NAC DOMAIN CONTAINING PROTEIN 44 (ANAC044)* within the cluster “meristematic cortex”. ANAC044 was described as a regulator of the cell cycle in response to DNA damage¹⁹⁶ and the gene was upregulated in RT following Cd exposure (data not shown). However, the *anac044* mutant did not display any different Cd-phenotype than wild-type plants (Figure 35).

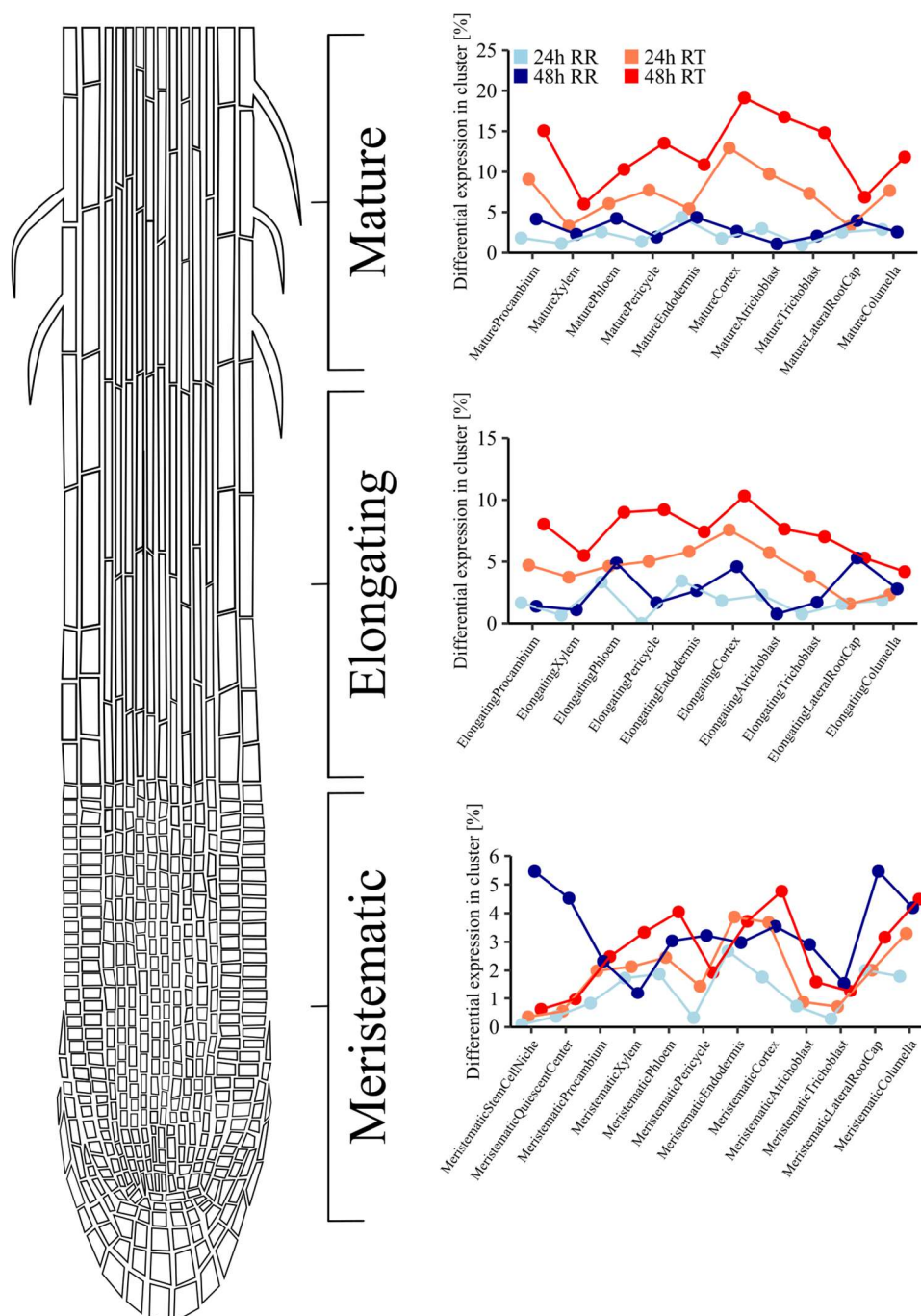


Figure 13: Integration of cellular information of a single cell root tip atlas into bulk RNA-seq data from RT and RR. Differentially expressed genes were mapped to clusters of genes specifically expressed in certain cell types of RT (see Methods, 5.1.8). The y- displays the percentage of genes from a given cluster that are differentially expressed at a given timepoint after Cd exposure in RR or RT.

Because a central goal was to identify the specific response of RT to Cd on a transcriptomic level, the RT-specific DEG resulting from Figure 9, B were assessed for expression changes across all samples by extracting their fold changes without implementing a threshold value during DEA. This step was necessary, since the statistical rigidity employed during DEA conflicts with the extraction of RT specific DEG. A given gene may significantly surpass the

fold change threshold in RT but fall only slightly below this threshold in RR. The threshold-free analysis revealed that the majority of RT DEG from Figure 9, B (63.3 %; 62 out of 98 genes) were also affected in RR (Table 9). GO analysis with the remaining 36 genes did not yield any significantly overrepresented terms (data not shown).

Additionally, the DEG were manually assessed for their expression patterns across the samples. This led to the identification of several genes that displayed either a specific response in RT or responded in a more pronounced way in RT than in RR. This was the case for the genes *ELIP* and *ELIP2*, *HRG* (*HYDROGEN PEROXIDE RESPONSIVE GENE*) 1 and 2, the transcription factor *MYB12*, and several *XTH* genes such as *XTH12*, *XTH13* and *XTH20*. The expression of *XTH20* was only significantly changed in RT after 24 h, even though it was much higher expressed in RR (Figure 14).

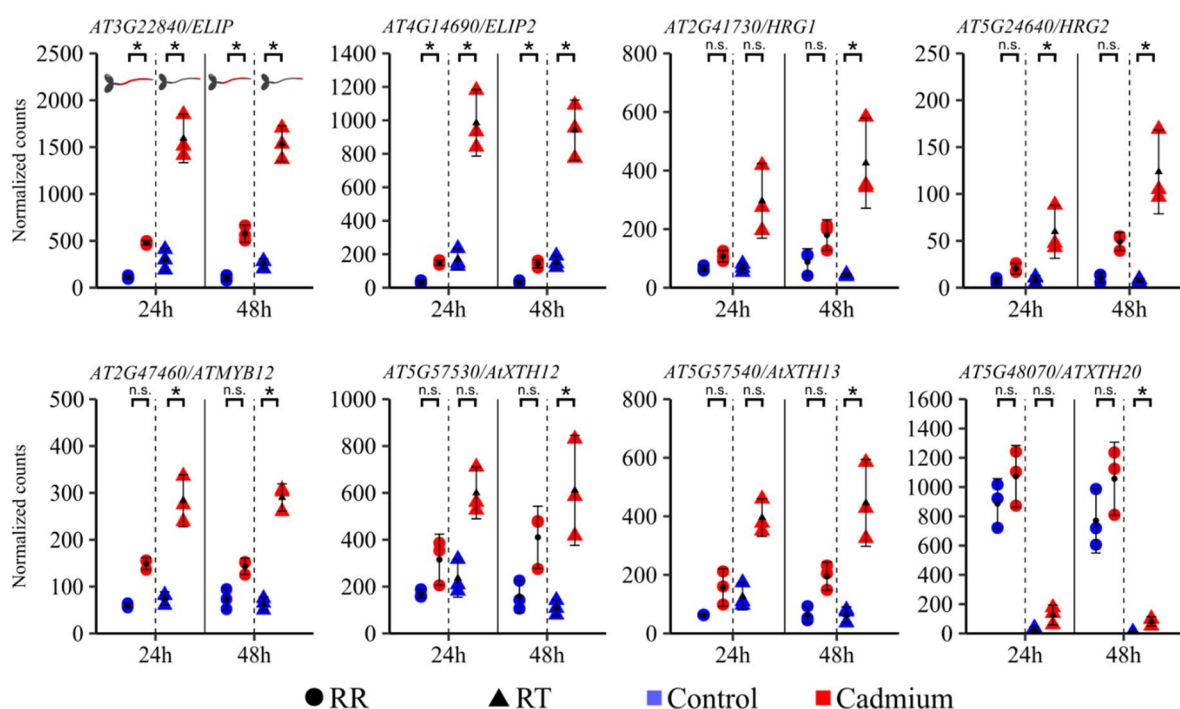


Figure 14: Expression of genes with a specific response to Cd in RT. The graph presents mean values with standard deviation. Differential expression was determined with DESeq2 ($\text{padj} \leq 0.05$; \log_2 fold change greater than 1 or smaller than -1, data from three independent experiments).

To assess the physiological function of these genes, related *A. thaliana* mutants were examined for their root growth phenotype under Cd exposure. The mutants *xth20*, *myb12* and *hrg2* were significantly more inhibited by Cd than the wild-type. By contrast, *elip1/2* and *hrg1* mutants showed no difference in growth under Cd compared to the wild-type (Figure 15). The phenotype of the *xth12* mutant could not be studied since no homozygous lines were successfully obtained

from the descendants of the segregating line SALK_008718. Additionally, no suitable line was available for investigating an *xth13* mutant.

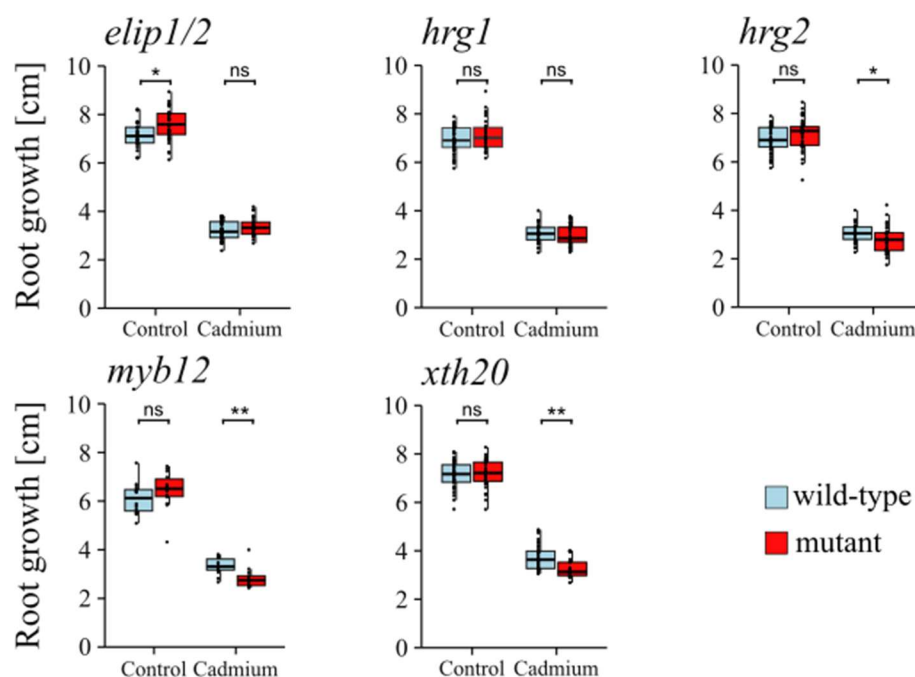


Figure 15: Primary root growth of mutants for RT-specific Cd-DEG. Plants were grown for 7 days on control plates and then transferred to control/Cd plates. Displayed are the root growth measurements 7 days after transfer. Asterisks indicate statistical significance ($p \leq 0.05$, Mann-Whitney U-test, data from three independent replications, $n = 15-30$).

A review of the literature indicated that many genes that display RT-specific induction upon treatment with Cd are regulated by the photomorphogenetic TF HY5. This was shown for *MYB12*¹⁹⁷, *ELIP1* and *ELIP2*¹⁸⁹ as well as *XTH12*, *XTH13* and *XTH20*¹⁹⁸. In addition to this, the *HYDROGEN PEROXIDE RESPONSIVE GENES HRG1* and *HRG2* were shown to be involved in ROS homeostasis in the root apical meristem, a process, for which a central regulatory role for HY5 was recently proposed^{121,199}.

To further address the action of HY5 in RT upon Cd exposure, the collective regulation of 297 high-confidence HY5 target genes¹⁸⁹ was compared to null-distributions representing the mean log₂ fold changes derived from random sampling of 10 000 *A. thaliana* gene lists (see Methods 5.1.9). This showed, that in both RR and RT, at both timepoints, the mean log₂ fold change of these target genes was significantly higher than mean of the background distributions. Noteworthy, the mean log₂ fold change of the target genes was higher in RT than in RR after 24 h (0.79 in RT vs. 0.69 in RR) and 48 h (0.89 in RT vs. 0.54 in RR) of Cd exposure (Figure 16, Figure 1).

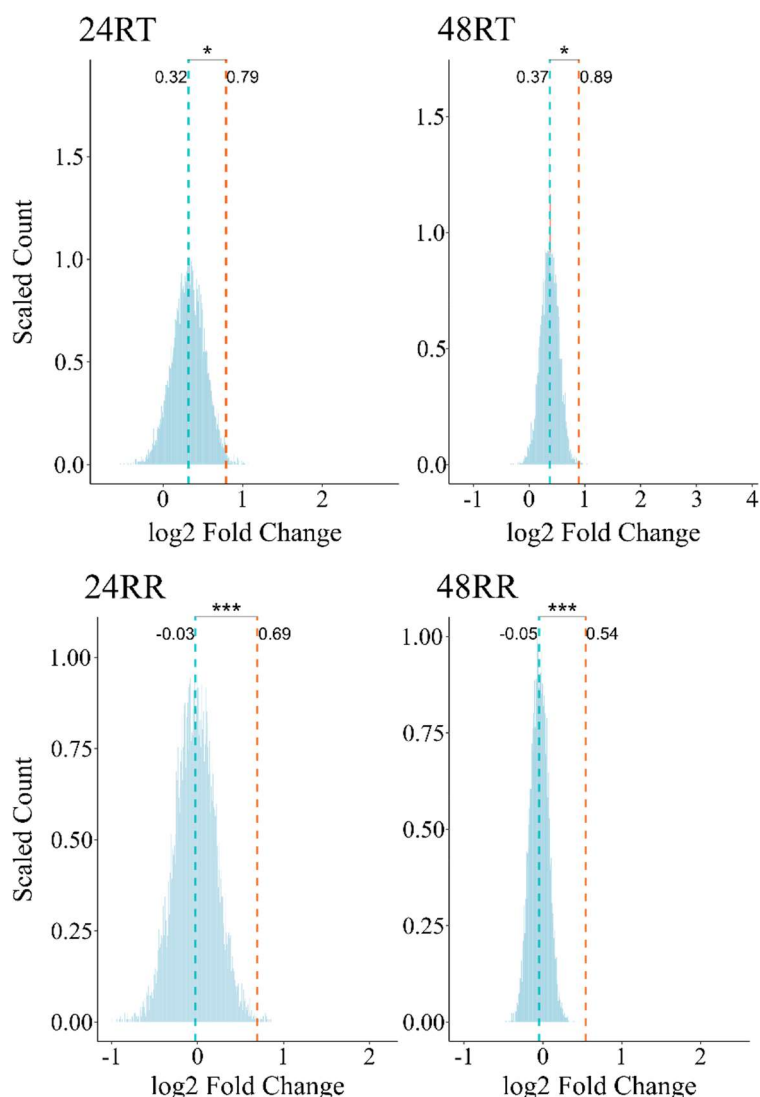


Figure 16: Average regulation of 297 HY5 target genes upon Cd exposure in comparison to random distributions. Background distributions resulted from the generation of 10 000 lists of 297 randomly chosen AGI codes and the calculation of the mean log2 fold change of each list between the control and Cd conditions. Dashed blue lines indicate the mean value of the null distribution. Dashed orange line indicates the mean log2 fold change of the HY5 target genes.

6.1.6 *hy5* mutants display increased sensitivity to Cd

Because the analysis of RNA-Seq data for genes that displayed a specific response to Cd in RT identified multiple genes that are regulated by HY5, the Cd phenotype of *hy5* mutants was investigated. Two independent mutant lines, *hy5_1* and *hy5_215*, both lacking functional HY5 were used. The *hy5_1* mutant has a T-DNA insertion in the coding sequence, whereas the *hy5_215* mutant displays a G-A substitution in the splicing acceptor site of the first intron, which leads to abnormal RNA processing¹⁸³.

Both of these mutants displayed reduced primary root growth in control conditions when compared to the wild-type (Figure 17, A and C, left). Normalization of the data to the mean of

the controls showed that both mutants displayed stronger growth inhibition by Cd than the wild-type (Figure 17, A and C, right).

Given that the abundance of the HY5 protein is strongly influenced by light²⁰⁰, the growth phenotype of *hy5* mutants under Cd exposure was examined in various light conditions, i.e. a root covered system and complete darkness. In either of these illumination conditions, the mutants exhibited a more pronounced reduction in growth due to Cd compared to the wild-type (Figure 17, B, D, E). Moreover, under these conditions, root growth of the mutants under control conditions was more comparable to the wild type than under complete illumination (Figure 17, B, D, E).

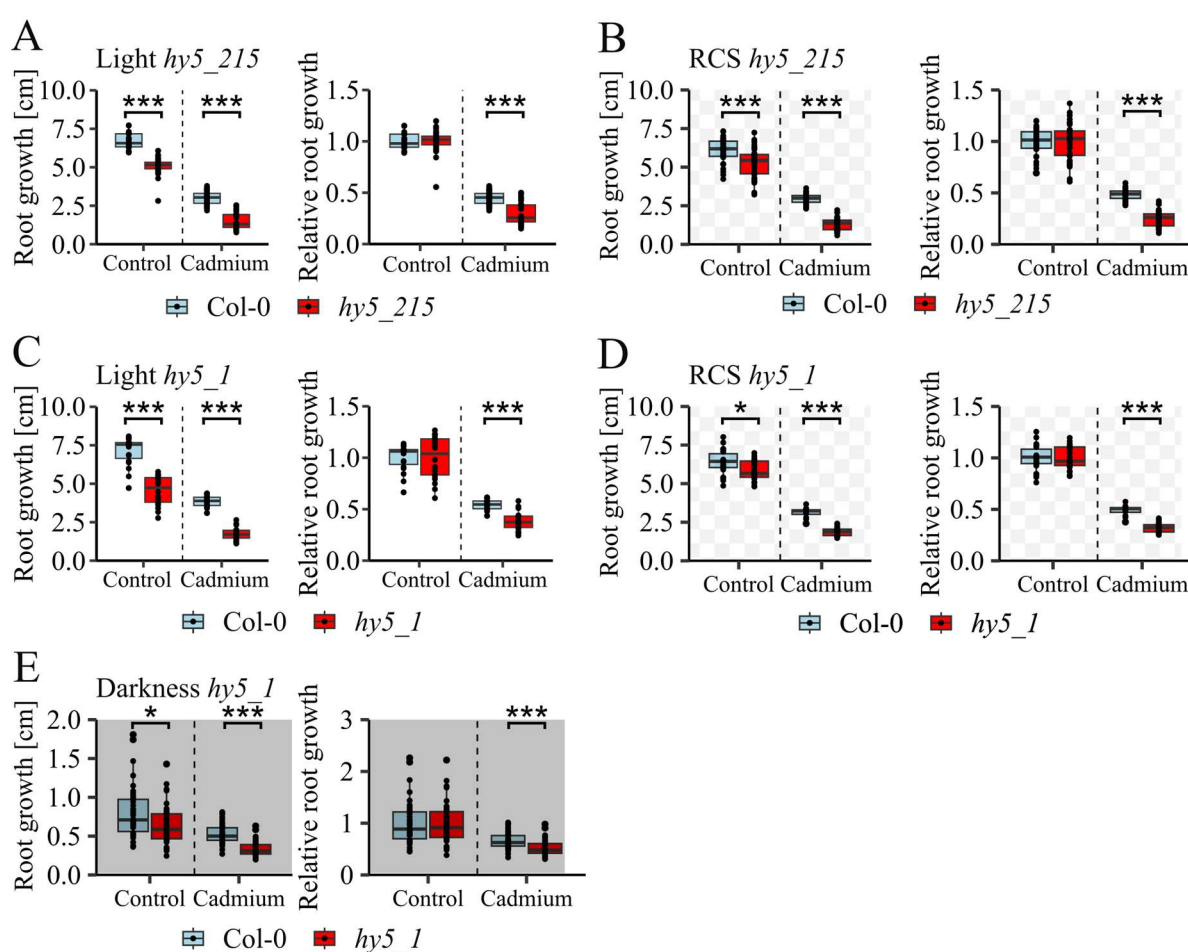


Figure 17: Increased growth susceptibility of *hy5* mutants towards Cd. A: Absolute (left) and relative (right) primary root growth of the *hy5_215* mutant with illuminated roots. B: Root growth of the *hy5_215* mutant in a root covered system (RCS). C: Root growth of the *hy5_1* mutant with illuminated roots. D: Root growth of the *hy5_1* mutant in a RCS. D: Root growth of the *hy5_1* mutant in darkness. All seedlings were germinated for 7 days in the respective light condition (Illuminated, RCS or darkness) on control medium and transferred to either control medium or medium with 25 μ M Cd and grown for additional 7 days. Data on the left side of each subsection are absolute growth values, data on the right side are growth values relative to the mean of the respective control. Asterisks indicate statistical significance (p ≤ 0.05, Mann-Whitney U-test, data from three independent replications, n = 17-50).

Given the pleiotropic effects connected to the loss-of-function of central transcriptional regulators such as HY5²⁰¹ that may also have general effects on growth performance under stress conditions, root growth of the *hy5_1* mutant under salt, osmotic (mannitol) and cold stress was compared to wild-type seedlings. Relative to the controls, *hy5_1* showed increased growth inhibition to mannitol and NaCl than Col-0 (Figure 18, A and B). By contrast, the mutant was less affected by cold stress than Col-0 (Figure 18, C).

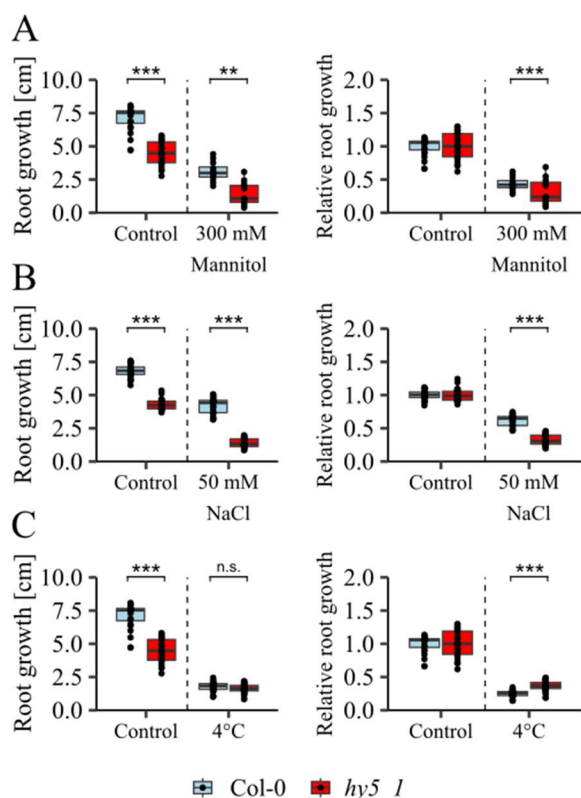


Figure 18: Primary root growth of Col-0 and *hy5_1* under various stress conditions. A: Growth under osmotic (mannitol) stress. B: Growth under NaCl stress. C: Growth under cold stress. Seedlings in A and B were germinated for 7 days under control conditions and transferred to either control medium or medium with Mannitol or NaCl and grown for additional 7 days. Control seedlings in C were grown under control conditions at room temperature for 14 days. Cold-treated seedlings in C were grown under control conditions for 35 days. Data on the left side are absolute growth values, data on the right side are growth values relative to the mean of the respective control. Asterisks indicate statistical significance ($p \leq 0.05$, Mann-Whitney U-test, data from three independent replications, $n = 20-30$).

6.1.7 HY5 loss-of-function leads to increased Cd accumulation

To analyse the underlying cause of the increased Cd sensitivity in the *hy5* mutants, metal contents in the roots and shoots of Col-0, *hy5_215* and *hy5_1* following Cd exposure were measured with ICP-OES. This showed that Cd contents in roots of the mutants were consistently higher after Cd exposure compared to the wild type. Cd levels in the shoots of both mutants were also higher than in Col-0 but this was not significant (Figure 19, A and B).

To further explore the association of HY5 loss-of-function with metal accumulation behaviour, phytochelatin (PC) and glutathione (GSH) levels were measured with HPLC. Phytochelatin have a general structure of $(\gamma\text{-Glu-Cys})_n\text{-Gly}$, where $n = 2\text{-}12$ ²⁰² and PCs with an n of 2, 3 and 4 were quantified. This showed that following treatment with Cd, the levels of PC2, PC3 and PC4 were significantly higher in roots of *hy5_215* than in Col-0 (Figure 19, A). In *hy5_1*, all three measured PCs were more abundant in the roots of the mutant, but only PC2 was significant (Figure 19, B). No significant difference in PC contents between the mutants and the wild type was determined in shoots. GSH contents in both Col-0 and *hy5_215* were reduced following Cd exposure, although this occurred to a greater extent in the wild-type. When comparing GSH contents in Col-0 and *hy5_1*, no significant difference was found (Figure 19, B).

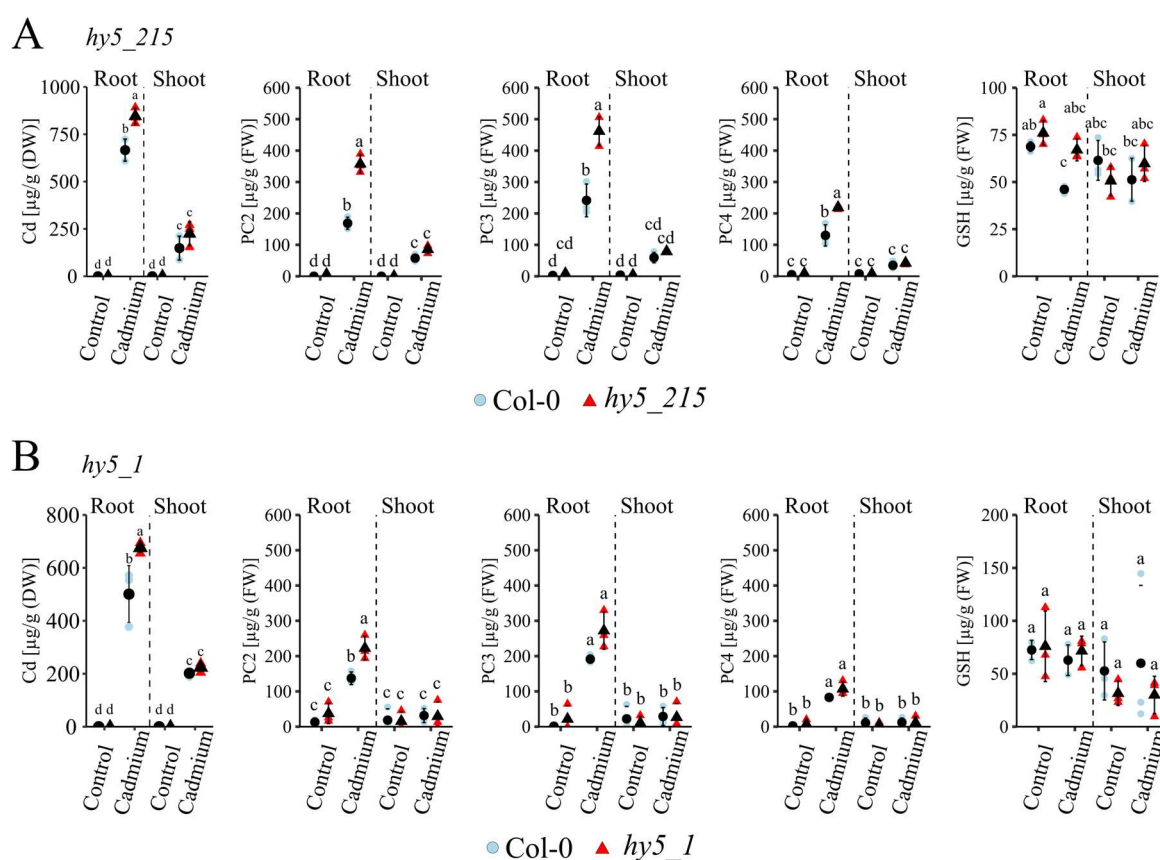


Figure 19: Cadmium (Cd), phytochelatin (PC) and glutathione (GSH) contents in Col-0 and two *hy5* mutants. A: Cd, PC and GSH levels of Col-0 and the *hy5_215* mutant. B: Cd, PC and GSH levels of Col-0 and the *hy5_1* mutant. For Cd, plants were germinated for 7 days on control plates, transferred to Cd or control medium and grown for additional 3 days. For PCs and GSH, plants were germinated for 9 days on control plates, transferred to Cd or control medium and grown for additional 3 days. Displayed are mean values \pm standard deviations of contents in μg per gram dry weight (DW) for Cd quantification and μg per gram fresh weight (FW) for thiol quantifications. Letters indicate statistical significance (ANOVA with Tukey HSD, $p \leq 0.05$, data from three independent replicates).

Because of the intricate relationship between Cd and Fe, Fe contents of *hy5* and Col-0 after Cd exposure were also analysed. Due to low Fe concentrations and limited sample quantity, only

in the comparison of Col-0 and *hy5_1*, the measured Fe concentrations were within the range of the calibration curve and therefore above the detection limit. This revealed differing root Fe homeostasis between the two genotypes after Cd exposure, since Fe contents in Col-0 roots decreased whereas in *hy5_1*, they remained stable (Figure 20).

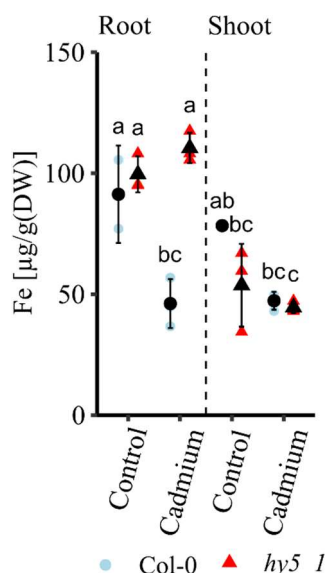


Figure 20: Iron (Fe), contents in Col-0 and the *hy5_1* mutant. Plants were germinated for 7 days on control plates, transferred to Cd or control medium and grown for additional 3 days. Displayed are mean values \pm standard deviations of contents in μg per gram dry weight (DW). Letters indicate statistical significance (ANOVA with Tukey HSD, $p \leq 0.05$, data from three independent replicates).

To further explore the role of HY5 in Fe homeostasis with and without the presence of Cd, we analysed primary root growth of Col-0 and *hy5_215* under various Fe concentrations in presence or absence of Cd. To remove any residual Fe^{2+} from the medium, 75 μM of the chelating agent FerroZine was added²⁰³. Under Fe deficiency (0 μM Fe + 75 μM FerroZine), root growth inhibition was significantly more pronounced in the *hy5_215* mutant compared to Col-0, indicating an increased sensitivity of *hy5_215* to Fe deficiency. There was no difference in growth between Col-0 and the mutant under combined stress from Fe deficiency and Cd. In addition, a surplus of Fe at 100 μM led to the disappearance of the increased Cd sensitivity of *hy5_215* (Figure 21).

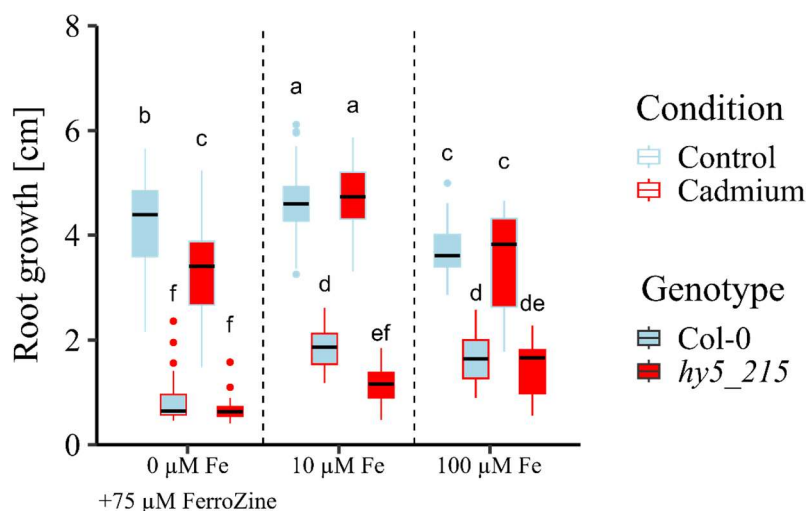


Figure 21: Primary root growth of Col-0 and *hy5_215* under different Fe concentrations in absence or presence of 25 µM Cd. Seedlings were grown for 10 days. Letters indicate statistical significance (ANOVA with Tukey HSD, $p \leq 0.05$, $n = 35-77$, data from three independent replications).

HY5 was reported to play a role in lateral root development²⁰⁴. To address the question, whether elevated Cd accumulation could result from an increased expansion of the root system, lateral and primary roots of Col-0 and the two *hy5* mutants were quantified. For this analysis, the whole root system was measured, as opposed to only the root after transfer like in previous experiments. This showed that the mutants had a significantly higher ratio of lateral to primary roots (LR/PR) (Figure 22, C). However, the sum of primary and lateral roots (LR+PR) was slightly higher in Col-0 compared to the mutants (Figure 22, D).

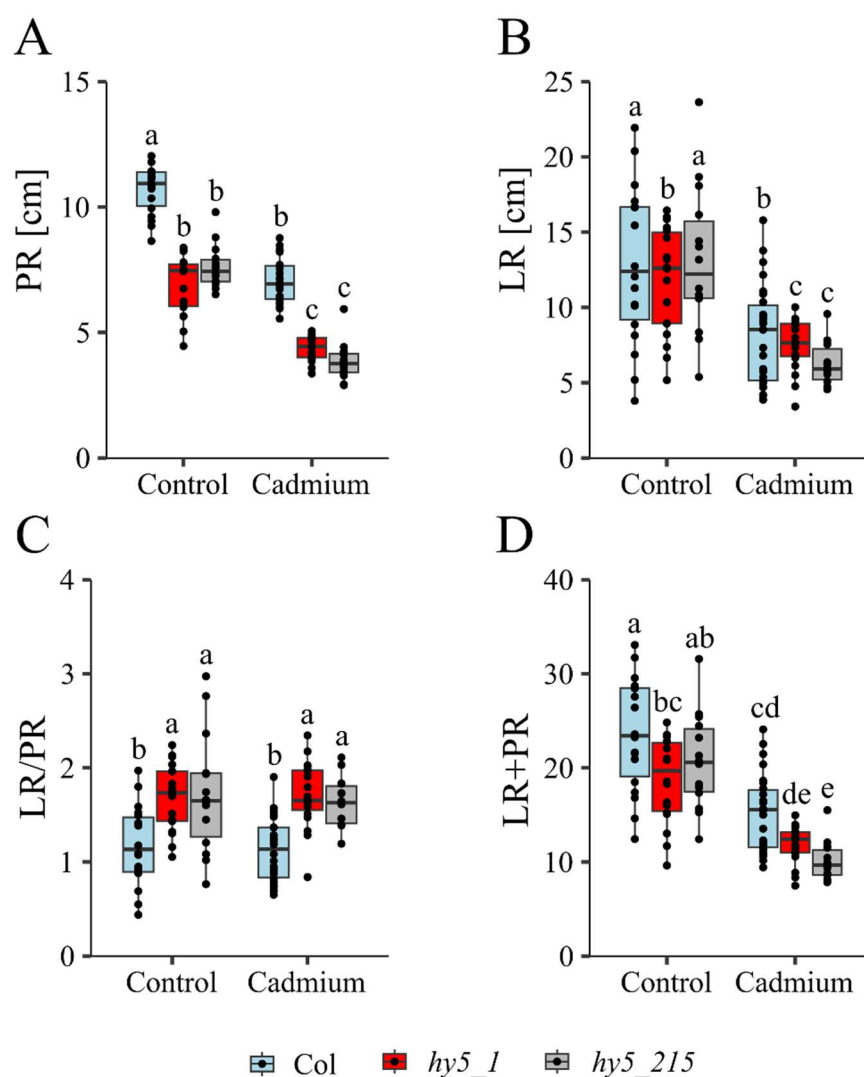


Figure 22: Primary and lateral root growth of Col and two *hy5* mutants under control conditions and cadmium (25 μ M) exposure. A: Primary root (PR) growth of Col, *hy5_1* and *hy5_215*. B: Lateral root (LR) growth. The sum of all lateral roots of one seedling is shown. C: Lateral root length divided by primary root length. The ratio of the primary root to all lateral roots of one seedling is shown. D: Lateral root length added to primary root length. The sum of all lateral roots and the primary root of one seedling is shown. Letters indicate statistical significance (ANOVA with Tukey HSD, $p \leq 0.05$, $n = 16-27$, data from three independent replicates).

6.1.8 Comparison of gene expression and elemental contents in RR and RT

PCA highlighted the root part as the main driver for variance in the transcriptomic dataset (Figure 9, A). To identify the trends underlying the strong difference between RR and RT, pooled control samples were used to perform DEA (24 h RR control + 48 h control versus 24 h RT control + 48 h control). This resulted in the identification of 1326 DEG that were more expressed in RT and 4544 DEG that were less expressed in RT (Figure 38, A).

To infer the functional categories of the DEG, GO overrepresentation analysis was done. The genes higher expressed in RT were related to cellular processes such as protein processing and

modification, RNA binding and ribosome assembly. Also, genes coding for cell wall modifying proteins such as xyloglucan/xyloglucosyl transferase activity were overrepresented (Figure 23, A). By contrast, the genes less expressed in RT were associated with ethylene synthesis and NAD/P(+) nucleosidase activity. In addition, GO terms related to sulfate or metal transmembrane transport activity were identified (Figure 23, B). This includes many members of the ZIP family of metal transporters, such as *IRT1* and the P1B-type ATPase HEAVY METAL ATPases *HMA4* and *HMA2* (Figure 23, C), several members of the sulfate transporter family SULTR, the molybdate transporters MOT1 and MOT2, the NRAMP transporters NRAMP4 and NRAMP5 and many high-affinity nitrate transporters such as *NRT2.1*. Related to the GO term ferric chelate reductase activity, the genes *FRO2*, *FRO3*, *FRO4*, *FRO5* and *FRO8* were less expressed in RT. Taken together, these results indicate that many genes related to nutrient homeostasis are expressed to a lower extent in RT compared to RR.

Similar to the transcriptomic data, elemental concentrations between RT and RR were compared in control conditions. This showed that Cu and P concentrations were significantly higher in RT. Zn and Mn were characterized by lower concentrations in RT compared to RR (Figure 23, D).

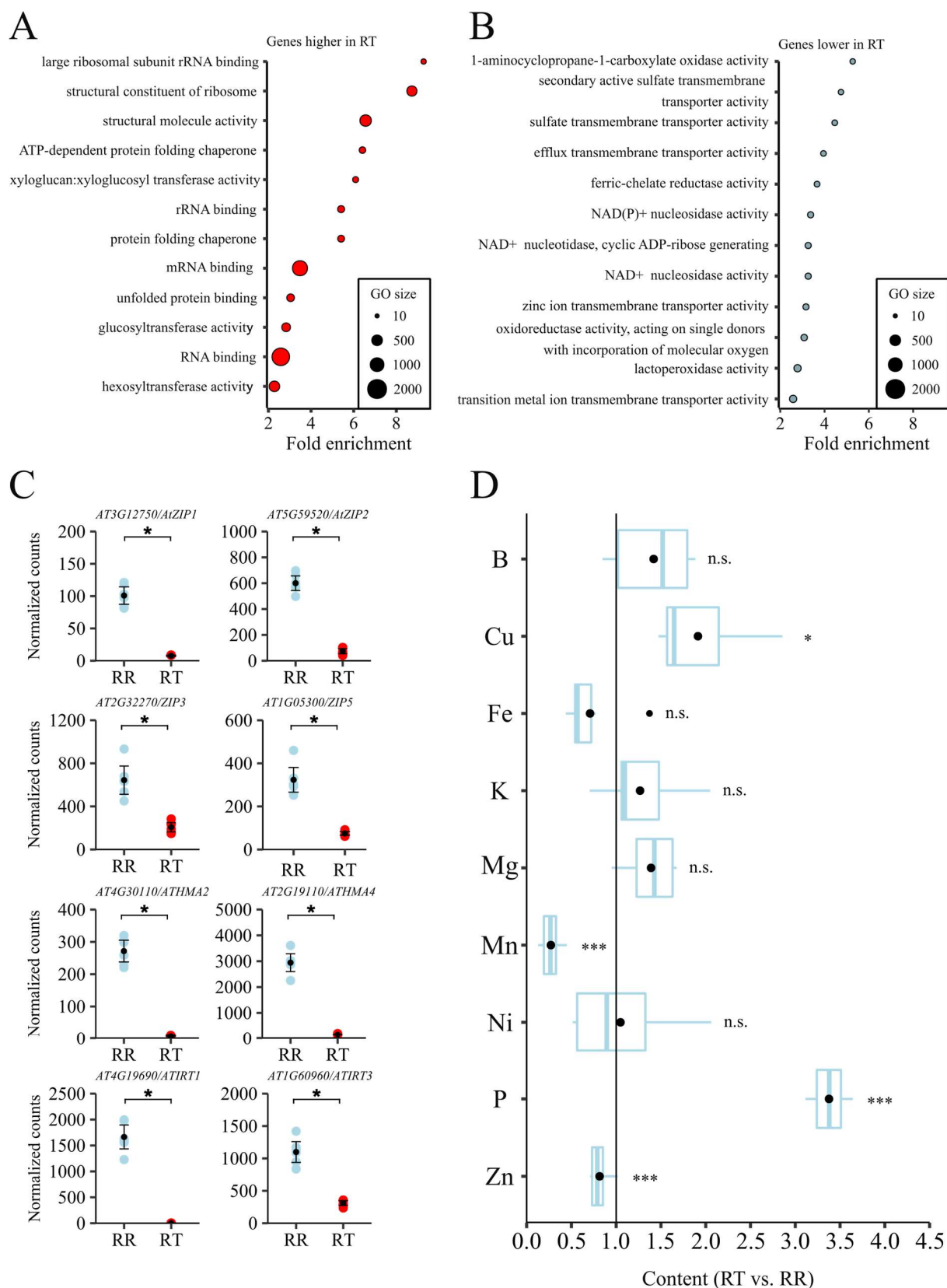


Figure 23: Comparison of gene expression and elemental contents in RR and RT. The analysis was done by combining the controls of RR (Control RR 24 h + Control RR 48 h) and the controls of RT (Control RT 24 h + Control RT 48 h). A: GO analysis of genes more expressed in RR than in RT. B: GO overrepresentation analysis of genes less expressed in RT compared to RR. Analysis was done with panther. C: Count-plots of selected metal homeostasis DEG that were less expressed in RT than

in RR. D: Elemental contents in RT versus RR. Values were obtained by dividing the contents of RT ($\mu\text{g}\cdot\text{g DW}^{-1}$) by the mean of the respective RR contents. Asterisks indicate statistical significance (Mann-Whitney U-test, $p \leq 0.05$, $n = 6$).

6.1.9 Comparison of Zn- and Cd excess on gene regulation in RT and RR

To assess the similarities and differences of the transcriptional response to Zn- and Cd-excess, the Cd-responsive DEG from both root sections were compared to the DEG from Thiébaut et al., which were obtained by similar treatment durations with a Zn concentration of 200 μM that led to a 50 % growth inhibition after 7 days¹⁸⁰ (Figure 24,

Table 10, Table 11, for simplicity, the DEG from 24 h after the respective treatment were combined with the ones from 48 h). In RR, 28 of the 105 Cd DEG were shared with the DEG from Zn-excess. These genes are largely related to Fe-homeostasis and include for example *VTL1*, *VTL2*, *VTL5*, *FRO3*, *FRO4*, *FEP2*, *FEP3*, *bHLH038*, *bHLH039*, *CYP82C4* and *S8H*. Interestingly, the two coumarin-biosynthesis related genes *CYP82C4* and *S8H* were upregulated under Zn-excess, whereas they were downregulated under Cd-excess conditions (Table 5, Table 6,¹⁸⁰). 60 genes were only differentially expressed after exposure to Zn, including for example the broad substrate range transporter *IRT1* and other Fe-homeostasis related genes like *FRO2* and *PYE*. In RT, 58 of the 126 Cd-DEG were also differentially expressed upon Zn excess, including the cell wall related genes *XTH12*, *XTH13* and *XTH20*. 364 DEG were only differentially expressed upon Zn-excess. Interestingly, the *ELIP* genes as well as *MYB12* can be found among the 68 Cd-exclusive DEG in RT.

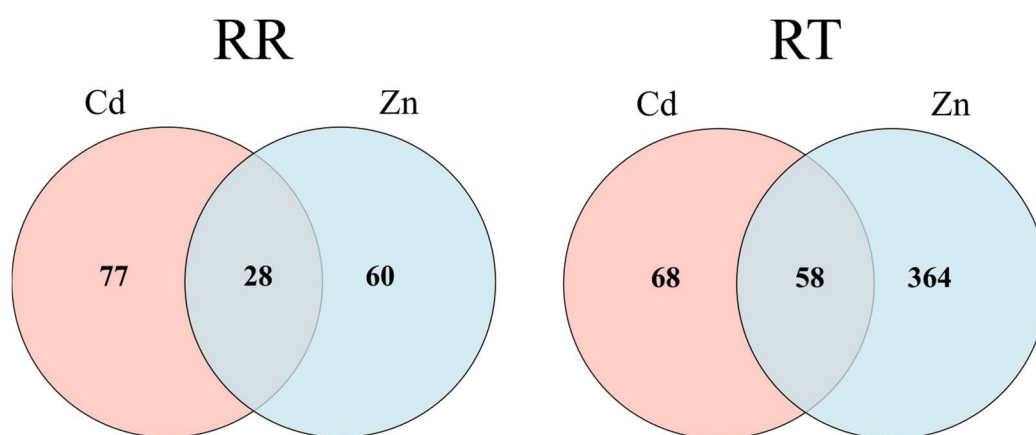


Figure 24: Comparison of DEG from RNA-Sequencing of *A. thaliana* root tips (RT) & rest of root (RR) after Cd-exposure and Zn exposure. DEG from the 24 h and 48 h timepoints were combined. Up- & downregulated genes are shown together. Differential expression was determined with DESeq2 ($\text{padj} \leq 0.05$; \log_2 fold change greater than 1 or smaller than -1, data from three independent experiments).

6.2 The effects of metallic UFP on *A. thaliana*

6.2.1 Development and characterization of controlled exposure experiments

To establish exposure conditions for experiments with plants, a self-made exposure chamber was integrated into the exhaust suction system of a brake test bench (Figure 39). The emission characteristics of three different use cases were assessed, which differed in the amount of kinetic energy (E_{kin}) stored in the rotary motion of the fly wheel. They represent a highway braking ($v_{start} = 20 \text{ m}\cdot\text{s}^{-1}$, $E_{kin} = 160 \text{ kJ}$), a braking typical for a cross country road ($v_{start} = 10 \text{ m}\cdot\text{s}^{-1}$, $E_{kin} = 40 \text{ kJ}$) and a city braking ($v_{start} = 5 \text{ m}\cdot\text{s}^{-1}$, $E_{kin} = 10 \text{ kJ}$). Brake pressure was kept constant at 2 MPa. The emission characteristics were determined by particle collection with ELPI+ and spICP-MS measurement of the ultra-fine fractions ($< 100 \text{ nm}$). This method facilitates the quantification of particles for each element, however due to the short-lived nature of particle signals, it is not possible to determine the composition of individual particles with spICP-MS^{193,194}. Therefore, the measured signals are referred to as **ultra-fine particle constituents (UFPC)**.

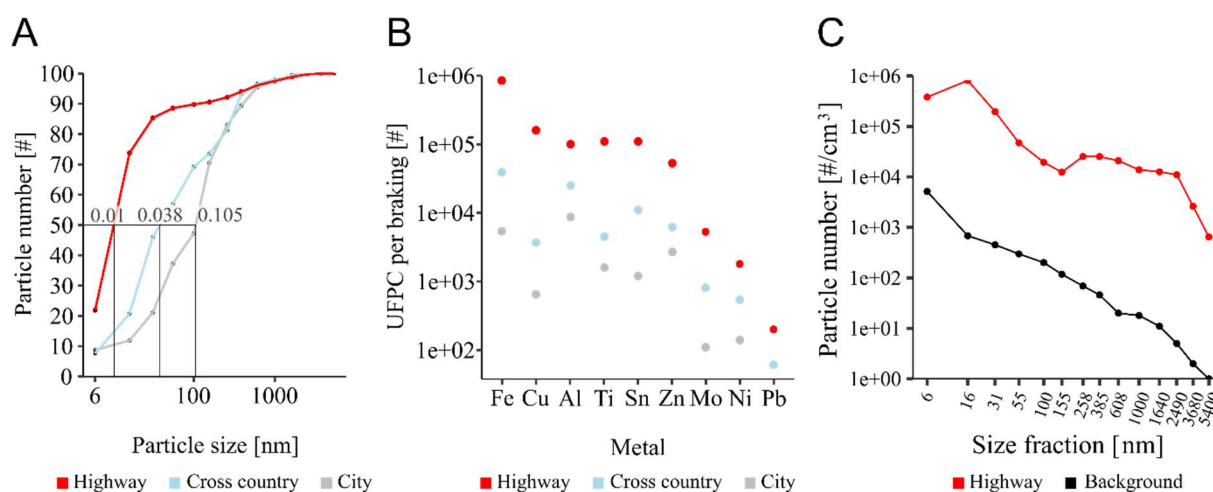


Figure 25: Characterization of particle emissions at the brake test bench. A: Cumulative distribution showing particle number versus size for the three use cases. The lines and numbers refer to D_{50} values in μm . B: Elemental characteristics and quantity of the UFPC emitted during one braking at the different use cases. Particles from 20 brakings were collected with ELPI+ and the ultra-fine fractions were analysed with spICP-MS. C: Number concentration of particles during one highway braking compared to the background concentration (no braking, only the suction activated). ELPI+ measurements and data processing were done by Marina Maier.

Generally, the highest particle concentration in the chamber occurred during the highway braking event, followed by the cross country and city use cases. Increasing E_{kin} led to a higher proportion of UFP in the total emissions, which can be inferred from the D_{50} values (City $D_{50} = 0.105 \mu\text{m}$, Cross country $D_{50} = 0.038 \mu\text{m}$, Highway $D_{50} = 0.01 \mu\text{m}$) (Figure 25, A). In the ultra-fine fractions ($< 100 \text{ nm}$), the highest number of UFPC for all elements were found after

the highway braking, followed by the cross country and the city braking manoeuvres. For Fe, the largest number of UFPC was measured, followed by Cu, Al, Ti, Sn, Zn, Mo, Ni and Pb (Figure 25, B).

To substantiate the spICP-MS analysis, the composition of fragmented brake pads was further analysed using X-ray fluorescence spectrometry (EDX) (see Methods, 5.2.5). This analysis revealed the presence of additional (transition-) metals in the pads, including Ba, Ti, Cr, Ca and K (Table 4).

Table 4: Composition of LowMet brake pads determined with X-Ray fluorescence. Measurements were conducted by Marina Maier.

Element	Content [mg/g]	Element	Content [mg/g]
Fe	131.9	Sr	0.54
Cu	129.8	W	0.44
Si	55.63	Cl	0.35
Mg	55.07	V	0.18
Al	47.82	Te	0.12
Zn	36.8	Na	0.1
S	28.6	Ni	0.09
Sn	24.48	Ga	0.08
Ba	17.26	Sb	0.07
Ti	16.85	Mo	0.03
Cr	13.09	Bi	0.02
Ca	9.92	Pb	0.02
P	6.32	Rb	0.02
K	1.6	Zr	0.01
Mn	1.42	As	0.01

6.2.2 Controlled exposure and UFP deposition on leaf surfaces

Because the highway use case clearly resulted in the highest concentration of UFP inside the exposure chamber, all exposure experiments were conducted under these conditions. For these experiments, the highway use case was contrasted with (i) an outside control, for which plants were placed outside of the exposure chamber and (ii) a background exposure, in which the suction of the brake test bench was activated, but no braking was done. Remaining brake wear in the exhaust pipes resulted in considerable particle concentration inside the chamber during the background exposure. However, at all size fractions, these concentrations were orders of magnitude lower than during the highway braking (Figure 25, C). In all exposure experiments involving the highway use case, a total of 45 braking actions was conducted. To manage the temperature increase of the brake discs during these events, the brakings were performed in sets

of three, with each set consisting of 15 brake applications followed by a 15-minute cooling period. These time windows were used for the background exposure and ensured that the temperature within the chamber remained below 30°C (Figure 41).

Following exposure to UFP, metallic particles from plant leaves were extracted and UFPC were analysed with spICP-MS. Prior to the analysis, the extraction method was validated by adding various concentrations of commercially available Cu-nanoparticles to leaf material of unexposed adult *A. thaliana* plants. The measurement resulted in linear relationships between different samples and the expected size distribution (Figure 40).

Following the exposure to 45 highway-braking iterations, Fe and Cu were the most abundant metals, whereas Al, Sn, Ti and Zn were approximately an order of magnitude less abundant. Mo, Ni and Pb UFPC were detected in comparably low concentrations. With the exception of Al and Fe, no UFPC were detected in samples from the background exposure. Furthermore, the extent of variance in the UFPC concentrations from three independent replications demonstrated that the exposure conditions were executable with high reproducibility (Figure 26).

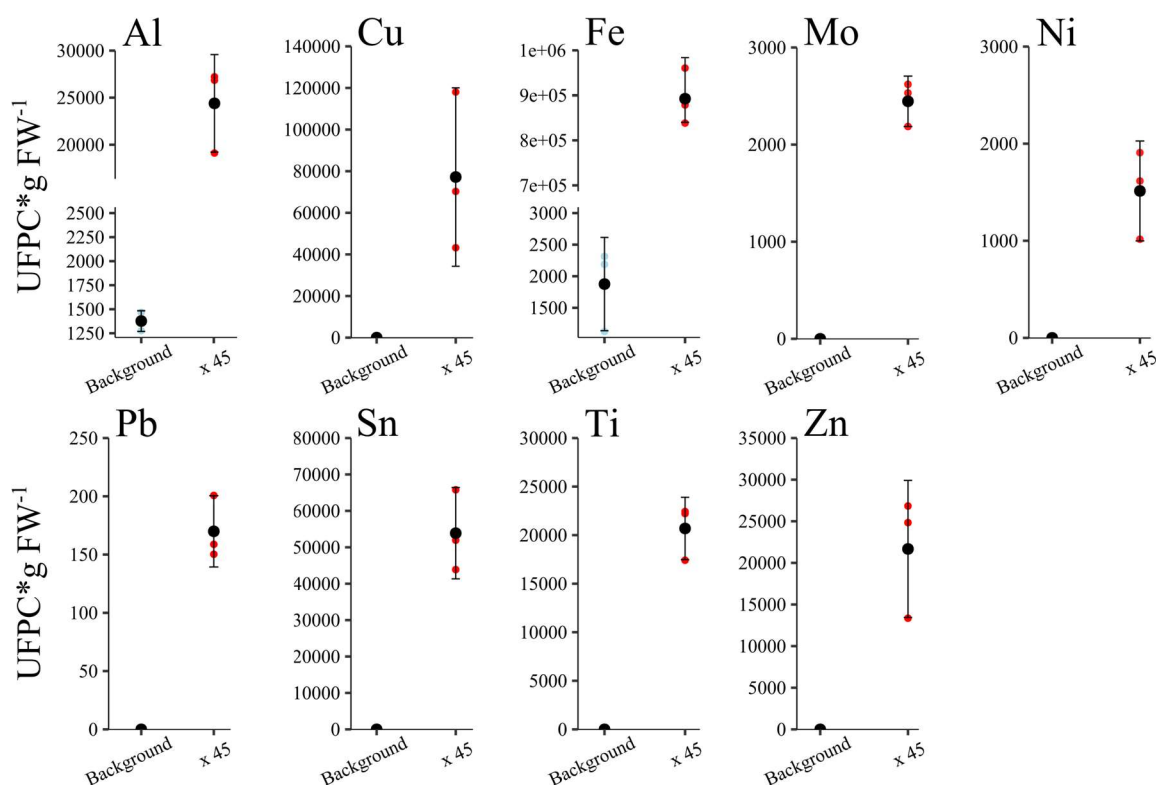


Figure 26: Measurement of UFPC on leaves of *A. thaliana* following exposure to 45 highway brakings. Rosette stage (4-5 week old) plants were placed in an exposure chamber integrated in the exhaust system of a brake test dynamometer and subjected to 45 highway-brakings or the background particle concentration. Particles were extracted from leaves and UFPC were quantified with spICP-MS. Data is shown as ultra-fine particle constituents per gram fresh weight (FW). Data is shown as single measured

values (blue/red dots), mean values (black dots) and +/- standard deviation. Data was collected from three independent exposure experiments. spICP-measurement and data preprocessing were done by Marina Maier.

Following exposure, the morphology, distribution and chemical properties of particles on leaf surfaces were further assessed with scanning electron microscopy (SEM) and EDX. This revealed a widespread abundance of particles across leaf surfaces of exposed plants. Smaller particles were detected mostly as constituents of larger agglomerates (Figure 27, A-C). Particles were constituted of metals such as Fe, Cu, Zn and Ba in these agglomerates, as determined with EDX (Figure 27, D).

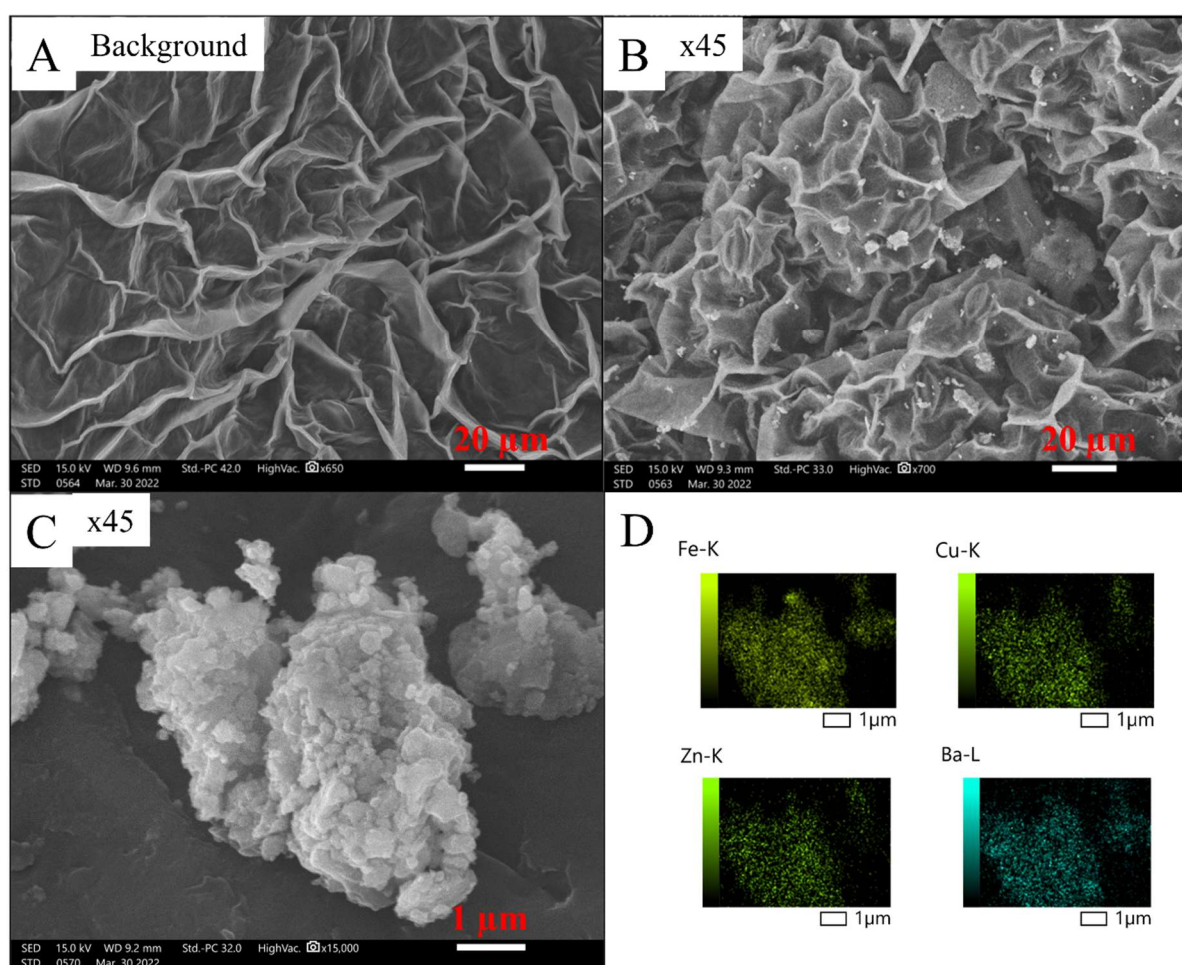


Figure 27: Scanning electron micrographs of *A. thaliana* leaves following exposure to 45 brakings. Rosette stage (4-5 week old) plants were placed in an exposure chamber integrated in the exhaust system of a brake test dynamometer and subjected to 45 highway-brakings. A: Overview of a leaf from a background-exposed plant. B: Overview of a leaf from a plant exposed to 45 highway brakings. C: Detail picture of a particle agglomerate found on a leaf of a plant exposed to brakings. D: EDX overlays that show the elements found in C. The scale bar is reported in each picture.

6.2.3 RNA sequencing of *A. thaliana* exposed to UFP from brake abrasion

As a proof of concept of the newly established exposure chamber and to gain insights into physiological consequences triggered by the exposure of plants to metallic UFP, RNA

sequencing was done with *A. thaliana* rosettes. Global gene expression was quantified 24 h after (a) plants were exposed to 45 highway brakings, (b) background exposure (i.e. no brakings but the activated airflow and residual particles in the system) and (c) control conditions were applied, meaning that plants were placed outside the exposure chamber.

PCA on the transcriptomic data showed that both exposures had similar effects on gene expression. The “background” and “45 brakings” transcriptomes are located in close proximity to each other, whereas they are clearly separated from the controls along PC1 (Figure 28, A). No significant DEG were extracted in a contrasting analysis of the “background” and “45 brakings” groups. However, the comparison of either of these groups with the control revealed 92 DEG for “background vs. control” and 150 DEG for “45 brakings vs. control” (Figure 28, B and C), indicating a larger effect on gene expression by the exposure with 45 brakings compared to the background exposure. Both groups showed a large overlap with 77 shared DEG. 15 DEG were specific to the comparison “background vs. control” and 73 DEG were specific to the comparison “45 brakings vs. control” (Figure 28, D).

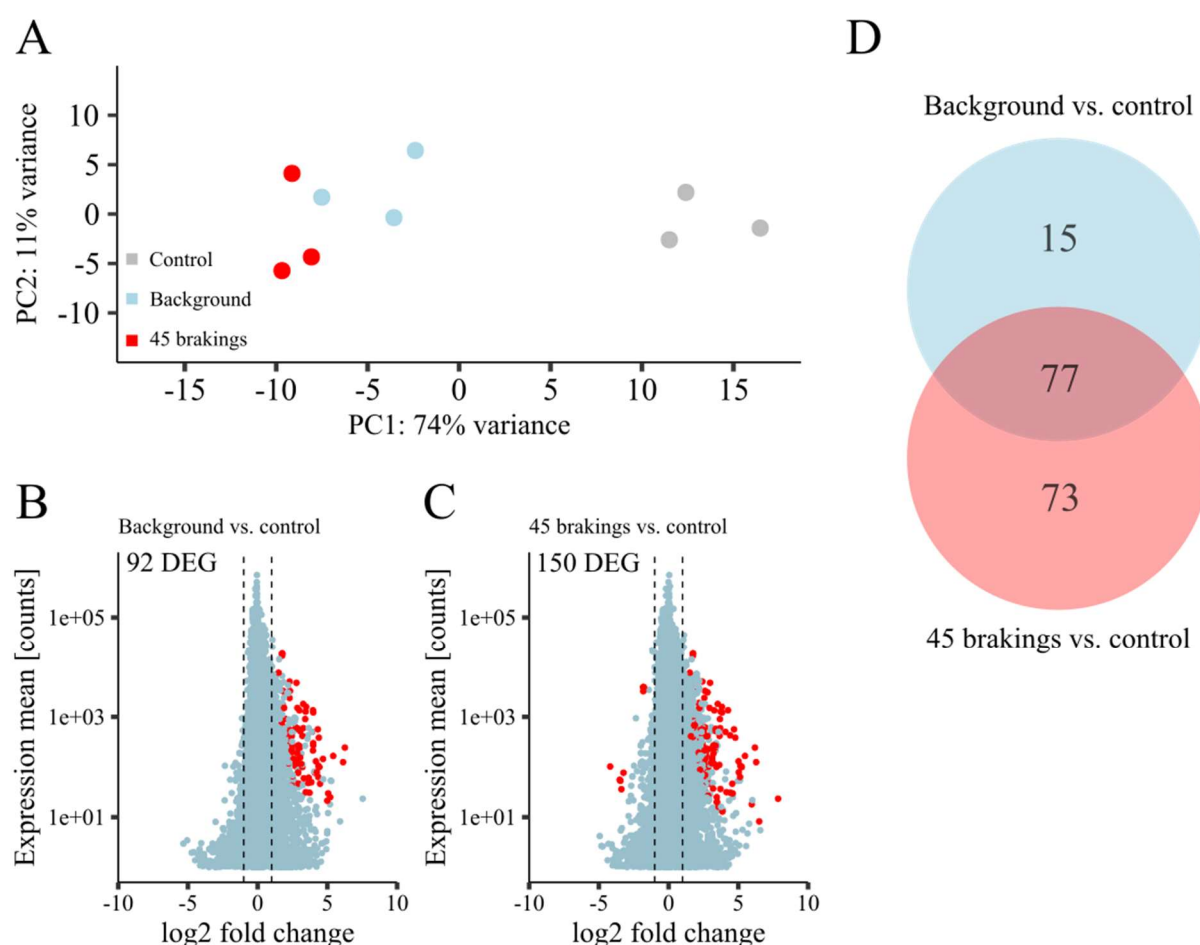


Figure 28: Transcriptomic analysis of *A. thaliana* after exposure to airborne particles from brake wear. A: Principal component analysis (PCA) showing the similarities of the different samples along the first two principal components. The percentage of

variance explained by each principal component is indicated. B and C: Volcano plots showing significant DEG (red) and not significantly differentially expressed genes (blue) when comparing the control transcriptomes to either the transcriptomes of background-exposed plants or (B) the transcriptomes of plants exposed to 45 highway brakings. Dashed vertical lines indicate the cutoff for the log₂ fold change. D: Venn diagrams displaying the quantity and overlap of DEG in the two comparisons. Genes were considered differentially expressed, when log 2fold change was greater than 1 or smaller than -1 and, padj ≤ 0.05.

Since PCA implied that both exposures (i.e. background and 45 brakings) resulted in similar changes in gene expression and DEA with the control group showed that the majority of DEG is shared between the two groups, the expression patterns of brake particle responsive DEG was investigated with greater depth. Plotting the fold change of the DEG versus the three sample groups demonstrated that the majority (134/150 DEG) exhibited either a progressive increment or decrement from the controls over the background exposure towards the exposure to 45 brakings (Figure 29, A). This implies that the expression of most of the genes that were responsive to the exposure to particles from 45 brakings was already affected by the background exposure.

The 150 particle-responsive DEG were functionally categorized with GO overrepresentation analysis. Of the 12 terms with the highest enrichment values, nine were associated with the response to biotic stress (Figure 29, B). These terms include three jasmonate-induced oxygenases (*JOX2*, *JOX3* and *JOX4*), which were upregulated under background exposure and to a stronger extent by the treatment with 45 brakings (Figure 29, C, Table 12). Other terms were associated with oxidative stress, response to wounding and response to fatty acid (Figure 29, B). Additionally, several metal homeostasis associated genes such as *BHLH38*, *BHLH39* and *COPT2* were significantly downregulated following the exposure to particles from 45 brakings (Figure 29, C).

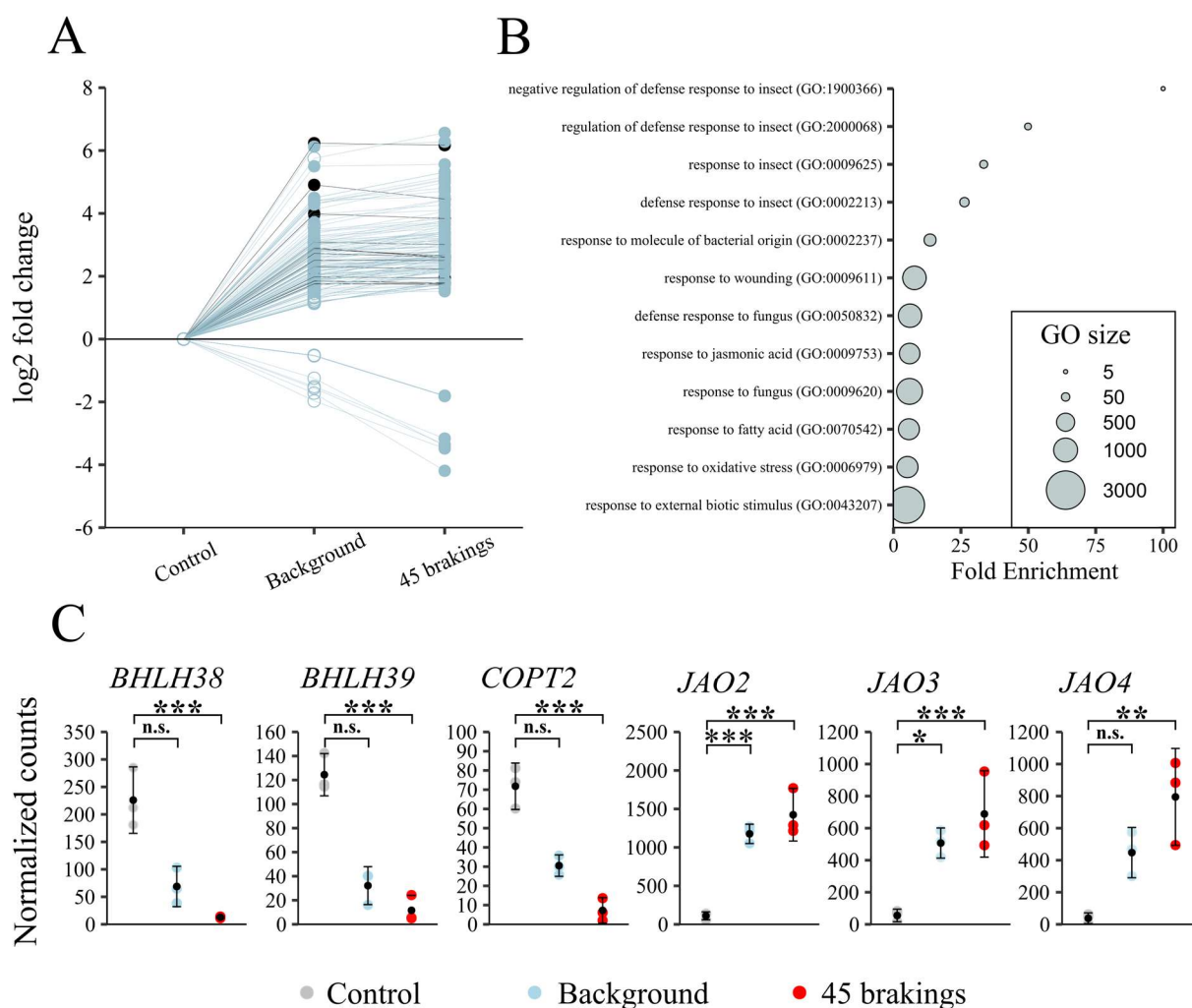


Figure 29: Characterization of brake-wear responsive genes. A: Cure array that shows the expression of the 150 brake wear responsive genes (Figure 28, C) over the three sample groups. Genes showing progressive increment/decrement are labelled in blue, genes with no progressive increment/decrement are labelled red. Significant DEG are indicated with filled circles, genes not significantly differentially expressed are indicated with non-filled circles (DESeq2, log 2fold change greater than 1 or smaller than -1 and, padj ≤ 0.05). B: GO overrepresentation analysis of the 150 genes that responded to the exposure (Figure 28, D, red). The 12 GO terms with the highest enrichment were selected. Analysis was done with panther. C: Count-plots of selected DEG. Asterisks indicate significant differences according to DESeq2 (DESeq2, log 2fold change greater than 1 or smaller than -1 and, padj ≤ 0.05).

6.2.4 Evaluation of aerial UFP concentration and leaf deposition in the field

With the aim of setting UFP deposition from controlled exposure into the context of real-life conditions, field experiments at three locations were performed. With a city center, a suburban and a rural site, these sites represent varying degrees of traffic volume. UFP quantification with ELPI+ showed that the city center location displayed the highest concentration ($\bar{x}_{08:00-18:00} = 26753 \text{ UFP} \cdot \text{cm}^{-3}$), followed by the suburban location ($\bar{x}_{08:00-18:00} = 6540 \text{ UFP} \cdot \text{cm}^{-3}$) and the rural site ($\bar{x}_{08:00-18:00} = 4137 \text{ UFP} \cdot \text{cm}^{-3}$) (Figure 30, A).

Following 14 days of exposure at these locations, metallic particles were extracted and UFPC were measured with spICP-MS using the same experimental approach described before (6.2.2, Figure 26). This resulted in a consistent pattern, with the highest number of UFPC for all elements found on leaves exposed at the city center, followed by the suburban and the rural locations. Fe UFPC were determined by far with the highest concentrations, followed by Sn, Zn, Al, Ti, Cu, Mo and Ni. Pb UFPC were only detected in low concentrations in samples from the inner-city location (Figure 30, B).

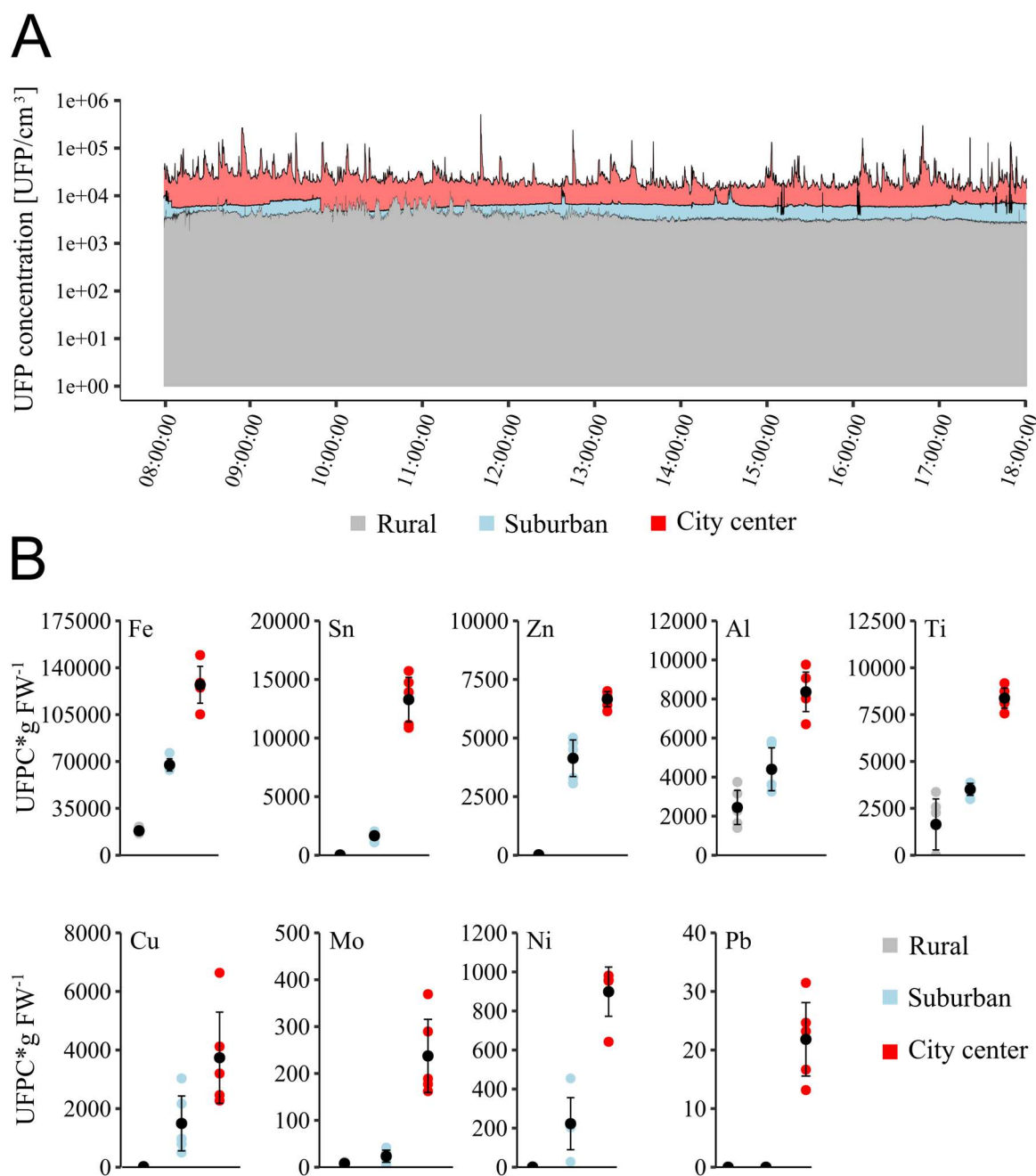


Figure 30: Outdoor exposure of *A. thaliana* at locations with varying traffic volume. A: Measurement of UFP (6-100 nm) with ELPI+ at a rural, a suburban and an inner-city location. ELPI+ measurements were done by Marina Maier. B: UFP deposition

on leaves of *A. thaliana* after field exposure. 4–5-week-old plants were placed at the sites for 14 days. Particles were extracted and UFPC were measured with spICP-MS. Data is shown as ultra-fine particle constituents (UFPC) per gram fresh weight (FW) and resulted from one exposure of five plants per site. spICP-MS measurements were done by Marina Maier.

To place the UFPC quantifications from controlled exposure into a real-world context, they were compared to the data from outdoor exposure. PCA was done to compare overall composite profiles of each field UFPC measurement to the one derived from dynamometer-exposure. This showed that the city center profiles were most closely located to the ones from controlled exposure along PC1 (Figure 31, A). Additionally, the extent of UFPC deposition on leaves of each outdoor location was compared to controlled exposure. Interestingly, UFPC for many metals displayed a difference of less than the factor 10 when UFPC concentrations from controlled exposure are compared to the mean of the city center location. An exception to this are Cu UFPC, for which greater factors were determined throughout (Figure 31, B).

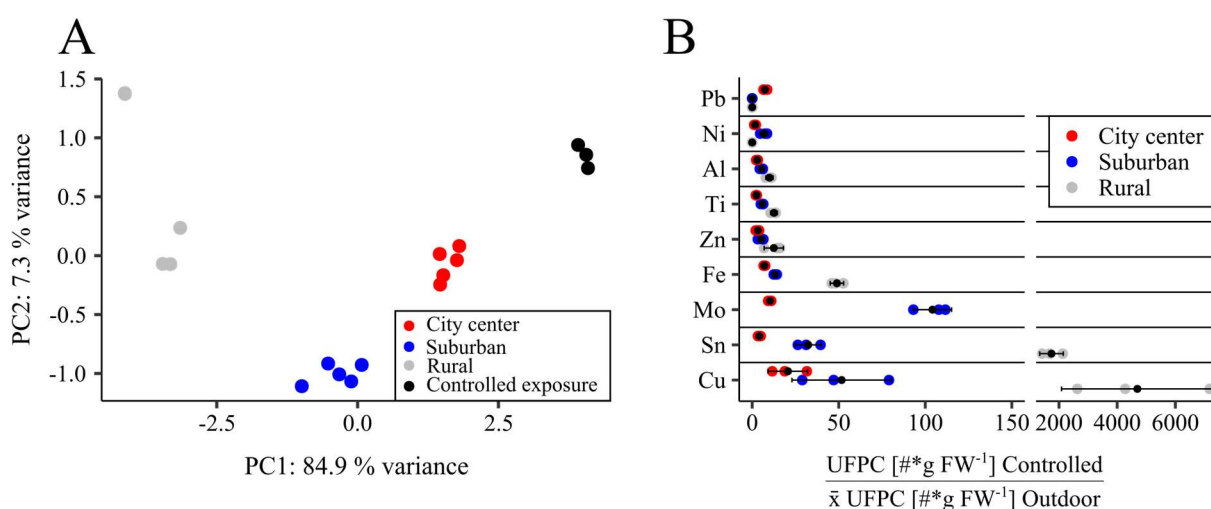


Figure 31: Comparison of UFPC quantifications from outdoor exposure with controlled exposure at the brake test bench. A: PCA with UFPC profiles from both exposures. The percentage of variance explained by each principal component is reported. B: UFPC contents from controlled exposure compared to the mean of the three outdoor exposure locations. Displayed are mean values \pm standard deviation.

7 Discussion

7.1 The effects of Cd on the root of *A. thaliana* with a special focus on the root tip

7.1.1 Differences in elemental contents between RT and RR

A key observation from the ICP-MS analysis was the lower Cd accumulation of RT compared to RR. Both after 24 h and 48 h, the Cd contents in RT were only 50 % of the contents found in RR (Figure 4, B). This finding was not specific to Cd, as under Zn excess, RT displayed lower Zn contents than RR¹⁸⁰. Differences in metal accumulation can be attributable to the morphological and cell biological characteristics as well as to biochemical properties of RT and RR.

For example, one key mechanisms for the mitigation of toxic effects from metals is their chelation and vacuolar sequestration²⁵. The existence of intracellular binding and sequestration sites for metals is regarded as a driving force for accumulation²⁰⁵. In the RAM, vacuoles are characterized by small diameter and their volume increases along with cellular elongation and maturation^{206,207}. Consequently, vacuolar storage capacities for PC-Cd complexes may differ in RT and RR and partially account for the lower Cd accumulation observed in RT.

Besides vacuoles, the plant cell wall is regarded as an important storage site for metals^{208–210} and its composition in cells along the longitudinal axis of the root must be dynamic to allow for cellular elongation and maturation^{119,211}. This requires major modifications of the wall components, which is reflected in the expression differences among cell wall genes, such as *XTH* genes, between RR and RT (Figure 23 , A). Hemicellulose and pectin are considered important polysaccharides in the context of metal adsorption^{212,213}, rendering alterations in their chemical properties and the cell wall composition overall important features for metal accumulation.

One of the defining features of RT in comparison with RR was the reduced expression of metal homeostasis genes (Figure 23). This included transmembrane transporters of the *ZIP* and *NRAMP* families as well as several *HMA* and *FRO* genes (Figure 23, B and C). The lower expression of transporter genes could contribute to the observed difference in Cd accumulation via a reduced influx. *IRT1* has been recognized as a key transporter for the entry of Cd into roots⁸¹ and its expression was strongly reduced in RT compared to RR, with RT displaying nearly no transcript (Figure 23, C). This is supported by previous results on the expression of

IRT1 in the apical and the basal regions of the root⁸¹. Moreover, additional transporters with a link to Cd uptake such as *ZIP6*⁸⁷ and *NRT2.1*⁶⁰ were found to have expression differences similar to *IRT1* (Figure 38).

7.1.2 The effect of Cd on the root metabolome

Untargeted metabolite analysis was conducted to assess the metabolomic changes triggered by Cd in RR and RT. This resulted in the detection of 2961 features, of which only 169 (5.7 %) could be annotated with putative metabolites. Low annotation rates of detected features are common, which continues to represent a significant bottleneck in non-targeted metabolomics studies^{214,215}. The plant metabolome consists of thousands of structurally different representatives, significantly complicating the association of measured signals with metabolite annotations^{216,217}. The analytical approach of this analysis concentrated either on an interpretation of global trends (Figure 6) or on entire substance classes (Figure 7) and avoided the examination of single features. Sideretin was treated as an exception, whose abundance matches the regulation of the respective biosynthesis gene *CYP82C4* and is discussed further below (see 7.1.3.1).

Because the determination of sample weight was not possible, biomass estimations for data normalization were done by counting the amount of collected root pieces for RR and RT samples (see Methods, 5.1.6; Figure 6, D), which disregards morphological differences in root diameter as well as in the presence of root hairs and lateral roots. A comparison of RT and RR with this method of data normalization suggested, that metabolite contents were strongly different in RR and RT, with RT displaying lower contents (Figure 6, A). This would be in line with a higher metabolic activity of differentiated and specialized cells in the mature regions of the root. Furthermore, substance-wise comparisons between RT and RR highlighted the consistently lower levels of flavonoids in RT, which is in alignment with previously published data²¹⁸ (Figure 34).

The statistical analysis of DAF was done based on a normalization on the total feature content in each respective sample (Figure 6, C). It identified a higher number of DAF in RR than in RT (731 DAF in RR vs. 492 DAF in RT), which is in agreement with lower Cd accumulation (Figure 4) and the observed differences in the transcriptomic response towards Cd (Figure 9). Moreover, it suggested an increased abundance of phytochelatins in Cd exposed plant samples (Figure 7). The synthesis of phytochelatins as a mechanism for Cd detoxification is a consistently documented response, to the extent that it can be considered a reliable indicator for validating the effectiveness of Cd treatment^{103,219–221}. Because the sulfhydryl groups of these

metabolites are essential structural elements for the chelation of metals, their increased abundance also requires modulations of sulfur assimilation at a transcriptomic level. Related genes were highlighted as a dominant part of the DEG resulting from the RNA-Seq analysis (Figure 10).

RR exhibited several flavonoid-related features with a lower concentration in response to Cd, whereas the opposite was observed for RT (Figure 7). The involvement of flavonoids in the response to Cd was highlighted in previous studies, for example, in a comparative study of two *A. halleri* populations from metal contaminated sites with different Cd-tolerance strategies (PL22, hyperaccumulating and I16, excluding), where flavonoid related transcripts and metabolites were more abundant in the hyperaccumulator accession ¹⁰⁵. Given the particular sensitivity of RT to ROS, flavonoids may assist in maintaining ROS homeostasis upon Cd stress by means of their antioxidative properties ²²². The indication of a role for flavonoids in RT during Cd stress is furthermore supported by the RT-specific upregulation of *MYB12* and the increased primary root growth sensitivity of *myb12* towards Cd (Figure 14, Figure 15). MYB12 was described as a regulator of the flavonoid biosynthetic pathway, specifically by regulating flavonol biosynthesis in the root ²²³. Together with the fact that MYB12 is transcriptionally regulated by HY5 ¹⁹⁷, this provides a framework to hypothesize an involvement of HY5 in maintaining ROS homeostasis in the RT via MYB12 and flavonols.

7.1.3 The effect of Cd on the root transcriptome

7.1.3.1 Cd exposure activates known Fe deficiency responses while repressing others

At the transcriptomic level, a prominent effect of Cd exposure was the induction of changes resembling those seen in Fe deficiency (Figure 10, Figure 11). This refers to the downregulation of *FER* and *VTL* genes and the upregulation of *bHLH38/39*, *IMA* and *FRO* genes, which were shown to follow Fe deprivation previously ^{71,72,78,224,225} and Cd exposure in this study (Figure 11, Table 5, Table 6). In agreement with metal quantifications using ICP-OES (Figure 20), Fe contents were also previously shown to be reduced in *A. thaliana* roots along with Cd treatment, which may be the result of a competition for the mutual uptake of the two metals by the transporter IRT1 ^{104,226}.

Under the assumption that an activation of Fe deficiency responses under Cd exposure is supposed to mitigate Fe deprivation, the downregulation of the two genes *S8H* and *CYP82C4* is counterintuitive (Figure 11). Both of these genes are implicated in the biosynthesis of catechol-type coumarins, which are Fe-mobilizing metabolites derived from the phenylpropanoid pathway ²²⁷. The fact that the metabolomic data also revealed a reduction of

sideretin contents (Figure 8), substantiates the existence of a distinctive effect of Cd on coumarin profiles, because mere Fe deficiency was shown to go along with elevated coumarin levels. Especially sideretin, which is synthesized by *CYP82C4*, was demonstrated to accumulate under low Fe and acidic pH^{227–229}. Despite these findings, the *cyp82c4* KO mutant described by Rajniak *et al.*, 2018²²⁷, which is unable to synthesize sideretin, displayed growth comparable to the wild type under Cd exposure (Figure 35). Interestingly, evidence points to an IRT1-independent mechanism for the uptake of Fe³⁺ complexed with the catechol-type coumarin fraxetin^{230,231}. This phytosiderophore-like pathway fosters speculations over a possible function of coumarins in Cd uptake. Additionally, the increase in *CYP82C4* expression along with elevated sideretin levels in RR upon Zn excess¹⁸⁰ adds weight to the idea of a mechanism that enables differentiation of essential elements from non-essential elements in coumarin-mediated metal uptake.

Even though the Cd treatment in this study and the Zn treatment in Thiébaut *et al.*¹⁸⁰ similarly resulted in a 50 % reduction in primary root growth after one week, the transcriptomic response in both root sections were overall largely different (Figure 24). This indicates that the physiological response towards a non-essential metal (Cd) on the one side and an essential metal (Zn) on the other side encompasses distinct molecular response mechanisms, even though the observable effect on root growth is similar.

7.1.3.2 Root growth inhibition without differential expression of cell cycle regulatory genes

With the aim to analyze the specific impact of Cd on the tissues in the root apex, RNA sequencing of RT and RR was done separately. RT include the RAM and EZ, which are essential to root growth by facilitating cellular division and elongation. Understanding the specific impact of Cd on the cell cycle in the RAM requires the extraction of Cd-responsive CCRG. However, despite a clear inhibition of root growth following Cd exposure, no significant expression changes of CCRG were observed (Figure 12). This reflects the results from the transcriptomic analysis of seedlings exposed to Zn concentrations that had a comparable inhibitory effect on root growth¹⁸⁰.

A crucial TF in this context is SUPPRESSOR OF GAMMA RESPONSE 1 (SOG1), which plays a key role in repressing cell division especially in response to genotoxic stress, which is a mechanism of Cd toxicity²³². SOG1 is activated by ATAXIA TELANGIECTASIA MUTATED (ATM) and ATM AND RAD3-RELATED (ATR) and regulates the response to DNA damage, including the induction of CDK inhibitors such as *SMR5* and *SMR7*¹⁹⁶. However, *SOG1* and

related downstream genes were not differentially expressed. Taken together, immediate growth inhibition as a result of metal toxicity appears to occur without altered expression of CCRG. It is known that many of these genes, including cyclins and cyclin dependent kinases are predominantly regulated at the post-translational level by mechanisms such as phosphorylation or proteolytic degradation²³³. Nonetheless, previous studies have also reported differential expression of CCRG in response to Cd exposure²³⁴. The fact that these previously reported changes occurred all under prolonged stress (i.e. > 5 days), suggests that transcriptional regulation of the cell cycle under Cd stress may be a consequence only of sustained exposure.

7.1.4 The specific impact of Cd on gene expression in root tips

The exploration of global trends in the transcriptomic dataset with PCA identified clear differences in the extent to which RT and RR responded to the exposure with Cd. In accordance with the lower extent of Cd accumulation (Figure 4, B), PCA showed that gene expression in RT was less perturbed than in RR (Figure 9, A).

Published scRNA-Seq data were used to integrate cellular information into bulk RNA-Seq data from RT, which showed a clear pattern in which mature gene clusters displayed the highest extent of differential expression (Figure 13). Cd has been shown to disrupt hormonal gradients critical for meristem maintenance, such as the distribution of auxin and cytokinin in RT^{122,123}. Thus, the transcriptional changes in mature gene clusters may reflect perturbed meristem maintenance and a stronger tendency towards differentiation into mature root cells in Cd-treated RT. Additionally, it is important to contextualize this trend by recognizing that toxic metal concentrations are linked to a reduction in the size of both RAM and EZ¹²³ (Figure 33). During sampling, RT were collected with equal size, irrespective of Cd-treatment. The high percentage of differential expression in mature gene clusters relative to others may therefore at least to an extent result from a higher number of mature cells – and transcripts specific to them - in the Cd samples compared to the controls (Figure 32).

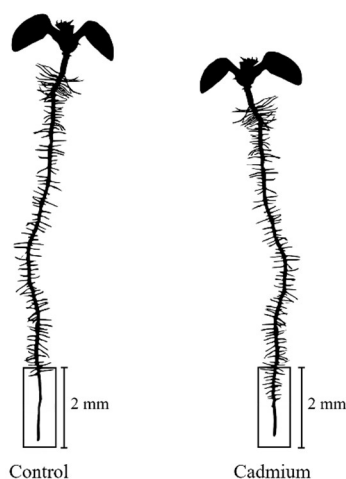


Figure 32: Schematic depiction of seedlings from control or Cd exposure. Cd is associated with smaller size of RAM/EZ, therefore the root apex with a fixed size of 2 mm contains a higher number of mature cells (characterized by root hairs).

The exploration of an RT-specific response was furthermore done as a manual gene-by-gene wise assessment of all DEG and resulted in the identification of HY5 target genes (Figure 14, 6.1.5). Importantly, all of these genes – with the exception of *XTH20* - did not exhibit higher expression in RR, making it unlikely that their upregulation in RT results from the smaller size of the RAM/EZ and the higher proportion of mature cells in Cd-treated RT samples compared to control RT samples (Figure 32).

Based on functional associations identified in previous research, these DEG fall into several categories. *MYB12* is involved in the biosynthesis of flavonols, a specific class of anthocyanins with photoprotective (and antioxidative, as mentioned in 7.1.2) properties via the regulation of genes like CHALCONE SYNTHASE and FLAVONOL SYNTHASE¹⁸⁴. In the case of *MYB12*, this activity is mostly restrained to roots, whereas *MYB11* and *MYB111* act in meristematic tissues and the hypocotyl, respectively²²³. Flavonols exhibit strong absorption in the UV spectrum, and their photoprotective role has been demonstrated with the *myb11/myb12/myb111* triple mutant. Similar to *hy5*, this mutant's ability to accumulate flavonols is impaired and it shows significantly increased sensitivity towards UV-B irradiation¹⁹⁷. In support of a specific role in RT, a recent study has connected *MYB12* to the regulation of cell division in the meristematic vascular tissue by a regulatory action on the TF complex TARGET OF MONOPTEROS 5 (TMO5)/ LONESOME HIGHWAY (LHW). TMO5/LHW controls proliferation through a modulation of the response to cytokinin in the meristem. *MYB12* was shown to interact with TMO5/LHW and dampen the induction of target gene expression and periclinal/ radial cell division. *MYB12* stands downstream of TMO5/LHW and its expression is induced by the cytokinin response, which establishes a negative feedback

mechanism. In this, MYB12 limits TMO5/LHW activity to regulate cellular proliferation rates during development of the root vasculature²³⁵. The *ELIP* genes were also induced specifically in RT and similar to *MYB12*, they are associated with photoprotection. ELIPs belong to the family of light-harvesting related proteins and their proposed function lies in the reduction of excitation pressure during high light stress²³⁶.

Secondly, the genes *HRG1* and *HRG2* have been identified as important components in maintaining ROS homeostasis within the root tip. Adequate distribution and homeostasis of $O_2^{\cdot -}$ and H_2O_2 in RT is regarded as an essential component of meristem maintenance and, consequently, for optimal root growth (see Introduction, Figure 2)^{120,237}. *HRG1* and *HRG2* exhibit specific responsiveness to H_2O_2 in the meristematic region, where their activity facilitates the removal of H_2O_2 , thereby ensuring the equilibrium of ROS levels in the root tip¹⁹⁹. Strikingly, this functional attribute has analogously been described for HY5¹²¹, which implies that the *HRG* genes may be integrated into HY5's regulatory framework to maintain ROS homeostasis in the RAM.

Lastly, several genes of the XTH family were identified to exhibit RT-specific induction following Cd exposure and to be under regulatory control of HY5. The XTH family represents a large group of 33 genes in *Arabidopsis thaliana* and it encodes proteins with xyloglucan endotransglucosylase (XET) or xyloglucan endo-hydrolase (XEH) activities, both of which are related to xyloglucan modifications within the cell wall²³⁸. Therefore, the differential expression of *XTH* genes suggests a specific impact of Cd on cell wall dynamics in the root tip. Interestingly, XTH proteins have previously been connected to metallic stress. For example, XTH17 and XTH31 play a role in aluminium resistance^{239,240}, while overexpression of a *Populus* XTH gene enhanced Cd tolerance in tobacco by reducing root Cd uptake²⁴¹. Similarly, *xth33* mutants displayed increased Cd resistance and lower root Cd accumulation, emphasizing the critical role of XTH genes in heavy metal stress responses²⁴².

Using a high confidence set of 297 target genes¹⁸⁹, the impact of HY5 on gene regulation in RT or RR following Cd exposure was further analyzed. Specifically, the mean fold change of these target genes was compared to a null distribution generated with 10 000 lists of randomly chosen AGI codes and their respective mean fold changes (Figure 16). In both RR and RT, this analysis indicated that HY5 targets are collectively upregulated, with a higher fold change than expected by chance. However, it is important to note that this high-confidence HY5 target set was derived from large-scale datasets based on whole seedlings, which may differ from the root-specific regulatory network of HY5.

7.1.5 HY5 affects Cd tolerance and accumulation

The identification of HY5 target genes as a specific part of the response of RT to Cd led to the phenotypic assessment of *hy5* mutants under Cd exposure. This revealed the increased growth susceptibility of the mutants under Cd exposure (Figure 17) and showed that a loss of functional HY5 is associated with increased cadmium accumulation (Figure 19).

HY5 is a transcription factor of the bZIP (basic leucine zipper) family and through the inhibition of seedling etiolation, it has a crucial role in plant development, which is reflected in the major morphogenetic alterations shown by loss-of-function mutants (Figure 37). Historically recognized for its role in light-regulated development, HY5 acts downstream of photoreceptors and promotes a developmental shift towards photomorphogenesis as soon as seedlings experience illumination. This causes an abolishment of the action of the E3 ligase complex consisting of COP1 (CONSTITUTIVE PHOTOMORPHOGENETIC 1) and SPAs (SUPPRESSOR OF *phyA-105*), which can then no longer promote HY5 degradation. Light-triggered activation of photoreceptors causes an inactivation of the repressive COP1/SPA activity by mechanisms such as the nuclear exclusion of COP1 or the degradation of SPA1^{243,244}. HY5 is known to bind primarily to the G-box motif in promoters of its target genes and its transcriptional activity depends on B-box containing proteins (BBX20-22) as cofactors¹⁹⁸. A mounting body of research over the last decades has revealed that the regulatory influence of HY5 extends beyond photomorphogenetic genes. For example also genes involved in circadian rhythm, ROS regulation, cell elongation, sucrose metabolism, terpene synthesis, defense signalling, nutrient uptake, anthocyanin biosynthesis and hormone signalling were shown to be under its control²⁰¹. Furthermore, HY5's role in the integration of abiotic environmental cues is evidenced by studies showing its function in the response to cold and salt stress^{245,246}. Also root-specific processes are regulated by HY5 and the TF is both translocated from shoots to roots and autonomously expressed in the root^{189,200}, where it facilitates transcriptional repression as well as induction of target genes²⁴⁷.

The widespread role of HY5 in orchestrating numerous facets of plant physiology, underscores its central role in plant biology but also demonstrates the inherent complexity of interpreting phenotypic outcomes in central regulatory gene knockouts. For example, loss-of-function of such fundamental transcriptional regulators may affect growth performance under various stress conditions, as demonstrated with the *hy5_1* mutant, which besides the Cd-phenotype, displayed increased sensitivity towards mannitol and NaCl (Figure 18). The widespread nature of HY5's functions necessitates careful dissection of direct and indirect effects and future work is required

to understand the mechanism, by which HY5 limits Cd accumulation. Some points however can be addressed on the basis of the underlying results.

For example, increased Cd accumulation may be a consequence of alterations in RSA such as an increase in root hair length and a higher lateral root density^{200,204}. Both of these parameters could contribute to Cd accumulation via an increased absorption and adsorption surface. Both *hy5* mutants exhibited a higher LR/PR ratio compared to the wild type, however, the sum of LR and PR was similar between the mutants and the wild type (Figure 22). Additionally, root development was shown to be strongly dependent on light signalling^{248,249} and increased Cd-sensitivity of *hy5* was consistently observed across various light conditions (Figure 17). This renders alterations of uptake mechanisms a more likely reason for the increased Cd accumulation of *hy5*.

Furthermore, HY5 has been labeled a “key regulator for light-mediated nutrient uptake and utilization” with a crucial role in light regulated nutrient uptake. This role encompasses the regulation of C assimilation in shoots and the modulation of genes related to N/P-assimilation and Cu²⁺ uptake²⁴⁷. However, the involvement of HY5 in regulating Fe homeostasis as well as its role in S-assimilation are particularly relevant in the context of the observed Cd phenotype. Its role in regulating the Fe-deficiency response was proposed by Mankotia et al., who observed the regulation of key genes for Fe uptake by HY5, including *FIT*, *FRO2* and *IRT1*. According to this study, HY5 also negatively regulates *BTS* and *PYE* to optimize root growth and Fe homeostasis under Fe-limitation²⁵⁰. *hy5* mutants failed to respond adequately to this condition, leading to impaired root growth under Fe-limitation. Additionally, Fe contents in *hy5* were reduced compared to Col-0 under sufficient Fe-supply²⁵⁰. These findings were only partially reproducible, since for example the increased susceptibility to Fe deficiency of *hy5* was confirmed (Figure 21). However, ICP-OES measurements indicated similar Fe concentrations in wild-type and *hy5-1* roots in control conditions and higher Fe concentrations in roots exposed to Cd. This is due to the decreased Fe concentrations in the wild-type after exposure to Cd, which does not occur in *hy5-1* (Figure 20). Consequently, the higher Cd accumulation of *hy5* may be a result of the disrupted control over Fe uptake under Cd stress. A hypothesis derived from these data would be that HY5 acts as a negative regulator of the Fe uptake machinery, that possibly dampens it under Cd exposure. This calls for a comparative transcriptomic analysis of the gene-regulatory networks governing Fe homeostasis along with specific investigations of proteins implicated in Fe uptake in the mutant and the wild-type. Besides a competitive uptake between Cd and Fe, the degradation of IRT1 following the recognition of non-Fe metals^{85,86}

may contribute to a reduction of cellular Fe levels during Cd exposure. Consequently, the assessment of lines expressing IRT1:GFP fusions under Cd excess in these genetic backgrounds could provide valuable insights.

In addition, the ascribed function of HY5 in S-assimilation^{251,252} is important to mention in a discussion of the Cd-accumulation phenotype. Thiol-containing molecules, such as GSH, PCs and metallothioneins are central for metal detoxification^{253,254}. HY5 was shown to directly bind the promoters of two essential genes for S-assimilation, *APR1* and *APR2* and positively regulates their expression^{251,252}. In the same study, slightly elevated GSH levels of *hy5* compared to WT were shown, which was reproduced in our analysis of *hy5_215* (Figure 19). Furthermore, the reduction of GSH levels by Cd exposure occurred to a lower extent in roots of the *hy5_215* mutant when compared to Col-0 (Figure 19). This is relevant for Cd accumulation, because correlations between the level of thiol compounds and accumulation of Cd (and arsenic) have been demonstrated several times (reviewed in²⁵⁵). Consequently, the disturbed S-metabolism of *hy5* mutants associated with higher GSH and PC levels may contribute to the observed elevated Cd accumulation.

Taken together, this study identified a previously unrecognized role of the photomorphogenetic TF HY5 by demonstrating an involvement limiting Cd accumulation. This adds to previous studies, which have expanded the perception of HY5 beyond its historical role in light-regulated plant development (reviewed in²⁴⁷). Notably, gene coexpression analysis on a large set of data representing responses to variance in nutritional availability highlighted the three light-signalling TFs HY5, PIF4 and NF-Y as possible master regulators coordinating nutrient utilization²⁵⁶. Together with this, the results presented here demonstrate that key regulators of plant development can have unrecognized roles in the response to edaphic conditions such as metal stress.

7.2 The effects of metallic UFP *A. thaliana*

7.2.1 Development of controlled exposure experiments

Existing studies addressing brake wear toxicity used liquid particle suspensions and studies on plants have assessed toxicity by applying particles directly to soil or growth medium. Brake wear samples were generated by grinding brake pads or collecting deposited PM^{181,182,257}. These studies may serve as an estimation of chemical toxicity potential but they cannot be seen as a replication of realistic airborne exposure to airborne brake wear particles and likely do not consider the large proportion of UFP in actual brake wear emissions. Here within, this was addressed by integrating an exposure chamber into the exhaust system of a brake-test dynamometer (Figure 39) and applying braking conditions that were shown to result in particles that are largely in the ultra-fine size fraction (Figure 25, A). This approach represents airborne exposure and it also reduces the steps between particle generation and plant exposure to a minimum.

Noteworthy, brake emissions were previously reported to exhibit larger fractions of UFP with increasing kinetic energies in the braking process, which aligns with the results described in 6.2.1²⁵⁸. Elemental characterisation furthermore showed an abundance of metals in the order Fe>Cu>Al>Ti>Sn>Zn>Mo>Ni>Pb (Figure 25, B), which is consistent with previous studies that identified Fe, Cu, Sn, Ti and Al as the major metals in airborne brake wear particles, while elements like Ni and Pb were reported in lower concentrations^{139,259}.

After exposure to 45 highway brakings, metallic particles were extracted from leaves and UFPC were measured with spICP-MS, which showed that the extent of particle deposition was mostly comparable between independent exposures (Figure 26). Moreover, spICP-MS showed, that elements in UFP deposited on leaves closely mirrored the elements that were measured in UFP collected with ELPI+ (Figure 25, B; Figure 26). In contrast, only Fe- and Al-UFPC were detected in the samples from background exposures. Given that Fe and Al are the two most abundant metals in the Earth's crust, their detection in background samples is coherent with a ubiquitous presence in environmental particulates²⁶⁰.

SEM of leaves exposed to airborne UFP demonstrated that the particles primarily assemble into aggregates (Figure 27). Transmission electron microscopy by Gonet *et al.*¹⁴⁹ also identified agglomeration of brake wear particles and led to the conclusion that larger particle size fractions are mostly composed of UFP agglomerates. Especially at elevated concentrations, airborne UFP form agglomerates due to van der Waals or electrostatic forces, which reduces the concentration

of individual UFP entities^{149,155}. These agglomerates can be disrupted by electrostatic impactors such as the ELPI+ system²⁶¹, which limits the ability of impactor measurements to assess the extent of UFP agglomeration within the chamber (Figure 25).

7.2.2 RNA sequencing of *A. thaliana* exposed to UFP from brake abrasion

To gain insights into the physiological response of plants to metallic UFP and as a proof of concept of the newly developed exposure chamber, RNA sequencing of *A. thaliana* was conducted. Global gene expression of plants outside of the exposure chamber was compared to (i) the background particle concentration in the brake dynamometer system (i.e. background exposure) and (ii) the particles originating from 45 highway braking events (i.e. 45 brakings). Both of these exposures triggered similar alterations in gene expression, as indicated by PCA (Figure 28, A). However, DEA highlighted their dissimilarity, with a higher number of DEG in the exposure to particles from 45 highway braking events (92 DEG after background versus 150 DEG after 45 brakings, Figure 28, D). Thus, a larger effect on gene expression was associated with the exposure to a greater number of particles.

Further analysis of the 150 brake wear responsive genes showed that the majority of them displayed a progressive increment or decrement in expression from the controls through the background exposure to the 45 brakings (Figure 29, A). Therefore, the data indicate that the background exposure triggered a transcriptional response of many genes that were even more strongly affected by the treatment with the wear of 45 brakings. This implies a saturating effect, in which a lower concentration of particles leads to similar effects compared to the higher concentration.

The similarity of both groups that were in the exposure chamber (i.e. background exposure and exposure to 45 brakings) in comparison to the outside controls (Figure 28, A) raises the question whether the transcriptomic changes are driven by the airflow of the suction unit as opposed to UFP. Both the functional nature of some DEG and the absence of markers for mechanical stress may be used to address this consideration. Among the 150 DEG identified by comparing the transcriptomes of plants exposed to 45 brakings to the outside controls were several metal homeostasis genes. This includes the two genes *bHLH38* and *bHLH39*, which have been reported to be key TFs for the regulation of Fe uptake-related gene expression by their interaction with FIT^{262,263} (Figure 29, C; Table 12). Additional DEG related to metal homeostasis were for instance the copper transmembrane transporter *COPT2*²⁶⁴ (Figure 29, C; Table 12) or *PLANT CADMIUM RESISTANCE 2 (PCR2)*, which has an ascribed role in metal detoxification²⁶⁵. The downregulation of *bHLH38*, *bHLH39* and *COPT2* represents a specific

impact on the gene regulatory network governing Fe and Cu uptake, which suggests that both treatments (i.e. background particles or particles from 45 brakings) led to excessive Cu and Fe concentrations within leaves. This appears even more probable in light of the fact, that Cu and Fe were the most abundant metals in the UFP released by the brake system (Figure 26). Apart from this, some *A. thaliana* genes, including members of the calmodulin and calmodulin-like protein families, were shown to be very reliable markers for mechanical stress²⁶⁶. The fact, that none of these *TCH* genes were among the 150 brake wear responsive genes renders a major impact of mechanical stress on the transcriptomes unlikely. Additionally, the impact of temperature on gene expression must be considered, as only the plants exposed to 45 braking events experienced an increase in temperature from ~22°C to ~30°C (Figure 41). However, the absence of marker genes for heat stress, such as heat shock transcription factors (HSFs) or heat shock proteins (HSPs) among the DEG (Table 12) makes an impact of the temperature increase on gene expression implausible²⁶⁷.

The transcriptomic data furthermore indicated an induction of oxidative stress (Figure 29, B), which aligns with existing studies suggesting oxidative stress, for example mediated by redox-active metals, as a mechanism underlying UFP toxicity¹⁴⁴. The responsiveness of several jasmonate-induced oxygenases (Figure 29, C) implies that UFP exposure may influence the specialized metabolism of plants. Given that many specialized metabolites are believed to act as toxins in the context of herbivore defense²⁶⁸, UFP exposure may lead to the synthesis of potentially harmful compounds in crop plants.

7.2.3 Comparison of field exposure with controlled dynamometer exposure

To contextualize the brake dynamometer-based exposure system with real-world data, outdoor experiments were conducted at three locations with varying levels of traffic exposure. Particle measurements at these sites revealed higher ambient UFP concentrations along with increasing traffic density (Figure 31), which aligns the perception of vehicular traffic as a major contributor to UFP emissions²⁶⁹. The mean PNC of the inner-city location ($\bar{x}_{08:00-18:00} = 26,753 \text{ UFP/cm}^3$) also reflects the dimensions of a measurement conducted in a Manchester street canyon, where a PNC of $27,000 \text{ UFP/cm}^3$ was reported^{269,270}.

The comparison of elemental UFPC profiles with PCA suggested, that UFP deposition in an inner-city location replicates the laboratory exposure most closely (Figure 31, A). Moreover, the comparison of UFPC deposition suggested, that the two exposures led to similar amounts of UFP on leaves (Figure 31, B). Therefore, the chosen brake-dynamometer-based approach tackles the problem of environmentally relevant UFP concentrations as another limitation of

previous toxicological studies (see 4.4.3). Moreover, as a result of the transcriptional response (Figure 28), it also promotes the assumption that environmentally occurring levels of UFP have an impact on physiological processes in plants. Due to the interactions of diverse environmental factors influencing plants in their natural environment, these effects may still be largely different from the ones described here within.

The exposure system introduced in this study represents a novel experimental platform for studying the toxicity of UFP from brake wear. In context of the transcriptomic data suggesting physiological responses related to metal homeostasis, follow-up studies in plants could further evaluate dose-related effects and long-term outcomes for development and fitness. Additionally, metabolomic studies may be used to further elucidate the impact of brake-wear UFP on the plant metabolome, as suggested by the differential expression of *JAO* genes (Figure 29). Moreover, the setup may also be used to shift the focus away from plants towards animal models, to contribute to an improved understanding regarding the effects of UFP on an expanded scope of organisms.

8 Supplementary information

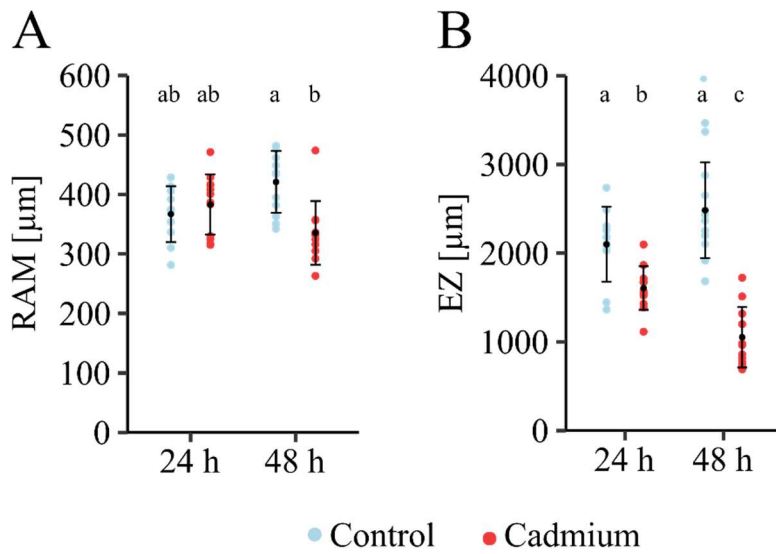


Figure 33: Impact of Cd on the size of the root apical meristem (RAM) and elongation zone (EZ). A: RAM size after exposure to Cd, defined as the distance from the quiescent center to the first elongated cortex cell. B: EZ size after Cd exposure, determined by measuring the distance from the first elongated cortex cell to the first root hair. Seedlings were germinated for 7 days under control conditions and transferred to either control medium or medium with Cd (25 μM) and grown for additional 24/ 48 h. Data stems from one biological replication (n = 10). Letters display statistical groups (ANOVA with Tukey HSD, $p \leq 0.05$).

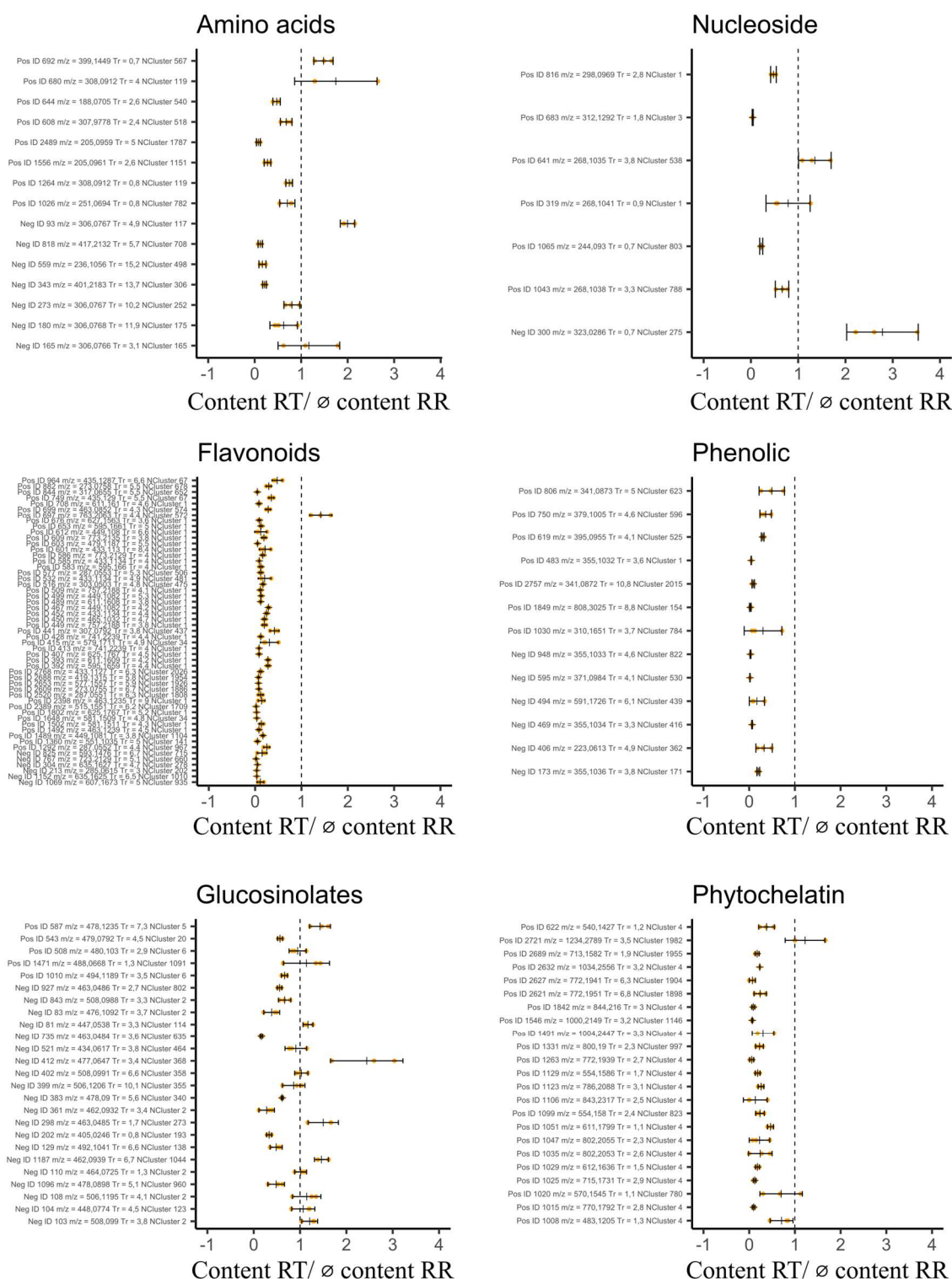


Figure 34: Metabolite contents of RT compared to RR by substance class. Metabolite data were normalized to the estimation of biomass (i.e. the amount of collected root pieces). Values were obtained by dividing the contents in control samples of RT by the mean of the control samples of RR (n = 3). Displayed are mean values \pm standard deviation.

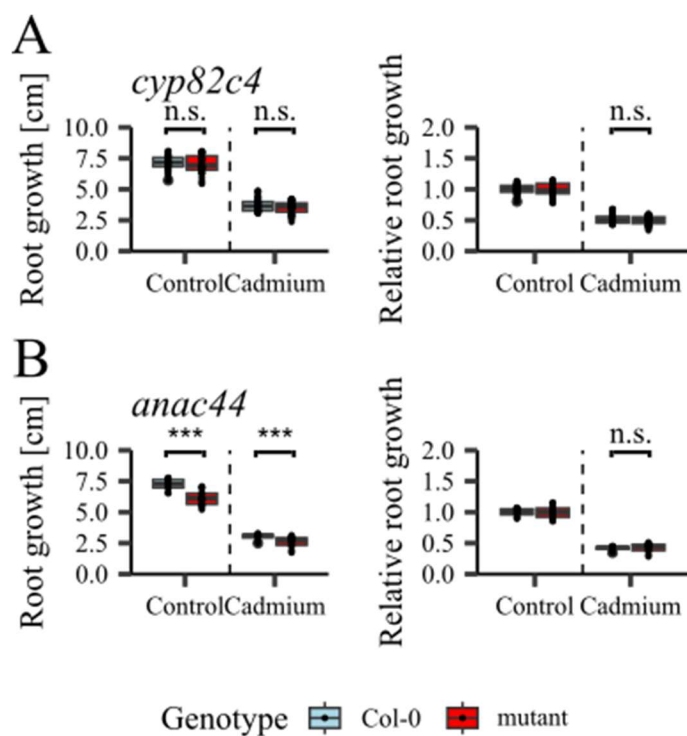


Figure 35: Primary root growth of Col-0 compared to the *cyp82c4* and *anac044* mutants under control conditions and Cd exposure. A: Growth of the *cyp82c4* mutant. B: Growth of the *anac044* mutant. Seedlings were germinated for 7 days under control conditions and transferred to either control medium or medium with Cd (25 μ M) and grown for additional 7 days. Data on the left side are absolute growth values, data on the right side are growth values relative to the mean of the respective control. Asterisks indicate statistical significance ($p \leq 0.05$, Mann-Whitney U-test, data from three independent replications, $n = 12-40$).

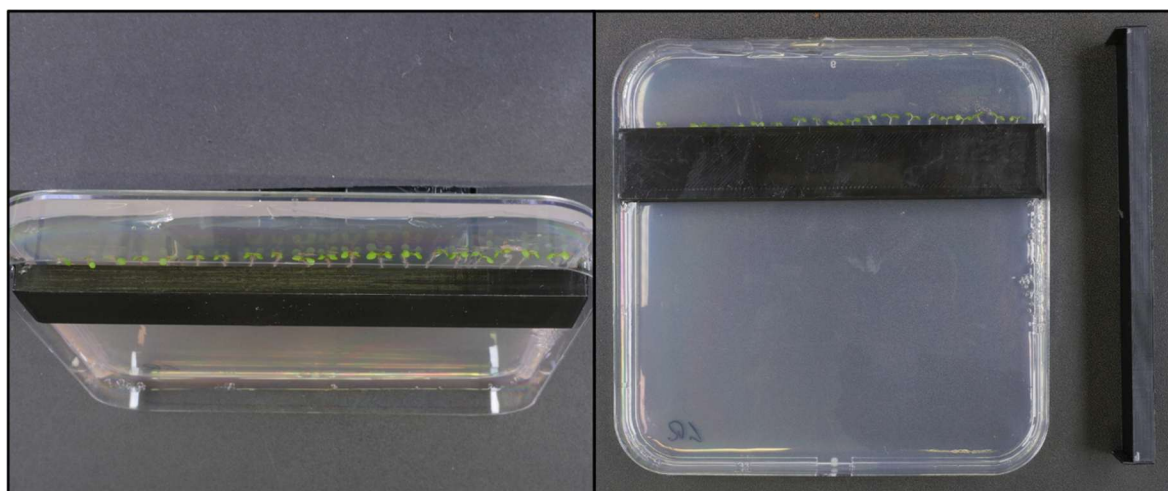


Figure 36: Depiction of the self-made PLA inlays for the root covered system (RCS). Plates were wrapped in aluminium foil downward of the inlay to keep the roots in darkness.

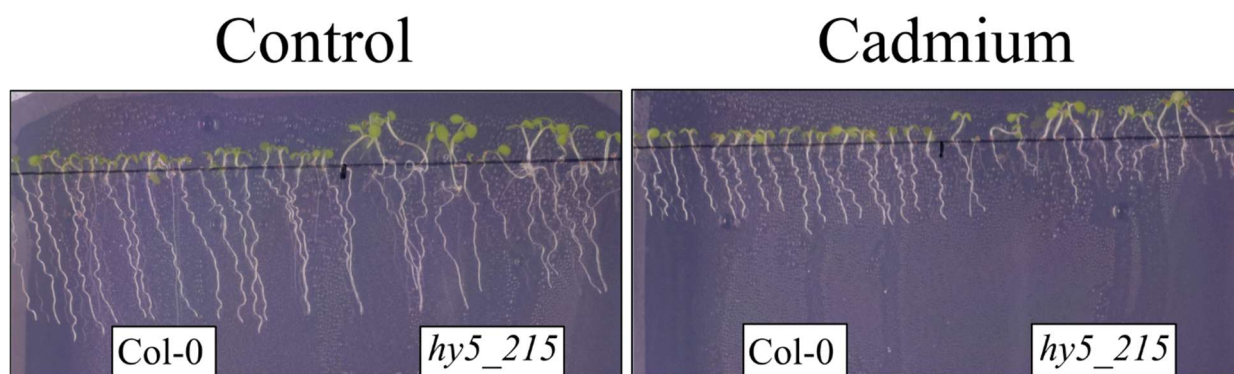


Figure 37: Pictures representing Col-0 and *hy5_215* seedlings after 9 days of growth on control or Cd (25 μ M) plates.

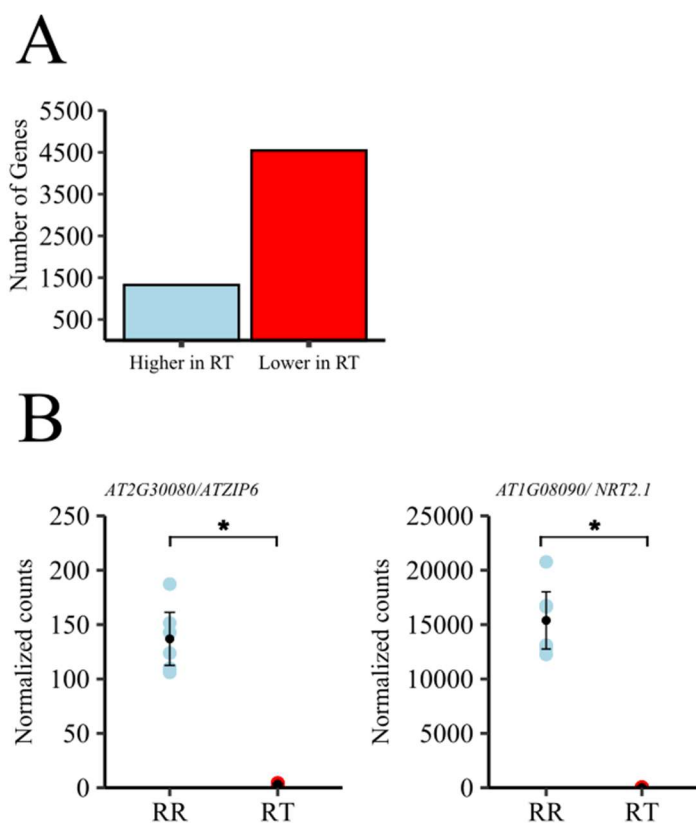


Figure 38: Supplementary data on the comparison of RR with RT. A: Number of genes higher or lower expressed in RT compared to RR. B: Expression of transporter genes related to Cd uptake. Data are from control conditions (Control 24 h and control 48 h p

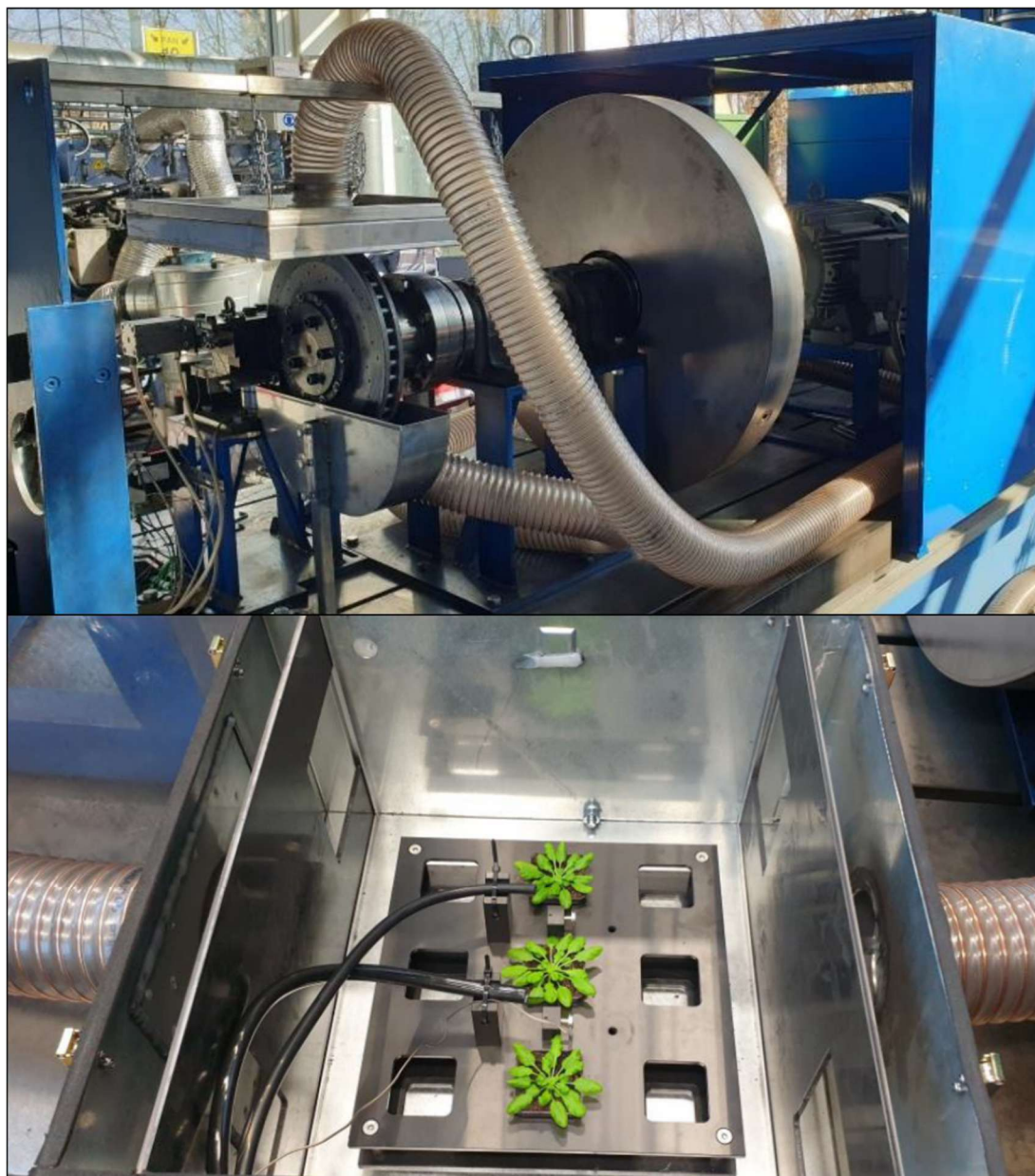


Figure 39: Depiction of the brake test dynamometer and exposure chamber (pictures modified from ¹⁶⁹). Top: Dynamometer with electric motor, 800 kg fly wheel, brake dust collection elements and brake calliper. Bottom: Exposure chamber for plants.

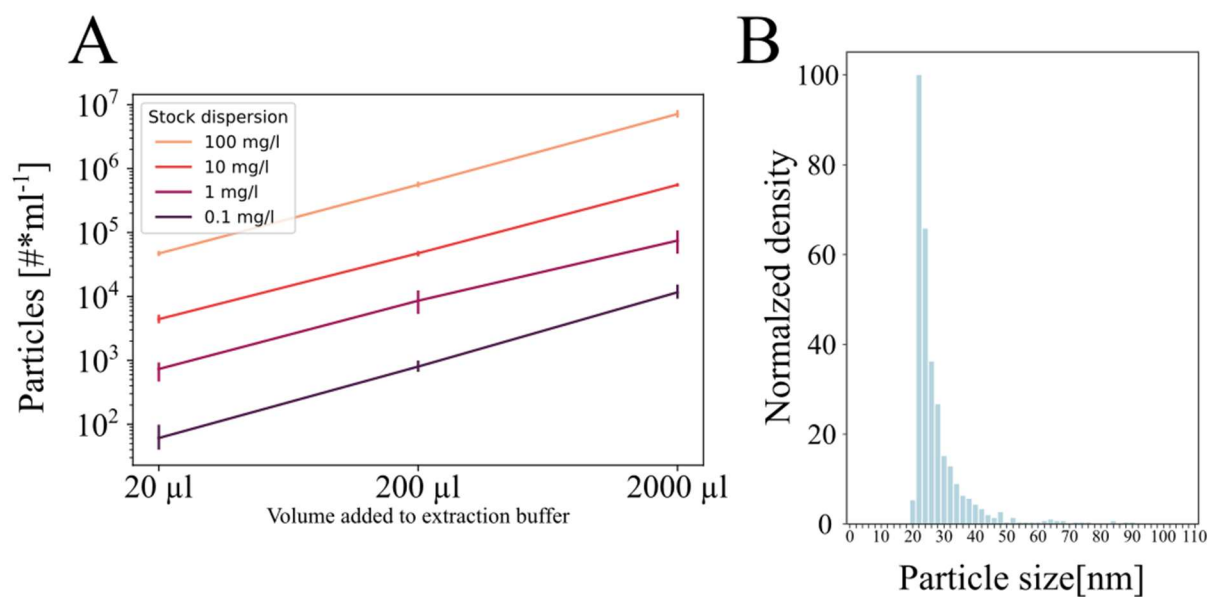


Figure 40: Validation of the extraction method for the measurement of UFP with spICP-MS. Different volumes of Cu-nanoparticle stock dispersions were added to prior to the extraction of UFP from leaf material. Only leaves not treated with particles were used and extracted as described in 5.2.7. Data from three independent extractions. Shown are mean values \pm standard deviation. B: Size distribution of the measured particles.

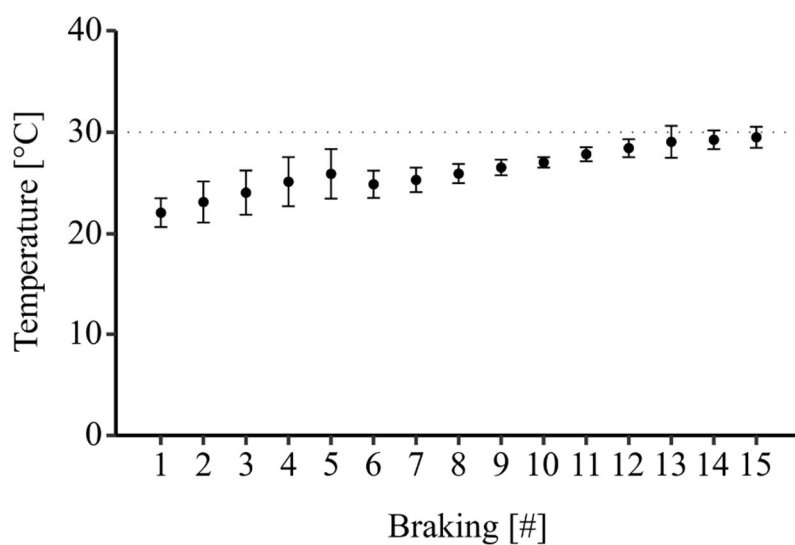


Figure 41: Temperature inside the exposure chamber during 15 successive brakings. Data is given as mean \pm standard deviation and originates from three successions of 15 braking processes.

Table 5: DEG in RR after 24 h of Cd exposure.

AGI	symbol	log2 fold change	padj
AT5G39100	<i>GLP6</i>	6.815308483	0.00233963
AT3G60140	<i>BGLU30</i>	5.450639321	2.3201E-06
AT1G09505	#NV	5.345350648	7.9589E-07
AT2G30766	<i>FEP1</i>	5.287923303	1.4761E-08
AT5G48850	<i>SDII</i>	5.133527024	1.3164E-26
AT1G23730	<i>BCA3</i>	5.056750474	1.1927E-06
AT2G44460	<i>BGLU28</i>	4.955787241	2.4691E-05
AT5G23990	<i>FRO5</i>	4.927512315	0.00968444
AT1G07367	#NV	4.474709935	2.8561E-07
AT3G56970	<i>BHLH038</i>	4.062774029	6.5329E-50
AT5G26220	<i>GGCT2;1</i>	3.993848308	2.2608E-11
AT2G32487	#NV	3.817724587	1.6256E-06
AT4G11393	<i>DEFL202</i>	3.715354928	1.3719E-09
AT1G47400	<i>FEP3</i>	3.699345826	4.4267E-12
AT1G47395	<i>FEP2</i>	3.536521397	3.1372E-17
AT3G49580	<i>LSU1</i>	3.48798024	4.8631E-16
AT3G56980	<i>BHLH039</i>	3.428875634	7.8982E-28
AT3G49570	<i>LSU3</i>	3.295397686	7.9589E-07
AT5G24660	<i>LSU2</i>	2.938036256	7.6715E-06
AT3G08860	<i>PYD4</i>	2.841820346	0.00299578
AT5G10180	<i>AST68</i>	2.612952405	2.009E-12
AT4G08620	<i>SULTR1;1</i>	2.52173955	5.8328E-05
AT2G14247	#NV	2.360730078	0.0020606
AT4G16370	<i>OPT3</i>	2.337978118	2.8809E-13
AT3G46900	<i>COPT2</i>	2.246235829	2.4315E-07
AT1G56430	<i>NAS4</i>	2.220886209	0.00070906
AT4G14690	<i>ELIP2</i>	2.166124149	0.00534184
AT2G16890	#NV	2.144016689	0.00434578
AT3G22840	<i>ELIP</i>	2.132958259	0.00027379
AT5G05250	#NV	2.07279194	7.7412E-05
AT4G32950	#NV	2.038186153	0.01700317
AT5G45070	<i>PP2-A8</i>	1.925463194	0.00520154
AT5G67370	<i>CGLD27</i>	1.884290224	0.02557831
AT5G53450	<i>ORGI</i>	1.869892522	1.3712E-17
AT5G15950	<i>SAMDC2</i>	1.836130911	0.04900506
AT1G23020	<i>FRO3</i>	1.620419719	0.03446418
AT1G70290	<i>TPS8</i>	-1.714927824	0.01987462
AT1G13260	<i>RAVI</i>	-1.746278028	0.00537129
AT1G30820	<i>CTPS1</i>	-1.746877066	0.00757541
AT5G14120	#NV	-1.835575952	0.01877374
AT1G80440	<i>KFB20</i>	-1.876004175	0.01256435
AT1G80380	<i>GLYK</i>	-1.893923037	0.00495936
AT5G65207	#NV	-1.916724428	0.02858384

AT5G19120	#NV	-1.977284166	0.00817455
AT3G15630	#NV	-2.074399035	0.03518231
AT1G02640	<i>BXL2</i>	-2.082300386	3.937E-05
AT5G22920	<i>RZPF34</i>	-2.222871612	0.00326852
AT3G25190	<i>VTL5</i>	-2.235619659	0.00012658
AT1G73120	#NV	-2.269496077	0.00016656
AT2G18700	<i>TPS11</i>	-2.308714133	5.0691E-06
AT2G15890	<i>CBP1</i>	-2.3127392	7.9589E-07
AT1G76590	<i>PLATZ2</i>	-2.36326255	0.00095444
AT1G28330	<i>DRM1</i>	-2.379763532	0.005229
AT4G31940	<i>CYP82C4</i>	-2.460989568	0.04248005
AT5G63160	<i>BT1</i>	-2.696594816	4.9778E-10
AT3G48360	<i>BT2</i>	-3.032786446	1.5857E-23
AT5G01600	<i>FER1</i>	-3.171012	1.1459E-33
AT5G20250	<i>DIN10</i>	-3.221023112	2.9796E-11
AT1G21140	<i>VTL1</i>	-3.284416076	5.3552E-08
AT1G76800	<i>VTL2</i>	-3.338662112	6.2874E-15
AT5G56550	<i>OXS3</i>	-3.393526273	0.01865942
AT3G15450	#NV	-3.865175163	1.3234E-05

Table 6: DEG in RR after 48 h of Cd exposure.

AGI	Symbol	log2 fold change	padj
AT1G12030	#NV	7.022278809	0.00203038
AT2G04050	#NV	6.631181343	1.6783E-07
AT2G44460	<i>BGLU28</i>	6.553581796	6.2228E-10
AT1G09505	#NV	6.288066329	5.9942E-11
AT2G20800	<i>NDB4</i>	6.184546766	2.0189E-06
AT1G23730	<i>BCA3</i>	5.733355034	1.3016E-09
AT2G30766	<i>FEP1</i>	5.541336863	2.8851E-21
AT5G23990	<i>FRO5</i>	5.39799277	0.00063954
AT2G00920	#NV	4.93036788	0.02498135
AT2G32487	#NV	4.778430909	2.0189E-06
AT5G39100	<i>GLP6</i>	4.637470853	0.00027456
AT4G11393	<i>DEFL202</i>	4.587261159	1.2069E-15
AT5G48850	<i>ATSD11</i>	4.406127848	3.6282E-19
AT5G39120	#NV	4.273412425	0.00606527
AT5G23980	<i>FRO4</i>	3.971436242	0.00508913
AT1G07367	#NV	3.909970669	1.9494E-08
AT3G60140	<i>BGLU30</i>	3.715015707	1.7187E-05
AT3G49570	<i>LSU3</i>	3.714804791	1.0553E-07
AT3G46900	<i>COPT2</i>	3.352772303	1.0908E-26
AT5G26220	<i>GGCT2;1</i>	3.276587686	4.1448E-07
AT3G56970	<i>BHLH038</i>	3.177978747	1.505E-30
AT3G49580	<i>LSU1</i>	3.161018509	7.7515E-12

AT3G56980	<i>BHLH039</i>	3.010363589	5.3819E-20
AT1G08100	<i>ACH2</i>	2.949610296	0.00026637
AT5G10180	<i>AST68</i>	2.941926999	1.1829E-18
AT4G08620	<i>SULTRI;1</i>	2.9326783	3.6206E-09
AT1G47400	<i>FEP3</i>	2.877219083	1.4535E-09
AT3G50610	<i>CEP9</i>	2.858575227	0.00985686
AT4G28850	<i>XTH26</i>	2.822332698	6.9981E-06
AT1G47395	<i>FEP2</i>	2.799198711	6.6328E-14
AT5G24660	<i>LSU2</i>	2.786334786	6.5055E-05
AT1G56430	<i>NAS4</i>	2.562152714	2.9148E-07
AT1G34510	#NV	2.545358992	0.03157675
AT3G59930	#NV	2.473155058	0.00304943
AT3G22840	<i>ELIP</i>	2.446921842	6.4651E-08
AT4G21680	<i>NPF7.2</i>	2.421262865	0.00012852
AT4G25010	<i>SWEET14</i>	2.397723714	0.00310008
AT1G53130	<i>GRI</i>	2.391272239	0.02101826
AT5G15950	<i>SAMDC2</i>	2.377761876	3.5205E-07
AT2G16890	#NV	2.372830975	4.7209E-05
AT4G16370	<i>OPT3</i>	2.356228022	3.0139E-14
AT3G54530	#NV	2.308803848	0.04984075
AT4G00910	#NV	2.200358482	0.02388221
AT4G14690	<i>ELIP2</i>	2.077221028	0.01053985
AT4G28790	#NV	2.073105056	0.04989211
AT5G67370	<i>CGLD27</i>	1.837052875	0.01486636
AT5G53450	<i>ORGI</i>	1.832523031	8.1952E-17
AT5G05250	#NV	1.791153181	0.01720259
AT1G23020	<i>FRO3</i>	1.694525914	0.00351824
AT5G23010	<i>GSMI</i>	-1.575607835	0.03190939
AT2G28470	<i>BGAL8</i>	-1.675093701	0.00987565
AT5G61590	<i>DEWAX</i>	-1.717711028	0.01111967
AT1G80920	<i>J8</i>	-1.752194947	0.02750293
AT4G38470	<i>STY46</i>	-1.768323116	0.02925331
AT3G09220	<i>LAC7</i>	-1.797961835	0.04641851
AT3G52840	<i>BGAL2</i>	-1.815789923	0.00642707
AT1G70290	<i>TPS8</i>	-1.840007079	0.00063954
AT1G30820	<i>CTPS1</i>	-1.881259137	0.00014694
AT5G19120	#NV	-1.92154944	0.01289089
AT2G02710	<i>PLP</i>	-1.968135401	0.00061245
AT5G10230	<i>ANN7</i>	-1.990598311	0.00159137
AT1G76590	<i>PLATZ2</i>	-2.009129417	0.04643261
AT4G36670	<i>PLT6</i>	-2.050463401	0.0047402
AT5G24490	#NV	-2.067519033	0.01933151
AT3G10020	#NV	-2.09600823	0.01486636
AT1G80380	<i>GLYK</i>	-2.107822956	1.9463E-05
AT5G65207	#NV	-2.120206421	0.0005178

AT5G14120	#NV	-2.149931021	9.771E-06
AT2G40300	<i>FER4</i>	-2.152457646	4.6269E-07
AT3G49790	#NV	-2.1583144	0.0048741
AT3G61060	<i>PP2-A13</i>	-2.204801816	0.00850997
AT5G44130	<i>FLA13</i>	-2.216827649	0.00612453
AT1G02640	<i>BXL2</i>	-2.232901414	3.4059E-07
AT3G25190	<i>VTL5</i>	-2.335889855	1.141E-05
AT3G15630	#NV	-2.337362814	0.00045033
AT4G08290	<i>UMAMIT20</i>	-2.357167455	2.3919E-05
AT2G15890	<i>CBP1</i>	-2.388198808	4.4653E-08
AT3G01175	#NV	-2.450641936	0.00511953
AT1G28330	<i>DRM1</i>	-2.483249927	0.00072564
AT2G18700	<i>TPS11</i>	-2.512054927	1.3592E-08
AT3G49160	#NV	-2.598299808	0.00010917
AT1G33055	#NV	-2.654021044	0.04873819
AT3G21670	<i>NPF6.4</i>	-2.708416851	0.00566421
AT5G13320	<i>GH3.12</i>	-2.733079606	0.02951421
AT1G21140	<i>VTL1</i>	-2.861558755	6.1541E-05
AT5G22920	<i>RZPF34</i>	-2.883645281	4.0916E-09
AT4G26288	#NV	-2.939563677	0.03302971
AT3G48360	<i>BT2</i>	-2.98163407	1.6145E-22
AT5G63160	<i>BT1</i>	-3.036005629	9.0466E-16
AT3G26740	<i>CCL</i>	-3.062265127	0.00501852
AT5G01600	<i>FER1</i>	-3.19778522	1.0642E-32
AT2G33830	<i>DRM2</i>	-3.233398657	0.02096864
AT5G20250	<i>DIN10</i>	-3.277606176	4.338E-12
AT1G76800	<i>VTL2</i>	-3.443626668	7.53E-14
AT5G56550	<i>OXS3</i>	-3.623803344	0.0011391
AT3G12900	<i>S8H</i>	-3.879944925	0.0273964
AT3G15450	#NV	-3.885258973	6.9038E-06
AT1G73120	#NV	-4.084232087	2.1412E-20
AT4G31940	<i>CYP82C4</i>	-5.810225276	1.6153E-21

Table 7: DEG in RT after 24 h of Cd exposure.

AGI	symbol	log2 fold change	padj
AT2G44460	<i>BGLU28</i>	6.577695027	0.00073221
AT5G10180	<i>AST68</i>	5.141148824	0.03852831
AT4G25100	<i>FSD1</i>	5.084518913	0.00074552
AT4G12735	#NV	4.408851608	1.466E-05
AT5G43450	#NV	4.332876956	3.554E-10
AT4G13420	<i>HAK5</i>	4.272967464	0.00030425
AT3G55090	<i>ABCG16</i>	3.543291555	0.00328759
AT5G48850	<i>ATSD11</i>	3.337954662	0.01069756
AT1G21120	<i>IGMT2</i>	3.099003804	0.02127084

AT2G04050	#NV	3.098419909	0.01069756
AT1G02920	<i>GST11</i>	3.068119638	0.00315786
AT4G28850	<i>XTH26</i>	2.950237472	2.4297E-06
AT5G59520	<i>AtZIP2</i>	2.912650273	2.2833E-15
AT3G54530	#NV	2.866655504	2.7117E-05
AT5G24640	#NV	2.807134785	0.01589473
AT2G38823	#NV	2.779392553	0.00820404
AT1G12200	<i>FMO</i>	2.669306897	0.03079468
AT2G20800	<i>NDB4</i>	2.650577824	0.00117156
AT4G14690	<i>ELIP2</i>	2.535617712	1.4376E-08
AT2G47520	<i>ERF71</i>	2.517916093	0.02343502
AT1G48300	<i>DGAT3</i>	2.415060509	1.8666E-09
AT3G22840	<i>ELIP</i>	2.412362341	5.9756E-08
AT5G24380	<i>YSL2</i>	2.261164514	0.00489187
AT1G18570	<i>MYB51</i>	2.186975991	0.04488428
AT5G65140	<i>TPPJ</i>	1.978984524	0.00117156
AT2G47460	<i>MYB12</i>	1.928420455	0.00055047
AT2G40300	<i>FER4</i>	-1.720084603	0.00254245
AT5G61440	<i>ACHT5</i>	-1.847071277	0.0005021
AT1G80920	<i>J8</i>	-2.030893608	0.0005982
AT3G61060	<i>PP2-A13</i>	-2.298824971	0.04909987
AT5G28770	<i>bZIP63</i>	-2.454590931	3.3461E-05
AT2G19800	<i>MIOX2</i>	-2.469422897	0.00188875
AT1G13420	<i>ST4B</i>	-2.471701138	0.00146531
AT5G22920	<i>RZPF34</i>	-2.519757863	6.9174E-05
AT5G18670	<i>BAM9</i>	-2.567111293	3.1389E-06
AT4G37610	<i>BT5</i>	-2.568476992	1.6209E-07
AT3G15630	#NV	-2.636383948	1.846E-05
AT1G28330	<i>DRM1</i>	-2.639906803	0.00147364
AT2G20670	#NV	-2.753697686	1.4376E-08
AT5G21940	#NV	-2.985674041	4.7728E-08
AT5G20250	<i>DIN10</i>	-3.0087417	1.5534E-08
AT5G01600	<i>FER1</i>	-3.283241586	7.4763E-37
AT2G25900	<i>ATCTH</i>	-3.309639052	3.6661E-06
AT3G51910	<i>HSFA7A</i>	-3.350343894	9.4441E-07
AT2G34180	<i>WL2</i>	-3.493816672	0.00104504
AT5G56550	<i>OXS3</i>	-3.650193462	0.03146883
AT3G15450	#NV	-4.411922793	4.9111E-08
AT3G47340	<i>ASN1</i>	-5.436326993	0.00031155

Table 8: DEG in RT after 48 h of Cd exposure.

AGI	Symbol	log2 fold change	padj
AT4G25100	<i>FSD1</i>	7.497308131	5.917E-07
AT1G10875	#NV	7.049053965	0.0015711

AT2G44460	<i>BGLU28</i>	6.494231387	0.0054266
AT5G10180	<i>AST68</i>	6.361569819	0.0029492
AT4G00130	#NV	6.251338953	0.0091595
AT1G29860	<i>WRKY71</i>	5.886874647	0.03048
AT1G33890	<i>IAN3</i>	5.839084435	0.0340132
AT5G43450	#NV	5.813182744	1.888E-15
AT3G46340	#NV	5.788672001	0.0493468
AT4G28850	<i>XTH26</i>	5.30865854	5.507E-18
AT1G34510	#NV	5.253589996	4.215E-06
AT1G74650	<i>MYB31</i>	5.085829616	0.0012092
AT2G04050	#NV	4.886385419	3.609E-06
AT4G12735	#NV	4.583631154	2.997E-07
AT2G38823	#NV	4.564490555	1.065E-08
AT2G28690	#NV	4.407625489	0.0045469
AT5G05250	#NV	4.282810511	0.0047798
AT4G13420	<i>HAK5</i>	4.232268717	0.0056879
AT2G05520	<i>GRP-3</i>	4.201083	6.753E-05
AT2G20520	<i>FLA6</i>	4.092068417	2.328E-08
AT1G34540	<i>CYP94D1</i>	4.082358557	0.0342216
AT5G24640	#NV	4.061599332	1.159E-08
AT1G59850	#NV	4.016361574	7.148E-06
AT5G21120	<i>EIL2</i>	4.004161606	0.0060763
AT5G11060	<i>KNAT4</i>	3.957850635	0.0398555
AT1G11920	#NV	3.938461557	0.0073319
AT3G54530	#NV	3.890546931	3.266E-13
AT3G55090	<i>ABCG16</i>	3.868328596	0.0054266
AT2G20800	<i>NDB4</i>	3.798900871	1.755E-10
AT5G48070	<i>XTH20</i>	3.787884804	8.156E-05
AT1G03660	#NV	3.735022852	3.934E-06
AT1G77380	<i>AAP3</i>	3.5184147	0.0045469
AT2G30660	#NV	3.483007724	0.0189139
AT1G59730	<i>ATH7</i>	3.463320695	0.0334916
AT5G26220	<i>GGCT2;1</i>	3.408817968	1.552E-05
AT5G49770	#NV	3.40786131	0.0008969
AT5G48850	<i>ATSD11</i>	3.384383885	0.0125089
AT4G08620	<i>SULTR1;1</i>	3.333480516	3.024E-08
AT1G21120	<i>IGMT2</i>	3.333477524	0.0102922
AT2G41730	#NV	3.327546757	5.528E-09
AT1G09932	#NV	3.274479833	0.0066243
AT4G30110	<i>HMA2</i>	3.194299017	1.661E-06
AT5G62480	<i>GSTU9</i>	3.116861386	8.714E-09
AT4G33666	#NV	3.042060747	0.014723
AT3G22800	#NV	3.038225057	0.0204313

AT2G47520	<i>ERF71</i>	3.014498123	0.0002661
AT4G20240	<i>CYP71A27</i>	2.99492163	9.536E-08
AT5G39580	#NV	2.986865497	0.0303037
AT3G48520	<i>CYP94B3</i>	2.968163792	0.0317254
AT1G12200	<i>FMO</i>	2.884001269	0.0149252
AT1G01453	#NV	2.832223578	0.001859
AT5G57540	<i>XTH13</i>	2.818927578	7.968E-06
AT1G76930	<i>EXT1</i>	2.80940255	0.0027987
AT1G53130	<i>GRI</i>	2.730332246	8.943E-07
AT5G56080	<i>NAS2</i>	2.724731539	1.645E-06
AT2G47010	#NV	2.713183915	1.394E-05
AT1G54970	<i>PRP1</i>	2.706405866	5.862E-05
AT2G39980	#NV	2.69370951	9.606E-05
AT4G25220	<i>G3Pp2</i>	2.656713055	0.0344207
AT4G14690	<i>ELIP2</i>	2.62852598	6.244E-10
AT2G31860	#NV	2.617380018	8.635E-06
AT5G03640	<i>AGC1-8</i>	2.612448104	0.0018424
AT1G30760	<i>BBE-like</i>	2.60260444	0.0360409
AT3G22840	<i>ELIP</i>	2.590208955	2.726E-10
AT5G25190	<i>ESE3</i>	2.587070149	0.0277997
AT5G59520	<i>ZIP2</i>	2.567894702	1.46E-10
AT4G37370	<i>CYP81D8</i>	2.540785378	0.0007007
AT4G19680	<i>IRT2</i>	2.539796892	0.0005731
AT4G37030	#NV	2.527706274	0.0288224
AT2G18690	#NV	2.480421824	6.571E-06
AT5G57530	<i>XTH12</i>	2.478885232	0.0007812
AT3G56290	#NV	2.463913364	0.0390514
AT2G02100	<i>LCR69</i>	2.461539281	0.0464308
AT4G25790	<i>CAPE4</i>	2.418736594	0.0027987
AT4G36110	<i>SAUR9</i>	2.381972057	0.0120666
AT1G48300	<i>DGAT3</i>	2.228828675	7.513E-09
AT3G49120	<i>PCB</i>	2.224545978	0.0290158
AT1G18570	<i>MYB51</i>	2.208643416	0.0278469
AT2G32020	#NV	2.204822528	0.0005093
AT2G47460	<i>MYB12</i>	2.200301663	4.221E-07
AT5G09220	<i>AAP2</i>	2.168143476	0.0091595
AT2G16740	<i>UBC29</i>	2.118480546	0.0303037
AT1G33700	#NV	2.053474547	0.001291
AT5G40690	#NV	2.012562765	0.0248075
AT3G50930	<i>BCS1</i>	2.003371057	0.0010783
AT1G32870	<i>ANAC013</i>	1.97001228	0.0022741
AT3G56360	#NV	1.956518133	0.001802
AT4G16370	<i>OPT3</i>	1.946910151	0.0173376

AT5G65140	<i>TPPJ</i>	1.900516917	0.0265579
AT2G30250	<i>WRKY25</i>	1.673133289	0.0427372
AT3G57520	<i>SIP2</i>	-1.512581283	0.0187685
AT2G30860	<i>GSTF7</i>	-1.630563906	0.0149252
AT2G39570	<i>ACR9</i>	-1.679368443	0.0127892
AT5G61440	<i>ACHT5</i>	-1.791749283	0.0007898
AT2G40300	<i>FER4</i>	-1.793027162	0.000687
AT4G32480	#NV	-1.959486459	0.0465442
AT1G72820	#NV	-2.026221875	0.0003013
AT5G24490	#NV	-2.04910573	0.0418481
AT4G27450	#NV	-2.057065048	0.0061972
AT5G28770	<i>bZIP63</i>	-2.156054945	0.0021876
AT2G19800	<i>MIOX2</i>	-2.238213887	0.0153877
AT5G65207	#NV	-2.301451437	0.007379
AT1G80920	<i>J8</i>	-2.307884488	2.69E-07
AT5G46890	#NV	-2.398680496	0.0005093
AT2G20670	#NV	-2.492296225	6.235E-07
AT3G61060	<i>PP2-A13</i>	-2.577071791	0.0004602
AT3G51910	<i>HSFA7A</i>	-2.661048608	0.0005731
AT4G37610	<i>BT5</i>	-2.661453131	7.758E-09
AT5G22920	<i>RZPF34</i>	-2.689546964	1.032E-06
AT5G18670	<i>BAM9</i>	-2.907729838	5.997E-10
AT3G15630	#NV	-2.914250819	3.226E-08
AT5G21940	#NV	-2.935208283	3.995E-08
AT1G26540	#NV	-3.033770399	0.0360409
AT1G28330	<i>DRM1</i>	-3.054189844	1.583E-06
AT5G20250	<i>DIN10</i>	-3.196309953	1.46E-10
AT3G49160	#NV	-3.227626033	4.349E-09
AT5G01600	<i>FER1</i>	-3.263842436	2.995E-34
AT2G25900	<i>CTH</i>	-3.435182431	2.484E-07
AT2G34180	<i>WL2</i>	-3.446411273	0.0001611
AT3G15450	#NV	-4.402222958	2.401E-08
AT3G47340	<i>ASNI</i>	-4.577881825	0.0001275
AT3G22235	<i>CYSTM8</i>	-6.294468773	0.0157555

Table 9: log2 fold changes of all significant DEG in RT at all timepoints in RR and RT according to Figure 9 B. log2 fold changes were calculated analogous to the main analysis in the results part, without a log2 fold change threshold in differential expression analysis (see Methods, 5.1.9).

AGI	Symbol	log2FC24RT	log2FC48RT	log2FC24RR	log2FC48RR
AT1G01453	<i>NA</i>	1.12	2.83	NA	1.02
AT1G02920	<i>ATGST11</i>	3.07	1.57	1.27	NA
AT1G03660	<i>NA</i>	1.89	3.74	NA	NA

AT1G09932	NA	1.54	3.27	NA	1.13
AT1G11920	NA	1.93	3.94	NA	2.07
AT1G12200	FMO	2.67	2.88	NA	NA
AT1G13420	ATST4B	-2.47	-2.04	NA	-1
AT1G18570	AtMYB51	2.19	2.21	NA	NA
AT1G21120	IGMT2	3.1	3.33	NA	NA
AT1G26540	NA	-1.97	-3.03	NA	-1.42
AT1G29860	ATWRKY71	3.75	5.89	NA	1.4
AT1G30760	AtBBE-like	1.21	2.6	NA	NA
AT1G32870	ANAC013	1.29	1.97	NA	0.71
AT1G33700	NA	1.09	2.05	NA	NA
AT1G33890	IAN3	2.87	5.84	NA	2.11
AT1G34540	CYP94D1	2.12	4.08	NA	NA
AT1G48300	DGAT3	2.42	2.23	0.62	NA
AT1G54970	ATPRP1	1.46	2.71	1.32	1.9
AT1G59730	ATH7	1.66	3.46	1	1.21
AT1G59850	NA	2.41	4.02	NA	1.19
AT1G72820	NA	-1.58	-2.03	-0.77	-0.84
AT1G74650	ATMYB31	2.55	5.09	NA	NA
AT1G76930	ATEXT1	2.06	2.81	NA	NA
AT1G77380	AAP3	1.83	3.52	NA	NA
AT2G02100	LCR69	1.7	2.46	NA	NA
AT2G05520	ATGRP-3	1.99	4.2	NA	NA
AT2G16740	UBC29	1.13	2.12	NA	NA
AT2G18690	NA	1.7	2.48	NA	NA
AT2G19800	MIOX2	-2.47	-2.24	-1.66	-2.08
AT2G20520	FLA6	2.42	4.09	1.96	1.79
AT2G20670	NA	-2.75	-2.49	-1.06	-1.63
AT2G25900	ATCTH	-3.31	-3.44	-2.39	-2.29
AT2G28690	NA	2.43	4.41	NA	NA
AT2G30250	ATWRKY25	1.18	1.67	NA	NA
AT2G30860	ATGSTF7	-0.98	-1.63	NA	-0.69
AT2G31860	NA	1.93	2.62	NA	0.95
AT2G32020	NA	1.12	2.2	NA	1.13
AT2G34180	ATWL2	-3.49	-3.45	-2.54	-1.71
AT2G38823	NA	2.78	4.56	NA	1.47
AT2G39570	ACR9	-1.55	-1.68	-0.8	-1.33
AT2G39980	NA	1.88	2.69	1.25	1.75
AT2G41730	HRG1	2.15	3.33	NA	1.04
AT2G47010	NA	1.42	2.71	0.87	NA
AT2G47460	ATMYB12	1.93	2.2	1.33	0.97
AT2G47520	AtERF71	2.52	3.01	NA	2.24
AT3G22235	AthCYSTM8	-2.49	-6.29	NA	NA
AT3G22800	NA	1.25	3.04	NA	NA
AT3G46340	NA	2.15	5.79	NA	NA

AT3G47340	<i>ASN1</i>	-5.44	-4.58	NA	NA
AT3G48520	<i>CYP94B3</i>	2.79	2.97	NA	NA
AT3G49120	<i>ATPCB</i>	1.29	2.22	NA	-1.13
AT3G50930	<i>AtBCS1</i>	1.16	2	NA	0.93
AT3G51910	<i>AT-HSFA7A</i>	-3.35	-2.66	-1.39	-1.6
AT3G55090	<i>ABCG16</i>	3.54	3.87	2.33	2.49
AT3G56290	<i>NA</i>	2.42	2.46	1.78	1.86
AT3G56360	<i>NA</i>	1.42	1.96	0.85	0.59
AT3G57520	<i>AtSIP2</i>	-1.41	-1.51	-1.16	-1.38
AT4G00130	<i>NA</i>	3.03	6.25	2.26	4.2
AT4G12735	<i>NA</i>	4.41	4.58	1.82	2.38
AT4G13420	<i>ATHAK5</i>	4.27	4.23	1.51	NA
AT4G19680	<i>ATIRT2</i>	1.23	2.54	1.47	1.66
AT4G20240	<i>CYP71A27</i>	1.32	2.99	NA	NA
AT4G25100	<i>ATFSD1</i>	5.08	7.5	NA	NA
AT4G25220	<i>AtG3Pp2</i>	1.99	2.66	NA	1.51
AT4G25790	<i>AtCAPE4</i>	1.53	2.42	NA	1.19
AT4G27450	<i>HUP54</i>	-0.92	-2.06	-0.98	-1.25
AT4G30110	<i>ATHMA2</i>	2.07	3.19	NA	1.45
AT4G32480	<i>NA</i>	-1.99	-1.96	-2.06	-1.81
AT4G33666	<i>NA</i>	1.39	3.04	NA	NA
AT4G36110	<i>SAUR9</i>	1.17	2.38	NA	1.64
AT4G37030	<i>NA</i>	1.49	2.53	NA	NA
AT4G37370	<i>CYP81D8</i>	1.97	2.54	NA	NA
AT4G37610	<i>BT5</i>	-2.57	-2.66	-1.56	-1.7
AT5G03640	<i>AGC1-8</i>	1.62	2.61	NA	0.87
AT5G09220	<i>AAP2</i>	0.97	2.17	NA	NA
AT5G11060	<i>KNAT4</i>	2.33	3.96	NA	NA
AT5G18670	<i>BAM9</i>	-2.57	-2.91	NA	-1.07
AT5G21120	<i>EIL2</i>	1.91	4	NA	1.88
AT5G21940	<i>NA</i>	-2.99	-2.94	-2.02	-1.77
AT5G24380	<i>ATYSL2</i>	2.26	1.45	1.36	1.08
AT5G24640	<i>HRG2</i>	2.81	4.06	1.53	2.26
AT5G25190	<i>ESE3</i>	1.63	2.59	NA	NA
AT5G28770	<i>AtbZIP63</i>	-2.45	-2.16	-1.28	-1.69
AT5G39580	<i>PRX62</i>	2.33	2.99	NA	NA
AT5G40690	<i>NA</i>	1.38	2.01	NA	NA
AT5G43450	<i>NA</i>	4.33	5.81	1.27	1.81
AT5G46890	<i>NA</i>	-2.09	-2.4	-1.2	-1.04
AT5G48070	<i>ATXTH20</i>	2.17	3.79	NA	NA
AT5G49770	<i>NA</i>	1.26	3.41	NA	NA
AT5G56080	<i>ATNAS2</i>	1.51	2.72	NA	NA
AT5G57530	<i>AtXTH12</i>	1.35	2.48	NA	1.38
AT5G57540	<i>AtXTH13</i>	1.65	2.82	1.32	1.62
AT5G59520	<i>AtZIP2</i>	2.91	2.57	1.08	1.05

AT5G61440	<i>ACHT5</i>	-1.85	-1.79	-1.23	-1.63
AT5G62480	<i>ATGSTU9</i>	1.89	3.12	NA	NA
AT5G65140	<i>TPPJ</i>	1.98	1.9	NA	NA
AT1G10875	<i>NA</i>	NA	7.05	NA	4.07
AT2G30660	<i>NA</i>	NA	3.48	NA	1.73

Table 10: Comparison of Cd-DEG with Zn-DEG in RR.

RR					
Only Cd		Only Zn		Shared	
AGI	Symbol	AGI	Symbol	AGI	Symbol
AT1G02640	<i>ATBXL2</i>	AT3G22060	<i>NA</i>	AT1G07367	<i>NA</i>
AT1G13260	<i>AtRAV1</i>	AT1G05300	<i>ZIP5</i>	AT1G09505	<i>NA</i>
AT1G23730	<i>ATBCA3</i>	AT2G32270	<i>ZIP3</i>	AT1G21140	<i>AtVTL1</i>
AT1G28330	<i>AtDRM1</i>	AT1G01580	<i>ATFRO2</i>	AT1G23020	<i>ATFRO3</i>
AT1G30820	<i>CTPS1</i>	AT4G19690	<i>ATIRT1</i>	AT1G47395	<i>FEP2</i>
AT1G70290	<i>ATTPS8</i>	AT1G78230	<i>NA</i>	AT1G47400	<i>FEP3</i>
AT1G73120	<i>NA</i>	AT1G60960	<i>ATIRT3</i>	AT1G56430	<i>ATNAS4</i>
AT1G76590	<i>PLATZ2</i>	AT1G52120	<i>NA</i>	AT1G76800	<i>AtVTL2</i>
AT1G80380	<i>GLYK</i>	AT1G56160	<i>ATMYB72</i>	AT2G14247	<i>NA</i>
AT1G80440	<i>KFB20</i>	AT5G02780	<i>GSTL1</i>	AT2G30766	<i>FEP1</i>
AT2G15890	<i>CBP1</i>	AT5G38820	<i>AtAvt6B</i>	AT3G25190	<i>AtVTL5</i>
AT2G16890	<i>NA</i>	AT3G12820	<i>AtMYB10</i>	AT3G46900	<i>COPT2</i>
AT2G18700	<i>ATTPS11</i>	AT2G41240	<i>BHLH100</i>	AT3G56970	<i>BHLH038</i>
AT2G32487	<i>NA</i>	AT3G61930	<i>NA</i>	AT3G56980	<i>BHLH039</i>
AT2G44460	<i>BGLU28</i>	AT3G58810	<i>ATMTP3</i>	AT4G11393	<i>DEFL202</i>
AT3G08860	<i>PYD4</i>	AT3G57157	<i>NA</i>	AT4G16370	<i>ATOPT3</i>
AT3G15450	<i>NA</i>	AT3G56090	<i>ATFER3</i>	AT4G31940	<i>CYP82C4</i>
AT3G15630	<i>NA</i>	AT3G58060	<i>MTP8</i>	AT5G01600	<i>ATFER1</i>
AT3G22840	<i>ELIP</i>	AT1G74770	<i>BTSL1</i>	AT5G05250	<i>NA</i>
AT3G48360	<i>ATBT2</i>	AT4G13420	<i>ATHAK5</i>	AT5G23990	<i>ATFRO5</i>
AT3G49570	<i>LSU3</i>	AT3G22910	<i>ACA13</i>	AT5G45070	<i>AtPP2-A8</i>
AT3G49580	<i>LSU1</i>	AT3G07720	<i>NA</i>	AT5G53450	<i>FBN11</i>
AT3G60140	<i>BGLU30</i>	AT5G03570	<i>ATIREG2</i>	AT5G67370	<i>CGLD27</i>
AT4G08620	<i>SULTRI;1</i>	AT5G04150	<i>BHLH101</i>	AT2G40300	<i>ATFER4</i>
AT4G14690	<i>ELIP2</i>	AT1G09560	<i>GLP5</i>	AT3G12900	<i>S8H</i>
AT4G32950	<i>NA</i>	AT4G19370	<i>MWL-2</i>	AT3G49160	<i>NA</i>
AT5G10180	<i>AST68</i>	AT4G19680	<i>ATIRT2</i>	AT3G59930	<i>NA</i>
AT5G14120	<i>NA</i>	AT3G22550	<i>FLZ8</i>	AT5G23980	<i>ATFRO4</i>
AT5G15950	<i>SAMDC2</i>	AT1G32380	<i>PRS2</i>		
AT5G19120	<i>NA</i>	AT3G50740	<i>UGT72E1</i>		
AT5G20250	<i>DIN10</i>	AT4G09110	<i>ATL35</i>		
AT5G22920	<i>AtRZPF34</i>	AT1G34760	<i>GF14</i>		
AT5G24660	<i>LSU2</i>	AT1G14550	<i>NA</i>		

AT5G26220	<i>AtGGCT2;1</i>	AT4G30120	<i>ATHMA3</i>		
AT5G39100	<i>GLP6</i>	AT4G33880	<i>RSL2</i>		
AT5G48850	<i>ATSDII</i>	AT3G47480	<i>CML47</i>		
AT5G56550	<i>ATOXS3</i>	AT1G30560	<i>AtG3Pp3</i>		
AT5G63160	<i>BT1</i>	AT1G14185	<i>NA</i>		
AT5G65207	<i>NA</i>	AT3G06890	<i>NA</i>		
AT1G08100	<i>ACH2</i>	AT1G52130	<i>NA</i>		
AT1G12030	<i>NA</i>	AT1G58290	<i>AtHEMA1</i>		
AT1G33055	<i>HUP32</i>	AT1G09932	<i>NA</i>		
AT1G34510	<i>NA</i>	AT2G05520	<i>ATGRP-3</i>		
AT1G53130	<i>GRI</i>	AT1G21250	<i>AtWAK1</i>		
AT1G80920	<i>AtJ8</i>	AT5G45080	<i>AtPP2-A6</i>		
AT2G00920	<i>NA</i>	AT1G49570	<i>NA</i>		
AT2G02710	<i>PLP</i>	AT3G50770	<i>CML41</i>		
AT2G04050	<i>NA</i>	AT1G53635	<i>NA</i>		
AT2G20800	<i>NDB4</i>	AT5G52720	<i>NA</i>		
AT2G28470	<i>BGAL8</i>	AT2G18800	<i>ATXTH21</i>		
AT2G33830	<i>AtDRM2</i>	AT2G16060	<i>AHB1</i>		
AT3G01175	<i>NA</i>	AT4G17680	<i>EBS1</i>		
AT3G09220	<i>LAC7</i>	AT4G33790	<i>CER4</i>		
AT3G10020	<i>HUP26</i>	AT1G19250	<i>FMO1</i>		
AT3G21670	<i>AtNPF6.4</i>	AT5G04730	<i>NA</i>		
AT3G26740	<i>CCL</i>	AT1G58320	<i>NA</i>		
AT3G49790	<i>NA</i>	AT3G47640	<i>PYE</i>		
AT3G50610	<i>CEP9</i>	AT1G06120	<i>ADSL.4</i>		
AT3G52840	<i>BGAL2</i>	AT5G24210	<i>PRLIP1</i>		
AT3G54530	<i>NA</i>	AT5G45105	<i>ZIP8</i>		
AT3G61060	<i>AtPP2-A13</i>				
AT4G00910	<i>NA</i>				
AT4G08290	<i>UMAMIT20</i>				
AT4G21680	<i>AtNPF7.2</i>				
AT4G25010	<i>AtSWEET14</i>				
AT4G26288	<i>NA</i>				
AT4G28790	<i>NA</i>				
AT4G28850	<i>ATXTH26</i>				
AT4G36670	<i>AtPLT6</i>				
AT4G38470	<i>STY46</i>				
AT5G10230	<i>ANN7</i>				
AT5G13320	<i>AtGH3.12</i>				
AT5G23010	<i>GSM1</i>				
AT5G24490	<i>NA</i>				
AT5G39120	<i>NA</i>				
AT5G44130	<i>FLA13</i>				
AT5G61590	<i>DEWAX</i>				

Table 11: Comparison of Cd-DEG with Zn-DEG in RT.

RT					
Only Cd		Only Zn		Shared	
AGI	Symbol	AGI	Symbol	AGI	Symbol
AT1G13420	<i>ATST4B</i>	AT1G60960	<i>ATIRT3</i>	AT1G02920	<i>ATGST11</i>
AT1G28330	<i>AtDRM1</i>	AT3G56090	<i>ATFER3</i>	AT1G12200	<i>FMO</i>
AT1G80920	<i>AtJ8</i>	AT4G31500	<i>ATR4</i>	AT1G18570	<i>AtMYB51</i>
AT2G04050	<i>NA</i>	AT5G61650	<i>CYCP4</i>	AT1G21120	<i>IGMT2</i>
AT2G19800	<i>MIOX2</i>	AT4G23700	<i>ATCHX17</i>	AT1G48300	<i>DGAT3</i>
AT2G20800	<i>NDB4</i>	AT5G47450	<i>ATTIP2;3</i>	AT2G20670	<i>NA</i>
AT2G25900	<i>ATCTH</i>	AT2G41100	<i>ATCAL4</i>	AT2G34180	<i>ATWL2</i>
AT2G38823	<i>NA</i>	AT5G23660	<i>AtSWEET12</i>	AT2G40300	<i>ATFER4</i>
AT2G44460	<i>BGLU28</i>	AT1G64160	<i>AtDIR5</i>	AT3G15450	<i>NA</i>
AT2G47460	<i>ATMYB12</i>	AT1G27020	<i>NA</i>	AT3G55090	<i>ABCG16</i>
AT2G47520	<i>AtERF71</i>	AT4G08290	<i>UMAMIT20</i>	AT3G61060	<i>AtPP2-A13</i>
AT3G15630	<i>NA</i>	AT1G20160	<i>ATSBT5.2</i>	AT4G28850	<i>ATXTH26</i>
AT3G22840	<i>ELIP</i>	AT2G22330	<i>CYP79B3</i>	AT5G01600	<i>ATFER1</i>
AT3G47340	<i>ASN1</i>	AT1G18590	<i>ATSOT17</i>	AT5G18670	<i>BAM9</i>
AT3G51910	<i>AT-HSFA7A</i>	AT3G56980	<i>BHLH039</i>	AT5G43450	<i>NA</i>
AT3G54530	<i>NA</i>	AT2G37750	<i>NA</i>	AT5G59520	<i>AtZIP2</i>
AT4G12735	<i>NA</i>	AT4G33050	<i>AtIQM1</i>	AT5G65140	<i>TPPJ</i>
AT4G13420	<i>ATHAK5</i>	AT3G26830	<i>CYP71B15</i>	AT1G01453	<i>NA</i>
AT4G14690	<i>ELIP2</i>	AT5G59780	<i>ATMYB59</i>	AT1G09932	<i>NA</i>
AT4G25100	<i>ATFSD1</i>	AT3G53980	<i>NA</i>	AT1G11920	<i>NA</i>
AT4G37610	<i>BT5</i>	AT3G48740	<i>AtSWEET11</i>	AT1G29860	<i>ATWRKY71</i>
AT5G10180	<i>AST68</i>	AT5G08240	<i>NA</i>	AT1G30760	<i>AtBBE-like</i>
AT5G20250	<i>DIN10</i>	AT3G28580	<i>NA</i>	AT1G33700	<i>NA</i>
AT5G21940	<i>NA</i>	AT2G20142	<i>NA</i>	AT1G33890	<i>IAN3</i>
AT5G22920	<i>AtRZPF34</i>	AT4G26260	<i>MIOX4</i>	AT1G34510	<i>NA</i>
AT5G24380	<i>ATYSL2</i>	AT5G06090	<i>ATGPAT7</i>	AT1G34540	<i>CYP94D1</i>
AT5G24640	<i>HRG2</i>	AT4G08780	<i>NA</i>	AT1G54970	<i>ATPRP1</i>
AT5G28770	<i>AtbZIP63</i>	AT5G57220	<i>CYP81F2</i>	AT1G59850	<i>NA</i>
AT5G48850	<i>ATSD11</i>	AT4G36610	<i>NA</i>	AT1G76930	<i>ATEXT1</i>
AT5G56550	<i>ATOXS3</i>	AT2G45220	<i>AtPME17</i>	AT1G77380	<i>AAP3</i>
AT5G61440	<i>ACHT5</i>	AT4G39950	<i>CYP79B2</i>	AT2G02100	<i>LCR69</i>
AT1G03660	<i>NA</i>	AT3G09220	<i>LAC7</i>	AT2G05520	<i>ATGRP-3</i>
AT1G10875	<i>NA</i>	AT5G64110	<i>NA</i>	AT2G16740	<i>UBC29</i>
AT1G26540	<i>NA</i>	AT1G47395	<i>FEP2</i>	AT2G18690	<i>NA</i>
AT1G32870	<i>ANAC013</i>	AT4G17340	<i>DELTA-TIP2</i>	AT2G20520	<i>FLA6</i>
AT1G53130	<i>GRI</i>	AT5G13580	<i>ABCG6</i>	AT2G39980	<i>NA</i>
AT1G59730	<i>ATH7</i>	AT3G04220	<i>NA</i>	AT2G47010	<i>NA</i>
AT1G72820	<i>NA</i>	AT3G11430	<i>ATGPAT5</i>	AT3G22800	<i>NA</i>

AT1G74650	<i>ATMYB31</i>	AT1G73260	<i>ATKTI1</i>	AT3G46340	<i>NA</i>
AT2G28690	<i>NA</i>	AT5G40170	<i>AtRLP54</i>	AT3G49120	<i>ATPCB</i>
AT2G30250	<i>ATWRKY25</i>	AT3G23250	<i>ATMYB15</i>	AT3G49160	<i>NA</i>
AT2G30660	<i>NA</i>	AT4G39940	<i>AKN2</i>	AT3G50930	<i>AtBCS1</i>
AT2G30860	<i>ATGSTF7</i>	AT5G23020	<i>IMS2</i>	AT3G56360	<i>NA</i>
AT2G31860	<i>NA</i>	AT1G69920	<i>ATGSTU12</i>	AT4G00130	<i>NA</i>
AT2G32020	<i>NA</i>	AT1G78230	<i>NA</i>	AT4G08620	<i>SULTR1;1</i>
AT2G39570	<i>ACR9</i>	AT4G22690	<i>CYP706A1</i>	AT4G16370	<i>ATOPT3</i>
AT2G41730	<i>HRG1</i>	AT4G36430	<i>NA</i>	AT4G19680	<i>ATIRT2</i>
AT3G22235	<i>AthCYSTM8</i>	AT3G29000	<i>NA</i>	AT4G25220	<i>AtG3Pp2</i>
AT3G48520	<i>CYP94B3</i>	AT2G23810	<i>TET8</i>	AT4G25790	<i>AtCAPE4</i>
AT3G56290	<i>NA</i>	AT4G25810	<i>XTH23</i>	AT4G37030	<i>NA</i>
AT3G57520	<i>AtSIP2</i>	AT5G57625	<i>AtCAPE5</i>	AT5G03640	<i>AGC1-8</i>
AT4G20240	<i>CYP71A27</i>	AT2G30750	<i>CYP71A12</i>	AT5G05250	<i>NA</i>
AT4G27450	<i>HUP54</i>	AT3G26470	<i>NA</i>	AT5G09220	<i>AAP2</i>
AT4G30110	<i>ATHMA2</i>	AT1G72900	<i>TN7</i>	AT5G21120	<i>EIL2</i>
AT4G32480	<i>NA</i>	AT5G19240	<i>NA</i>	AT5G39580	<i>PRX62</i>
AT4G33666	<i>NA</i>	AT2G28570	<i>NA</i>	AT5G48070	<i>ATXTH20</i>
AT4G36110	<i>SAUR9</i>	AT4G02380	<i>AtLEA5</i>	AT5G57530	<i>AtXTH12</i>
AT4G37370	<i>CYP81D8</i>	AT1G07135	<i>NA</i>	AT5G57540	<i>AtXTH13</i>
AT5G11060	<i>KNAT4</i>	AT3G15356	<i>NA</i>		
AT5G24490	<i>NA</i>	AT2G46600	<i>NA</i>		
AT5G25190	<i>ESE3</i>	AT2G38860	<i>DJ-1e</i>		
AT5G26220	<i>AtGGCT2;1</i>	AT5G25250	<i>FLOT1</i>		
AT5G40690	<i>NA</i>	AT3G17690	<i>ATCNGC19</i>		
AT5G46890	<i>NA</i>	AT1G19020	<i>HUP35</i>		
AT5G49770	<i>NA</i>	AT1G21130	<i>IGMT4</i>		
AT5G56080	<i>ATNAS2</i>	AT1G74360	<i>GRACE</i>		
AT5G62480	<i>ATGSTU9</i>	AT1G67148	<i>NA</i>		
AT5G65207	<i>NA</i>	AT3G23430	<i>ATPHO1</i>		

Table 12: 150 brake-wear responsive DEG (referring to Figure 28, C)

ID	AGI	Symbol	log2 fold change	padj
AT1G02610/NP_001321865.1	AT1G02610	<i>NA</i>	2.667513823	0.002615
AT1G02610/NP_001321866.1	AT1G02610	<i>NA</i>	2.858507487	0.004598
AT1G02610/NP_171761.2	AT1G02610	<i>NA</i>	2.696367308	0.001662
AT1G07135/NP_172193.2	AT1G07135	<i>NA</i>	1.901842089	0.028828
AT1G10585/NP_001320606.1	AT1G10585	<i>NA</i>	2.801729361	0.031697
AT1G10585/NP_563873.2	AT1G10585	<i>NA</i>	2.795561747	0.002591
AT1G14780/NP_172931.1	AT1G14780	<i>NA</i>	2.837399153	4.51E-06
AT1G14870/NP_001320690.1	AT1G14870	<i>AtPCR2</i>	2.236584593	0.003544
AT1G14870/NP_172940.1	AT1G14870	<i>AtPCR2</i>	2.216352262	0.004944
AT1G15010/NP_563962.1	AT1G15010	<i>NA</i>	3.635247484	1.70E-09
AT1G17020/NP_173145.1	AT1G17020	<i>ATSRG1</i>	2.678491165	0.000156

AT1G19610/NP_173391.2	AT1G19610	<i>LCR78</i>	3.34557878	4.96E-15
AT1G28480/NP_174170.1	AT1G28480	<i>GRX480</i>	2.502541684	0.003446
AT1G29090/NP_564321.2	AT1G29090	<i>NA</i>	5.961644264	0.004293
AT1G44350/NP_175086.1	AT1G44350	<i>ILL6</i>	1.709413222	0.011187
AT1G52000/NP_001320196.1	AT1G52000	<i>NA</i>	1.782289864	0.004746
AT1G52000/NP_175612.1	AT1G52000	<i>NA</i>	1.782289864	0.004746
AT1G52030/NP_001321720.1	AT1G52030	<i>F-ATMBP</i>	1.680284669	0.046198
AT1G52400/NP_001031175.1	AT1G52400	<i>ATBG1</i>	1.749935156	0.002486
AT1G52400/NP_001185204.1	AT1G52400	<i>ATBG1</i>	1.749498075	0.002149
AT1G52400/NP_175649.1	AT1G52400	<i>ATBG1</i>	1.749498075	0.002149
AT1G53830/NP_175786.1	AT1G53830	<i>ATPME2</i>	3.42793053	1.17E-06
AT1G54575/NP_001323261.1	AT1G54575	<i>NA</i>	2.244575964	0.005421
AT1G54575/NP_974028.1	AT1G54575	<i>NA</i>	2.244575964	0.005421
AT1G60730/NP_001185274.1	AT1G60730	<i>NA</i>	1.641172778	0.004598
AT1G60730/NP_564762.2	AT1G60730	<i>NA</i>	1.632046519	0.005978
AT1G61255/NP_683457.1	AT1G61255	<i>NA</i>	2.444110243	0.047886
AT1G66570/NP_176830.1	AT1G66570	<i>ATSUC7</i>	4.593010466	0.021144
AT1G68290/NP_176996.1	AT1G68290	<i>AtBFN2</i>	2.405776629	6.17E-09
AT1G69880/NP_177146.1	AT1G69880	<i>ATH8</i>	5.01674952	3.05E-15
AT1G73260/NP_565061.1	AT1G73260	<i>ATKTI1</i>	2.607827329	0.035404
AT1G74010/NP_177541.1	AT1G74010	<i>NA</i>	2.778385614	2.87E-08
AT1G76930/NP_565143.1	AT1G76930	<i>ATEXT1</i>	2.558117625	1.44E-09
AT1G76930/NP_849895.1	AT1G76930	<i>ATEXT1</i>	2.60772421	5.87E-10
AT2G02990/NP_178399.1	AT2G02990	<i>ATRNS1</i>	4.081707037	1.80E-07
AT2G15780/NP_565380.1	AT2G15780	<i>NA</i>	3.45427561	0.001638
AT2G17740/NP_179365.1	AT2G17740	<i>VLG</i>	2.276424353	0.000933
AT2G22880/NP_179873.1	AT2G22880	<i>VQ12</i>	3.020372547	0.036401
AT2G26020/NP_180172.1	AT2G26020	<i>PDF1.2b</i>	6.190433077	0.000119
AT2G28120/NP_180379.1	AT2G28120	<i>OTU1</i>	2.296458821	6.73E-05
AT2G29480/NP_180509.1	AT2G29480	<i>ATGSTU2</i>	6.498289207	0.013632
AT2G32200/NP_001323680.1	AT2G32200	<i>AthCYSTM5</i>	2.668702777	0.049411
AT2G32200/NP_180779.2	AT2G32200	<i>AthCYSTM5</i>	2.668702777	0.049411
AT2G37130/NP_181250.1	AT2G37130	<i>NA</i>	2.235273728	0.041905
AT2G38240/NP_181359.1	AT2G38240	<i>JAO4</i>	4.413751901	0.003926
AT2G38530/NP_181387.1	AT2G38530	<i>AtLtpI-5</i>	2.41894324	0.003832
AT2G39030/NP_565898.1	AT2G39030	<i>NATA1</i>	4.259643238	1.49E-09
AT2G39518/NP_001078023.1	AT2G39518	<i>CASPL4D2</i>	2.634534285	5.51E-05
AT2G41260/NP_181659.2	AT2G41260	<i>ATM17</i>	3.467663834	0.022933
AT2G41260/NP_973656.1	AT2G41260	<i>ATM17</i>	3.467663834	0.022933
AT2G41810/NP_181712.1	AT2G41810	<i>NA</i>	2.866187168	0.003978
AT2G43510/NP_181879.1	AT2G43510	<i>ATTII</i>	3.819287576	2.27E-15
AT2G45220/NP_566038.1	AT2G45220	<i>AtPME17</i>	2.378010483	1.53E-09
AT2G47550/NP_566103.1	AT2G47550	<i>NA</i>	3.71413245	4.12E-06
AT3G04070/NP_001118568.1	AT3G04070	<i>ANAC047</i>	2.516567731	0.000131
AT3G04070/NP_187057.2	AT3G04070	<i>ANAC047</i>	2.56920179	4.59E-05

AT3G11480/NP_187755.2	AT3G11480	<i>ATBSMT1</i>	7.850618947	0.022749
AT3G13790/NP_001189881.1	AT3G13790	<i>ATBFRUCT1</i>	2.227861723	9.70E-06
AT3G13790/NP_001327313.1	AT3G13790	<i>ATBFRUCT1</i>	2.140631694	0.000262
AT3G13790/NP_001327314.1	AT3G13790	<i>ATBFRUCT1</i>	2.140631694	0.000262
AT3G13790/NP_001327315.1	AT3G13790	<i>ATBFRUCT1</i>	2.140631694	0.000262
AT3G13790/NP_566464.1	AT3G13790	<i>ATBFRUCT1</i>	2.226929204	2.17E-05
AT3G14990/NP_001030698.1	AT3G14990	<i>AtDJ1A</i>	1.741912113	0.000457
AT3G14990/NP_188117.1	AT3G14990	<i>AtDJ1A</i>	1.743575745	0.000212
AT3G14990/NP_850588.1	AT3G14990	<i>AtDJ1A</i>	1.741912113	0.000457
AT3G15720/NP_001078162.1	AT3G15720	<i>NA</i>	1.983098532	0.027002
AT3G15720/NP_001327674.1	AT3G15720	<i>NA</i>	2.016374073	0.022121
AT3G15720/NP_001327675.1	AT3G15720	<i>NA</i>	1.983098532	0.027002
AT3G15720/NP_566524.1	AT3G15720	<i>NA</i>	1.972628199	0.030793
AT3G22600/NP_566712.1	AT3G22600	<i>LTPG5</i>	1.92382752	0.035807
AT3G22620/NP_566713.1	AT3G22620	<i>LTPG20</i>	2.237189026	0.000237
AT3G28210/NP_001327074.1	AT3G28210	<i>PMZ</i>	2.594128649	0.039202
AT3G28210/NP_189461.1	AT3G28210	<i>PMZ</i>	2.594128649	0.039202
AT3G28220/NP_189462.1	AT3G28220	<i>NA</i>	1.522327337	0.006229
AT3G45060/NP_190092.1	AT3G45060	<i>ATNRT2.6</i>	2.844897252	7.87E-06
AT3G46280/NP_190213.2	AT3G46280	<i>NA</i>	2.314386017	0.000738
AT3G48520/NP_190421.1	AT3G48520	<i>CYP94B3</i>	5.47864211	9.38E-06
AT3G49620/NP_190531.2	AT3G49620	<i>DIN11</i>	3.099699899	6.23E-19
AT3G55970/NP_001325581.1	AT3G55970	<i>ATJRG21</i>	3.650239036	0.000802
AT3G55970/NP_191156.1	AT3G55970	<i>ATJRG21</i>	3.701272072	0.000175
AT3G59930/NP_191552.2	AT3G59930	<i>NA</i>	2.688195927	2.62E-14
AT4G05100/NP_192419.1	AT4G05100	<i>AtMYB74</i>	2.641588041	0.008712
AT4G12470/NP_192984.1	AT4G12470	<i>AZII</i>	2.719068303	1.95E-06
AT4G12480/NP_192985.1	AT4G12480	<i>EARLII</i>	3.523897184	0.000136
AT4G12490/NP_192986.1	AT4G12490	<i>AZI3</i>	3.279360581	0.00039
AT4G12495/NP_001328954.1	AT4G12495	<i>NA</i>	3.385012437	4.46E-05
AT4G12500/NP_192987.1	AT4G12500	<i>NA</i>	3.378576098	9.30E-16
AT4G15610/NP_001329530.1	AT4G15610	<i>CASPL1D1</i>	2.447592214	1.90E-06
AT4G15610/NP_567472.1	AT4G15610	<i>CASPL1D1</i>	2.531685816	1.78E-08
AT4G16240/NP_193359.1	AT4G16240	<i>NA</i>	3.130913066	3.88E-07
AT4G18170/NP_193551.1	AT4G18170	<i>ATWRKY28</i>	2.374676155	0.000462
AT4G22467/NP_001329811.1	AT4G22467	<i>NA</i>	4.783753472	2.15E-08
AT4G22470/NP_193978.2	AT4G22470	<i>AtDHγPRP1</i>	4.692947438	9.77E-10
AT4G23210/NP_001078435.1	AT4G23210	<i>CRK13</i>	3.366999079	0.000142
AT4G23210/NP_001329247.1	AT4G23210	<i>CRK13</i>	3.131462036	1.70E-05
AT4G23210/NP_001329248.1	AT4G23210	<i>CRK13</i>	3.075063403	6.83E-05
AT4G23210/NP_194052.2	AT4G23210	<i>CRK13</i>	3.22171384	8.45E-07
AT4G23210/NP_849427.1	AT4G23210	<i>CRK13</i>	3.075063403	6.83E-05
AT4G24000/NP_001328486.1	AT4G24000	<i>ATCSLG2</i>	4.566145243	0.000749
AT4G31800/NP_001320110.1	AT4G31800	<i>ATWRKY18</i>	2.415928422	7.85E-07
AT4G31800/NP_001329847.1	AT4G31800	<i>ATWRKY18</i>	2.247780656	0.00015

AT4G31800/NP_567882.1	AT4G31800	<i>ATWRKY18</i>	2.310551497	1.68E-05
AT4G33465/NP_001328489.1	AT4G33465	<i>SCRL22</i>	2.66717532	0.00197
AT4G36670/NP_195385.1	AT4G36670	<i>AtPLT6</i>	2.166706474	9.00E-08
AT4G37520/NP_001190944.1	AT4G37520	<i>NA</i>	1.74248489	0.00058
AT4G37520/NP_195468.1	AT4G37520	<i>NA</i>	1.74248489	0.00058
AT4G37990/NP_195512.1	AT4G37990	<i>ATCAD8</i>	3.835258931	1.44E-07
AT5G01380/NP_195758.1	AT5G01380	<i>NA</i>	3.581785787	0.03964
AT5G05340/NP_196153.1	AT5G05340	<i>PRX52</i>	2.78861158	4.38E-10
AT5G05600/NP_001330807.1	AT5G05600	<i>JAO2</i>	3.682132106	3.02E-24
AT5G05600/NP_196179.1	AT5G05600	<i>JAO2</i>	3.735077906	1.16E-11
AT5G07010/NP_568177.1	AT5G07010	<i>ATST2A</i>	3.218866238	3.39E-13
AT5G09440/NP_196506.1	AT5G09440	<i>EXL4</i>	2.115952361	1.53E-09
AT5G13330/NP_196837.1	AT5G13330	<i>Rap2.6L</i>	2.620794089	0.036155
AT5G14180/NP_001330559.1	AT5G14180	<i>MPLI</i>	5.236454649	4.54E-20
AT5G14180/NP_001330560.1	AT5G14180	<i>MPLI</i>	5.122716415	4.57E-13
AT5G14180/NP_001330561.1	AT5G14180	<i>MPLI</i>	5.236454649	4.54E-20
AT5G14180/NP_001330562.1	AT5G14180	<i>MPLI</i>	5.030886458	5.01E-16
AT5G14180/NP_568295.2	AT5G14180	<i>MPLI</i>	5.141814067	1.43E-20
AT5G20230/NP_197523.1	AT5G20230	<i>ATBCB</i>	2.791140323	2.87E-06
AT5G24080/NP_001330805.1	AT5G24080	<i>NA</i>	2.420437568	0.02544
AT5G24080/NP_001330806.1	AT5G24080	<i>NA</i>	2.835748818	0.019506
AT5G24080/NP_568438.2	AT5G24080	<i>NA</i>	2.835748818	0.019506
AT5G39580/NP_198774.1	AT5G39580	<i>PRX62</i>	3.857873658	0.042332
AT5G43570/NP_001330099.1	AT5G43570	<i>NA</i>	4.152047952	3.77E-06
AT5G43570/NP_199170.2	AT5G43570	<i>NA</i>	4.439653318	1.72E-06
AT5G43580/NP_199171.3	AT5G43580	<i>UPI</i>	2.515053051	4.18E-07
AT5G44430/NP_199256.1	AT5G44430	<i>PDF1.2c</i>	6.279075791	0.008712
AT5G44572/NP_001078711.1	AT5G44572	<i>NA</i>	2.212480135	3.14E-10
AT5G44574/NP_001078712.1	AT5G44574	<i>NA</i>	2.255758422	0.024577
AT5G44575/NP_850920.1	AT5G44575	<i>NA</i>	2.583430495	3.08E-05
AT5G47330/NP_199544.1	AT5G47330	<i>NA</i>	2.936409737	2.92E-05
AT5G49520/NP_199763.1	AT5G49520	<i>ATWRKY48</i>	2.162147947	0.002149
AT5G59320/NP_568905.1	AT5G59320	<i>LTP3</i>	2.973921698	1.55E-06
AT5G61890/NP_200995.1	AT5G61890	<i>ERF114</i>	3.257124267	2.54E-06
AT5G65870/NP_201388.1	AT5G65870	<i>ATPSK5</i>	1.603424681	0.004061
AT5G67310/NP_201532.2	AT5G67310	<i>CYP81G1</i>	3.189408059	0.008712
AT5G67480/NP_001330470.1	AT5G67480	<i>ATBT4</i>	1.855116944	1.68E-05
AT5G67480/NP_201549.1	AT5G67480	<i>ATBT4</i>	1.855116944	1.68E-05
AT5G67480/NP_975007.1	AT5G67480	<i>ATBT4</i>	1.86190401	1.37E-05
AT1G13609/NP_001031041.1	AT1G13609	<i>NA</i>	-3.236385826	3.24E-05
AT1G13609/NP_001184986.1	AT1G13609	<i>NA</i>	-3.455785892	0.00015
AT3G46900/NP_190274.1	AT3G46900	<i>COPT2</i>	-3.385430922	5.35E-05
AT3G56970/NP_191256.1	AT3G56970	<i>BHLH038</i>	-4.191307279	3.99E-13
AT3G56980/NP_191257.1	AT3G56980	<i>BHLH039</i>	-3.510079856	0.000299
AT4G25100/NP_001031710.1	AT4G25100	<i>ATFSD1</i>	-1.816361075	3.34E-20

AT4G25100/NP_001190834.1	AT4G25100	<i>ATFSDI</i>	-1.804425242	3.09E-19
AT4G25100/NP_194240.1	AT4G25100	<i>ATFSDI</i>	-1.804425242	3.09E-19
AT4G25100/NP_849440.1	AT4G25100	<i>ATFSDI</i>	-1.804425242	3.09E-19
AT4G25100/NP_849441.1	AT4G25100	<i>ATFSDI</i>	-1.804425242	3.09E-19

9 References

- (1) Darwin, C. On the Origin of Species by Means of Natural Selection, Or The Preservation of Favoured Races in the Struggle for Life; J. Murray, 1861.
- (2) Mojzsis, S. J.; Arrhenius, G.; McKeegan, K. D.; Harrison, T. M.; Nutman, A. P.; Friend, C. R. L. Evidence for Life on Earth before 3,800 Million Years Ago. *Nature* **1996**, 384 (6604), 55–59. <https://doi.org/10.1038/384055a0>.
- (3) Dodd, M. S.; Papineau, D.; Grenne, T.; Slack, J. F.; Rittner, M.; Pirajno, F.; O’Neil, J.; Little, C. T. S. Evidence for Early Life in Earth’s Oldest Hydrothermal Vent Precipitates. *Nature* **2017**, 543 (7643), 60–64. <https://doi.org/10.1038/nature21377>.
- (4) Bell, E. A.; Boehnke, P.; Harrison, T. M.; Mao, W. L. Potentially Biogenic Carbon Preserved in a 4.1 Billion-Year-Old Zircon. *Proc. Natl. Acad. Sci.* **2015**, 112 (47), 14518–14521. <https://doi.org/10.1073/pnas.1517557112>.
- (5) Lyons, T. W.; Reinhard, C. T.; Planavsky, N. J. The Rise of Oxygen in Earth’s Early Ocean and Atmosphere. *Nature* **2014**, 506 (7488), 307–315. <https://doi.org/10.1038/nature13068>.
- (6) Dunsworth, H. M. Origin of the Genus Homo. *Evol. Educ. Outreach* **2010**, 3 (3), 353–366. <https://doi.org/10.1007/s12052-010-0247-8>.
- (7) Abramson, G.; Laguna, M. F.; Kuperman, M. N.; Monjeau, A.; Lanata, J. L. On the Roles of Hunting and Habitat Size on the Extinction of Megafauna. *Quat. Int.* **2017**, 431, 205–215. <https://doi.org/10.1016/j.quaint.2015.08.043>.
- (8) Glikson, A. Fire and Human Evolution: The Deep-Time Blueprints of the Anthropocene. *Anthropocene* **2013**, 3, 89–92. <https://doi.org/10.1016/j.ancene.2014.02.002>.
- (9) Weisdorf, J. L. From Foraging To Farming: Explaining The Neolithic Revolution. *J. Econ. Surv.* **2005**, 19 (4), 561–586. <https://doi.org/10.1111/j.0950-0804.2005.00259.x>.
- (10) Lewis, S. L.; Maslin, M. A. Defining the Anthropocene. *Nature* **2015**, 519 (7542), 171–180. <https://doi.org/10.1038/nature14258>.
- (11) Calvin, K.; Dasgupta, D.; Krinner, G.; Mukherji, A.; Thorne, P. W.; Trisos, C.; Romero, J.; Aldunce, P.; Barrett, K.; Blanco, G.; Cheung, W. W. L.; Connors, S.; Denton, F.; Diongue-Niang, A.; Dodman, D.; Garschagen, M.; Geden, O.; Hayward, B.; Jones, C.; Jotzo, F.; Krug, T.; Lasco, R.; Lee, Y.-Y.; Masson-Delmotte, V.; Meinshausen, M.; Mintenbeck, K.; Mokssit, A.; Otto, F. E. L.; Pathak, M.; Pirani, A.; Poloczanska, E.; Pörtner, H.-O.; Revi, A.; Roberts, D. C.; Roy, J.; Ruane, A. C.; Skea, J.; Shukla, P. R.; Slade, R.; Slangen, A.; Sokona, Y.; Sörensson, A. A.; Tignor, M.; Van Vuuren, D.; Wei, Y.-M.; Winkler, H.; Zhai, P.; Zommers, Z.; Hourcade, J.-C.; Johnson, F. X.; Pachauri, S.; Simpson, N. P.; Singh, C.; Thomas, A.; Totin, E.; Arias, P.; Bustamante, M.; Elgizouli, I.; Flato, G.; Howden, M.; Méndez-Vallejo, C.; Pereira, J. J.; Pichs-Madruga, R.; Rose, S. K.; Saheb, Y.; Sánchez Rodríguez, R.; Ürges-Vorsatz, D.; Xiao, C.; Yassaa, N.; Alegría, A.; Armour, K.; Bednar-Fiedl, B.; Blok, K.; Cissé, G.; Dentener, F.; Eriksen, S.; Fischer, E.; Garner, G.; Guivarch, C.; Haasnoot, M.; Hansen, G.; Hauser, M.;

- Hawkins, E.; Hermans, T.; Kopp, R.; Leprince-Ringuet, N.; Lewis, J.; Ley, D.; Ludden, C.; Niamir, L.; Nicholls, Z.; Some, S.; Szopa, S.; Trewin, B.; Van Der Wijst, K.-I.; Winter, G.; Witting, M.; Birt, A.; Ha, M.; Romero, J.; Kim, J.; Haites, E. F.; Jung, Y.; Stavins, R.; Birt, A.; Ha, M.; Orendain, D. J. A.; Ignon, L.; Park, S.; Park, Y.; Reisinger, A.; Cammaramo, D.; Fischlin, A.; Fuglestvedt, J. S.; Hansen, G.; Ludden, C.; Masson-Delmotte, V.; Matthews, J. B. R.; Mintenbeck, K.; Pirani, A.; Poloczanska, E.; Leprince-Ringuet, N.; Péan, C. IPCC, 2023: Climate Change 2023: Synthesis Report. Contribution of Working Groups I, II and III to the Sixth Assessment Report of the Intergovernmental Panel on Climate Change [Core Writing Team, H. Lee and J. Romero (Eds.)]. IPCC, Geneva, Switzerland., First.; Intergovernmental Panel on Climate Change (IPCC), 2023. <https://doi.org/10.59327/IPCC/AR6-9789291691647>.
- (12) Steffen, W.; Richardson, K.; Rockström, J.; Cornell, S. E.; Fetzer, I.; Bennett, E. M.; Biggs, R.; Carpenter, S. R.; de Vries, W.; de Wit, C. A.; Folke, C.; Gerten, D.; Heinke, J.; Mace, G. M.; Persson, L. M.; Ramanathan, V.; Reyers, B.; Sörlin, S. Planetary Boundaries: Guiding Human Development on a Changing Planet. *Science* **2015**, 347 (6223), 1259855. <https://doi.org/10.1126/science.1259855>.
- (13) Rockström, J.; Donges, J. F.; Fetzer, I.; Martin, M. A.; Wang-Erlandsson, L.; Richardson, K. Planetary Boundaries Guide Humanity's Future on Earth. *Nat. Rev. Earth Environ.* **2024**, 5 (11), 773–788. <https://doi.org/10.1038/s43017-024-00597-z>.
- (14) Richardson, K.; Steffen, W.; Lucht, W.; Bendtsen, J.; Cornell, S. E.; Donges, J. F.; Drüke, M.; Fetzer, I.; Bala, G.; von Bloh, W.; Feulner, G.; Fiedler, S.; Gerten, D.; Gleeson, T.; Hofmann, M.; Huiskamp, W.; Kummu, M.; Mohan, C.; Nogués-Bravo, D.; Petri, S.; Porkka, M.; Rahmstorf, S.; Schaphoff, S.; Thonicke, K.; Tobian, A.; Virkki, V.; Wang-Erlandsson, L.; Weber, L.; Rockström, J. Earth beyond Six of Nine Planetary Boundaries. *Sci. Adv.* 9 (37), eadh2458. <https://doi.org/10.1126/sciadv.adh2458>.
- (15) McLaughlin, M. J.; Smolders, E.; Zhao, F. J.; Grant, C.; Montalvo, D. Managing Cadmium in Agricultural Systems. In *Advances in Agronomy*; Elsevier, 2021; Vol. 166, pp 1–129. <https://doi.org/10.1016/bs.agron.2020.10.004>.
- (16) Kumar, S.; Kumar, S.; Mohapatra, T. Interaction Between Macro- and Micro-Nutrients in Plants. *Front. Plant Sci.* **2021**, 12. <https://doi.org/10.3389/fpls.2021.665583>.
- (17) Rawat, J.; Pandey, N.; Saxena, J. Role of Potassium in Plant Photosynthesis, Transport, Growth and Yield. In *Role of Potassium in Abiotic Stress*; Iqbal, N., Umar, S., Eds.; Springer Nature: Singapore, 2022; pp 1–14. https://doi.org/10.1007/978-981-16-4461-0_1.
- (18) WHITE, P. J.; BROADLEY, M. R. Calcium in Plants. *Ann. Bot.* **2003**, 92 (4), 487–511. <https://doi.org/10.1093/aob/mcg164>.
- (19) Clemens, S. The Cell Biology of Zinc. *J. Exp. Bot.* **2022**, 73 (6), 1688–1698. <https://doi.org/10.1093/jxb/erab481>.
- (20) Mukhopadhyay, S.; Mandal, S. K.; Bhaduri, S.; Armstrong, W. H. Manganese Clusters with Relevance to Photosystem II. *Chem. Rev.* **2004**, 104 (9), 3981–4026. <https://doi.org/10.1021/cr0206014>.

- (21) Mansilla, N.; Racca, S.; Gras, D. E.; Gonzalez, D. H.; Welchen, E. The Complexity of Mitochondrial Complex IV: An Update of Cytochrome c Oxidase Biogenesis in Plants. *Int. J. Mol. Sci.* **2018**, *19* (3), 662. <https://doi.org/10.3390/ijms19030662>.
- (22) Redinbo, M. R.; Yeates, T. O.; Merchant, S. Plastocyanin: Structural and Functional Analysis. *J. Bioenerg. Biomembr.* **1994**, *26* (1), 49–66. <https://doi.org/10.1007/BF00763219>.
- (23) Hanke, G.; Mulo, P. Plant Type Ferredoxins and Ferredoxin-Dependent Metabolism. *Plant Cell Environ.* **2013**, *36* (6), 1071–1084. <https://doi.org/10.1111/pce.12046>.
- (24) Hansen, C. C.; Nelson, D. R.; Møller, B. L.; Werck-Reichhart, D. Plant Cytochrome P450 Plasticity and Evolution. *Mol. Plant* **2021**, *14* (8), 1244–1265. <https://doi.org/10.1016/j.molp.2021.06.028>.
- (25) Lin, Y.-F.; Aarts, M. G. M. The Molecular Mechanism of Zinc and Cadmium Stress Response in Plants. *Cell. Mol. Life Sci. CMLS* **2012**, *69* (19), 3187–3206. <https://doi.org/10.1007/s00018-012-1089-z>.
- (26) Mittler, R.; Zandalinas, S. I.; Fichman, Y.; Van Breusegem, F. Reactive Oxygen Species Signalling in Plant Stress Responses. *Nat. Rev. Mol. Cell Biol.* **2022**, *23* (10), 663–679. <https://doi.org/10.1038/s41580-022-00499-2>.
- (27) Metal Toxicity in Plants: Perception, Signaling and Remediation; Gupta, D. K., Sandalio, L. M., Eds.; Springer: Berlin, Heidelberg, 2012. <https://doi.org/10.1007/978-3-642-22081-4>.
- (28) Mansoor, S.; Ali, A.; Kour, N.; Bornhorst, J.; AlHarbi, K.; Rinklebe, J.; Abd El Moneim, D.; Ahmad, P.; Chung, Y. S. Heavy Metal Induced Oxidative Stress Mitigation and ROS Scavenging in Plants. *Plants* **2023**, *12* (16), 3003. <https://doi.org/10.3390/plants12163003>.
- (29) Souguir, D.; Ferjani, E.; Ledoigt, G.; Goupil, P. Sequential Effects of Cadmium on Genotoxicity and Lipoperoxidation in Vicia Faba Roots. *Ecotoxicology* **2011**, *20* (2), 329–336. <https://doi.org/10.1007/s10646-010-0582-0>.
- (30) Roldán-Arjona, T.; Ariza, R. R. Repair and Tolerance of Oxidative DNA Damage in Plants. *Mutat. Res. Mutat. Res.* **2009**, *681* (2), 169–179. <https://doi.org/10.1016/j.mrrev.2008.07.003>.
- (31) Al Mahmud, J.; Bhuyan, M. H. M. B.; Anee, T. I.; Nahar, K.; Fujita, M.; Hasanuzzaman, M. Reactive Oxygen Species Metabolism and Antioxidant Defense in Plants Under Metal/Metalloid Stress. In *Plant Abiotic Stress Tolerance: Agronomic, Molecular and Biotechnological Approaches*; Hasanuzzaman, M., Hakeem, K. R., Nahar, K., Alharby, H. F., Eds.; Springer International Publishing: Cham, 2019; pp 221–257. https://doi.org/10.1007/978-3-030-06118-0_10.
- (32) Richards, S. L.; Wilkins, K. A.; Swarbreck, S. M.; Anderson, A. A.; Habib, N.; Smith, A. G.; McAinsh, M.; Davies, J. M. The Hydroxyl Radical in Plants: From Seed to Seed. *J. Exp. Bot.* **2015**, *66* (1), 37–46. <https://doi.org/10.1093/jxb/eru398>.

- (33) Pham, A. N.; Xing, G.; Miller, C. J.; Waite, T. D. Fenton-like Copper Redox Chemistry Revisited: Hydrogen Peroxide and Superoxide Mediation of Copper-Catalyzed Oxidant Production. *J. Catal.* **2013**, 301, 54–64. <https://doi.org/10.1016/j.jcat.2013.01.025>.
- (34) Krämer, U. Metal Homeostasis in Land Plants: A Perpetual Balancing Act Beyond the Fulfilment of Metalloproteome Cofactor Demands. *Annu. Rev. Plant Biol.* **2024**, 75 (Volume 75, 2024), 27–65. <https://doi.org/10.1146/annurev-arplant-070623-105324>.
- (35) Krämer, U.; Clemens, S. Functions and Homeostasis of Zinc, Copper, and Nickel in Plants. In *Molecular Biology of Metal Homeostasis and Detoxification: From Microbes to Man*; Tamas, M. J., Martinoia, E., Eds.; Springer: Berlin, Heidelberg, 2006; pp 215–271. https://doi.org/10.1007/4735_96.
- (36) Jozefczak, M.; Remans, T.; Vangronsveld, J.; Cuypers, A. Glutathione Is a Key Player in Metal-Induced Oxidative Stress Defenses. *Int. J. Mol. Sci.* **2012**, 13 (3), 3145–3175. <https://doi.org/10.3390/ijms13033145>.
- (37) Semane, B.; Cuypers, A.; Smeets, K.; Van Belleghem, F.; Horemans, N.; Schat, H.; Vangronsveld, J. Cadmium Responses in *Arabidopsis thaliana*: Glutathione Metabolism and Antioxidative Defence System. *Physiol. Plant.* **2007**, 129 (3), 519–528. <https://doi.org/10.1111/j.1399-3054.2006.00822.x>.
- (38) Zlobin, I. E.; Kartashov, A. V.; Shpakovski, G. V. Different Roles of Glutathione in Copper and Zinc Chelation in *Brassica napus* Roots. *Plant Physiol. Biochem.* **2017**, 118, 333–341. <https://doi.org/10.1016/j.plaphy.2017.06.029>.
- (39) Faizan, M.; Alam, P.; Hussain, A.; Karabulut, F.; Tonny, S. H.; Cheng, S. H.; Yusuf, M.; Adil, M. F.; Sehar, S.; Alomrani, S. O.; Albalawi, T.; Hayat, S. Phytochelatins: Key Regulator against Heavy Metal Toxicity in Plants. *Plant Stress* **2024**, 11, 100355. <https://doi.org/10.1016/j.stress.2024.100355>.
- (40) Cobbett, C.; Goldsbrough, P. PHYTOCHELATINS AND METALLOTHIONEINS: Roles in Heavy Metal Detoxification and Homeostasis. *Annu. Rev. Plant Biol.* **2002**, 53 (Volume 53, 2002), 159–182. <https://doi.org/10.1146/annurev.arplant.53.100301.135154>.
- (41) García-García, J. D.; Sánchez-Thomas, R.; Saavedra, E.; Fernández-Velasco, D. A.; Romero-Romero, S.; Casanova-Figueroa, K. I.; Mendoza-Cózatl, D. G.; Moreno-Sánchez, R. Mapping the Metal-Catalytic Site of a Zinc-Activated Phytochelatin Synthase. *Algal Res.* **2020**, 47, 101890. <https://doi.org/10.1016/j.algal.2020.101890>.
- (42) Cobbett, C. S. Phytochelatins and Their Roles in Heavy Metal Detoxification. *Plant Physiol.* **2000**, 123 (3), 825–832. <https://doi.org/10.1104/pp.123.3.825>.
- (43) Koffler, B. E.; Bloem, E.; Zellnig, G.; Zechmann, B. High Resolution Imaging of Subcellular Glutathione Concentrations by Quantitative Immunoelectron Microscopy in Different Leaf Areas of *Arabidopsis*. *Micron* **2013**, 45, 119–128. <https://doi.org/10.1016/j.micron.2012.11.006>.

- (44) Noctor, G.; Mhamdi, A.; Chaouch, S.; Han, Y.; Neukermans, J.; Marquez-Garcia, B.; Queval, G.; Foyer, C. H. Glutathione in Plants: An Integrated Overview. *Plant Cell Environ.* **2012**, 35 (2), 454–484. <https://doi.org/10.1111/j.1365-3040.2011.02400.x>.
- (45) Irving, H.; Williams, R. J. P. Order of Stability of Metal Complexes. *Nature* **1948**, 162 (4123), 746–747. <https://doi.org/10.1038/162746a0>.
- (46) Clemens, S. Metal Ligands in Micronutrient Acquisition and Homeostasis. *Plant Cell Environ.* **2019**, 42 (10), 2902–2912. <https://doi.org/10.1111/pce.13627>.
- (47) Burkhead, J. L.; Gogolin Reynolds, K. A.; Abdel-Ghany, S. E.; Cohu, C. M.; Pilon, M. Copper Homeostasis. *New Phytol.* **2009**, 182 (4), 799–816. <https://doi.org/10.1111/j.1469-8137.2009.02846.x>.
- (48) Macomber, L.; Imlay, J. A. The Iron-Sulfur Clusters of Dehydratases Are Primary Intracellular Targets of Copper Toxicity. *Proc. Natl. Acad. Sci.* **2009**, 106 (20), 8344–8349. <https://doi.org/10.1073/pnas.0812808106>.
- (49) Krężel, A.; Maret, W. The Biological Inorganic Chemistry of Zinc Ions. *Arch. Biochem. Biophys.* **2016**, 611, 3–19. <https://doi.org/10.1016/j.abb.2016.04.010>.
- (50) Van Assche, F.; Clijsters, H. Effects of Metals on Enzyme Activity in Plants. *Plant Cell Environ.* **1990**, 13 (3), 195–206. <https://doi.org/10.1111/j.1365-3040.1990.tb01304.x>.
- (51) Skórzyńska-Polit, E.; Drażkiewicz, M.; Krupa, Z. The Activity of the Antioxidative System in Cadmium-Treated Arabidopsis Thaliana. *Biol. Plant.* **2003**, 47 (1), 71–78. <https://doi.org/10.1023/A:1027332915500>.
- (52) Jin, Y. H.; Clark, A. B.; Slebos, R. J. C.; Al-Refai, H.; Taylor, J. A.; Kunkel, T. A.; Resnick, M. A.; Gordenin, D. A. Cadmium Is a Mutagen That Acts by Inhibiting Mismatch Repair. *Nat. Genet.* **2003**, 34 (3), 326–329. <https://doi.org/10.1038/ng1172>.
- (53) Banerjee, S.; Flores-Rozas, H. Cadmium Inhibits Mismatch Repair by Blocking the ATPase Activity of the MSH2-MSH6 Complex. *Nucleic Acids Res.* **2005**, 33 (4), 1410–1419. <https://doi.org/10.1093/nar/gki291>.
- (54) Angulo-Bejarano, P. I.; Puente-Rivera, J.; Cruz-Ortega, R. Metal and Metalloid Toxicity in Plants: An Overview on Molecular Aspects. *Plants* **2021**, 10 (4), 635. <https://doi.org/10.3390/plants10040635>.
- (55) Huang, S.; Yamaji, N.; Ma, J. F. Metal Transport Systems in Plants. *Annu. Rev. Plant Biol.* **2024**, 75 (Volume 75, 2024), 1–25. <https://doi.org/10.1146/annurev-arplant-062923-021424>.
- (56) Lasat, M. M. Phytoextraction of Metals from Contaminated Soil: A Review of Plant/Soil/Metal Interaction and Assessment of Pertinent Agronomic Issues. *J. Hazard. Subst. Res.* **1999**, 2 (1). <https://doi.org/10.4148/1090-7025.1015>.

- (57) Shuman, L. M. Chemical Forms of Micronutrients in Soils. In *Micronutrients in Agriculture*; John Wiley & Sons, Ltd, 1991; pp 113–144. <https://doi.org/10.2136/sssabookser4.2ed.c5>.
- (58) Zeng, G.; Wan, J.; Huang, D.; Hu, L.; Huang, C.; Cheng, M.; Xue, W.; Gong, X.; Wang, R.; Jiang, D. Precipitation, Adsorption and Rhizosphere Effect: The Mechanisms for Phosphate-Induced Pb Immobilization in Soils—A Review. *J. Hazard. Mater.* **2017**, 339, 354–367. <https://doi.org/10.1016/j.jhazmat.2017.05.038>.
- (59) Frey, P. A.; Reed, G. H. The Ubiquity of Iron. *ACS Chem. Biol.* **2012**, 7 (9), 1477–1481. <https://doi.org/10.1021/cb300323q>.
- (60) Colombo, C.; Palumbo, G.; He, J.-Z.; Pinton, R.; Cesco, S. Review on Iron Availability in Soil: Interaction of Fe Minerals, Plants, and Microbes. *J. Soils Sediments* **2014**, 14 (3), 538–548. <https://doi.org/10.1007/s11368-013-0814-z>.
- (61) Makita, H. Iron-Oxidizing Bacteria in Marine Environments: Recent Progresses and Future Directions. *World J. Microbiol. Biotechnol.* **2018**, 34 (8), 110. <https://doi.org/10.1007/s11274-018-2491-y>.
- (62) Morrissey, J.; Guerinot, M. L. Iron Uptake and Transport in Plants: The Good, the Bad, and the Ionome. *Chem. Rev.* **2009**, 109 (10), 4553–4567. <https://doi.org/10.1021/cr900112r>.
- (63) Saleem, A.; Zulfiqar, A.; Saleem, M. Z.; Ali, B.; Saleem, M. H.; Ali, S.; Tufekci, E. D.; Tufekci, A. R.; Rahimi, M.; Mostafa, R. M. Alkaline and Acidic Soil Constraints on Iron Accumulation by Rice Cultivars in Relation to Several Physio-Biochemical Parameters. *BMC Plant Biol.* **2023**, 23 (1), 397. <https://doi.org/10.1186/s12870-023-04400-x>.
- (64) Martín-Barranco, A.; Thomine, S.; Vert, G.; Zelazny, E. A Quick Journey into the Diversity of Iron Uptake Strategies in Photosynthetic Organisms. *Plant Signal. Behav.* 16 (11), 1975088. <https://doi.org/10.1080/15592324.2021.1975088>.
- (65) Thomine, S.; Vert, G. Iron Transport in Plants: Better Be Safe than Sorry. *Curr. Opin. Plant Biol.* **2013**, 16 (3), 322–327. <https://doi.org/10.1016/j.pbi.2013.01.003>.
- (66) Robe, K.; Izquierdo, E.; Vignols, F.; Rouached, H.; Dubos, C. The Coumarins: Secondary Metabolites Playing a Primary Role in Plant Nutrition and Health. *Trends Plant Sci.* **2021**, 26 (3), 248–259. <https://doi.org/10.1016/j.tplants.2020.10.008>.
- (67) Vélez-Bermúdez, I. C.; Schmidt, W. How Plants Recalibrate Cellular Iron Homeostasis. *Plant Cell Physiol.* **2022**, 63 (2), 154–162. <https://doi.org/10.1093/pcp/pcab166>.
- (68) Spiridon, A.; Oburger, E.; Valadbeigi, Y.; Kloimböck, T.; Stanetty, C.; Kratena, N.; Draskovits, M.; Causon, T.; Hann, S. Surveying the Mugineic Acid Family: Ion Mobility – Quadrupole Time-of-Flight Mass Spectrometry (IM-QTOFMS) Characterization and Tandem Mass Spectrometry (LC-ESI-MS/MS) Quantification of All Eight Naturally Occurring Phytosiderophores. *Anal. Chim. Acta* **2023**, 1278, 341718. <https://doi.org/10.1016/j.aca.2023.341718>.

- (69) Naranjo-Arcos, M. A.; Bauer, P.; Naranjo-Arcos, M. A.; Bauer, P. Iron Nutrition, Oxidative Stress, and Pathogen Defense. In *Nutritional Deficiency*; IntechOpen, 2016. <https://doi.org/10.5772/63204>.
- (70) Mai, H.-J.; Lindermayr, C.; von Toerne, C.; Fink-Straube, C.; Durner, J.; Bauer, P. Iron and FER-LIKE IRON DEFICIENCY-INDUCED TRANSCRIPTION FACTOR-Dependent Regulation of Proteins and Genes in Arabidopsis Thaliana Roots. *PROTEOMICS* **2015**, 15 (17), 3030–3047. <https://doi.org/10.1002/pmic.201400351>.
- (71) Riaz, N.; Guerinot, M. L. All Together Now: Regulation of the Iron Deficiency Response. *J. Exp. Bot.* **2021**, 72 (6), 2045–2055. <https://doi.org/10.1093/jxb/erab003>.
- (72) Kim, S. A.; LaCroix, I. S.; Gerber, S. A.; Guerinot, M. L. The Iron Deficiency Response in Arabidopsis Thaliana Requires the Phosphorylated Transcription Factor URI. *Proc. Natl. Acad. Sci.* **2019**, 116 (50), 24933–24942. <https://doi.org/10.1073/pnas.1916892116>.
- (73) Pu, M. N.; Liang, G. The Transcription Factor POPEYE Negatively Regulates the Expression of bHLH Ib Genes to Maintain Iron Homeostasis. *J. Exp. Bot.* **2023**, 74 (8), 2754–2767. <https://doi.org/10.1093/jxb/erad057>.
- (74) Selote, D.; Samira, R.; Matthiadis, A.; Gillikin, J. W.; Long, T. A. Iron-Binding E3 Ligase Mediates Iron Response in Plants by Targeting Basic Helix-Loop-Helix Transcription Factors. *Plant Physiol.* **2015**, 167 (1), 273–286. <https://doi.org/10.1104/pp.114.250837>.
- (75) Hindt, M. N.; Akmakjian, G. Z.; Pivarski, K. L.; Punshon, T.; Baxter, I.; Salt, D. E.; Guerinot, M. L. BRUTUS and Its Paralogs, BTS LIKE1 and BTS LIKE2, Encode Important Negative Regulators of the Iron Deficiency Response in Arabidopsis Thaliana†. *Metallomics* **2017**, 9 (7), 876–890. <https://doi.org/10.1039/c7mt00152e>.
- (76) Li, M.; Zhang, J.; Jin, H.; Feng, D.; Wang, J.; Wang, H.-B.; Liu, B. The Iron Deficiency Response Regulators IAA-LEUCINE RESISTANT3 and bHLH104 Possess Different Targets and Have Distinct Effects on Photosynthesis in Arabidopsis. *J. Plant Biol.* **2019**, 62 (2), 109–119. <https://doi.org/10.1007/s12374-018-0360-8>.
- (77) Li, Y.; Lu, C. K.; Li, C. Y.; Lei, R. H.; Pu, M. N.; Zhao, J. H.; Peng, F.; Ping, H. Q.; Wang, D.; Liang, G. IRON MAN Interacts with BRUTUS to Maintain Iron Homeostasis in Arabidopsis. *Proc. Natl. Acad. Sci.* **2021**, 118 (39), e2109063118. <https://doi.org/10.1073/pnas.2109063118>.
- (78) Grillet, L.; Lan, P.; Li, W.; Mokkapati, G.; Schmidt, W. IRON MAN Is a Ubiquitous Family of Peptides That Control Iron Transport in Plants. *Nat. Plants* **2018**, 4 (11), 953–963. <https://doi.org/10.1038/s41477-018-0266-y>.
- (79) Mankotia, S.; Dubey, A.; Jakhar, P.; Satbhai, S. B. ELONGATED HYPOCOTYL 5 (HY5) and POPEYE (PYE) Regulate Intercellular Iron Transport in Plants. May 7, 2024. <https://doi.org/10.1101/2024.05.06.592684>.
- (80) Tissot, N.; Robe, K.; Gao, F.; Grant-Grant, S.; Boucherez, J.; Bellegarde, F.; Maghiaoui, A.; Marcelin, R.; Izquierdo, E.; Benhamed, M.; Martin, A.; Vignols, F.; Roschztardt, H.;

- Gaymard, F.; Briat, J.-F.; Dubos, C. Transcriptional Integration of the Responses to Iron Availability in Arabidopsis by the bHLH Factor ILR3. *New Phytol.* **2019**, *223* (3), 1433–1446. <https://doi.org/10.1111/nph.15753>.
- (81) Vert, G.; Grotz, N.; Dédaldéchamp, F.; Gaymard, F.; Guerinot, M. L.; Briat, J.-F.; Curie, C. IRT1, an Arabidopsis Transporter Essential for Iron Uptake from the Soil and for Plant Growth. *Plant Cell* **2002**, *14* (6), 1223–1233. <https://doi.org/10.1105/tpc.001388>.
- (82) Korshunova, Y. O.; Eide, D.; Gregg Clark, W.; Lou Guerinot, M.; Pakrasi, H. B. The IRT1 Protein from Arabidopsis Thaliana Is a Metal Transporter with a Broad Substrate Range. *Plant Mol. Biol.* **1999**, *40* (1), 37–44. <https://doi.org/10.1023/A:1026438615520>.
- (83) Connolly, E. L.; Fett, J. P.; Guerinot, M. L. Expression of the IRT1 Metal Transporter Is Controlled by Metals at the Levels of Transcript and Protein Accumulation. *Plant Cell* **2002**, *14* (6), 1347–1357. <https://doi.org/10.1105/tpc.001263>.
- (84) Rogers, E. E.; Eide, D. J.; Guerinot, M. L. Altered Selectivity in an Arabidopsis Metal Transporter. *Proc. Natl. Acad. Sci.* **2000**, *97* (22), 12356–12360. <https://doi.org/10.1073/pnas.210214197>.
- (85) Dubeaux, G.; Neveu, J.; Zelazny, E.; Vert, G. Metal Sensing by the IRT1 Transporter-Receptor Orchestrates Its Own Degradation and Plant Metal Nutrition. *Mol. Cell* **2018**, *69* (6), 953–964.e5. <https://doi.org/10.1016/j.molcel.2018.02.009>.
- (86) Spielmann, J.; Cointy, V.; Devime, F.; Ravanel, S.; Neveu, J.; Vert, G. Differential Metal Sensing and Metal-Dependent Degradation of the Broad Spectrum Root Metal Transporter IRT1. *Plant J.* **2022**, *112* (5), 1252–1265. <https://doi.org/10.1111/tpj.16010>.
- (87) Spielmann, J.; Ahmadi, H.; Scheepers, M.; Weber, M.; Nitsche, S.; Carnol, M.; Bosman, B.; Kroymann, J.; Motte, P.; Clemens, S.; Hanikenne, M. The Two Copies of the Zinc and Cadmium ZIP6 Transporter of Arabidopsis Halleri Have Distinct Effects on Cadmium Tolerance. *Plant Cell Environ.* **2020**, *43* (9), 2143–2157. <https://doi.org/10.1111/pce.13806>.
- (88) Guan, M.; Chen, M.; Cao, Z. NRT2.1, a Major Contributor to Cadmium Uptake Controlled by High-Affinity Nitrate Transporters. *Ecotoxicol. Environ. Saf.* **2021**, *218*, 112269. <https://doi.org/10.1016/j.ecoenv.2021.112269>.
- (89) Clemens, S.; Ma, J. F. Toxic Heavy Metal and Metalloid Accumulation in Crop Plants and Foods. *Annu. Rev. Plant Biol.* **2016**, *67* (1), 489–512. <https://doi.org/10.1146/annurev-arplant-043015-112301>.
- (90) Khan, Z.; Elahi, A.; Bukhari, D. A.; Rehman, A. Cadmium Sources, Toxicity, Resistance and Removal by Microorganisms-A Potential Strategy for Cadmium Eradication. *J. Saudi Chem. Soc.* **2022**, *26* (6), 101569. <https://doi.org/10.1016/j.jscs.2022.101569>.
- (91) Kubier, A.; Wilkin, R. T.; Pichler, T. Cadmium in Soils and Groundwater: A Review. *Appl. Geochem. J. Int. Assoc. Geochem. Cosmochem.* **2019**, *108*, 1–16. <https://doi.org/10.1016/j.apgeochem.2019.104388>.

- (92) Clemens, S.; Aarts, M. G. M.; Thomine, S.; Verbruggen, N. Plant Science: The Key to Preventing Slow Cadmium Poisoning. *Trends Plant Sci.* **2013**, *18* (2), 92–99. <https://doi.org/10.1016/j.tplants.2012.08.003>.
- (93) Enjavinejad, S. M.; Zahedifar, M.; Moosavi, A. A.; Khosravani, P. Integrated Application of Multiple Indicators and Geographic Information System-Based Approaches for Comprehensive Assessment of Environmental Impacts of Toxic Metals-Contaminated Agricultural Soils and Vegetables. *Sci. Total Environ.* **2024**, *926*, 171747. <https://doi.org/10.1016/j.scitotenv.2024.171747>.
- (94) Kobayashi, E.; Suwazono, Y.; Dochi, M.; Honda, R.; Kido, T. Influence of Consumption of Cadmium-Polluted Rice or Jinzu River Water on Occurrence of Renal Tubular Dysfunction and/or Itai-Itai Disease. *Biol. Trace Elem. Res.* **2009**, *127* (3), 257–268. <https://doi.org/10.1007/s12011-008-8239-z>.
- (95) Environment, U. N. Final review of scientific information on cadmium | UNEP - UN Environment Programme. <https://www.unep.org/resources/report/final-review-scientific-information-cadmium> (accessed 2024-08-12).
- (96) Charkiewicz, A. E.; Omeljaniuk, W. J.; Nowak, K.; Garley, M.; Nikliński, J. Cadmium Toxicity and Health Effects—A Brief Summary. *Molecules* **2023**, *28* (18), 6620. <https://doi.org/10.3390/molecules28186620>.
- (97) List of Classifications. <https://monographs.iarc.who.int/list-of-classifications> (accessed 2024-08-12).
- (98) Yan, L.-J.; Allen, D. C. Cadmium-Induced Kidney Injury: Oxidative Damage as a Unifying Mechanism. *Biomolecules* **2021**, *11* (11), 1575. <https://doi.org/10.3390/biom11111575>.
- (99) Cadmium: From Toxicity to Essentiality; Sigel, A., Sigel, H., Sigel, R. K., Eds.; Metal Ions in Life Sciences; Springer Netherlands: Dordrecht, 2013; Vol. 11. <https://doi.org/10.1007/978-94-007-5179-8>.
- (100) Tolerable weekly intake for cadmium | EFSA. <https://www.efsa.europa.eu/en/efsajournal/pub/1975> (accessed 2024-08-12).
- (101) Zhao, D.; Wang, P.; Zhao, F.-J. Dietary Cadmium Exposure, Risks to Human Health and Mitigation Strategies. *Crit. Rev. Environ. Sci. Technol.* **2023**, *53* (8), 939–963. <https://doi.org/10.1080/10643389.2022.2099192>.
- (102) Haider, F. U.; Liqun, C.; Coulter, J. A.; Cheema, S. A.; Wu, J.; Zhang, R.; Wenjun, M.; Farooq, M. Cadmium Toxicity in Plants: Impacts and Remediation Strategies. *Ecotoxicol. Environ. Saf.* **2021**, *211*, 111887. <https://doi.org/10.1016/j.ecoenv.2020.111887>.
- (103) Howden, R.; Goldsbrough, P. B.; Andersen, C. R.; Cobbett, C. S. Cadmium-Sensitive, Cad1 Mutants of Arabidopsis Thaliana Are Phytochelatin Deficient. *Plant Physiol.* **1995**, *107* (4), 1059–1066. <https://doi.org/10.1104/pp.107.4.1059>.

- (104) Lejková, A.; Giehl, R. F. H.; Hartmann, A.; Fargašová, A.; von Wirén, N. Heavy Metals Induce Iron Deficiency Responses at Different Hierarchic and Regulatory Levels. *Plant Physiol.* **2017**, 174 (3), 1648–1668. <https://doi.org/10.1104/pp.16.01916>.
- (105) Corso, M.; Schwartzman, M. S.; Guzzo, F.; Souard, F.; Malkowski, E.; Hanikenne, M.; Verbruggen, N. Contrasting Cadmium Resistance Strategies in Two Metallicolous Populations of *Arabidopsis Halleri*. *New Phytol.* **2018**, 218 (1), 283–297. <https://doi.org/10.1111/nph.14948>.
- (106) Weber, M.; Trampeczynska, A.; Clemens, S. Comparative Transcriptome Analysis of Toxic Metal Responses in *Arabidopsis Thaliana* and the Cd²⁺-Hypertolerant Facultative Metallophyte *Arabidopsis Halleri*. *Plant Cell Environ.* **2006**, 29 (5), 950–963. <https://doi.org/10.1111/j.1365-3040.2005.01479.x>.
- (107) Oono, Y.; Yazawa, T.; Kawahara, Y.; Kanamori, H.; Kobayashi, F.; Sasaki, H.; Mori, S.; Wu, J.; Handa, H.; Itoh, T.; Matsumoto, T. Genome-Wide Transcriptome Analysis Reveals That Cadmium Stress Signaling Controls the Expression of Genes in Drought Stress Signal Pathways in Rice. *PLOS ONE* **2014**, 9 (5), e96946. <https://doi.org/10.1371/journal.pone.0096946>.
- (108) Naeem, A.; Zafar, M.; Khalid, H.; Zia-ur-Rehman, M.; Ahmad, Z.; Ayub, M. A.; Farooq Qayyum, M. Chapter 12 - Cadmium-Induced Imbalance in Nutrient and Water Uptake by Plants. In *Cadmium Toxicity and Tolerance in Plants*; Hasanuzzaman, M., Prasad, M. N. V., Fujita, M., Eds.; Academic Press, 2019; pp 299–326. <https://doi.org/10.1016/B978-0-12-814864-8.00012-7>.
- (109) Hassan, Z.; Aarts, M. G. M. Opportunities and Feasibilities for Biotechnological Improvement of Zn, Cd or Ni Tolerance and Accumulation in Plants. *Environ. Exp. Bot.* **2011**, 72 (1), 53–63. <https://doi.org/10.1016/j.envexpbot.2010.04.003>.
- (110) Lane, T. W.; Saito, M. A.; George, G. N.; Pickering, I. J.; Prince, R. C.; Morel, F. M. M. A Cadmium Enzyme from a Marine Diatom. *Nature* **2005**, 435 (7038), 42–42. <https://doi.org/10.1038/435042a>.
- (111) Rogers, E. D.; Benfey, P. N. Regulation of Plant Root System Architecture: Implications for Crop Advancement. *Curr. Opin. Biotechnol.* **2015**, 32, 93–98. <https://doi.org/10.1016/j.copbio.2014.11.015>.
- (112) Zanetti, M. E.; Blanco, F.; Ferrari, M.; Ariel, F.; Benoit, M.; Niebel, A.; Crespi, M. Epigenetic Control during Root Development and Symbiosis. *Plant Physiol.* **2024**, 196 (2), 697–710. <https://doi.org/10.1093/plphys/kiae333>.
- (113) Ren, M.; Li, Y.; Zhu, J.; Zhao, K.; Wu, Z.; Mao, C. Phenotypes and Molecular Mechanisms Underlying the Root Response to Phosphate Deprivation in Plants. *Int. J. Mol. Sci.* **2023**, 24 (6), 5107. <https://doi.org/10.3390/ijms24065107>.
- (114) Lux, A.; Martinka, M.; Vaculík, M.; White, P. J. Root Responses to Cadmium in the Rhizosphere: A Review. *J. Exp. Bot.* **2011**, 62 (1), 21–37. <https://doi.org/10.1093/jxb/erq281>.

- (115) Wang, H.-Q.; Xuan, W.; Huang, X.-Y.; Mao, C.; Zhao, F.-J. Cadmium Inhibits Lateral Root Emergence in Rice by Disrupting OsPIN-Mediated Auxin Distribution and the Protective Effect of OsHMA3. *Plant Cell Physiol.* **2021**, *62* (1), 166–177. <https://doi.org/10.1093/pcp/pcaa150>.
- (116) Bahmani, R.; Kim, D.; Modareszadeh, M.; Hwang, S. Cadmium Enhances Root Hair Elongation through Reactive Oxygen Species in Arabidopsis. *Environ. Exp. Bot.* **2022**, *196*, 104813. <https://doi.org/10.1016/j.envexpbot.2022.104813>.
- (117) Sofo, A.; Khan, N. A.; D'Ippolito, I.; Reyes, F. Subtoxic Levels of Some Heavy Metals Cause Differential Root-Shoot Structure, Morphology and Auxins Levels in Arabidopsis Thaliana. *Plant Physiol. Biochem.* **2022**, *173*, 68–75. <https://doi.org/10.1016/j.plaphy.2022.01.027>.
- (118) Perilli, S.; Di Mambro, R.; Sabatini, S. Growth and Development of the Root Apical Meristem. *Curr. Opin. Plant Biol.* **2012**, *15* (1), 17–23. <https://doi.org/10.1016/j.pbi.2011.10.006>.
- (119) Verbelen, J.-P.; Cnodder, T. D.; Le, J.; Vissenberg, K.; Baluška, F. The Root Apex of Arabidopsis Thaliana Consists of Four Distinct Zones of Growth Activities: Meristematic Zone, Transition Zone, Fast Elongation Zone and Growth Terminating Zone. *Plant Signal. Behav.* **2006**, *1* (6), 296–304. <https://doi.org/10.4161/psb.1.6.3511>.
- (120) Wells, D. M.; Wilson, M. H.; Bennett, M. J. Feeling UPBEAT about Growth: Linking ROS Gradients and Cell Proliferation. *Dev. Cell* **2010**, *19* (5), 644–646. <https://doi.org/10.1016/j.devcel.2010.10.017>.
- (121) Li, J.; Zeng, J.; Tian, Z.; Zhao, Z. Root-Specific Photoreception Directs Early Root Development by HY5-Regulated ROS Balance. *Proc. Natl. Acad. Sci.* **2024**, *121* (6), e2313092121. <https://doi.org/10.1073/pnas.2313092121>.
- (122) Bruno, L.; Pacenza, M.; Forgione, I.; Lamerton, L. R.; Greco, M.; Chiappetta, A.; Bitonti, M. B. In Arabidopsis Thaliana Cadmium Impact on the Growth of Primary Root by Altering SCR Expression and Auxin-Cytokinin Cross-Talk. *Front. Plant Sci.* **2017**, *8*. <https://doi.org/10.3389/fpls.2017.01323>.
- (123) Yuan, H.-M.; Huang, X. Inhibition of Root Meristem Growth by Cadmium Involves Nitric Oxide-Mediated Repression of Auxin Accumulation and Signalling in Arabidopsis. *Plant Cell Environ.* **2016**, *39* (1), 120–135. <https://doi.org/10.1111/pce.12597>.
- (124) Leonardo, B.; Emanuela, T.; Letizia, M. M.; Antonella, M.; Marco, M.; Fabrizio, A.; Beatrice, B. M.; Adriana, C. Cadmium Affects Cell Niches Maintenance in Arabidopsis Thaliana Post-Embryonic Shoot and Root Apical Meristem by Altering the Expression of WUS/WOX Homolog Genes and Cytokinin Accumulation. *Plant Physiol. Biochem.* **2021**, *167*, 785–794. <https://doi.org/10.1016/j.plaphy.2021.09.014>.
- (125) Cui, W.; Wang, H.; Song, J.; Cao, X.; Rogers, H. J.; Francis, D.; Jia, C.; Sun, L.; Hou, M.; Yang, Y.; Tai, P.; Liu, W. Cell Cycle Arrest Mediated by Cd-Induced DNA Damage in

- Arabidopsis Root Tips. *Ecotoxicol. Environ. Saf.* **2017**, 145, 569–574. <https://doi.org/10.1016/j.ecoenv.2017.07.074>.
- (126) Petit, J. R.; Jouzel, J.; Raynaud, D.; Barkov, N. I.; Barnola, J.-M.; Basile, I.; Bender, M.; Chappellaz, J.; Davis, M.; Delaygue, G.; Delmotte, M.; Kotlyakov, V. M.; Legrand, M.; Lipenkov, V. Y.; Lorius, C.; Pépin, L.; Ritz, C.; Saltzman, E.; Stievenard, M. Climate and Atmospheric History of the Past 420,000 Years from the Vostok Ice Core, Antarctica. *Nature* **1999**, 399 (6735), 429–436. <https://doi.org/10.1038/20859>.
- (127) Etheridge, D. M.; Steele, L. P.; Langenfelds, R. L.; Francey, R. J.; Barnola, J.-M.; Morgan, V. I. Natural and Anthropogenic Changes in Atmospheric CO₂ over the Last 1000 Years from Air in Antarctic Ice and Firn. *J. Geophys. Res. Atmospheres* **1996**, 101 (D2), 4115–4128. <https://doi.org/10.1029/95JD03410>.
- (128) Chapter 2 - A Very Brief History of Particulate Pollution. In *Case Studies in Nanotoxicology and Particle Toxicology*; Gatti, A. M., Montanari, S., Eds.; Academic Press: Boston, 2015; pp 7–11. <https://doi.org/10.1016/B978-0-12-801215-4.00002-9>.
- (129) Bellouin, N.; Haywood, J. Climatology of Tropospheric Aerosols☆. In *Reference Module in Earth Systems and Environmental Sciences*; Elsevier, 2020. <https://doi.org/10.1016/B978-0-12-409548-9.12436-4>.
- (130) Hammer, M. S.; van Donkelaar, A.; Martin, R. V.; McDuffie, E. E.; Lyapustin, A.; Sayer, A. M.; Hsu, N. C.; Levy, R. C.; Garay, M. J.; Kalashnikova, O. V.; Kahn, R. A. Effects of COVID-19 Lockdowns on Fine Particulate Matter Concentrations. *Sci. Adv.* **2021**, 7 (26), eabg7670. <https://doi.org/10.1126/sciadv.abg7670>.
- (131) Terzano, C.; Di Stefano, F.; Conti, V.; Graziani, E.; Petroianni, A. Air Pollution Ultrafine Particles: Toxicity beyond the Lung. *Eur. Rev. Med. Pharmacol. Sci.* **2010**, 14 (10), 809–821.
- (132) Abulikemu, A.; Zhang, X.; Su, X.; Meng, T.; Su, W.; Shi, Q.; Yu, T.; Niu, Y.; Yu, H.; Yuan, H.; Zhou, C.; Yang, H.; Zhang, Y.; Wang, Y.; Dai, Y.; Duan, H. Particulate Matter, Polycyclic Aromatic Hydrocarbons and Metals, Platelet Parameters and Blood Pressure Alteration: Multi-Pollutants Study among Population. *Sci. Total Environ.* **2024**, 941, 173657. <https://doi.org/10.1016/j.scitotenv.2024.173657>.
- (133) Giechaskiel, B.; Joshi, A.; Ntziachristos, L.; Dilara, P. European Regulatory Framework and Particulate Matter Emissions of Gasoline Light-Duty Vehicles: A Review. *Catalysts* **2019**, 9 (7), 586. <https://doi.org/10.3390/catal9070586>.
- (134) Xu, H. M.; Cao, J. J.; Ho, K. F.; Ding, H.; Han, Y. M.; Wang, G. H.; Chow, J. C.; Watson, J. G.; Khol, S. D.; Qiang, J.; Li, W. T. Lead Concentrations in Fine Particulate Matter after the Phasing out of Leaded Gasoline in Xi'an, China. *Atmos. Environ.* **2012**, 46, 217–224. <https://doi.org/10.1016/j.atmosenv.2011.09.078>.
- (135) Seyferth, D. The Rise and Fall of Tetraethyllead. 2. *Organometallics* **2003**, 22 (25), 5154–5178. <https://doi.org/10.1021/om030621b>.

- (136) Meena, V.; Dotaniya, M. L.; Saha, J. K.; Das, H.; Patra, A. K. Impact of Lead Contamination on Agroecosystem and Human Health. In *Lead in Plants and the Environment*; Gupta, D. K., Chatterjee, S., Walther, C., Eds.; Springer International Publishing: Cham, 2020; pp 67–82. https://doi.org/10.1007/978-3-030-21638-2_4.
- (137) Yang, Q.; Liu, G.; Falandysz, J.; Yang, L.; Zhao, C.; Chen, C.; Sun, Y.; Zheng, M.; Jiang, G. Atmospheric Emissions of Particulate Matter-Bound Heavy Metals from Industrial Sources. *Sci. Total Environ.* **2024**, 947, 174467. <https://doi.org/10.1016/j.scitotenv.2024.174467>.
- (138) Lopez, B.; Wang, X.; Chen, L.-W. A.; Ma, T.; Mendez-Jimenez, D.; Cobb, L. C.; Frederickson, C.; Fang, T.; Hwang, B.; Shiraiwa, M.; Park, M.; Park, K.; Yao, Q.; Yoon, S.; Jung, H. Metal Contents and Size Distributions of Brake and Tire Wear Particles Dispersed in the Near-Road Environment. *Sci. Total Environ.* **2023**, 883, 163561. <https://doi.org/10.1016/j.scitotenv.2023.163561>.
- (139) Grigoratos, T.; Martini, G. Brake Wear Particle Emissions: A Review. *Environ. Sci. Pollut. Res.* **2015**, 22 (4), 2491–2504. <https://doi.org/10.1007/s11356-014-3696-8>.
- (140) Power, A. L.; Tennant, R. K.; Stewart, A. G.; Gosden, C.; Worsley, A. T.; Jones, R.; Love, J. The Evolution of Atmospheric Particulate Matter in an Urban Landscape since the Industrial Revolution. *Sci. Rep.* **2023**, 13 (1), 8964. <https://doi.org/10.1038/s41598-023-35679-3>.
- (141) Ghude, S. D.; Chate, D. M.; Jena, C.; Beig, G.; Kumar, R.; Barth, M. C.; Pfister, G. G.; Fadnavis, S.; Pithani, P. Premature Mortality in India Due to PM_{2.5} and Ozone Exposure. *Geophys. Res. Lett.* **2016**, 43 (9), 4650–4658. <https://doi.org/10.1002/2016GL068949>.
- (142) Schraufnagel, D. E.; Balmes, J. R.; Cowl, C. T.; De Matteis, S.; Jung, S.-H.; Mortimer, K.; Perez-Padilla, R.; Rice, M. B.; Riojas-Rodriguez, H.; Sood, A.; Thurston, G. D.; To, T.; Vanker, A.; Wuebbles, D. J. Air Pollution and Noncommunicable Diseases: A Review by the Forum of International Respiratory Societies' Environmental Committee, Part 2: Air Pollution and Organ Systems. *Chest* **2019**, 155 (2), 417–426. <https://doi.org/10.1016/j.chest.2018.10.041>.
- (143) Raaschou-Nielsen, O.; Beelen, R.; Wang, M.; Hoek, G.; Andersen, Z. J.; Hoffmann, B.; Stafoggia, M.; Samoli, E.; Weinmayr, G.; Dimakopoulou, K.; Nieuwenhuijsen, M.; Xun, W. W.; Fischer, P.; Eriksen, K. T.; Sørensen, M.; Tjønneland, A.; Ricceri, F.; de Hoogh, K.; Key, T.; Eeftens, M.; Peeters, P. H.; Bueno-de-Mesquita, H. B.; Meliefste, K.; Oftedal, B.; Schwarze, P. E.; Nafstad, P.; Galassi, C.; Migliore, E.; Ranzi, A.; Cesaroni, G.; Badaloni, C.; Forastiere, F.; Penell, J.; De Faire, U.; Korek, M.; Pedersen, N.; Östenson, C.-G.; Pershagen, G.; Fratiglioni, L.; Concin, H.; Nagel, G.; Jaensch, A.; Ineichen, A.; Naccarati, A.; Katsoulis, M.; Trichopoulou, A.; Keuken, M.; Jedynska, A.; Kooter, I. M.; Kukkonen, J.; Brunekreef, B.; Sokhi, R. S.; Katsouyanni, K.; Vineis, P. Particulate Matter Air Pollution Components and Risk for Lung Cancer. *Environ. Int.* **2016**, 87, 66–73. <https://doi.org/10.1016/j.envint.2015.11.007>.
- (144) Kelly, F. J.; Fussell, J. C. Size, Source and Chemical Composition as Determinants of Toxicity Attributable to Ambient Particulate Matter. *Atmos. Environ.* **2012**, 60, 504–526. <https://doi.org/10.1016/j.atmosenv.2012.06.039>.

- (145) Sukumaran, K.; Botterhorn, K. L.; Schwartz, J.; Gauderman, J.; Cardenas-Iniguez, C.; McConnell, R.; Hackman, D. A.; Berhane, K.; Ahmadi, H.; Abad, S.; Habre, R.; Herting, M. M. Associations between Fine Particulate Matter Components, Their Sources, and Cognitive Outcomes in Children Ages 9–10 Years Old from the United States. *Environ. Health Perspect.* **2024**, 132 (10), 107009. <https://doi.org/10.1289/EHP14418>.
- (146) Chen, H.; Kwong, J. C.; Copes, R.; Tu, K.; Villeneuve, P. J.; Donkelaar, A. van; Hystad, P.; Martin, R. V.; Murray, B. J.; Jessiman, B.; Wilton, A. S.; Kopp, A.; Burnett, R. T. Living near Major Roads and the Incidence of Dementia, Parkinson's Disease, and Multiple Sclerosis: A Population-Based Cohort Study. *The Lancet* **2017**, 389 (10070), 718–726. [https://doi.org/10.1016/S0140-6736\(16\)32399-6](https://doi.org/10.1016/S0140-6736(16)32399-6).
- (147) Kahn, R. A.; Sayer, A. M. Satellites and Satellite Remote Sensing | Aerosol Measurements. In *Reference Module in Earth Systems and Environmental Sciences*; Elsevier, 2023. <https://doi.org/10.1016/B978-0-323-96026-7.00001-1>.
- (148) Chapter 6: Short-lived Climate Forcers. https://www.ipcc.ch/report/ar6/wg1/chapter/chapter-6/?utm_source=chatgpt.com (accessed 2025-02-11).
- (149) Gonet, T.; Maher, B. A.; Nyirő-Kósa, I.; Pósfai, M.; Vaculík, M.; Kukutschová, J. Size-Resolved, Quantitative Evaluation of the Magnetic Mineralogy of Airborne Brake-Wear Particulate Emissions. *Environ. Pollut.* **2021**, 288, 117808. <https://doi.org/10.1016/j.envpol.2021.117808>.
- (150) Schraufnagel, D. E. The Health Effects of Ultrafine Particles. *Exp. Mol. Med.* **2020**, 52 (3), 311–317. <https://doi.org/10.1038/s12276-020-0403-3>.
- (151) Hong, G.; Jee, Y.-K. Special Issue on Ultrafine Particles: Where Are They from and How Do They Affect Us? *Exp. Mol. Med.* **2020**, 52 (3), 309–310. <https://doi.org/10.1038/s12276-020-0395-z>.
- (152) Saha, P. K.; Zimmerman, N.; Malings, C.; Hauryliuk, A.; Li, Z.; Snell, L.; Subramanian, R.; Lipsky, E.; Apte, J. S.; Robinson, A. L.; Presto, A. A. Quantifying High-Resolution Spatial Variations and Local Source Impacts of Urban Ultrafine Particle Concentrations. *Sci. Total Environ.* **2019**, 655, 473–481. <https://doi.org/10.1016/j.scitotenv.2018.11.197>.
- (153) Schmid, O.; Möller, W.; Semmler-Behnke, M.; A. Ferron, G.; Karg, E.; Lipka, J.; Schulz, H.; Kreyling, W. G.; Stoeger, T. Dosimetry and Toxicology of Inhaled Ultrafine Particles. *Biomarkers* **2009**, 14 (sup1), 67–73. <https://doi.org/10.1080/13547500902965617>.
- (154) Chang, C.-Y.; You, R.; Armstrong, D.; Bandi, A.; Cheng, Y.-T.; Burkhardt, P. M.; Becerra-Dominguez, L.; Madison, M. C.; Tung, H.-Y.; Zeng, Z.; Wu, Y.; Song, L.; Phillips, P. E.; Porter, P.; Knight, J. M.; Putluri, N.; Yuan, X.; Marciano, D. C.; McHugh, E. A.; Tour, J. M.; Catic, A.; Maneix, L.; Burt, B. M.; Lee, H.-S.; Corry, D. B.; Kheradmand, F. Chronic Exposure to Carbon Black Ultrafine Particles Reprograms Macrophage Metabolism and Accelerates Lung Cancer. *Sci. Adv.* **2022**, 8 (46), eabq0615. <https://doi.org/10.1126/sciadv.abq0615>.

- (155) Bruinink, A.; Wang, J.; Wick, P. Effect of Particle Agglomeration in Nanotoxicology. *Arch. Toxicol.* **2015**, *89* (5), 659–675. <https://doi.org/10.1007/s00204-015-1460-6>.
- (156) Das, A.; Pantzke, J.; Jeong, S.; Hartner, E.; Zimmermann, E. J.; Gawlitta, N.; Offer, S.; Shukla, D.; Huber, A.; Rastak, N.; Meščeriakovas, A.; Ivleva, N. P.; Kuhn, E.; Binder, S.; Gröger, T.; Oeder, S.; Delaval, M.; Czech, H.; Sippula, O.; Schnelle-Kreis, J.; Di Bucchianico, S.; Sklorz, M.; Zimmermann, R. Generation, Characterization, and Toxicological Assessment of Reference Ultrafine Soot Particles with Different Organic Content for Inhalation Toxicological Studies. *Sci. Total Environ.* **2024**, *951*, 175727. <https://doi.org/10.1016/j.scitotenv.2024.175727>.
- (157) Ferin, J.; Oberdörster, G.; Penney, D. P. Pulmonary Retention of Ultrafine and Fine Particles in Rats. *Am. J. Respir. Cell Mol. Biol.* **2012**. <https://doi.org/10.1165/ajrcmb/6.5.535>.
- (158) Donaldson, K.; Brown, D.; Clouter, A.; Duffin, R.; MacNee, W.; Renwick, L.; Tran, L.; Stone, V. The Pulmonary Toxicology of Ultrafine Particles. *J. Aerosol Med. Off. J. Int. Soc. Aerosols Med.* **2002**, *15* (2), 213–220. <https://doi.org/10.1089/089426802320282338>.
- (159) Elder, A.; Gelein, R.; Silva, V.; Feikert, T.; Opanashuk, L.; Carter, J.; Potter, R.; Maynard, A.; Ito, Y.; Finkelstein, J.; Oberdörster, G. Translocation of Inhaled Ultrafine Manganese Oxide Particles to the Central Nervous System. *Environ. Health Perspect.* **2006**, *114* (8), 1172–1178. <https://doi.org/10.1289/ehp.9030>.
- (160) Qi, Y.; Wei, S.; Xin, T.; Huang, C.; Pu, Y.; Ma, J.; Zhang, C.; Liu, Y.; Lynch, I.; Liu, S. Passage of Exogenous Fine Particles from the Lung into the Brain in Humans and Animals. *Proc. Natl. Acad. Sci.* **2022**, *119* (26), e2117083119. <https://doi.org/10.1073/pnas.2117083119>.
- (161) Kwon, H.-S.; Ryu, M. H.; Carlsten, C. Ultrafine Particles: Unique Physicochemical Properties Relevant to Health and Disease. *Exp. Mol. Med.* **2020**, *52* (3), 318–328. <https://doi.org/10.1038/s12276-020-0405-1>.
- (162) Gasser, M.; Riediker, M.; Mueller, L.; Perrenoud, A.; Blank, F.; Gehr, P.; Rothen-Rutishauser, B. Toxic Effects of Brake Wear Particles on Epithelial Lung Cells in Vitro. *Part. Fibre Toxicol.* **2009**, *6*, 30. <https://doi.org/10.1186/1743-8977-6-30>.
- (163) Directive - 1999/30 - EN - EUR-Lex. <https://eur-lex.europa.eu/eli/dir/1999/30/oj/eng> (accessed 2025-02-11).
- (164) Directive - 2008/50 - EN - EUR-Lex. <https://eur-lex.europa.eu/eli/dir/2008/50/oj/eng> (accessed 2025-02-11).
- (165) L_202402881EN.000101.fmx.xml. <https://eur-lex.europa.eu/eli/dir/2024/2881/oj/eng> (accessed 2025-02-11).
- (166) WHO global air quality guidelines: particulate matter (PM_{2.5} and PM₁₀), ozone, nitrogen dioxide, sulfur dioxide and carbon monoxide. <https://www.who.int/publications/i/item/9789240034228> (accessed 2025-02-11).
- (167) WHO Ambient Air Quality Database, 2022 Update: Status Report, 1st ed.; World Health Organization: Geneva, 2023.

- (168) Vallabani, N. V. S.; Gruzieva, O.; Elihn, K.; Juárez-Facio, A. T.; Steimer, S. S.; Kuhn, J.; Silvergren, S.; Portugal, J.; Piña, B.; Olofsson, U.; Johansson, C.; Karlsson, H. L. Toxicity and Health Effects of Ultrafine Particles: Towards an Understanding of the Relative Impacts of Different Transport Modes. *Environ. Res.* **2023**, *231*, 116186. <https://doi.org/10.1016/j.envres.2023.116186>.
- (169) Richtmann, L.; Opel, T.; Maier, M.; Langhof, N.; Clemens, S. Establishment of a System to Analyze Effects of Airborne Ultra-Fine Particulate Matter from Brake Wear on Plants under Realistic Exposure Conditions. *J. Hazard. Mater.* **2024**, *469*, 134084. <https://doi.org/10.1016/j.jhazmat.2024.134084>.
- (170) Watson, J. G.; Tropp, R. J.; Kohl, S. D.; Wang, X.; Chow, J. C. Filter Processing and Gravimetric Analysis for Suspended Particulate Matter Samples. *Aerosol Sci. Eng.* **2017**, *1* (2), 93–105. <https://doi.org/10.1007/s41810-017-0010-4>.
- (171) Kero, I. T.; Jørgensen, R. B. Comparison of Three Real-Time Measurement Methods for Airborne Ultrafine Particles in the Silicon Alloy Industry. *Int. J. Environ. Res. Public. Health* **2016**, *13* (9), 871. <https://doi.org/10.3390/ijerph13090871>.
- (172) Shahid, M.; Dumat, C.; Khalid, S.; Schreck, E.; Xiong, T.; Niazi, N. K. Foliar Heavy Metal Uptake, Toxicity and Detoxification in Plants: A Comparison of Foliar and Root Metal Uptake. *J. Hazard. Mater.* **2017**, *325*, 36–58. <https://doi.org/10.1016/j.jhazmat.2016.11.063>.
- (173) Liu, L.; Guan, D.; Peart, M. R.; Wang, G.; Zhang, H.; Li, Z. The Dust Retention Capacities of Urban Vegetation—a Case Study of Guangzhou, South China. *Environ. Sci. Pollut. Res.* **2013**, *20* (9), 6601–6610. <https://doi.org/10.1007/s11356-013-1648-3>.
- (174) Sheikh, H. A.; Maher, B. A.; Woods, A. W.; Tung, P. Y.; Harrison, R. J. Efficacy of Green Infrastructure in Reducing Exposure to Local, Traffic-Related Sources of Airborne Particulate Matter (PM). *Sci. Total Environ.* **2023**, *903*, 166598. <https://doi.org/10.1016/j.scitotenv.2023.166598>.
- (175) Wang, H.; Maher, B. A.; Ahmed, I. A.; Davison, B. Efficient Removal of Ultrafine Particles from Diesel Exhaust by Selected Tree Species: Implications for Roadside Planting for Improving the Quality of Urban Air. *Environ. Sci. Technol.* **2019**, *53* (12), 6906–6916. <https://doi.org/10.1021/acs.est.8b06629>.
- (176) Wang, W.-N.; Tarafdar, J. C.; Biswas, P. Nanoparticle Synthesis and Delivery by an Aerosol Route for Watermelon Plant Foliar Uptake. *J. Nanoparticle Res.* **2013**, *15* (1), 1417. <https://doi.org/10.1007/s11051-013-1417-8>.
- (177) El-Shetehy, M.; Moradi, A.; Maceroni, M.; Reinhardt, D.; Petri-Fink, A.; Rothen-Rutishauser, B.; Mauch, F.; Schwab, F. Silica Nanoparticles Enhance Disease Resistance in Arabidopsis Plants. *Nat. Nanotechnol.* **2021**, *16* (3), 344–353. <https://doi.org/10.1038/s41565-020-00812-0>.
- (178) Schreck, E.; Foucault, Y.; Sarret, G.; Sobanska, S.; Cécillon, L.; Castrec-Rouelle, M.; Uzu, G.; Dumat, C. Metal and Metalloid Foliar Uptake by Various Plant Species Exposed to

Atmospheric Industrial Fallout: Mechanisms Involved for Lead. *Sci. Total Environ.* **2012**, 427–428, 253–262. <https://doi.org/10.1016/j.scitotenv.2012.03.051>.

(179) Richtmann, L.; Prochetto, S.; Thiébaud, N.; Sarthou, M. C. M.; Boutet, S.; Hanikenne, M.; Clemens, S.; Verbruggen, N. Arabidopsis Thaliana Root Responses to Cd Exposure: Insights into Root Tip-Specific Changes and the Role of HY5 in Limiting Cd Accumulation and Promoting Tolerance. *Plant J.* **2025**, 122 (6), e70298. <https://doi.org/10.1111/tpj.70298>.

(180) Thiébaud, N.; Sarthou, M.; Richtmann, L.; Pergament Persson, D.; Ranjan, A.; Schloesser, M.; Boutet, S.; Rezende, L.; Clemens, S.; Verbruggen, N.; Hanikenne, M. Specific Redox and Iron Homeostasis Responses in the Root Tip of Arabidopsis upon Zinc Excess. *New Phytol.* **2025**, 246 (4), 1796–1815. <https://doi.org/10.1111/nph.70105>.

(181) Piacentini, D.; Falasca, G.; Canepari, S.; Massimi, L. Potential of PM-Selected Components to Induce Oxidative Stress and Root System Alteration in a Plant Model Organism. *Environ. Int.* **2019**, 132, 105094. <https://doi.org/10.1016/j.envint.2019.105094>.

(182) Maiorana, S.; Teoldi, F.; Silvani, S.; Mancini, A.; Sanguineti, A.; Mariani, F.; Cella, C.; Lopez, A.; Potenza, M. A. C.; Lodi, M.; Dupin, D.; Sanvito, T.; Bonfanti, A.; Benfenati, E.; Baderna, D. Phytotoxicity of Wear Debris from Traditional and Innovative Brake Pads. *Environ. Int.* **2019**, 123, 156–163. <https://doi.org/10.1016/j.envint.2018.11.057>.

(183) Oyama, T.; Shimura, Y.; Okada, K. The Arabidopsis HY5 Gene Encodes a bZIP Protein That Regulates Stimulus-Induced Development of Root and Hypocotyl. *Genes Dev.* **1997**, 11 (22), 2983–2995. <https://doi.org/10.1101/gad.11.22.2983>.

(184) Mehrtens, F.; Kranz, H.; Bednarek, P.; Weisshaar, B. The Arabidopsis Transcription Factor MYB12 Is a Flavonol-Specific Regulator of Phenylpropanoid Biosynthesis. *Plant Physiol.* **2005**, 138 (2), 1083–1096. <https://doi.org/10.1104/pp.104.058032>.

(185) Boutet, S.; Barreda, L.; Perreau, F.; Totozafy, J.-C.; Mauve, C.; Gakière, B.; Delannoy, E.; Martin-Magniette, M.-L.; Monti, A.; Lepiniec, L.; Zanetti, F.; Corso, M. Untargeted metabolomic analyses reveal the diversity and plasticity of the specialized metabolome in seeds of different *Camelina sativa* genotypes. *Plant J.* **2022**, 110 (1), 147–165. <https://doi.org/10.1111/tpj.15662>.

(186) Ritchie, M. E.; Phipson, B.; Wu, D.; Hu, Y.; Law, C. W.; Shi, W.; Smyth, G. K. Limma Powers Differential Expression Analyses for RNA-Sequencing and Microarray Studies. *Nucleic Acids Res.* **2015**, 43 (7), e47. <https://doi.org/10.1093/nar/gkv007>.

(187) Love, M. I.; Huber, W.; Anders, S. Moderated Estimation of Fold Change and Dispersion for RNA-Seq Data with DESeq2. *Genome Biol.* **2014**, 15 (12), 550. <https://doi.org/10.1186/s13059-014-0550-8>.

(188) Shahan, R.; Hsu, C.-W.; Nolan, T. M.; Cole, B. J.; Taylor, I. W.; Greenstreet, L.; Zhang, S.; Afanassiev, A.; Vlot, A. H. C.; Schiebinger, G.; Benfey, P. N.; Ohler, U. A Single-Cell Arabidopsis Root Atlas Reveals Developmental Trajectories in Wild-Type and Cell Identity Mutants. *Dev. Cell* **2022**, 57 (4), 543–560.e9. <https://doi.org/10.1016/j.devcel.2022.01.008>.

- (189) Burko, Y.; Seluzicki, A.; Zander, M.; Pedmale, U. V.; Ecker, J. R.; Chory, J. Chimeric Activators and Repressors Define HY5 Activity and Reveal a Light-Regulated Feedback Mechanism[OPEN]. *Plant Cell* **2020**, 32 (4), 967–983. <https://doi.org/10.1105/tpc.19.00772>.
- (190) Pischke, E.; Barozzi, F.; Colina Blanco, A. E.; Kerl, C. F.; Planer-Friedrich, B.; Clemens, S. Dimethylmonothioarsenate Is Highly Toxic for Plants and Readily Translocated to Shoots. *Environ. Sci. Technol.* **2022**, 56 (14), 10072–10083. <https://doi.org/10.1021/acs.est.2c01206>.
- (191) Laughton, S.; Laycock, A.; Bland, G.; von der Kammer, F.; Hofmann, T.; Casman, E. A.; Lowry, G. V. Methanol-Based Extraction Protocol for Insoluble and Moderately Water-Soluble Nanoparticles in Plants to Enable Characterization by Single Particle ICP-MS. *Anal. Bioanal. Chem.* **2021**, 413 (2), 299–314. <https://doi.org/10.1007/s00216-020-03014-8>.
- (192) Nazar, M. F.; Shah, S. S.; Eastoe, J.; Khan, A. M.; Shah, A. Separation and Recycling of Nanoparticles Using Cloud Point Extraction with Non-Ionic Surfactant Mixtures. *J. Colloid Interface Sci.* **2011**, 363 (2), 490–496. <https://doi.org/10.1016/j.jcis.2011.07.070>.
- (193) Yamanaka, M.; Itagaki, T.; Wilbur, S. Acquire NP Data for up to 16 Elements in Rapid Multi-Element Nanoparticle Analysis Mode.
- (194) Soffey, E.; Jones, C.; Kelinske, M. Rapid Multielement Nanoparticle Analysis Using Single-Particle ICP-MS/MS. **2019**, 34, 10–20.
- (195) Vandepoele, K.; Raes, J.; De Veylder, L.; Rouzé, P.; Rombauts, S.; Inzé, D. Genome-Wide Analysis of Core Cell Cycle Genes in Arabidopsis. *Plant Cell* **2002**, 14 (4), 903–916. <https://doi.org/10.1105/tpc.010445>.
- (196) Takahashi, N.; Ogita, N.; Takahashi, T.; Taniguchi, S.; Tanaka, M.; Seki, M.; Umeda, M. A Regulatory Module Controlling Stress-Induced Cell Cycle Arrest in Arabidopsis. *eLife* **2019**, 8, e43944. <https://doi.org/10.7554/eLife.43944>.
- (197) Stracke, R.; Favory, J.-J.; Gruber, H.; Bar^{TEL}niewoehner, L.; Bar^{TEL}s, S.; Binkert, M.; Funk, M.; Weisshaar, B.; Ulm, R. The Arabidopsis bZIP Transcription Factor HY5 Regulates Expression of the PFG1/MYB12 Gene in Response to Light and Ultraviolet-B Radiation. *Plant Cell Environ.* **2010**, 33 (1), 88–103. <https://doi.org/10.1111/j.1365-3040.2009.02061.x>.
- (198) Bursch, K.; Toledo-Ortiz, G.; Pireyre, M.; Lohr, M.; Braatz, C.; Johansson, H. Identification of BBX Proteins as Rate-Limiting Cofactors of HY5. *Nat. Plants* **2020**, 6 (8), 921–928. <https://doi.org/10.1038/s41477-020-0725-0>.
- (199) Gong, F.; Yao, Z.; Liu, Y.; Sun, M.; Peng, X. H₂O₂ Response Gene 1/2 Are Novel Sensors or Responders of H₂O₂ and Involve in Maintaining Embryonic Root Meristem Activity in Arabidopsis Thaliana. *Plant Sci.* **2021**, 310, 110981. <https://doi.org/10.1016/j.plantsci.2021.110981>.
- (200) Zhang, Y.; Wang, C.; Xu, H.; Shi, X.; Zhen, W.; Hu, Z.; Huang, J.; Zheng, Y.; Huang, P.; Zhang, K.-X.; Xiao, X.; Hao, X.; Wang, X.; Zhou, C.; Wang, G.; Li, C.; Zheng, L. HY5 Contributes to Light-Regulated Root System Architecture Under a Root-Covered Culture System. *Front. Plant Sci.* **2019**, 10. <https://doi.org/10.3389/fpls.2019.01490>.

- (201) Gangappa, S. N.; Botto, J. F. The Multifaceted Roles of HY5 in Plant Growth and Development. *Mol. Plant* **2016**, *9* (10), 1353–1365. <https://doi.org/10.1016/j.molp.2016.07.002>.
- (202) Schulz, H.; Härtling, S.; Tanneberg, H. The Identification and Quantification of Arsenic-Induced Phytochelatins—Comparison between Plants with Varying As Sensitivities. *Plant Soil* **2008**, *303* (1), 275–287. <https://doi.org/10.1007/s11104-007-9507-y>.
- (203) Maurer, F.; Müller, S.; Bauer, P. Suppression of Fe Deficiency Gene Expression by Jasmonate. *Plant Physiol. Biochem.* **2011**, *49* (5), 530–536. <https://doi.org/10.1016/j.plaphy.2011.01.025>.
- (204) Qian, Y.; Wang, X.; Liu, Y.; Wang, X.; Mao, T. HY5 Inhibits Lateral Root Initiation in Arabidopsis through Negative Regulation of the Microtubule-Stabilizing Protein TPXL5. *Plant Cell* **2023**, *35* (3), 1092–1109. <https://doi.org/10.1093/plcell/koac358>.
- (205) Clemens, S. Toxic Metal Accumulation, Responses to Exposure and Mechanisms of Tolerance in Plants. *Biochimie* **2006**, *88* (11), 1707–1719. <https://doi.org/10.1016/j.biochi.2006.07.003>.
- (206) Cui, Y.; Cao, W.; He, Y.; Zhao, Q.; Wakazaki, M.; Zhuang, X.; Gao, J.; Zeng, Y.; Gao, C.; Ding, Y.; Wong, H. Y.; Wong, W. S.; Lam, H. K.; Wang, P.; Ueda, T.; Rojas-Pierce, M.; Toyooka, K.; Kang, B.-H.; Jiang, L. A Whole-Cell Electron Tomography Model of Vacuole Biogenesis in Arabidopsis Root Cells. *Nat. Plants* **2019**, *5* (1), 95–105. <https://doi.org/10.1038/s41477-018-0328-1>.
- (207) Kaiser, S.; Scheuring, D. To Lead or to Follow: Contribution of the Plant Vacuole to Cell Growth. *Front. Plant Sci.* **2020**, *11*. <https://doi.org/10.3389/fpls.2020.00553>.
- (208) Richter, J.; Ploderer, M.; Mongelard, G.; Gutierrez, L.; Hauser, M.-T. Role of CrRLK1L Cell Wall Sensors HERCULES1 and 2, THESEUS1, and FERONIA in Growth Adaptation Triggered by Heavy Metals and Trace Elements. *Front. Plant Sci.* **2017**, *8*. <https://doi.org/10.3389/fpls.2017.01554>.
- (209) Xiao, Y.; Wu, X.; Liu, D.; Yao, J.; Liang, G.; Song, H.; Ismail, A. M.; Luo, J.-S.; Zhang, Z. Cell Wall Polysaccharide-Mediated Cadmium Tolerance Between Two Arabidopsis Thaliana Ecotypes. *Front. Plant Sci.* **2020**, *11*. <https://doi.org/10.3389/fpls.2020.00473>.
- (210) Corso, M.; An, X.; Jones, C. Y.; Gonzalez-Doblas, V.; Schvartzman, M. S.; Malkowski, E.; Willats, W. G. T.; Hanikenne, M.; Verbruggen, N. Adaptation of Arabidopsis Halleri to Extreme Metal Pollution through Limited Metal Accumulation Involves Changes in Cell Wall Composition and Metal Homeostasis. *New Phytol.* **2021**, *230* (2), 669–682. <https://doi.org/10.1111/nph.17173>.
- (211) Cajero Sánchez, W.; García-Ponce, B.; Sánchez, M. de la P.; Álvarez-Buylla, E. R.; Garay-Arroyo, A. Identifying the Transition to the Maturation Zone in Three Ecotypes of Arabidopsis Thaliana Roots. *Commun. Integr. Biol.* **2017**, *11* (1), e1395993. <https://doi.org/10.1080/19420889.2017.1395993>.

- (212) Guo, X.; Liu, Y.; Zhang, R.; Luo, J.; Song, Y.; Li, J.; Wu, K.; Peng, L.; Liu, Y.; Du, Y.; Liang, Y.; Li, T. Hemicellulose Modification Promotes Cadmium Hyperaccumulation by Decreasing Its Retention on Roots in *Sedum Alfredii*. *Plant Soil* **2020**, 447 (1–2), 241–255. <https://doi.org/10.1007/s11104-019-04339-9>.
- (213) Krzesłowska, M. The Cell Wall in Plant Cell Response to Trace Metals: Polysaccharide Remodeling and Its Role in Defense Strategy. *Acta Physiol. Plant.* **2011**, 33 (1), 35–51. <https://doi.org/10.1007/s11738-010-0581-z>.
- (214) Chaleckis, R.; Meister, I.; Zhang, P.; Wheelock, C. E. Challenges, Progress and Promises of Metabolite Annotation for LC–MS-Based Metabolomics. *Curr. Opin. Biotechnol.* **2019**, 55, 44–50. <https://doi.org/10.1016/j.copbio.2018.07.010>.
- (215) Novoa-del-Toro, E. M.; Witting, M. Navigating Common Pitfalls in Metabolite Identification and Metabolomics Bioinformatics. *Metabolomics* **2024**, 20 (5), 103. <https://doi.org/10.1007/s11306-024-02167-2>.
- (216) Cui, L.; Lu, H.; Lee, Y. H. Challenges and Emergent Solutions for LC-MS/MS Based Untargeted Metabolomics in Diseases. *Mass Spectrom. Rev.* **2018**, 37 (6), 772–792. <https://doi.org/10.1002/mas.21562>.
- (217) Guo, J.; Yu, H.; Xing, S.; Huan, T. Addressing Big Data Challenges in Mass Spectrometry-Based Metabolomics. *Chem. Commun.* **2022**, 58 (72), 9979–9990. <https://doi.org/10.1039/D2CC03598G>.
- (218) Santelia, D.; Henrichs, S.; Vincenzetti, V.; Sauer, M.; Bigler, L.; Klein, M.; Bailly, A.; Lee, Y.; Friml, J.; Geisler, M.; Martinoia, E. Flavonoids Redirect PIN-Mediated Polar Auxin Fluxes during Root Gravitropic Responses *. *J. Biol. Chem.* **2008**, 283 (45), 31218–31226. <https://doi.org/10.1074/jbc.M710122200>.
- (219) Clemens, S.; Simm, C. *Schizosaccharomyces Pombe* as a Model for Metal Homeostasis in Plant Cells: The Phytochelatin-Dependent Pathway Is the Main Cadmium Detoxification Mechanism. *New Phytol.* **2003**, 159 (2), 323–330. <https://doi.org/10.1046/j.1469-8137.2003.00811.x>.
- (220) Clemens, S. Evolution and Function of Phytochelatin Synthases. *J. Plant Physiol.* **2006**, 163 (3), 319–332. <https://doi.org/10.1016/j.jplph.2005.11.010>.
- (221) Brunetti, P.; Zanella, L.; Proia, A.; De Paolis, A.; Falasca, G.; Altamura, M. M.; Sanità di Toppi, L.; Costantino, P.; Cardarelli, M. Cadmium Tolerance and Phytochelatin Content of *Arabidopsis* Seedlings Over-Expressing the Phytochelatin Synthase Gene AtPCS1. *J. Exp. Bot.* **2011**, 62 (15), 5509–5519. <https://doi.org/10.1093/jxb/err228>.
- (222) Shomali, A.; Das, S.; Arif, N.; Sarraf, M.; Zahra, N.; Yadav, V.; Aliniaiefard, S.; Chauhan, D. K.; Hasanuzzaman, M. Diverse Physiological Roles of Flavonoids in Plant Environmental Stress Responses and Tolerance. *Plants* **2022**, 11 (22), 3158. <https://doi.org/10.3390/plants11223158>.

- (223) Stracke, R.; Ishihara, H.; Huep, G.; Barsch, A.; Mehrrens, F.; Niehaus, K.; Weisshaar, B. Differential Regulation of Closely Related R2R3-MYB Transcription Factors Controls Flavonol Accumulation in Different Parts of the Arabidopsis Thaliana Seedling. *Plant J.* **2007**, 50 (4), 660–677. <https://doi.org/10.1111/j.1365-313X.2007.03078.x>.
- (224) Gollhofer, J.; Timofeev, R.; Lan, P.; Schmidt, W.; Buckhout, T. J. Vacuolar-Iron-Transporter1-Like Proteins Mediate Iron Homeostasis in Arabidopsis. *PLOS ONE* **2014**, 9 (10), e110468. <https://doi.org/10.1371/journal.pone.0110468>.
- (225) Tabata, R.; Kamiya, T.; Imoto, S.; Tamura, H.; Ikuta, K.; Tabata, M.; Hirayama, T.; Tsukagoshi, H.; Tanoi, K.; Suzuki, T.; Hachiya, T.; Sakakibara, H. Systemic Regulation of Iron Acquisition by Arabidopsis in Environments with Heterogeneous Iron Distributions. *Plant Cell Physiol.* **2022**, 63 (6), 842–854. <https://doi.org/10.1093/pcp/pcac049>.
- (226) Vert, G.; Grotz, N.; Dédaldéchamp, F.; Gaymard, F.; Guerinot, M. L.; Briat, J.-F.; Curie, C. IRT1, an Arabidopsis Transporter Essential for Iron Uptake from the Soil and for Plant Growth. *Plant Cell* **2002**, 14 (6), 1223–1233. <https://doi.org/10.1105/tpc.001388>.
- (227) Rajniak, J.; Giehl, R. F. H.; Chang, E.; Murgia, I.; von Wirén, N.; Sattely, E. S. Biosynthesis of Redox-Active Metabolites in Response to Iron Deficiency in Plants. *Nat. Chem. Biol.* **2018**, 14 (5), 442–450. <https://doi.org/10.1038/s41589-018-0019-2>.
- (228) Vélez-Bermúdez, I. C.; Schmidt, W. Plant Strategies to Mine Iron from Alkaline Substrates. *Plant Soil* **2023**, 483 (1), 1–25. <https://doi.org/10.1007/s11104-022-05746-1>.
- (229) Robe, K.; Conejero, G.; Gao, F.; Lefebvre-Legendre, L.; Sylvestre-Gonon, E.; Rofidal, V.; Hem, S.; Rouhier, N.; Barberon, M.; Hecker, A.; Gaymard, F.; Izquierdo, E.; Dubos, C. Coumarin Accumulation and Trafficking in Arabidopsis Thaliana: A Complex and Dynamic Process. *New Phytol.* **2021**, 229 (4), 2062–2079. <https://doi.org/10.1111/nph.17090>.
- (230) Vélez-Bermúdez, I. C.; Schmidt, W. How Plants Recalibrate Cellular Iron Homeostasis. *Plant Cell Physiol.* **2022**, 63 (2), 154–162. <https://doi.org/10.1093/pcp/pcab166>.
- (231) Robe, K.; Stassen, M.; Chamieh, J.; Gonzalez, P.; Hem, S.; Santoni, V.; Dubos, C.; Izquierdo, E. Uptake of Fe-Fraxetin Complexes, an IRT1 Independent Strategy for Iron Acquisition in Arabidopsis Thaliana. *bioRxiv* August 4, 2021, p 2021.08.03.454955. <https://doi.org/10.1101/2021.08.03.454955>.
- (232) Hendrix, S.; Iven, V.; Eekhout, T.; Huybrechts, M.; Pecqueur, I.; Horemans, N.; Keunen, E.; De Veylder, L.; Vangronsveld, J.; Cuypers, A. Suppressor of Gamma Response 1 Modulates the DNA Damage Response and Oxidative Stress Response in Leaves of Cadmium-Exposed Arabidopsis Thaliana. *Front. Plant Sci.* **2020**, 11. <https://doi.org/10.3389/fpls.2020.00366>.
- (233) Inzé, D.; Veylder, L. D. Cell Cycle Regulation in Plant Development1. *Annu. Rev. Genet.* **2006**, 40 (Volume 40, 2006), 77–105. <https://doi.org/10.1146/annurev.genet.40.110405.090431>.

- (234) Huybrechts, M.; Cuypers, A.; Deckers, J.; Iven, V.; Vandionant, S.; Jozefczak, M.; Hendrix, S. Cadmium and Plant Development: An Agony from Seed to Seed. *Int. J. Mol. Sci.* **2019**, *20* (16), 3971. <https://doi.org/10.3390/ijms20163971>.
- (235) Wybouw, B.; Arents, H. E.; Yang, B.; Nolf, J.; Smet, W.; Vandorpe, M.; Minne, M.; Luo, X.; De Clercq, I.; Van Damme, D.; Glanc, M.; De Rybel, B. The Transcription Factor AtMYB12 Is Part of a Feedback Loop Regulating Cell Division Orientation in the Root Meristem Vasculature. *J. Exp. Bot.* **2023**, *74* (6), 1940–1956. <https://doi.org/10.1093/jxb/erad020>.
- (236) Montané, M.-H.; Kloppstech, K. The Family of Light-Harvesting-Related Proteins (LHCs, ELIPs, HLIPs): Was the Harvesting of Light Their Primary Function? *Gene* **2000**, *258* (1), 1–8. [https://doi.org/10.1016/S0378-1119\(00\)00413-3](https://doi.org/10.1016/S0378-1119(00)00413-3).
- (237) Tsukagoshi, H.; Busch, W.; Benfey, P. N. Transcriptional Regulation of ROS Controls Transition from Proliferation to Differentiation in the Root. *Cell* **2010**, *143* (4), 606–616. <https://doi.org/10.1016/j.cell.2010.10.020>.
- (238) Ishida, K.; Yokoyama, R. Reconsidering the Function of the Xyloglucan Endotransglucosylase/Hydrolase Family. *J. Plant Res.* **2022**, *135* (2), 145–156. <https://doi.org/10.1007/s10265-021-01361-w>.
- (239) Zhu, X. F.; Wan, J. X.; Sun, Y.; Shi, Y. Z.; Braam, J.; Li, G. X.; Zheng, S. J. Xyloglucan Endotransglucosylase-Hydrolase17 Interacts with Xyloglucan Endotransglucosylase-Hydrolase31 to Confer Xyloglucan Endotransglucosylase Action and Affect Aluminum Sensitivity in Arabidopsis. *Plant Physiol.* **2014**, *165* (4), 1566–1574. <https://doi.org/10.1104/pp.114.243790>.
- (240) Zhu, X. F.; Shi, Y. Z.; Lei, G. J.; Fry, S. C.; Zhang, B. C.; Zhou, Y. H.; Braam, J.; Jiang, T.; Xu, X. Y.; Mao, C. Z.; Pan, Y. J.; Yang, J. L.; Wu, P.; Zheng, S. J. XTH31, Encoding an in Vitro XEH/XET-Active Enzyme, Regulates Aluminum Sensitivity by Modulating in Vivo XET Action, Cell Wall Xyloglucan Content, and Aluminum Binding Capacity in Arabidopsis. *Plant Cell* **2012**, *24* (11), 4731–4747. <https://doi.org/10.1105/tpc.112.106039>.
- (241) Han, Y.; Sa, G.; Sun, J.; Shen, Z.; Zhao, R.; Ding, M.; Deng, S.; Lu, Y.; Zhang, Y.; Shen, X.; Chen, S. Overexpression of *Populus euphratica* Xyloglucan Endotransglucosylase/Hydrolase Gene Confers Enhanced Cadmium Tolerance by the Restriction of Root Cadmium Uptake in Transgenic Tobacco. *Environ. Exp. Bot.* **2014**, *100*, 74–83. <https://doi.org/10.1016/j.envexpbot.2013.12.021>.
- (242) Kong, X.; Li, C.; Zhang, F.; Yu, Q.; Gao, S.; Zhang, M.; Tian, H.; Zhang, J.; Yuan, X.; Ding, Z. Ethylene Promotes Cadmium-Induced Root Growth Inhibition through EIN3 Controlled XTH33 and LSU1 Expression in Arabidopsis. *Plant Cell Environ.* **2018**, *41* (10), 2449–2462. <https://doi.org/10.1111/pce.13361>.
- (243) Hoecker, U. The Activities of the E3 Ubiquitin Ligase COP1/SPA, a Key Repressor in Light Signaling. *Curr. Opin. Plant Biol.* **2017**, *37*, 63–69. <https://doi.org/10.1016/j.pbi.2017.03.015>.

- (244) Han, Y.-J.; Kim, S.-H.; Kim, J.-I. Phytochrome Phosphorylation in Plant Light Signaling. *Front. Plant Sci.* **2024**, *15*. <https://doi.org/10.3389/fpls.2024.1259720>.
- (245) Yang, J.; Qu, X.; Li, T.; Gao, Y.; Du, H.; Zheng, L.; Ji, M.; Zhang, P.; Zhang, Y.; Hu, J.; Liu, L.; Lu, Z.; Yang, Z.; Zhang, H.; Yang, J.; Jiao, Y.; Zheng, X. HY5-HDA9 Orchestrates the Transcription of HsfA2 to Modulate Salt Stress Response in Arabidopsis. *J. Integr. Plant Biol.* **2023**, *65* (1), 45–63. <https://doi.org/10.1111/jipb.13372>.
- (246) Li, Y.; Shi, Y.; Li, M.; Fu, D.; Wu, S.; Li, J.; Gong, Z.; Liu, H.; Yang, S. The CRY2–COP1–HY5–BBX7/8 Module Regulates Blue Light-Dependent Cold Acclimation in Arabidopsis. *Plant Cell* **2021**, *33* (11), 3555–3573. <https://doi.org/10.1093/plcell/koab215>.
- (247) Mankotia, S.; Jakhar, P.; Satbhai, S. B. HY5: A Key Regulator for Light-Mediated Nutrient Uptake and Utilization by Plants. *New Phytol.* **2024**, *241* (5), 1929–1935. <https://doi.org/10.1111/nph.19516>.
- (248) Li, J.; Zeng, J.; Tian, Z.; Zhao, Z. Root-Specific Photoreception Directs Early Root Development by HY5-Regulated ROS Balance. *Proc. Natl. Acad. Sci.* **2024**, *121* (6), e2313092121. <https://doi.org/10.1073/pnas.2313092121>.
- (249) Miotto, Y. E.; da Costa, C. T.; Offringa, R.; Kleine-Vehn, J.; Maraschin, F. dos S. Effects of Light Intensity on Root Development in a D-Root Growth System. *Front. Plant Sci.* **2021**, *12*, 778382. <https://doi.org/10.3389/fpls.2021.778382>.
- (250) Mankotia, S.; Singh, D.; Monika, K.; Kalra, M.; Meena, H.; Meena, V.; Yadav, R. K.; Pandey, A. K.; Satbhai, S. B. ELONGATED HYPOCOTYL 5 Regulates and Affects Iron Acquisition and Homeostasis in Arabidopsis Thaliana. *Plant J.* **2023**, *114* (6), 1267–1284. <https://doi.org/10.1111/tpj.16191>.
- (251) Lee, B.-R.; Koprivova, A.; Kopriva, S. The Key Enzyme of Sulfate Assimilation, Adenosine 5'-Phosphosulfate Reductase, Is Regulated by HY5 in Arabidopsis. *Plant J.* **2011**, *67* (6), 1042–1054. <https://doi.org/10.1111/j.1365-313X.2011.04656.x>.
- (252) Mankotia, S.; Jakhar, P.; Satbhai, S. B. HY5: A Key Regulator for Light-Mediated Nutrient Uptake and Utilization by Plants. *New Phytol.* **2024**, *241* (5), 1929–1935. <https://doi.org/10.1111/nph.19516>.
- (253) Clemens, S.; Aarts, M. G. M.; Thomine, S.; Verbruggen, N. Plant Science: The Key to Preventing Slow Cadmium Poisoning. *Trends Plant Sci.* **2013**, *18* (2), 92–99. <https://doi.org/10.1016/j.tplants.2012.08.003>.
- (254) Chen, L.; Ma, L.; Bai, Q.; Zhu, X.; Zhang, J.; Wei, Q.; Li, D.; Gao, C.; Li, J.; Zhang, Z.; Liu, C.; He, Z.; Zeng, X.; Zhang, A.; Qu, W.; Zhuang, Z.; Chen, W.; Xiao, Y. Heavy Metal-Induced Metallothionein Expression Is Regulated by Specific Protein Phosphatase 2A Complexes*. *J. Biol. Chem.* **2014**, *289* (32), 22413–22426. <https://doi.org/10.1074/jbc.M114.548677>.

- (255) Sun, S.-K.; Chen, J.; Zhao, F.-J. Regulatory Mechanisms of Sulfur Metabolism Affecting Tolerance and Accumulation of Toxic Trace Metals and Metalloids in Plants. *J. Exp. Bot.* **2023**, 74 (11), 3286–3299. <https://doi.org/10.1093/jxb/erad074>.
- (256) Brumbarova, T.; Ivanov, R. The Nutrient Response Transcriptional Regulome of Arabidopsis. *iScience* **2019**, 19, 358–368. <https://doi.org/10.1016/j.isci.2019.07.045>.
- (257) Selley, L.; Schuster, L.; Marbach, H.; Forsthuber, T.; Forbes, B.; Gant, T. W.; Sandström, T.; Camiña, N.; Athersuch, T. J.; Mudway, I.; Kumar, A. Brake Dust Exposure Exacerbates Inflammation and Transiently Compromises Phagocytosis in Macrophages†. *Metallomics* **2020**, 12 (3), 371–386. <https://doi.org/10.1039/c9mt00253g>.
- (258) Mathissen, M.; Scheer, V.; Vogt, R.; Benter, T. Investigation on the Potential Generation of Ultrafine Particles from the Tire–Road Interface. *Atmos. Environ.* **2011**, 45 (34), 6172–6179. <https://doi.org/10.1016/j.atmosenv.2011.08.032>.
- (259) Wahlström, J.; Olander, L.; Olofsson, U. Size, Shape, and Elemental Composition of Airborne Wear Particles from Disc Brake Materials. *Tribol. Lett.* **2010**, 38 (1), 15–24. <https://doi.org/10.1007/s11249-009-9564-x>.
- (260) Ronov, A. B.; Yaroshevsky, A. A. Chemical Composition of the Earth's Crust. In *The Earth's Crust and Upper Mantle*; American Geophysical Union (AGU), 1969; pp 37–57. <https://doi.org/10.1029/GM013p0037>.
- (261) Kero, I.; Naess, M. K.; Tranell, G. Particle Size Distributions of Particulate Emissions from the Ferroalloy Industry Evaluated by Electrical Low Pressure Impactor (ELPI). *J. Occup. Environ. Hyg.* **2015**, 12 (1), 37–44. <https://doi.org/10.1080/15459624.2014.935783>.
- (262) Cai, Y.; Li, Y.; Liang, G. FIT and bHLH Ib Transcription Factors Modulate Iron and Copper Crosstalk in Arabidopsis. *Plant Cell Environ.* **2021**, 44 (5), 1679–1691. <https://doi.org/10.1111/pce.14000>.
- (263) Yuan, Y.; Wu, H.; Wang, N.; Li, J.; Zhao, W.; Du, J.; Wang, D.; Ling, H.-Q. FIT Interacts with AtbHLH38 and AtbHLH39 in Regulating Iron Uptake Gene Expression for Iron Homeostasis in Arabidopsis. *Cell Res.* **2008**, 18 (3), 385–397. <https://doi.org/10.1038/cr.2008.26>.
- (264) del Pozo, T.; Cambiazo, V.; González, M. Gene Expression Profiling Analysis of Copper Homeostasis in Arabidopsis Thaliana. *Biochem. Biophys. Res. Commun.* **2010**, 393 (2), 248–252. <https://doi.org/10.1016/j.bbrc.2010.01.111>.
- (265) Song, W.-Y.; Choi, K. S.; Kim, D. Y.; Geisler, M.; Park, J.; Vincenzetti, V.; Schellenberg, M.; Kim, S. H.; Lim, Y. P.; Noh, E. W.; Lee, Y.; Martinoia, E. Arabidopsis PCR2 Is a Zinc Exporter Involved in Both Zinc Extrusion and Long-Distance Zinc Transport[W]. *Plant Cell* **2010**, 22 (7), 2237–2252. <https://doi.org/10.1105/tpc.109.070185>.
- (266) Braam, J.; Davis, R. W. Rain-, Wind-, and Touch-Induced Expression of Calmodulin and Calmodulin-Related Genes in Arabidopsis. *Cell* **1990**, 60 (3), 357–364. [https://doi.org/10.1016/0092-8674\(90\)90587-5](https://doi.org/10.1016/0092-8674(90)90587-5).

- (267) Haider, S.; Raza, A.; Iqbal, J.; Shaukat, M.; Mahmood, T. Analyzing the Regulatory Role of Heat Shock Transcription Factors in Plant Heat Stress Tolerance: A Brief Appraisal. *Mol. Biol. Rep.* **2022**, 49 (6), 5771–5785. <https://doi.org/10.1007/s11033-022-07190-x>.
- (268) Erb, M.; Reymond, P. Molecular Interactions Between Plants and Insect Herbivores. *Annu. Rev. Plant Biol.* **2019**, 70 (Volume 70, 2019), 527–557. <https://doi.org/10.1146/annurev-arplant-050718-095910>.
- (269) Kumar, P.; Morawska, L.; Birmili, W.; Paasonen, P.; Hu, M.; Kulmala, M.; Harrison, R. M.; Norford, L.; Britter, R. Ultrafine Particles in Cities. *Environ. Int.* **2014**, 66, 1–10. <https://doi.org/10.1016/j.envint.2014.01.013>.
- (270) Longley, I. D.; Gallagher, M. W.; Dorsey, J. R.; Flynn, M.; Allan, J. D.; Alfarra, M. R.; Inglis, D. A Case Study of Aerosol (4.6 nm < DP < 10 μm) Number and Mass Size Distribution Measurements in a Busy Street Canyon in Manchester, UK. *Atmos. Environ.* **2003**, 37 (12), 1563–1571. [https://doi.org/10.1016/S1352-2310\(03\)00010-4](https://doi.org/10.1016/S1352-2310(03)00010-4).

10 Acknowledgements

Mein besonderer Dank gilt Prof. Dr. Clemens, der mir die Möglichkeit gegeben hat, diese Doktorarbeit anzufertigen. Die kontinuierliche Unterstützung sowie das Vertrauen in meine Arbeit waren maßgeblich für deren Erfolg. Besonders hervorheben möchte ich den Wert des jahrelangen regelmäßigen Austausches, der mein Verständnis von Wissenschaft und argumentativer Klarheit mit Sicherheit langfristig geprägt hat.

Auch gegenüber Dr. Michael Weber und Prof. Dr. Angelika Mustroph will ich meine Dankbarkeit für den angenehmen Austausch und die vielen fachlichen Anregungen ausdrücken.

Ebenso möchte ich mich bei Prof. Dr. Nathalie Verbruggen und Prof. Dr. Marc Hanikenne bedanken, die mich in ihr Forschungsprojekt eingebunden haben und dadurch einen großen Teil dieser Dissertation ermöglicht haben. Bei Noémie Thiébaud bedanke ich mich für das freundschaftliche Verhältnis und das maßgebliche Aufbauen meiner Programmierkenntnisse in R. Bei Dr. Manon Sarthou und Dr. Santiago Prochetto möchte ich mich für die Mitarbeit bei dem eingereichten Manuskript bedanken.

Mein Dank gilt auch dem Bayerischen Landesamt für Umwelt (LfU), das mit dem Forschungsvorhaben BayÖkotox einen weiteren großen Teil der Arbeit ermöglicht hat. Insbesondere möchte ich meine Wertschätzung für die hervorragende Zuarbeit durch Dr. Marina Maier ausdrücken. Ebenso gilt Dr. Thorsten Opel und Dr. Nico Langhof meine Dankbarkeit für die gute Zusammenarbeit.

Darüber hinaus will ich meinen Dank für die angenehme Arbeitsatmosphäre und den freundschaftlichen Umgang gegenüber meinen Kollegen am Lehrstuhl ausdrücken.

Zuletzt will ich die Bedeutung meiner Familie und meiner Freunde hervorheben, die durch ihre stetige Unterstützung und Ermutigung zu dieser Dissertation beigetragen haben. Mein tiefster und größter Dank gilt jedoch meiner Frau, die mir durch unerschütterlichen Rückhalt in jeder Phase dieser Zeit eine unschätzbare Stütze war.

11 Eidesstaatliche Versicherungen und Erklärungen

(§ 9 Satz 2 Nr. 3 PromO BayNAT)

Hiermit versichere ich eidesstattlich, dass ich die Arbeit selbstständig verfasst und keine anderen als die von mir angegebenen Quellen und Hilfsmittel benutzt habe (vgl. Art. 97 Abs. 1 Satz 8 BayHIG).

(§ 9 Satz 2 Nr. 3 PromO BayNAT)

Hiermit erkläre ich, dass ich die Dissertation nicht bereits zur Erlangung eines akademischen Grades eingereicht habe und dass ich nicht bereits diese oder eine gleichartige Doktorprüfung endgültig nicht bestanden habe.

(§ 9 Satz 2 Nr. 4 PromO BayNAT)

Hiermit erkläre ich, dass ich Hilfe von gewerblichen Promotionsberatern bzw. -vermittlern oder ähnlichen Dienstleistern weder bisher in Anspruch genommen habe noch künftig in Anspruch nehmen werde.

(§ 9 Satz 2 Nr. 7 PromO BayNAT)

Hiermit erkläre ich mein Einverständnis, dass die elektronische Fassung meiner Dissertation unter Wahrung meiner Urheberrechte und des Datenschutzes einer gesonderten Überprüfung unterzogen werden kann.

(§ 9 Satz 2 Nr. 8 PromO BayNAT)

Hiermit erkläre ich mein Einverständnis, dass bei Verdacht wissenschaftlichen Fehlverhaltens Ermittlungen durch universitätsinterne Organe der wissenschaftlichen Selbstkontrolle stattfinden können

Ort, Datum, Unterschrift